Università degli Studi "G. d'Annunzio"

Chieti-Pescara

School of Advanced Studies "G. d'Annunzio"

Research Doctorate Program in Biomolecular and Pharmaceutical Sciences

Cycle XXXVII

Study and implementation of innovative catalytic and photoelectrochemical cycles in the energy supply chain of smart grids for the production of green hydrogen and its storage in high-efficiency molecular matrices

Department of Medical, Oral and Biotechnological Sciences

Disciplinary Scientific Field CHEM-05/A

PhD Candidate

Nadia Barbacane

Coordinator of the PhD course

Prof. Assunta Pandolfi, PhD

Tutor

Prof. Pietro Di Profio, PhD

Academic Years 2021/2024

The PhD scholarship was co-financed with resources from the National Operational Program for Research and Innovation 2014-2020, ESF REACT-EU resources Action IV.4 “Doctorates and research contracts on innovation topics” and Action IV.5 “Doctorates on green related topics”.

Statement about the requirements of Ministerial Decree n. 1061/2021 – Action IV.5 – PhD programs on green related topics

As stated in the subject MD 1061/2021, and the ensuing calls for its implementation, the PhD scholarship pertaining to the present PhD thesis has been assigned with the mandatory condition that the candidate would carry out their research activities following a specific and binding research project.

The present research topic is on the study and implementation of innovative catalytic and electrochemical cycles in the energy chain of “smart grids” for the production of green hydrogen, and its storage into highly efficient molecular matrices. This research project has been developed in cooperation with a sponsoring Company, DG Impianti Industriali SpA.

The Call mandated that the candidate would spend at least 6 months working in and for the Company, developing industrial and economic aspects of the project’s Topic. The candidate fulfilled this requirement, and the results of the investigation related to the industrial interests carried by DG Impianti Industriali SpA have been partially reported in Sections 1.1, 1.2 and 1.4 of the theses. A few selected results were withdrawn from publication due to issues related to intellectual property rights, according to the regulations by the National Legislation, the University internal regulations, and the subject MD 1061/2021 and ensuing Call.

Table of contents

CHAPTER 1. Introduction

1.1 The role of oil & gas in the energy transition 1

1.2 Energy mix: where does our energy come from? 6

1.2.1 Energy system heavily relied on fossil fuels: The United States 9

1.2.2 Energy system based on renewables: Sweden and Norway 13

1.2.3 Energy system that uses nuclear: France 16

1.3 Hydrogen: the smallest in size, one of the greatest in importance 18

1.3.1 An overview of hydrogen production methods 22
Gray, black and brown hydrogen 22
Blue hydrogen 24
Turquoise hydrogen 27
White and orange hydrogen 28
Yellow hydrogen 29
Pink, red and purple hydrogen 30
Green hydrogen 32

1.4 Evolving the energy grid: the role of smart grids 34

1.4.1 Efficient hydrogen production and distribution networks through smart grids 37

1.4.2 Hydrogen production costs 40

1.5 Conclusions 46

1.6 Aim of this work 48

1.7 References 49

CHAPTER 2. Green hydrogen production

2.1 The water splitting reaction: the chemistry behind green hydrogen 59

2.1.1 Photocatalytic water splitting 60

2.1.2 Thermochemical water splitting 62

2.1.3 Electrolytic water splitting 64
Reaction mechanism in the electrocatalytic hydrogen evolution 68
Reaction mechanism in the electrocatalytic oxygen evolution 70

2.2 Overview of current catalysts used for Hydrogen Production 72

2.2.1 State-of-the-art catalyst: platinum and its properties 72
Overpotential 74
Tafel slope 74
Turnover frequency (TOF) 75
Electrochemically Active Surface Area (ECSA) 76
Stability 77

2.2.2 Strategies for enhancing platinum catalyst efficiency in HER 77
Nanostructuring 78
Alloying 79
Doping 79
Vacancy-rich materials 80
Carbon-based composite 81

2.3 Exploration of an innovative supporting material: graphene 82

Electrical conductivity 83
Electronic mobility 84
Flexibility and elasticity 85

2.3.1 Graphene production methods 86

2.3.2 Synthesis of Graphene Oxide: Modified Hummers Method 89

2.4 Aim of this work 89

2.5 References 93

CHAPTER 3. Hydrogen production: experimental section

3.1 Graphene liquid phase exfoliation 101

3.1.1 Introduction 101

3.1.2 Materials and methods 102

3.1.3 Discussion and characterization 102

3.1.4 Conclusions 105

3.2 Synthesis of graphene oxide using Modified Hummers method and reduced graphene oxide 107

3.2.1 Introduction 107

3.2.2 Materials and methods 109

3.2.3 Discussion and characterization 109

3.2.4 Conclusions 112

3.3 Synthesis of Copper and Iron Nanoparticles and their size control using inverted micelles 113

3.3.1 Introduction 113

3.3.2 Materials and methods 113

3.3.3 Discussion and characterization 114

3.3.4 Conclusions 118

3.4 Wet chemical synthesis of the trimetallic nanocomposite 120

3.4.1 Introduction 120

3.4.2 Materials and methods 120

3.4.3 Discussion and characterization 121

3.4.4 Conclusions 136

3.5 Electrochemical reduction of graphitic support and Pt, Cu, and Fe nanoparticles 137

3.5.1 Introduction 137

3.5.2 Materials and methods 138

3.5.3 Discussion and characterization 139

3.5.4 Conclusions 144

3.6 Electroreduced platinum nanoparticles anchored on reduced graphene oxide functionalized with para-aminophenyl groups for hydrogen evolution reaction 146

3.6.1 Introduction 146

3.6.2 Materials and methods 147

3.6.3 Discussion and characterization 148

3.6.4 Conclusions 157

3.7 Electrochemical deposition of the trimetallic nanocomposite 159

3.7.1 Introduction 159

3.7.2 Materials and methods 159

3.7.3 Discussion and characterization 160

3.7.4 Conclusions 178

3.8 References 179

CHAPTER 4. Hydrogen storage

4.1 Overview of the traditional storage methods 185

4.1.1 Physical-based storage 186

Physical Storage of Hydrogen in Compressed Gas 187

Liquid/Cryogenic Hydrogen Storage 188
Cryo-compressed hydrogen storage 189

4.1.2 Material-based hydrogen storage 189
Chemical Adsorption 189
Physical Adsorption 190

4.1.3 Emerging Technologies 190
Magnesium-based alloys 190
Nanostructured metal oxides 190
Perovskite oxides 191
Clathrate hydrates 191

4.2 Innovative storage methods: high-efficiency molecular matrices 192

4.2.1 Clathrate hydrate: “the burning ices” 192

4.2.2 History of the clathrate hydrates 194

4.2.3 The main structures of gas hydrates 197
Semi-clathrate hydrates 198
Mixed hydrates 198

4.3 Formation and stabilization of clathrate hydrates 198

4.3.1 Van der Waals and Platteeuw thermodynamic model 199

4.3.2 Kinetic model 201

4.3.3 Co-Formers 202

4.3.4 Promoters 203
Thermodynamic promoters of hydrogen hydrates 203
Tetrahydrofuran (THF) 204

4.3.5 Inhibitors 205

4.3.6 Self-preservation of hydrates 206

4.4 Aim of this work 206

4.5 References 207

CHAPTER 5. Hydrogen storage: experimental section

5.1 Investigation of tuning effect of THF-H_2 binary clathrates 213

5.1.1 Introduction 213

5.1.2 Materials and methods 214

5.1.3 Discussion and characterization 217

5.1.4 Conclusions 227

5.2 References 229

Posters and Orals 231

Publications 232

Acknowledgments 233

« Do what you can,
with what you have,
where you are. »

T. Roosevelt

CHAPTER 1

Introduction

1.1 The role of oil & gas in the energy transition

Energy has always been a fundamental element that has driven human success and progress to this day. From February 2023 to January 2024, the global surface air temperature of the globe was 1.52 °C higher than pre-industrial levels (1850-1900),[1] exceeding the 1.5 °C limit, which was outlined in the 2015 Paris Agreement and related in the COP 28 UAE Consensus in December 2023.[2] The energy transition that we are currently living – the gradual replacement of conventional fossil fuels with energy sources that are more sustainable and renewable – is the most significant weapon available to governments in their fight against global warming.

Gases such as carbon dioxide (CO_2), methane (CH_4), and nitrogen oxide (NO_x) are present in nature known as greenhouse gases (GHG), without which the temperature of the Earth would be excessively low and incompatible with life. These gases are transparent to solar radiation: they allow the arrival of solar rays on our planet, but they are able to retain much of the infrared radiation emitted by the Earth's surface, giving rise to an increase in temperature, commonly known as the *greenhouse effect*. There was a key moment in the history of the Earth in which it was overturned by

the hand of man that coincides with the Industrial Revolution. In the middle of the 18th century the use of fossil fuels became the main source of energy, replacing wind, water and wood, the main materials used in pre-industrial production processes. The speed and efficiency of new technologies have led to growing well-being and significant economic and demographic development. The Industrial Revolution certainly had a significant impact on the abundance and availability of food supplies, health care and quality of life but the population growth and the enormous number of pollutants to support it have caused the climate disruption we are experiencing today. It is widely reported in the scientific literature that the main cause of the rapid increase in global temperatures is linked to the massive release of CO_2 into the atmosphere.[3–5] This means that reducing CO_2 emissions is essential to change things and ensure a more sustainable future for both us and future generations. Replacing fossil fuels across all sectors with technologies that use electricity from renewable sources can make a significant contribution to decarbonization.[6] For these reasons, in the next few years we will witness a transformation of the oil & gas sector, the main sector involved. Nevertheless, oil & gas will not disappear anytime soon. Although it sounds contradictory, that is more of a description. Indeed, when the demand for fossil energies is anticipated to decline over the coming decades, they will still make up a sizeable portion of the energy sources and that will remain true even if global progress toward net zero emission is significantly accelerated.[7] The most daunting and equally critical challenge for the oil & gas sector is to ensure that everyone, far and wide, has access to a global energy supply that is simultaneously competitive, affordable and reliable. All three of these factors are closely intertwined. If they are not addressed, progress in the energy transition may not be sufficient as trade-offs will continue to exist. Recent history is a case in point: despite Germany being one of the most climate-aware countries, following Russia's invasion of Ukraine in 2022, it was forced to respond to the threat of energy shortages by reopening its coal-fired power plants to keep its economy running and ensure an adequate energy supply for its citizens.[8]

With this background in mind, there are two main questions to address: how can the oil & gas sector contribute to the energy transition and what precisely can it do?

How can the oil & gas sector contribute to the energy transition?

According to recent estimates, in conjunction with population growth, energy demand will increase by 3-4% annually until 2050.[9] The oil & gas sector currently covers 80% of global primary energy demand and is expected to reach a growth peak around 2030 and then gradually start to decline. Meanwhile, low-carbon energy sources such as renewables will continue to grow and could contribute 65-85% of global supply sources by 2050.[10] Oil & gas currently provide approximately 170 million barrels of easily accessible, reasonably priced energy per day, which is difficult to replace.[11] One of the aspects to take into consideration is that energy demand is ideally directly proportional to demographic development but in reality, technological and demographic progress travel at different speeds. Around 775 million people worldwide, 1 out of 10, are thought to lack access to electricity, making it difficult for them to light their homes, refrigerate their food, or stay cool in the face of rising temperatures.[12–15] Additionally, approximately 2.4 billion people depend on highly polluting biomass fuels like coal, charcoal, and animal waste for cooking and heating and 4.7 billion people live below what is known as "the empowerment line", which is the ability to safely meet the necessities like food, shelter, healthcare, education, energy, and water.[16] In 2023 the geographic distribution reflected the significant differences in the correlations between regional energy consumption and population size that exist between the nations of the Northern and Southern Hemispheres. The average energy consumption per person was 30 GJ in South Asia, Africa, and Southern and Central America. In comparison, the average energy consumption per person in the Middle East, The Commonwealth of Independent States (CIS), and North America was 180 GJ. The ratio in North America was nearly three times higher than the 77 GJ global average (Figure 1).

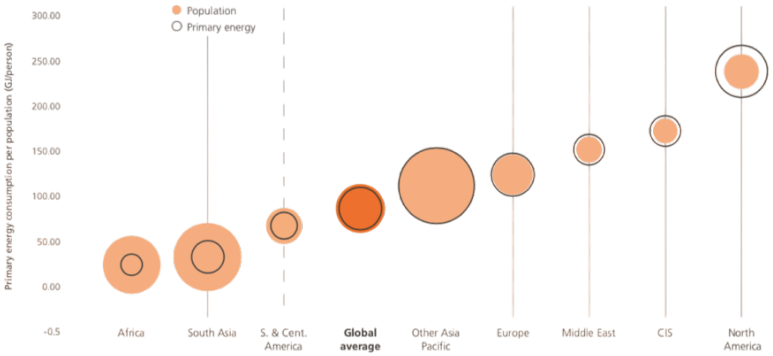


Figure 1. Primary energy consumption per population. Today, both Africa and South Asia have low levels of energy demand relative to the size of their population unlike North America.[15]

Greenhouse gas emissions per capita show a similar trend. The graph in Figure 2 shows a global average of 6.7 $MtCO_2e$ produced in 2023. Below this value Africa, South Asia, and Southern and Central America produced an average of 2 $MtCO_2e$, while the amount of CO_2 released by Other Asia Pacific, Middle East and the CIS, 11,5 $MtCO_2e$, was well above the global average. The only two nations to exceed the global average for primary energy consumption per GDP are Europe and North America, even though their CO_2 concentrations are lower than the global average.

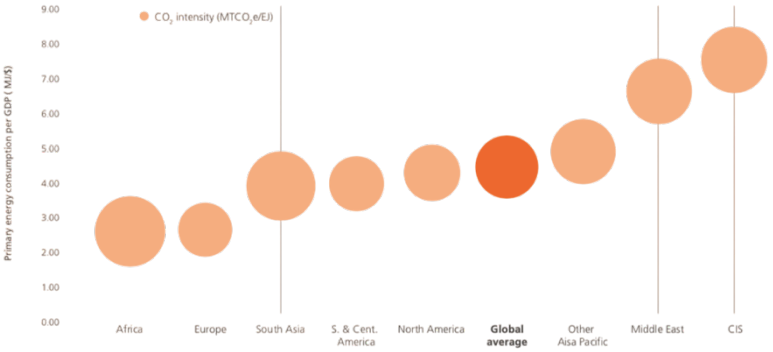


Figure 2. Primary energy consumption per GDP (MJ/$). Europe and Southern & Central America are the only regions to be below both the global average for CO_2 Intensity and Energy Consumption per GDP.[15]

In essence, the energy transition is exactly what its name suggests: the world cannot simply stop using fossil fuels from one day to the next. The oil & gas sector plays a fundamental role in coordinating social, economic, political and above all environmental aspects.

A confused transition that ignores sustainability, affordability, reliability and competitiveness runs the risk of losing public support, making the path to net zero even more difficult than it already is and posing a threat to lives and livelihoods. While the new system is being built simultaneously, the oil and gas sector has two tasks: to ensure that the current system can continue to support and improve people's way of life, making investments in renewables competitive and politically acceptable, while achieving the lowest possible emissions.

What precisely can the oil & gas industry do?

According to the COP28 held in Dubai in 2023, methane emissions should be reduced to almost zero by 2030. Methane is a powerful greenhouse gas produced by the energy sector that contributes about 30% of the temperature increase. Intensive livestock farming, landfill waste and energy plants account for 40% of man-made emissions.

As specified by the Global Methane Assessment (GMA),[17] a 45% reduction in global methane emissions by 2030 is without a doubt the most economical way to keep global warming to 1.5 °C. This strategy has substantial potential benefits for the economy and is in line with the Paris Agreement.

About 20% of these methane emissions, or roughly 5% of total GHG emissions in CO_2 equivalent, are caused by fugitive methane emissions (FME) from fossil fuels, while 40 Mt of methane or roughly 1.5% of global GHG emissions are caused by fugitive methane emissions from natural gas activities. Several companies are already working to reduce fugitive emissions through blockchain technology and satellite and laser-based monitoring, the most frequently used methods.

The second pledge is to operate at net zero emissions by 2050. Opportunities include, but are not limited to, electrifying furnaces, pumps, and motors; improving energy efficiency; and reducing transportation emissions by using artificial intelligence for preventive maintenance.

Longer term, and possibly more potently, the oil & gas sector has a wealth of resources that could allow it to lead the development of promising but expensive and still in its infancy decarbonization technologies like hydrogen and carbon capture, utilization and storage (CCUS).[11]

Carbon capture is a key component of all net-zero scenarios. Carbon capture is already being used by major oil and gas companies for improved oil recovery. Technically and financially, it would be a huge success if they could make it work on a much larger scale.

The oil and gas sector offers advantages to both CCUS and hydrogen, particularly its capacity to build large-scale projects, its knowledge of related technologies, and its pipeline infrastructure. Technologies such as hydrogen and CCUS, currently in the prototyping or demonstration phase, could account for nearly half of emissions reductions between now and 2050.[18] The oil and gas industry could discover profitable low-carbon strategies that can help it navigate the transition to a low-carbon future by leveraging its current strengths in this high-potential area.

1.2 Energy mix: where does our energy come from?

The term "energy mix" refers to a set of different primary energy sources from which secondary energy is produced for direct use, such as electricity. Primary energy is energy that occurs naturally and has not been subjected to any human-designed conversion process. It includes the energy contained in raw fuels and other forms of energy, including waste, received as input into a system. Primary energy can be non-renewable or renewable while secondary energy are forms of energy that have been transformed from primary energy sources.

Coal, oil, gas, nuclear, hydropower, solar, wind, and biofuels are just a few of the many different energy sources that come to mind when we think about

energy mixes today. A few centuries ago, however, our energy mixes were relatively homogeneous, and the transition between different sources was extremely slow. Figure 3 illustrates the world's primary energy consumption since 1800: until the middle of the 19th century, the most common energy source in the world was traditional biomass, solid fuels like wood, crop waste, or charcoal. However, by the turn of the 20th century, coal had become the dominant energy source, followed by gas, oil, and hydropower. Nuclear power was only introduced in 1960s, while renewables like wind and solar appeared later in 1980s.

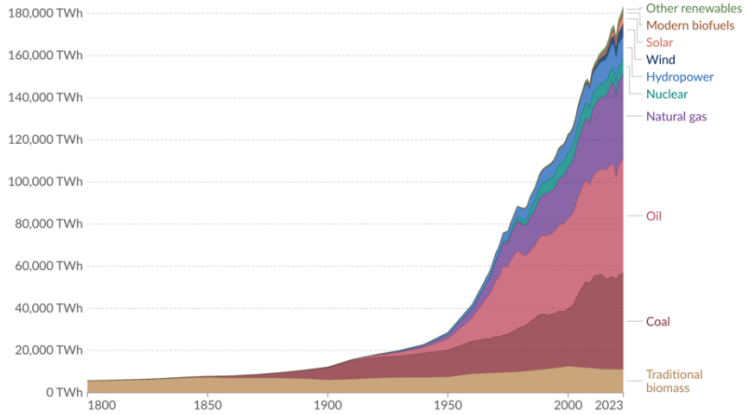


Figure 3. Global primary energy consumption by source.[19]

A new challenge that differs greatly from the past is the pace and scope of the energy transition we require today to move from fossil fuels to low-carbon energy. Most markets have recovered and surpassed the pre-pandemic levels of 2019 after resolving supply chain issues, which has led to an unprecedented increase in production and consumption in 2023.

The way a country's energy system is organized is one of the most crucial components in managing the country's economic policies. A robust and resilient economy is currently impossible without a comprehensive plan that includes alternative solutions to manage both energy surpluses and deficits. Countries often face ineffective systems due to political and economic issues, which are too often influenced by changes in energy

supply. In fact, national energy policy can be divided into two main categories:

Non-diversified energy: large-scale use of a single energy source, whether renewable or not, from either domestic or imported sources. Examples could include the republic of South Africa (15289 kWh of 22302 kWh, 69%) and China (17913 kWh of 33245 kWh, 53%);[15]

Diversified energy: despite supply fluctuations caused by nature, the nations' energy supply is consistent due to the utilization of a variety of energy sources. Examples include Sweden (12203 kWh, 22% of the total consumed, which was produced from oil, 11376 kWh, 21% from nuclear power, 16165 kWh, 30% from hydroelectric power, and 8401 kWh, 15% from wind power out of a total of 54699 kWh) and Canada (31171 kWh, or 31% of the total consumed, which was produced from oil, 31130 kWh, 31% from natural sources).[15]

In a world that is expanding economically and demographically, energy diversification is the cornerstone of a plan to reach the Net-Zero goal while guaranteeing energy access and supply security. The following diagrams in Figure 4 show the breakdown of the energy mix - fossil fuels, nuclear and renewables - by country.

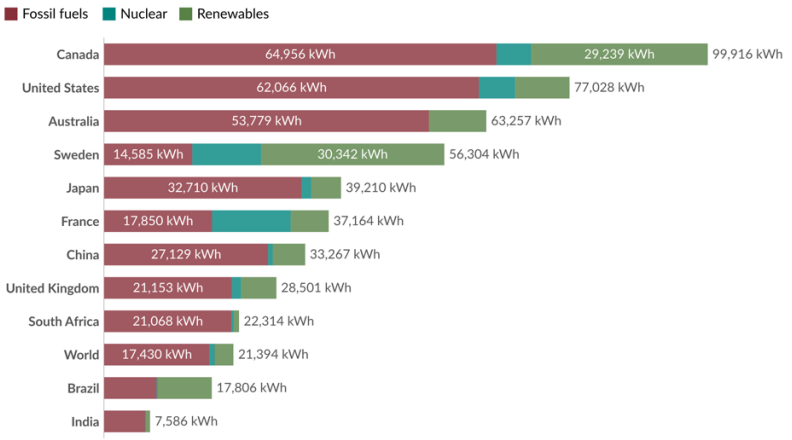


Figure 4. Energy supply distribution according to per capita energy from fossil fuel, nuclear and renewables, 2023.[19]

As is intuitive to understand, energy resources are not distributed evenly around the Earth. The diversification of the energy approach that we are witnessing is evolving based on the availability or otherwise of a given energy source in a country, both due to local availability and political considerations. While fossil fuel deposits are influenced by animals and climate that inhabited the area millions of years ago, as well as weather affects renewables energy supply, political influences play an important role in the formulation, implementation, and public support of nuclear energy policies, which are controversial due to their environmental risks and benefits. Three models that illustrate various facets of three distinct energetic systems can be established to better understand the criticalities of energy source distribution.

1.2.1 *Energy system heavily relied on fossil fuels: The United States*

Today, the United States, with its 21,102.20 TWh, is the world's second largest producer and consumer of energy, after China with 38,677.41 TWh[15] (Figure 5).

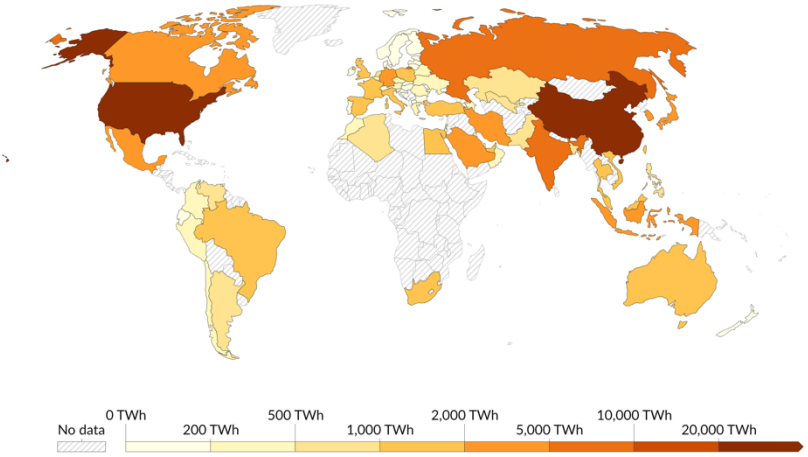


Figure 5. Fossil fuel consumption measured in terawatt-hours.[19]

The energy demand in the United States is largely driven by fossil fuels, with petroleum accounting for 34.8%, natural gas 27.5%, and coal 17.9%. In

contrast, nuclear and renewable energy make up 9.6% and 8.3% respectively.[20] International trade in coal, oil, and gas increased by 53% in 2023 compared to 2000. Beginning in the early 2000s, the expansion of unconventional oil and gas has changed the energy system in North America over the last 20 years. Consequently, over the last decade, the area has transitioned from being a net importer of energy to a net exporter. North American oil production exceeded domestic consumption by 16% in 2023, while gas production was 14% higher than demand.[15]In 2024, the market for natural gas and crude oil had to negotiate a challenging environment that included fluctuating demand, tightened geopolitical tensions, macroeconomic weakness, and a persistent emphasis on the energy transition.[21] Brent crude oil prices showed a minimal average monthly change and a monthly range-bound movement between $74 and $90 per barrel, making it one of the most stable years in the previous 25 years.[22] Almost $136 billion in buybacks and $213 billion in dividends were paid out by the oil and gas sector globally between January 2024 and mid-November 2024. In order to maintain strong financial performance and investor trust, oil and gas companies have prioritized high-return investments and kept production efficiency as their top priority. Over the past four years, the industry's net profit has increased by almost 16%, but its capital expenditures have increased by 53%. In fact, oilfield services reported the best performance in the last 34 years for the years 2023-2024. The resultant of a massive production of fossil fuels brings two main consequences. Energy sector generates millions of jobs around the United States, with an 8% of the gross domestic product.[23] Furthermore, many people are encouraged to make investments in the oil and gas sector due to the fact that there are currently no special credits or deductions available to the oil & gas sector. The U.S. tax code has allowed corporate taxpayers to recover costs since its inception, and even in the *Tax Cuts and Jobs Act of 2017*. These cost recovery mechanisms available for each sector should in no way be confused with "subsidies", i.e., direct public spending or "tax loopholes".

But the economic aspect hinders the push for energy transition. It is well known that CO_2 produced by human activities is the main factor causing global warming.[3–5] According to the Annual Energy Outlook (EIA, 2023), depending on economic growth and the cost of producing zero-carbon technologies, U.S. CO_2 emissions from energy-related sources, such as transportation (vehicles, aviation), industrial processes, electricity generation (coal, natural gas, and oil), and residential and commercial processes, are 25–38% lower than they were in 2005, far short of the 50-52% target (Figure 6).

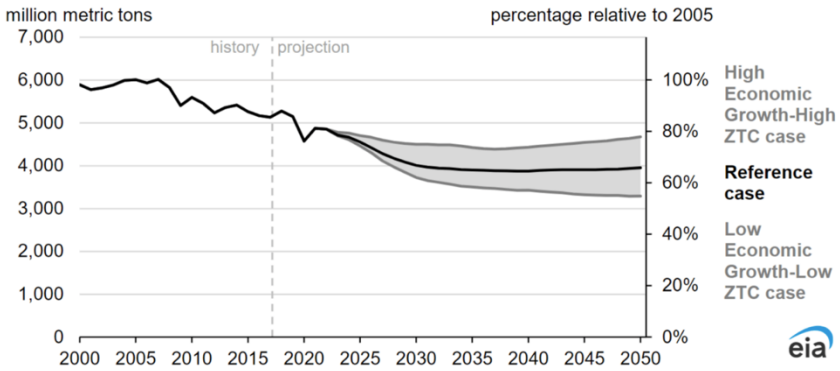


Figure 6. Total U.S. energy-related carbon dioxide emissions, by AEO2023 (2000-2050). Shaded regions represent maximum and minimum values for each projection year across the AEO2023 Reference case and side cases. ZTC=Zero-Carbon Technology Cost.[24]

The United States' withdrawal from the Paris Agreement could have a significant impact on the amount of CO_2 released into the atmosphere. Xu Gong et al. investigated how United States political choices have an effect on the financial results of fossil fuel and renewable energy companies under the Paris Agreement.[25] They used a multi-criteria approach to decision analysis, the Technique for Order of Preference by Similarity to Ideal Solution (TOPSIS). The foundation of TOPSIS is the idea that the alternative that is selected should have the two shortest geometric distances from the positive ideal solution (PIS) and the negative ideal solution (NIS). Due to anticipation, renewable energy companies' average TOPSIS scores

increased by 6.05% during pre-Paris negotiations (2013-2015) and then by 3.7% during the Obama administration (2015-2016). Trump's withdrawal announcement (2016-2018) caused a 7.4% drop, while Biden's government and focus on climate change raised renewable energy companies' scores by 5.51% (2018-2019). These changes demonstrate how closely politics and energy finance are related. Despite this current picture, some businesses are investing more in low-carbon technology initiatives in an effort to mitigate the risks connected to the conventional oil and gas market. Analyst Wood Mackenzie predicts that by 2025, at least three large-scale projects will have reached final investment decision (FID), boosting investment in the US blue hydrogen market, totaling over 1.5 million tons per annum (Mtpa) in capacity, ten times higher than FIDs for green hydrogen[26] (Figure 7).

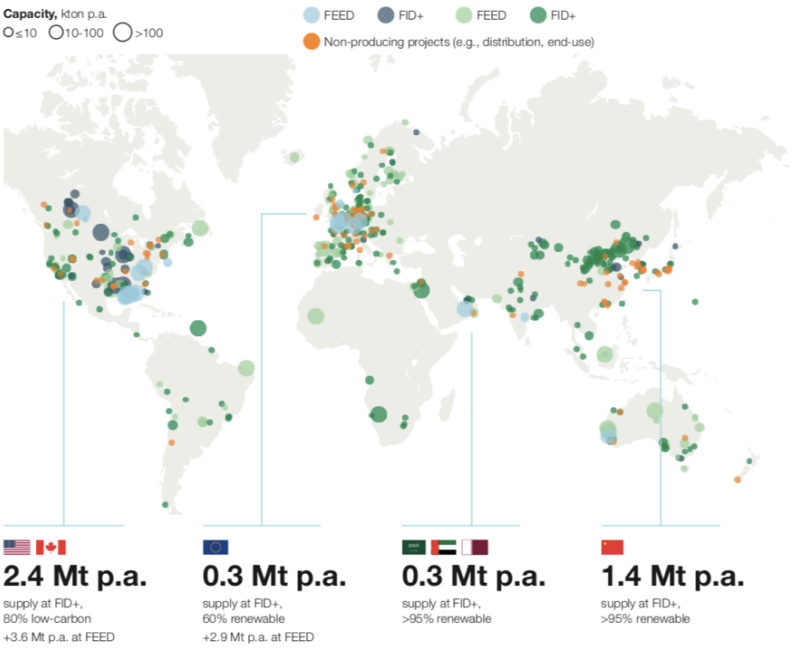


Figure 7. Clean hydrogen FID+ projects globally. Size of bubble indicate production capacity in 2030.[27]

In addition, there will be a substantial uptick in project cancellations and significant headwinds for the green hydrogen industry in the upcoming year. This would solidify the United States as the world's top producer of blue hydrogen, as it currently has the most post-FID blue hydrogen capacity (2.4 Mt) and additional 3.6 Mt in Front End Engineering and Design (FEED).[27]

1.2.2 *Energy system based on renewables: Sweden and Norway*

In some countries, the environmental aspect of the energy transition represents a strong determining factor in the public debate on the creation of plans for the development of new energy sources that accompany the new "green wave". The nations making the greatest push in this direction are clearly those characterized by a prosperous social and economic fabric that can bear the costs of environmentally friendly energy policies without compromising the quality of life of individual nations. Figure 8 shows the global distribution of energy supply.

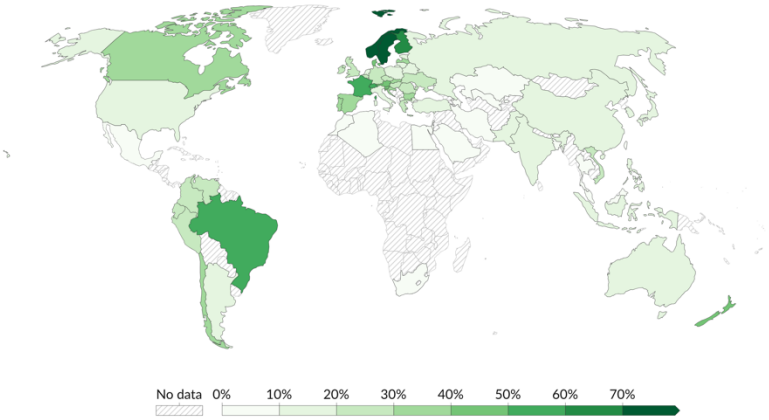


Figure 8. Share of renewable energy compared to total production for each country. The nations shaded in gray did not submit any numerical data.[19]

It is easy to recognize that the Nordic countries are the countries with the biggest push towards renewable energy. The energy supply of Sweden and Norway is represented by 74.1% and 72.1% respectively of the total

available energy sources.[19] Since the 1970s, Sweden has made an effort to lead and be at the forefront of environmental and climate issues.[28] The Stockholm Conference, held in Sweden in 1972, was a watershed in the recognition of environmental issues as global concerns. According to France's first environment minister, Robert Poujade, "Sweden was considered the best example in terms of the environment".[29] Being the tenth largest crude oil exporter in the world, Norway is one of the most unusual situations to take into account. A national fund known as *Oljefondet* (Oil Fund), later renamed *Statens pensjonsfond utland* (Government Pension Fund Global), was established to reinvest the proceeds from the sale of hydrocarbons in the development of renewable energy systems since the country could have met all of its energy needs through self-production thanks to domestic oil production.[30,31]

The fund invested more than one billion dollars in Copenhagen Infrastructure Partners (CIP)[32] in 2024 alone, focusing on the renewable energy industry.

Norway is an excellent example of a developed country that uses a consistent amount of renewable energy. The presence of hydropower at 64% of total supply in 2023 (353.48 TWh out of 553.08 TWh total supplied) is indicative of a self-supporting energetic economy.

Figure 9 demonstrates the astonishing consistency of the hydropower plant distribution across the country, demonstrating once more how this country was able to secure a carbon neutral and fully independent energy supply through investments made with money reinvested from oil exports. The following are the benefits of this kind of energy system:

- *Independence from foreign supplies*: since these systems produce electricity from renewable sources, no energetic raw materials need to be imported. This significantly lowers the quantity and price of generated energy's natural fluctuations
- *Clean energy* an estimated 4 billion tons of CO_2 emissions should be avoided if hydroelectric power plants were to replace coal-fired ones.

The primary drawbacks are:

- *Geographical restriction*: it is challenging to supply countries with high energy consumption since the plant must be constructed in locations with ideal qualities
- *Low capacity*: the capacity factor of renewable energy is the ratio of the average energy produced over time to the energy that could have been produced

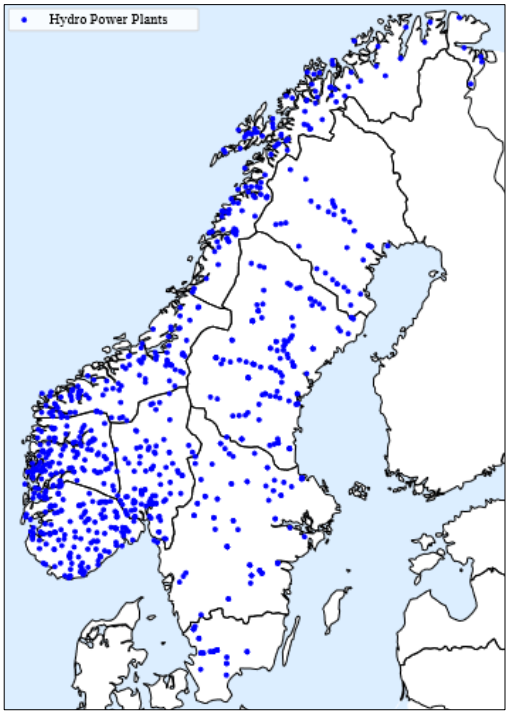


Figure 9. Distribution of hydropower plants between Norway and Sweden.[33]

- *Cost of construction*: compared to conventional sources, the cost of a plant per kilowatt generated is much higher, which makes it extremely challenging to build them in less developed parts of the world. It should

be remembered that compared to conventional sources, such power plants can only deliver far lower power outputs

- *Discontinuity in electricity supply* due to the close relationship between renewable energy sources and natural fluctuations, it is impossible to determine with precision how much power is needed to guarantee a steady supply, necessitating the use of batteries. It is clear that, at least in the current situation, a completely renewable energy supply is not only a feasible scenario but also one that is only an option in a small number of countries worldwide. In certain situations, CAPEX cannot be justified as having a sufficiently alluring Return of Investment (ROI) for both public and private financiers due to the low powers generated and high costs.

1.2.3 *Energy system that uses nuclear: France*

France is an extremely intriguing case study to investigate further because it is clear that the percentage of nuclear energy supplied (843.04 TWh of nuclear energy out of a total of 2406.63 TWh, corresponding to 35% of the national energy supply) is significantly higher than the global average as shown in Figure 10.

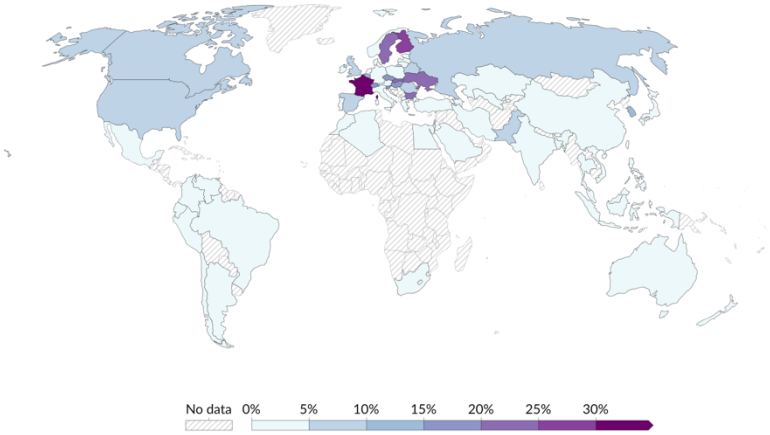


Figure 10. Share of primary energy consumption from nuclear, 2023[19]

French nuclear power began to develop in the 19th century, when Henri Becquerel studied natural radioactivity and Mr. and Mrs. Curie studied the radioactivity of different radioisotopes. The first nuclear reactor was constructed in 1956, but significant technological and infrastructure advancements did not take place until 1973, coinciding with the Yom Kippur War-induced oil crisis and the emergence of the OPEC cartel. This program aimed to make the French economy rely almost exclusively on nuclear energy. Because it was not discussed beforehand outside of Parliament, this move was viewed as extremely controversial by the public and scientific community. In fact, it gave rise to the Groupement des scientifiques pour l'information sur l'énergie nucléaire, which is currently regard as the largest nuclear community in the world.

As a quick comparison with the Scandinavian countries, the drive to create an energy economy that is less reliant on oil was motivated by practical considerations rather than ideological ones. After his plan was announced, Pierre Messmer responded to criticism by saying "France has no oil but has many thinking heads". However, a daring action that enabled a titanic feat.

In 2022, France relied on five major suppliers of uranium to power its power plants: Uzbekistan (12.9%), Namibia (15.8%), Australia (13.9%), Kazakhstan (37.3%), and Niger (20.2%).[34] The case study of Niger, a former French colony, is the most fascinating. The company Oran (previously Areva) is in charge of uranium extraction nationwide, and it controls three uranium mines: the Aïr mines, the Akokan mining site and the Imouraren mine. The most crucial thing to keep in mind is that the French government controls 90% of Oran, which essentially means that the mines in Niger are French properties. As a result, the raw material's price drops significantly, enabling the massive development of nuclear energy.[35] However, France is in a position to rely heavily on economy due to the low cost of the raw material and the efforts made over the past century to develop nuclear technologies. With fifty-eight nuclear reactors constructed nationwide, seven nuclear energy research facilities, and three nuclear waste collection

sites, France is able to complete the uranium exploitation cycle entirely within its borders, according to an analysis of the map in Figure 11.

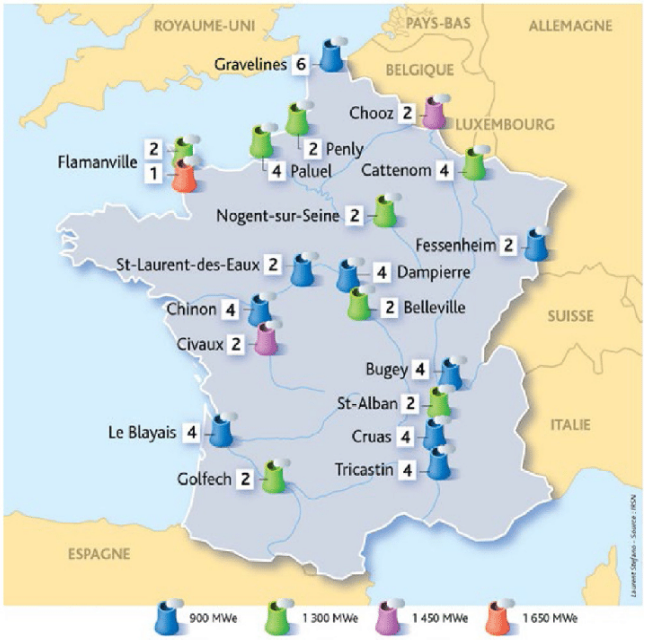


Figure 11. Nationwide distribution of the nuclear plants in France in 2018. EPR Flamanville 1650 MWe under construction. Numbers represent the number of reactors per power station.[36]

1.3 Hydrogen: the smallest in size, one of the greatest in importance

One proton and one electron make up the most basic and prevalent element in the universe: Hydrogen. Hydrogen was discovered by the English physicist Henry Cavendish in 1766, who called it "inflammable air".[37] Seven years later, French chemist Antoine Lavoisier gave it the name hydrogen, which derives from the Greek *hydro* for "water" and *genus* for "generate" meaning water forming.[38] Also, he showed that a molecule of hydrogen is made by two atoms. With its weight of 2.016×10^{-3} kg/mol, hydrogen is the lightest molecule and the richest in energy per-unit mass (142 MJ/kg), almost three times higher than liquid fuels (47 MJ/kg).[39]

Though hydrogen is the most common element constituting ~70% of the visible universe, free hydrogen is not readily available on Earth. Because it is produced from other sources of energy, it is known as an energy carrier: it stores and transports energy produced from other resources, like fossil fuels, water and biomass.[40] It is a clean-burning fuel, and when combined with oxygen in a fuel cell, hydrogen produces heat and electricity with only water vapor as a by-product. The fact that it does not produce carbon dioxide or other greenhouse gases makes one think of a "hydrogen economy". A British geneticist and evolutionary biologist, John Burdon Sanderson Haldane, theorized the concept of a society that uses hydrogen as the primary means of energy storage in 1923.[41] Anticipating the exhaustion of Britain's coal reserves for power generation, Haldane proposed a network of hydrogen-generating windmills to produce hydrogen and oxygen for long-term energy storage through electrolysis. The term "hydrogen economy" itself was originally coined by John Bockris during a talk he gave in the 1970s at General Motors Technical Center.[42] In Bockris' innovative vision, supported by nuclear and solar power, hydrogen would help address growing concern about fossil fuel depletion and, with its abundance in the universe, would satisfy humanity's energy demand. Also, by serving as an energy carrier for end-uses in which electrification is not suitable, nations could reduce their dependence on fossil fuel from politically unstable regions and improved, economic stability.[43] In 1970, Lawrence W. Jones of the University of Michigan published a technical report in which he echoed Bockris' dual rationale of energy security and environmental protection.[44] In contrast to Haldane and Bockris, Jones was primarily concerned with nuclear power as an energy source for electrolysis, and particularly hydrogen in the transportation sector, where he regarded aviation and heavy goods transport as the top priorities. In addition, he proposed hydrogen as an alternative fuel for cars, buses, and trains, but he did not consider hydrogen as a source of energy for homes. During the 2000s, some critics and proponents of alternative technologies described hydrogen economy attention as hype, and investors lost money when the bubble

burst. The energy carrier regained popularity in the 2010s with the formation of the World Hydrogen Council in 2017. Commercial hydrogen fuel cell vehicles were released by several manufacturers, with Toyota, Hyundai, and Chinese industry groups planning to increase the number of cars into the hundreds of thousands within a decade. The worldwide significance of hydrogen in cars is decreasing when compared to earlier forecasts, as only 70,200 hydrogen vehicles were purchased by the end of 2022, while 26 million electric vehicles were sold.[45] The early 2020s outlook on the hydrogen economy reflects earlier perspectives, highlighting the importance of integrating electricity and hydrogen, and utilizing electrolysis as the primary method for hydrogen production. Their primary focus is on limiting global warming to 1.5 °C[46] and giving precedence to the creation, distribution, and application of green hydrogen for heavy industry (examples include using high heat procedures with power, raw materials for creating eco-friendly ammonia and natural compounds, and as a substitute for coal-based coke in steel production.), long-distance transport (e.g., shipping, aviation and to a lesser extent heavy goods vehicles), and storing energy in the long run. The realization of an economy based on renewable hydrogen, depicted in Figure 12, relies on using renewable energy sources to produce hydrogen.

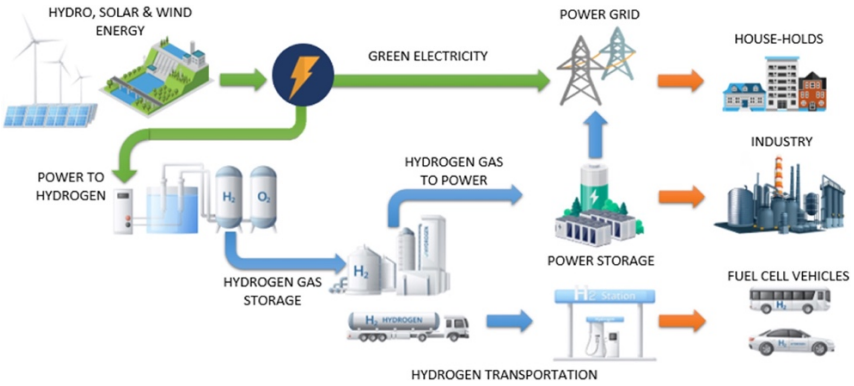


Figure 12. Vision of a renewable hydrogen economy.

In 2021, 94 million tons of molecular hydrogen was produced. Around one-sixth of this total came from the petrochemical industry's processes. More than 98% of hydrogen is produced in specialized facilities using fossil fuels. Less than 1% of dedicated hydrogen production is low carbon, such as steam fossil fuel reforming with carbon capture and storage, hydrogen produced through electrolysis or extracted from the subsoil.

While its potential is significant, overcoming barriers to its daily use is crucial. Some key challenges and considerations surrounding hydrogen as an energy solution are given in Table 1. Ongoing research is indeed promising, with innovations in all these areas gradually addressing the challenges. Nowadays, renewable energy sources such as energy storages are worldwide integrated into smart grids.[47]

Table 1. Main hindering barriers to hydrogen economy.

Production costs	Innovative hydrogen production methods, such as electrolysis, can be expensive, especially if powered by renewable energy.
Environmental impact	Traditional hydrogen production methods are cheaper but not equally ecofriendly.
Infrastructure development	A widespread hydrogen economy requires substantial investment in brand new infrastructures, including production facilities, pipelines and refueling stations or in adapting existing ones.
Storage and transport	Hydrogen has a low energy density by volume, 1 kg of hydrogen gas occupies over 11 m^3 at room temperature and atmospheric pressure[39,] which poses challenges for storage and transportation, two of the main problems hindering the diffusion of hydrogen economy. The classical storage methods based on compression and liquefaction are an established and efficient approach, but they involve huge problems of safety and the associated costs of compression work and cooling are not negligible.
Safety concerns	Hydrogen is a flammable gas and requires careful handling and storage to ensure safety. Developing robust safety protocols and technologies is essential for public acceptance.
Scaling up technologies	Scaling up production and usage technologies is necessary for hydrogen to become a viable option in various sectors, from transportation to industry.

1.3.1 An overview of hydrogen production methods

Even though hydrogen burns cleanly, not all hydrogen production processes are equally ecofriendly.[40] A color coding has been adopted to indicate the source of energy, the source of hydrogen, the production technique, and whether or not CO2 is developed and released or captured during hydrogen production. Gray, blue, and green hydrogen are three types that are certainly the most well-known but even if there is still much confusion surrounding the hydrogen classification and production techniques are constantly being updated, almost everyone agrees on indicating at least twelve types of hydrogen.

Gray, black and brown hydrogen

The most common form of hydrogen produced is gray hydrogen, extracted from natural gas or methane through a process called steam reforming of natural gas, or also known as steam methane reforming (SMR). This is one of the cheapest hydrogen production technologies in terms of operation and production costs. The SMR unit receives desulfurized methane at a pressure of 35 bar and a high temperature (697-827 °C) in the presence of a nickel-based catalyst. Additionally, in order to produce the steam required for the process, the SMR boiler must be heated. In this process three distinct reactions occur and are reported in Table 2. Except for the Equation 2 which is mildly exothermic, the positive free energy values indicate that these reactions are highly endothermic, that means that a large amount of heat is necessary to keep a constant temperature during the process. The combustion of gases generated by a pressure swing adsorption (PSA) unit produces this heat and it is the point at which CH_4, and steam react to produce CO and H2.[48,49] Optimal steam methane reforming operating conditions lie within a temperature range of 800-900 °C at a pressure of 20-30 bar. Following that, CO is subjected to another reforming process using water-gas shift (WGS) reactors at approximately 197-246 °C and 347-547 °C, which results in additional H_2 production.[50,51]

Table 2. Reactions involved in the steam reforming process.

Reaction	Name	Heat of reaction ΔH°298K (kJ/mol)	#
$CH_4 + H_2O \rightarrow CO + 3\,H_2$	Steam reforming reaction	206	(1)
$CO + H_2O \rightarrow CO_2 + H_2$	Water-gas shift reaction	−41	(2)
$CH_4 + 2H_2O \rightarrow CO_2 + 4H_2$	Direct steam reforming reaction	165	(3)

Black coal (anthracite, bituminous and sub-bituminous), brown coal (lignin) and biomass are treated by gasification to obtain black or brown hydrogen when CO_2 is not separated through carbon capture process.

During gasification the fossil-based carbonaceous or organic materials are partially oxidized at high temperatures, with a controlled amount of oxygen and steam to produce gaseous fuel, conventionally denoted as synthesis gas. The syngas is composed of carbon monoxide (CO) and hydrogen (H_2) with small quantities of carbon dioxide (CO_2), nitrogen (N_2), methane (CH_4) and other light hydrocarbons. As gasifier fuels, biomass and coal vary in many properties, such as calorific value or coarse analyses, fixed carbon, volatile matter, ash content and moisture content. For example, the organic matter in biomass contains a large fraction of volatile material, namely 70–80 wt%. Coals range from lignite with approximate volatile matter of 27% to anthracite with an average of 5%, with sub-bituminous and bituminous coals intermediate between these values.

Also, it has been observed that lower oxygen content in the fuel corresponds to a higher carbon boundary temperature. Optimum gasification temperatures were found to increase from 782 °C for biomass (average composition $CH_{1.4}O_{0.6}$) to 1668 °C for gasification of coal (average composition $CH_{0.95}O_{0.2}$) gasification.[52] The reactions involved during gasification are reported in Table 3.

Table 3. Reactions involved in the gasification process.[53]

Reaction	Name	Heat of reaction $\Delta H°_{298K}$ (kJ/mol)	#
$C_{(s)} + O_2 \rightarrow CO_2$	Carbon combustion reaction	−394	(4)
$C_{(s)} + \frac{1}{2} O_2 \rightarrow CO$	Carbon partial oxidation reaction	−123	(5)
$C_{(s)} + CO_2 \rightarrow 2\ CO$	Boudouard reaction	172	(6)
$C_{(s)} + H_2O \rightarrow CO + H_2$	Water-gas reaction	131	(7)
$C_{(s)} + 2\ H_2O \rightarrow CO_2 + 2\ H_2$	Water-gas reaction	77	(8)
$C_{(s)} + 2\ H_2 \rightarrow CH_4$	Methanation reaction	−75	(9)
$CH_4 + H_2O \rightarrow CO + 3\ H_2$	Steam reforming reaction	206	(1)
$CO + H_2O \rightarrow CO_2 + H_2$	Water-gas shift reaction	−41	(2)

Blue hydrogen

When steam reforming is followed by a CO_2 capture process (CCS), blue hydrogen is obtained. This process can therefore be considered carbon neutral (Figure 13).

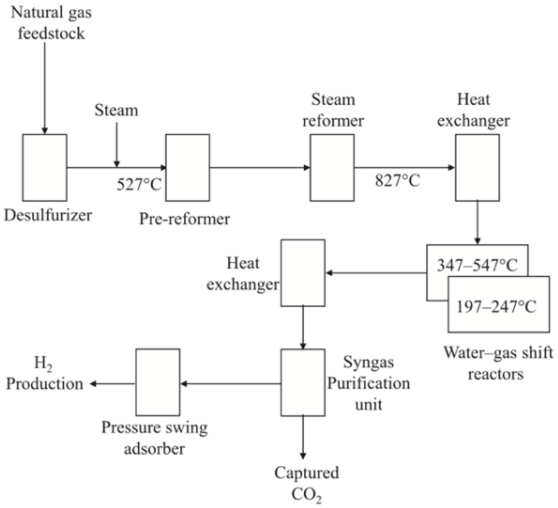


Figure 13. Conventional SMR process for H_2 production with carbon capture.[54,55]

Although the way blue hydrogen is produced is considered carbon neutral, the role of blue hydrogen in the energy transition is a controversial topic and it can't be a long-term strategy. While producing blue hydrogen could increase production costs and make it more difficult to compete with other options, it is a necessary step in the transition between gray and green hydrogen. Producing blue hydrogen has advantages and disadvantages:

- Potential to reduce carbon emissions: when compared to other options and conventional production methods, blue hydrogen has the potential to significantly reduce carbon emissions. The CO_2 produced during the manufacturing of blue hydrogen is sequestered and kept underground. Theoretically, this leads to carbon-neutral procedures.
- Availability on short notice: when compared to green hydrogen, blue hydrogen can be produced much more quickly thanks to technological and industrial advances. Companies with limited resources who find they are not getting enough energy for their operations may find this advantageous.
- The processes surrounding blue hydrogen continue to improve although there is still much to be done, the technology for producing blue hydrogen has made significant progress. Investment in the production method ensures that the procedures will remain cheaper and more efficient. It is possible that these expenses will serve purposes other than blue hydrogen.
- There is a risk of CH_4 and CO_2 emissions: the fact that methane will escape is the main worry when it comes to blue hydrogen. Fugitive leaks, or methane leaks from drilling, extraction, and transportation operations, are a consequence of natural gas production. Methane initially appears to be a better choice because it doesn't last as long as carbon dioxide. But methane is a far more power greenhouse gas than carbon dioxide: 28 or 36 tons of carbon dioxide can have the same impact as one ton of methane. Furthermore, although carbon dioxide is captured during the blue hydrogen production process, the capture

method is not infallible. Carbon dioxide can leak out during capture and storage due to inefficiencies and leaks.

- Producing blue hydrogen can be energy intensive because both steam methane reforming and carbon capture requires a lot of energy. The use of fossil fuels is not avoided, which would offset some of the advantages of using blue hydrogen in terms of reducing emissions.
- Carbon capture and storage technologies can be complex and expensive to implement. The long-term storage of the captured carbon dioxide can also be difficult, and their efficacy can vary based o geological conditions. Despite its advantages, these obstacles may lead to increased expenses and make it harder for blue hydrogen production to compete with other options.

Several plants of CCS to produce blue hydrogen are currently active. Table 4 shows some of the facilities that associate CCS to hydrogen production from fossil fuels.

Table 4. Hydrogen production from fossil fuels with CCS.[56]

Facility	H_2 production capacity	H_2 production process	Hydrogen use	Operational commencement
Enid Fertilizer	200 tons per day of H_2 in syngas	Methane reformation	Fertilizer production	1982
Great Plains Synfuel	1,300 tons per day of H_2 in syngas	Coal gasification	Synthetic natural gas production	2000
Air Products	500 tons H_2 per day	Methane reformation	Petroleum refining	2013
Coffeyville	200 tons H_2 per day	Petroleum coke gasification	Fertilizer production	2013

Quest	900 tons H_2 per day	Methane reformation	Bitumen upgrading (synthetic oil production)	2015
Alberta Carbon Trunk Line-Sturgeon	240 tons H_2 per day	Asphaltene residue gasification	Bitumen upgrading (synthetic oil production)	2020
Alberta Carbon Trunk Line-Nutrien	800 tons H_2 per day	Methane reformation	Fertilizer production	2020
Sinopec Qilu	100 tons H_2 per day	Coal/coke gasification	Fertilizer production	2021

Turquoise hydrogen

Turquoise hydrogen is another option that is frequently overlooked in environmental studies. This label refers to the hydrogen produced through pyrolysis reaction, where hydrocarbons are broken down into smaller molecules giving solid carbon and gaseous hydrogen simultaneously, eliminating the need for carbon capture and storage. The pyrolysis reaction can occur both in the presence and in the absence of a catalyst (Figure 14).

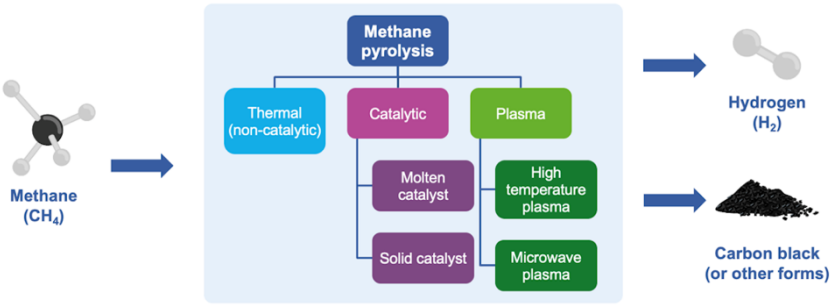


Figure 14. Three types of methane pyrolysis process.[57]

Naturally, to obtain a good conversion yield in the absence of a catalyst it is necessary to work at higher temperatures. Working in the absence of catalyst and at temperatures between 900 and 1000 °C the reaction yields are approximately 40% - 65%. To increase the yield to 90%, temperatures above 1200 °C are required.[58] In this temperature range, several homologous hydrocarbons in the gaseous state produced by a radical chain reaction are present. Although the reaction steps are not yet fully understood, it is accepted that the development of the methyl radical is necessary (Equations 10-12).

$$CH_4 \rightarrow CH_3 \cdot + H \cdot \quad (10)$$

$$CH_4 + H \cdot \rightarrow CH_3 \cdot + H_2 \quad (11)$$

$$2\,CH_3 \cdot \rightarrow C_2H_6 \quad (12)$$

The overall reduction of hydrocarbons to produce black carbon and hydrogen is described by Equation 13:

$$2CH_4 \rightarrow C_2H_6 + H_2 \rightarrow C_2H_4 + 2H_2 \rightarrow C_2H_2 + 3H_2 \rightarrow 2C + 4H_2 \quad (13)$$

From the overall reaction, we can state that 1 kg of hydrogen obtained, 3 kg of black carbon are produced. Depending on its grade, the solid carbon byproduct can be utilized in a variety of industries. For example, rubber black is used as a reinforcing material in tires,[59] while specialty black can be used to make polymers, inks, coatings, battery materials, and many other products.[60] Investigations into its potential as a soil additive are also in progress. Certain methane pyrolysis procedures can also yield graphite, hydrocarbons, or graphene.[61] The production of such products could provide operators of pyrolysis plants with beneficial revenue streams.

White and orange hydrogen

White hydrogen is the only spontaneous form of hydrogen naturally found in underground deposits created by fracking. It is obtained from the

serpentinization reaction, a reduction of water to hydrogen that occurs in conjunction with anoxic and abiotic oxidation of ferrous iron to the ferric iron:

$$2FeO + H_2O \rightarrow Fe_2O_3 + H_2 \quad (14)$$

This oxidation finds the best reaction conditions beneath the ocean floor, where seawater percolates into peridotites, which are magnesium silicate rocks that contain up to 10 wt% ferrous iron.[62,63] At oceanic ridges where serpentinization is most active, it is estimated that between 1 and 2 Mt of hydrogen are produced annually.[64]

According to the same principles as white hydrogen, orange hydrogen is produced primarily by the Earth. On the other hand, orange hydrogen takes a proactive approach and looks for ways to trigger the reaction rather than employing a passive investigation/exploitation strategy. In order to accomplish this, water is injected in situ into reactive formations that have been identified, and the hydrogen-saturated water is collected from recovery wells around the injection point.

Yellow hydrogen

The term "yellow hydrogen" is used by some to describe hydrogen that is produced through water electrolysis using primarily solar energy,[65–67] while others believe that this hydrogen is produced through electrolysis using a combination of fossil and renewable energy from the grid.[68–70] This can be confusing because, although electrolysis do not involve the production of CO_2, energy supply sources are classified oppositely when it comes to solar (renewable) and the mix from the grid (non-renewable).

Solar energy is the cleanest and most abundant renewable energy source available. This energy from the sun is converted into thermal energy through solar thermal panels or electrical energy through photovoltaic systems.

To produce thermal energy, solar radiation is channeled and collected in a device called a "thermal accumulator" that heats the water contained in

large tanks. The heat obtained can then be used both domestically and industrially to heat homes, swimming pools, greenhouses and buildings.
To produce electrical energy, the photons in the light radiation interact with the electrons from the semiconductor materials used to make the panel. This phenomenon is known as the photovoltaic effect. As a result, photovoltaic energy can generate hot water even in cold climates on sunny days, because it only needs light, unlike solar thermal energy, which needs the heat of the sun. In a traditional photovoltaic cell, the smallest part of a module, a thin sheet of semiconductor material (nowadays mainly monocrystalline silicon) is appropriately treated during the production phase by "doping" it with phosphorus and boron atoms to determine an unstable junction, with "gaps" and excess electrons in the atoms. An electromagnetic field is produced when photons strike a cell with sufficient energy, which excites electrons and allows them to move and escape electrostatic forces. As a result, a flow of internal charges is produced as electrons move from the negative layer of the cell to its positive layer and back again. By adding the effect over the entire surface of the photovoltaic module, and then over an entire string of modules, it is possible to convey these charges to an external circuit, obtaining voltage values that generate a flow of direct current that can then be converted, via an inverter, into alternating current that can be used at home.

Pink, red and purple hydrogen

Nuclear fission is a specific disintegration process in which heavy nuclei, like those of uranium, thorium or plutonium isotopes, split into two positively charged fragments that violently repel one another and move away with high kinetic energy when they are properly bombarded with neutrons. In addition, other neutrons are released, starting a chain reaction that allows the nuclear reactor to be kept running, producing energy continuously and constantly. The heat generated by fission reactions in nuclear power plants enables the heating of water to the point where steam is produced. Similar to traditional fossil fuel (oil, coal or natural gas) thermal power plants, the

energy released as heat is converted first into mechanical energy and then into electrical energy. In fact, the steam generated powers a turbine, which in turn activates an alternator (Figure 15).

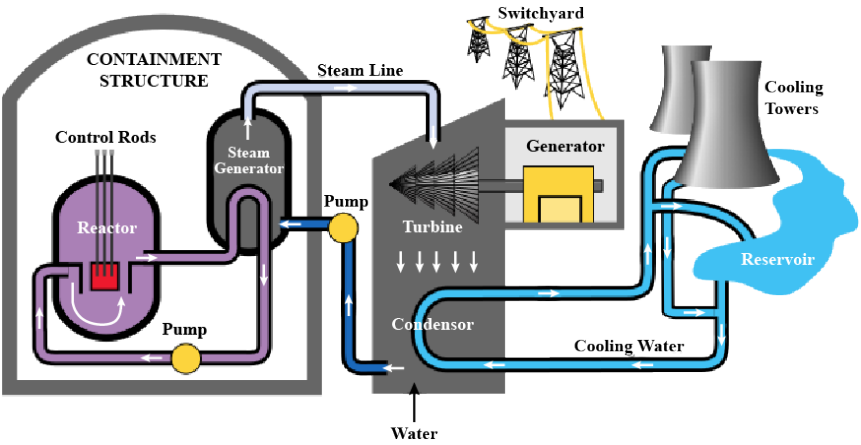


Figure 15. Scheme of a nuclear power plant.

Pink hydrogen is produced by electrolysis powered by electricity obtained from nuclear energy, while to produce red hydrogen the heat released during fission reaction is exploited. The tag for purple hydrogen indicates that it was produced by both electrolysis and thermolysis.

The benefits and drawbacks of nuclear energy have long been debated, particularly with regard to its effects on the environment. On the one hand, nuclear energy is a clean and reasonably priced energy source that can generate a significant amount of electricity without releasing greenhouse gases like CO_2. However, there are also some serious drawbacks to nuclear energy, such as the creation of radioactive waste, the potential for nuclear mishaps, and the potential for nuclear proliferation. When it comes to benefits, nuclear energy offers several advantages. First of all, nuclear energy is extremely efficient, capable of producing large amounts of electricity from a relatively small amount of nuclear material. In addition, nuclear energy is also quite cheap, due to the low cost of nuclear fuel and the fact that nuclear power plants are able to operate for long periods of time

without interruption. On the other hand, nuclear energy has some serious drawbacks. Radioactive waste is the first issue, which needs to be properly disposed of to avoid contaminating the environment. The potential for nuclear accidents like those at Chernobyl and Fukushima also raises questions regarding the safety of nuclear facilities. Lastly, there is the risk of nuclear proliferation, which involves the potential for nuclear material to end up in the hands of terrorist organizations or other nations working on nuclear weapons development.

Green hydrogen

Green hydrogen is produced through the water splitting reaction in a process known as electrolysis, in which electricity is used to split the water molecule into hydrogen and oxygen, the only byproduct. The process to obtain green hydrogen is powered entirely by electricity from renewable energy sources, such as solar, wind, geothermal, biomass or hydropower.
The overall water splitting (OWS) follows the reaction in Equation 15:

$$2\,H_2O \rightarrow O_2 + 2\,H_2 \qquad (15)$$

The overall water splitting can be divided into two half-cell reactions which are oxygen evolution reaction (OER) at the anode and hydrogen evolution reaction (HER) at the cathode. In this process, four transfer electrons on the OER side and two on the HER side are involved. More information about this process is given in Chapter 2.
To be considered 100% clean, green hydrogen must be produced using electricity from renewable sources, such as hydro, wind or solar power. Green hydrogen production stands out as one of the most promising solutions and is essential to decarbonization initiatives. However, a number of factors have a significant impact on the scalability and efficiency of green hydrogen production. The catalysts used, operating temperature, pressures, feed water purity, and the kind of electrolyzer technology are all factors that contribute to make hydrogen production expensive and affect scalability

and competitiveness. Despite this, some countries are pioneering this technology. Some examples are given in Table 5. To date, the largest operating facility for the production of green hydrogen is located in Fukushima Hydrogen Energy Research Field (FH2R). With rated power operation, FH2R can generate up to 1,200 Nm^3 of hydrogen per hour. While developing low-cost, green hydrogen production technology, FH2R will adapt to supply and demand in the power grid to optimize the use of renewable energy, which is prone to significant fluctuation.

Table 5. Examples of the world's largest renewable hydrogen production facilities.[56]

Facility	H_2 production capacity	H_2 production process	Operational commencement
Fukushima	2.4 tons of H_2 per day	10 MW electrolyzers powered by 20 MW solar PV	2019
Neom	650 tons of H_2 per day	4GW wind and solar PV powered electrolyzers	Expected after 2025
AREH	4800 tons of H_2 per day	23GW wind and solar PV powered electrolyzers	Possible after 2028

A summary of the color codes is represented in Figure 16.

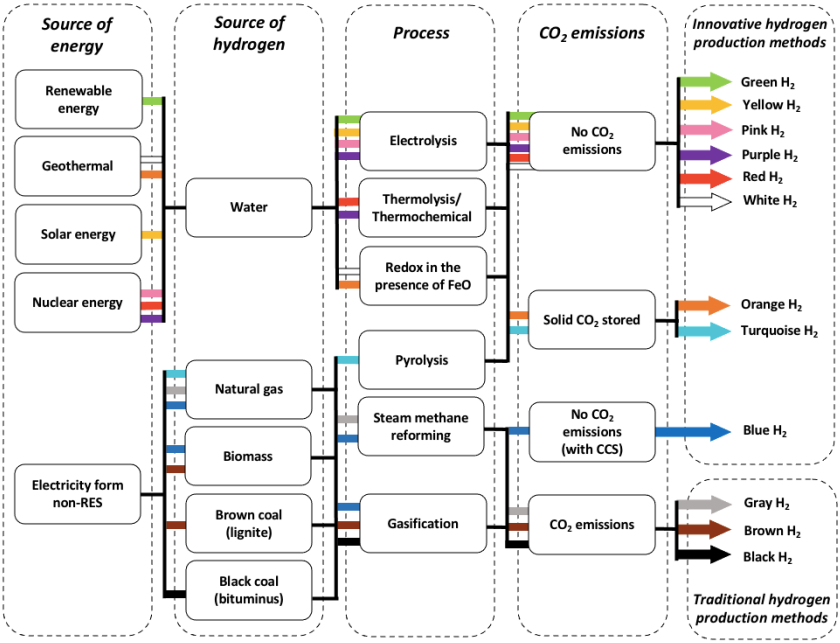


Figure 16. Summary of the source of energy and hydrogen, the production process and the CO_2 emissions associated with the following proposed colors referred to hydrogen: green, yellow, white, pink, purple, red, orange, turquoise, blue, gray, brown and black.

1.4 Evolving the energy grid: the role of smart grids

A smart grid is an electricity network built on digital technology, sensors and software that supplies electricity to end-users through a two-way communication network. The two major features of current smart grids are energy-saving and emission reduction.[47] Smart grids represent a revolution in the way we manage electricity: through real-time consumption monitoring and analysis systems, smart grids can manage energy demand more effectively, reducing consumption peaks and optimizing the use of available resources. Also, they facilitate the integration of renewable energy sources, such as solar and wind, allowing for greater diversification of energy resources. This lessens greenhouse gas emissions and reliance on fossil fuels. By integrating advanced communication and automation

technologies, these networks enable more efficient and sustainable energy management.[71] According to the Electric Power Research Institute, as shown in Figure 17, by incorporating information and communications technology into every aspect of power generation, delivery, and consumption, a smart grid has the potential to drastically reduce costs, increase efficiency, and minimize environmental impact.[72–74] The advent of smart cities and electric vehicles powered by batteries is causing more cities worldwide to switch to renewable energy sources. Most of the technologies involved have already reached maturity, but investments in smart grids need to more than double through to 2030 to get on track with the Net-Zero Emissions by 2050 Scenario. The International Energy Agency's Tracking Clean Energy Progress[75] (TCEP) assesses recent developments in over 50 energy system components that are critical to clean energy transitions. The assessed components include sectors, subsectors, technologies, infrastructure, and cross-cutting strategies. A total of three components from more than 50 tracked in the 2023 edition are fully "on track" with the Net-Zero by 2050 Scenario trajectory: solar photovoltaic cells (PV), electric vehicles, and lighting. Solar PV in this edition was upgraded, as its annual growth of 26% in 2022 aligns with the average compound annual growth rate needed in the Net-Zero Scenario between now and 2030. While many components of clean energy technology implementation, are not yet fully on track globally, many other advances in 2022 have been extremely rapid. Some highlights from the “Tracking Clean Energy Progress 2023”[75] are given in Table 6. Continued investment and collaboration among governments, industries, and research institutions will be the key to realize hydrogen’s full potential in a sustainable energy future. Those parts of the energy system for which clean technologies are already available and costs are falling rapidly, such as electricity generation and passenger cars, are progressing faster but all areas of energy production and use need to be decarbonized for a full transition to net-zero emissions. It is crucial to bring clean technologies to market quickly, particularly in those parts of the energy system that are harder to address, like heavy industry and long-distance transportation.

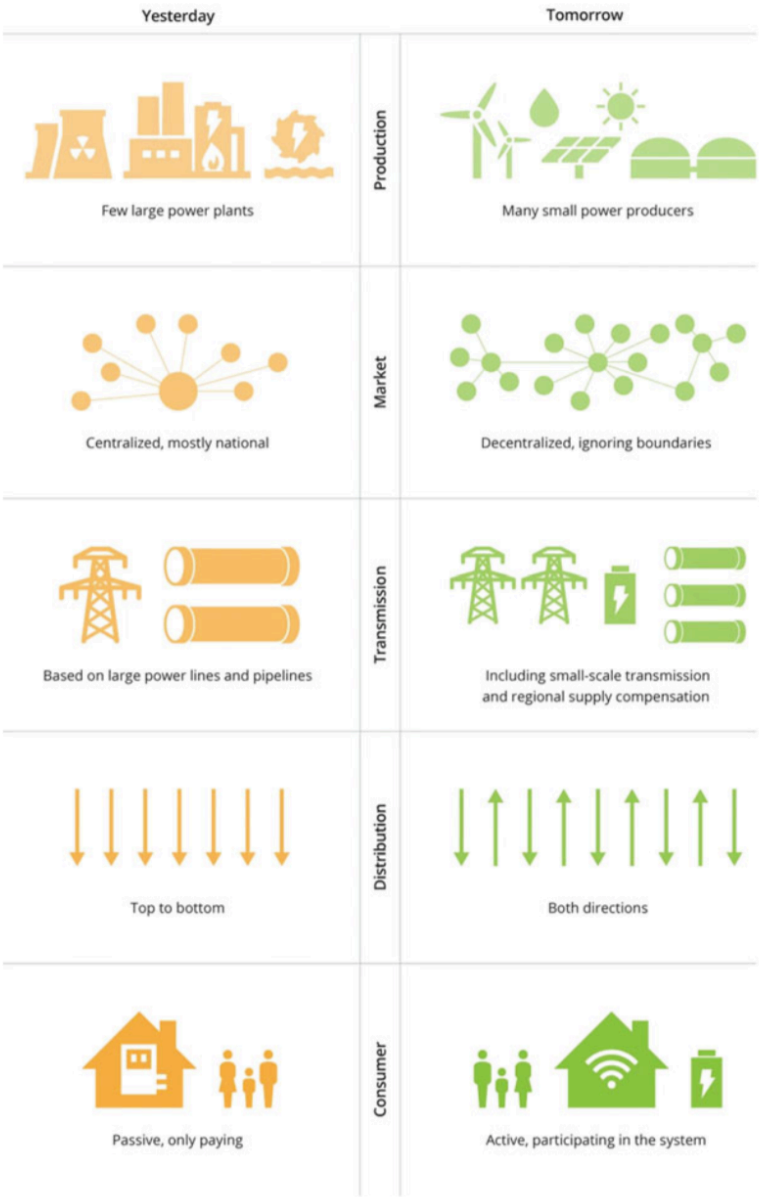


Figure 17. Expected structural changes in the energy system made possible by the increased use of digital tools.[76]

The transition is occurring at different speeds across regions and sectors. Nearly 95% of electric car were sold in 2022 in China, United States and Europe. Meanwhile, nearly 75% of carbon capture capacity is in North America and Europe. As a result, the global evaluation of a technology as "on track" does not necessarily imply that it is on track in all countries. On the other hand, a technology that is "off track" globally could be progressing more quickly in some countries. There have been positive advances in innovation in the past few years, but we need to accelerate our efforts to bring novel low emission technologies to these markets as quickly as possible.

Table 6. Main components of clean energy technology deployment.[75]

Electric vehicles	Sales grew of 55% reaching a record high of more than 10 million: for the first time ever, announced manufacturing capacity for electric vehicle batteries is sufficient to meet 2030 demand requirements.
Nuclear	After capacity additions has remained stable from 2019 to 2021, the growth in 2022 by 40%, with 8 GW newly installed represents a clear step forward.
Heat pumps	2023 signs another record year, with 11% growth in sales, close to the 15% average compound annual growth needed to fully align with the expected scenario.
Electrolyzers	Installed capacity grew by more than 20%, while electrolyzer manufacturing capacity grew by more than 25% and is likely to reach almost 3 GW by the end of 2023, a more than four-fold increase in total capacity compared to 2022, based on current pipeline of projects under development and their expected operating dates.
Energy efficiency	Vitality proficiency of the economy in general developed by more than twice the level the past year. This can be a positive step forward taking after a long time of moderately frail enhancements.

1.4.1 *Efficient hydrogen production and distribution networks through smart grids*

Hydrogen production in smart grids is a concept that integrates renewable energy sources, hydrogen generation technologies, and grid management

systems to create a more efficient, flexible, and sustainable energy system. Smart grids, which utilize advanced technologies like sensors, communication systems, and automated control, enable better management of energy flows between producers, consumers, and storage systems, enhancing the integration of hydrogen production as part of the grid's operations. It is worth noting that the instability of renewable energy affects the network, causing voltage fluctuations, lightning and frequency changes, reducing the quality of power supply.[77,78] Smart grids can accommodate the intermittent nature of renewable energy, such as solar and wind, by adjusting the demand for hydrogen production. When there is an overproduction of electricity, excess power can be directed towards electrolyzers to be converted into hydrogen, stored or converted into synthetic fuels for transport, and then used when demand is high or renewable generation is low. This is particularly useful for long-duration storage, which is challenging for batteries. During low renewable energy periods, hydrogen production can be scaled back, maintaining grid stability (Figure 18).

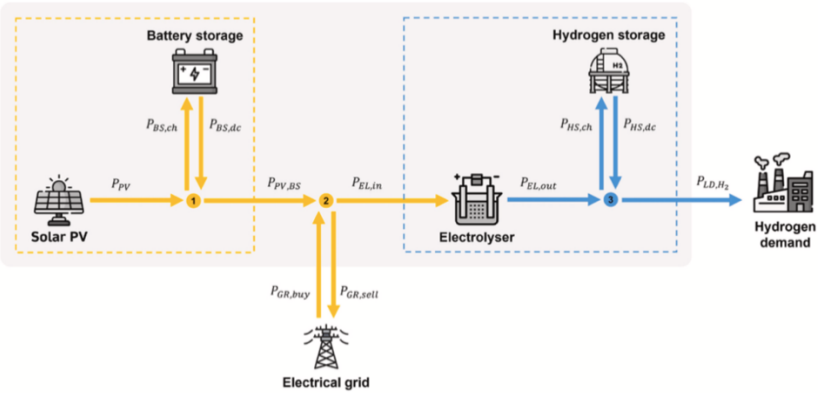


Figure 18. Layout of the power-to-hydrogen system.[79]

One of the main advantages of smart grids is the decentralized hydrogen production. On-site production eliminates the need for transportation and allows for flexible, on-purpose production. Hydrogen can be produced close to the point of use, reducing transmission losses, and improving the overall

efficiency of the energy system. For example, electrolyzers can be installed at renewable energy generation sites or in industrial facilities, and hydrogen can be used on-site or transported to other areas of the grid. Large-scale systems linked to a hydrogen delivery/distribution network that transports the product hydrogen to the point of use in a gaseous or liquid state by pipeline or truck will be referred to as centralized hydrogen production in the future.[80] Large, centralized facilities are driven by the need to reduce certain production costs by allowing for high-capacity factors and increasing unit size (economy of scale). Furthermore, the use of nuclear as a primary energy source or big hydroelectric power only makes sense for large-scale, centralized hydrogen generation. Because of their low power densities and generally sporadic availability, renewable energy sources will encourage a relatively dispersed structure of hydrogen generation. Distributed hydrogen generation from renewable sources must be adjusted to the current gas and electricity grids' direct injection (DI) and maybe alternate usage of renewable energy. This is true for both hydrogen generation from biomass, which will have a limited capacity due to the challenge of transporting biomass, and hydrogen production by electrolysis using wind or photovoltaic electricity. Widely accessible gas and electricity grids can assist in optimizing the patterns for more centralized or decentralized hydrogen production as well as moving the point of use of distributed renewable energy to more centralized sites. Installing a network of small-scale hydrogen production units as essential components of energy hubs seems like a reasonable short-term strategy for the introduction phase of future applications of hydrogen as part of the energy economy.[81] For early low-demand stages, small SMR or electrolyzer units, which are competitors at this scale, are appealing. They don't need transportation or delivery infrastructure, and they require less total capital investment. However, because they lack the benefits of the economies of scale factor and the increased storage efficiency of large plants, they have disadvantages in terms of limited efficiency and high hydrogen costs. Additionally, managing a network of several small hydrogen units necessitates extra labor to

establish and uphold constant, high quality and safety requirements as well as cost-effective smart grid control. A comparative cost analysis study of the planned networks of hydrogen refueling stations has revealed that, when compared to onsite production, gaseous batch transport, or dedicated pipelines, tank truck delivery of liquid hydrogen is the most cost-effective option for consumptions under 600 Nm^3/h. Dedicated hydrogen pipelines, however, prove to be the most cost-effective on a broader scale.[82] In any event, the necessary purity and pressure levels to be supplied by the hydrogen generation process are determined by the actual distribution and use cases. The mixing of hydrogen streams from various sources could be an issue if the dispersed hydrogen generation is linked to a pipeline grid, unless each source has minimal quality standards. On the other hand, when hydrogen is produced in a distributed manner and used locally rather than being connected to a larger grid, the necessary purity and pressure levels can be tailored to meet specific needs. This flexibility allows for greater opportunities for economic optimization.

1.4.2 *Hydrogen production costs*

Experts predict that by 2050, the demand for hydrogen will have significantly increased, coincident with an expansion of production capacities, as the conversion of processes to hydrogen must occur on a global scale. There is a significant purpose to the growth of global electrolysis capabilities that can produce green hydrogen using renewable electricity. One of the biggest obstacles during an energy price crisis is achieving economically competitive hydrogen production costs. Delivering green hydrogen at the lowest specific cost also requires a cost-optimal design of power-to-hydrogen (PtH) systems, including the electrolyzers and renewable energy generators. According to several studies, the current costs of producing hydrogen using PEM electrolysis and electricity from renewable sources range from 0.7 €/kg to 13.5 €/kg.[83–87] Numerous boundary conditions, including energy sources and production nations, are

taken into account in these analyses. Cost can increase to 57.6 €/kg if storage technologies are considered and off-grid use is planned.[88]

Development curves for the cost of producing hydrogen are based on the ratio of electrolysis to renewables (Ely-RES-ratio) and the load curves and technology parameters that have been specified. Locations and renewable energy sources are distinguished. At every location and energy source analyzed, the associated costs of producing hydrogen fall as renewable energy increase.

Depending on the size of the PV park, the optimal Ely-RES-Ratio for the "PV Global High Full Load Hours (FLH)" scenario falls between 60 and 73%. With an installed PV capacity of 50 MW and an ideal ratio of 73%, the lowest costs of producing hydrogen are achieved. With this system configuration, the electrolysis's full load hours are a total of 2885. The costs of producing hydrogen are substantially higher than those in the corresponding optimum when the Ely-RES-Ratio is less than 10%. The levelized cost of hydrogen (LCOH) range begins at an Ely-RES-Ratio of approximately 20%, at 0.5 MW PV power. The LCOH range changes to 15% at 50 MW installed PV power as RES power increases (Figure 19). The LCOH range achieves an Ely-RES ratio of 100%, across all PV power classes, which leads to a wide bandwidth in which the lowest possible LCOH values are found.

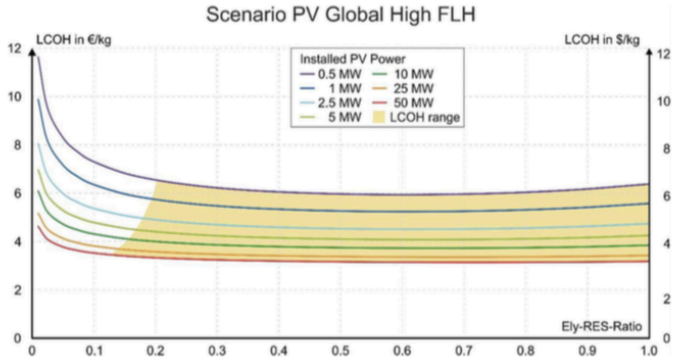


Figure 19. LCOH for the scenario "PV Global High FLH" with an installed PV power range from 0.5 MW to 50 MW. The LCOH range is shaded in yellow.[89]

According to the scenario “PV Global Low FLH”, the optimal Ely-RES-Ratio falls between 13.6% and 14%. At 50 MW of installed PV power, a 14% optimization is achieved, yielding 2435 full load hours of electrolysis. However, the LCOH range is narrower and at a lower level than in the places with higher full load hours of renewable energy source (FLH_RES) (Figure 20).

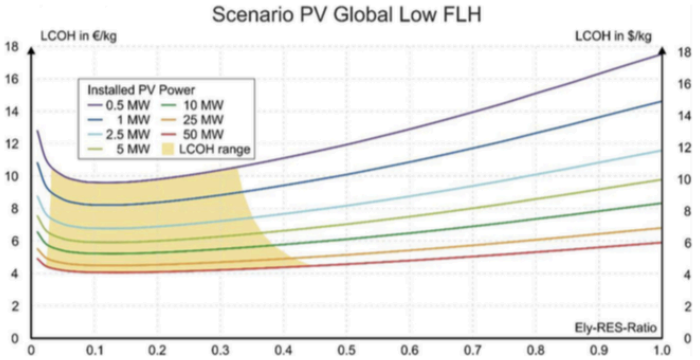


Figure 20. LCOH for the scenario “PV Global Low FLH” with an installed PV power range from 0.5 MW to 50 MW. The LCOH range is shaded in yellow.[89]

It is possible to find overlaps in the LCOH range between the two global PV locations. At 0.5 MW PV power, this overlap is in the range of 20 to 30% and at 50 MW PV power, it drops to 15 to 40%.

The range of hydrogen production costs for PV parks with lower power is also much wider than for those with high power when considering the locations in relation to the power classes. The range is approximately equal to 38% for 0.5 MW PV capacity, between the “PV Global High FLH” and “PV Global Low FLH” locations, while it is about 23% for 50 MW PV capacity (Figure 21).

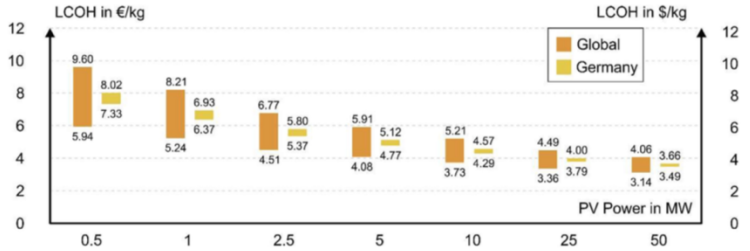


Figure 21. Range of the minimum hydrogen production costs depending on the installed PV power in MW for the global scenarios (orange) and the locations in Germany (yellow). The values are stated in €/kg.[89]

There are two primary conclusions drawn from a comparison of all LCOH ranges. When the Ely-RES-Ratio is higher, sites with higher FLH_RES exhibit a wider LCOH range. Accordingly, before installing an electrolyzer, a more thorough analysis of the optimal Ely-RES-Ratio and the most cost-effective LCOH is necessary for locations with low FLH_RES. All PV plant sizes and FLH_RES investigated have nearly optimal hydrogen production costs when and Ely-Res-Ratio between 20 and 30% is chosen. The task for plant designers is greatly simplified by reducing the range of appropriate electrolysis plant size. When the PV parks' full load hours are compared to the ideal Ely-RES-Ratio, it is evident that the installed PV power has little effect on the ideal ratio at low FLH_RES. Higher FLH_RES can cause a 13% variation in the ideal Ely-RES-Ratio. Therefore, as the PV park's power increases, so does the installable electrolysis power. The result of a comparative analysis indicates that there is an optimal value for the costs of producing hydrogen for every value of PV power. The lowest production costs are found at 3.14€/kg for the highest PV power. For 0.5 MW of PV capacity at the global low FLH site, the reachable LCOH increases to 9.60€/kg respectively.

When it comes to wind farm installation, electrolysis average efficiencies range from 61.6% to 66.1%, corresponding to a slight improvement in average efficiency from lower to higher wind power compared to PV installations. At installed wind capacities of 50 MW, the lowest costs of

producing hydrogen are found. Thus, the lower the achievable LCOH, the grater the installed capacity of wind power. The optimal Ely-RES-Ratio for the "Wind Global High FLH" scenario varies from 91% to 143%, contingent on the wind park's power. Because electrolysis is more efficient when operating at partial load as opposed to full capacity, the ideal Ely-RES-Ratio of over 100% is achieved. By weighing the higher installation costs against the savings from increased system efficiency, the developed calculation model calculates the optimal outcome. The LCOH with 2.53€/kg was lowest at 50 MW of installed wind power with an Ely-RES-Ratio of 143%. The result of this constellation is approximately 4537 full load hours of electrolysis. The LCOH range begins at roughly 30% and increase to 100% with an installed wind power of 0.5 MW. For a wind park with 50 MW, the range changes to 20% (Figure 22). The optimal Ely-RES-Ratio for the "Wind Global Low FLH" scenario is between 3.3% and 3.8%. 50 MW of installed wind power and an optimal Ely-RES-Ratio of 3.8% results in the lowest hydrogen production costs, at 3.48€/kg.

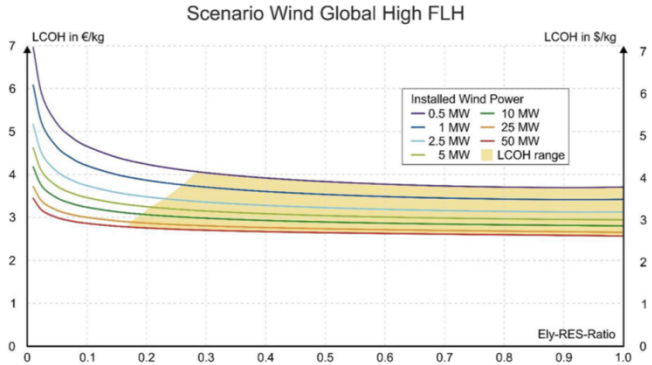


Figure 22. LCOH for the scenario "Wind Global High FLH" with an installed wind power range from 0.5 MW to 50 MW. The LCOH range is shaded in yellow.[89]

In contrast to the "Wind Global High FLH" scenario, the LCOH range is significantly more constrained and has a lower Ely-RES-Ratio. Comparing the upper Ely-RES-Ratios to all other scenarios, the LCOH is extremely high. This is because of the extremely low FLH_RES. As a result, there is a limit to how economically feasible a plant operation can be (Figure 23).

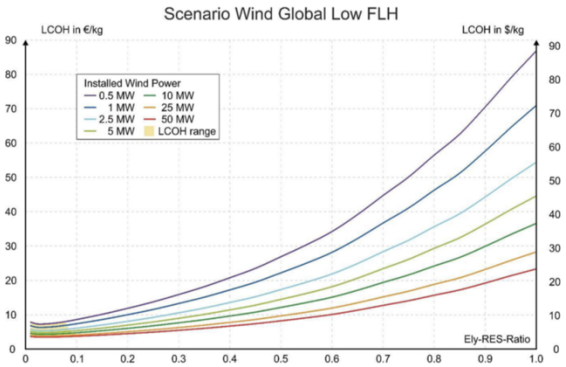


Figure 23. LCOH for the scenario "Wind Global Low FLH" with an installed wind power range from 0.5 MW to 50 MW. The LCOH range is shaded in yellow.[89]

Figure 24 displays the lowest LCOH that can be achieved for every wind scenario relative to the wind park's installed capacity. The descriptions for PV are comparable to the correlations concerning the bandwidths of the costs of producing hydrogen for various power classes. Between the scenarios, the variations are roughly 50% for 0.5 MW of wind power and 27% for 50 MW. Only a small portion of the lower range of global fluctuations is covered by the LCOH in Germany. It is possible to attribute the similar LCOH between the German and global high FLH_RES scenarios to the similar full load hours of electrolysis (FLH_H2). Due primarily to the highest FLH_RES, the offshore scenario exhibits the lowest LCOH at all wind capacities.

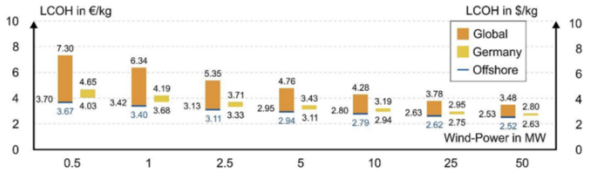


Figure 24. Range of the minimum hydrogen production costs depending on the installed wind power in MW for the global scenarios (orange) and the locations in Germany (yellow). The offshore location is marked with blue and the resulting LCOH are in blue. The values are stated in €/kg.[89]

1.5 Conclusions

As part of an energy transition aimed at reducing greenhouse gas emissions to zero, CO_2-free hydrogen has begun to become increasingly widespread in recent years. Since green hydrogen, which is obtained from renewable energy and burns to produce water, has many potential applications in industry, transport and buildings, it is considered one of the most important keys to the energy transition. The hydrogen economy, which has been talked about for decades, is currently in a different state than before due to the rapid growth and falling price of kWh generated by photovoltaic and wind energy.[90] For the development of hydrogen, RES, especially non-programmable ones, play two roles: an "active" part in Power-to-Gas as "energy suppliers" to generate green hydrogen for use in different sectors or as a feedstock to produce ammonia, methanol and synthetic fuels for various uses;[91] and an "interested" party in a Gas-to-Power from hydrogen to electricity for storage, even long-term, as well as ancillary services for greater integration of renewable energy sources (RES) into the electricity grid, to compensate for their non-programmability and unpredictability.[92]
Green hydrogen has been and is being discussed more and more in recent years, from Australia to Chile, through China, the Middle East, Africa, Europe and North America. Particularly with regard to plans for huge electrolysis plants powered by renewables, significant advances and cost reductions for electrolyzers, and vast land and sea transport infrastructures.[93]
As concerned hydrogen transportation, the global project pipeline has not only matured but also expanded seven-fold since 2020, from 228 projects in 2021 to 1,572 projects in 2024. A greater percentage of projects have progressed from announcements to more advanced stages over time. Investments in front end engineering design (FEED) stage projects rose by a factor of 20 between 2020 and 2024.[27]
As concerned the production of approximately 95 Mt of hydrogen in 2022, the following production is available with different technologies in rounded percentages: 62% from gas (with steam methane reforming, SMR); 21% from coal; 16% as a by-product of industrial processes; 0.5% from oil; 0.6%

from fossil fuels with CCUS; 0.2% from electricity. Around 0.7% of hydrogen was produced in total with zero emissions.[94] With the exception of the EU, the sharp increase in gas prices (currently the main raw material for hydrogen production) following the invasion of Ukraine caused hydrogen consumption worldwide to increase by 3% in 2022 compared to 2021. Global production increased by around 2% in 2023 compared to 2022. Water electrolysis production also increased significantly, but still only makes up a small share of renewable hydrogen, while overall low-emission hydrogen production is less than 1%. However, the total installed capacity of electrolyzers for hydrogen production reached 1.1 GW in 2023. A report by the Hydrogen Council points out that this represents a 60% increase over the installed capacity in 2022 for 250 MW out of 400, mainly due to the Kuqa project in China, which uses electrolyzers with Chinese technology. At the end of 2023, China had 610 MW of the 1.1 GW of electrolyzers needed to produce hydrogen globally, followed by the United States and Germany with 60 MW each, and Spain, Taiwan, Sweden and Canada.

Over the past four years, the industry has witnessed an astounding seven-fold increase in hydrogen capacity reaching FID globally; however, the pace and scale of deployment has not been adequate to meet climate commitments. Compared to the current investment of USD 75 billion past FID, an eight-fold increase in hydrogen investments is needed until 2030 in order to accelerate the decarbonization of the global energy system.[27]

Government and corporate decision makers must work together to address this issue. To mobilize private capital and advance mature projects this decade, government incentives and enabling legislative frameworks are essential. Along with building enabling midstream infrastructure, addressing the project delays seen today will require greater regulatory clarity and certainty, as well as support for demand drivers over the next two years. Governments and industry have a unique opportunity to jointly leverage the undeniable progress made in the hydrogen sector over the past four years, opening the door to cost-efficiency gains for energy systems, as well as environmental and socioeconomic benefits for global economies.

1.6 Aim of this work

The work carried out for this thesis is developed through different phases, each aimed at deepening crucial issues related to the production and storage of green hydrogen. The first part involved an in-depth bibliographic research, aimed at acquiring a solid knowledge of the state of the art regarding the plants used for the production of green hydrogen and for its subsequent storage in molecular matrices. This research phase was carried out in collaboration with the company DG Impianti Industriali SpA., which provided fundamental support for the collection and analysis of data.

Thanks to the information collected, the research project was oriented towards the synthesis of platinum-based catalysts. The choice to focus on this material derives from its excellent catalytic properties in the hydrogen production process, but also from the need to reduce its use. In fact, platinum is a rare element in nature and its high cost represents a major challenge for the economic sustainability of the process. Therefore, different strategies were explored to reduce the amount of platinum used, while maintaining the efficiency of the process.

Furthermore, a significant part of the work has been devoted to innovative methods of hydrogen storage, with particular attention to clathrate hydrates. Hydrogen storage in molecular matrices, although not yet used on a large scale, represents a promising technology. In fact, compared to traditional storage methods, this technique offers important advantages, such as the possibility of storing hydrogen at significantly lower pressures and with more efficient storage volumes. This solves some of the main problems related to conventional methods, making this technology one of the most promising for the future.

1.7 References

1. Copernicus: 2024 is the first year to exceed 1.5°C above pre-industrial level. https://climate.copernicus.eu/copernicus-2024-first-year-exceed-15degc-above-pre-industrial-level (2025).
2. *'The UAE Consensus Forward', COP28 UAE*.
3. Kabir, M. *et al.* Climate change due to increasing concentration of carbon dioxide and its impacts on environment in 21st century; a mini review. *J King Saud Univ Sci* 35, 102693 (2023).
4. YUE, X.-L. & GAO, Q.-X. Contributions of natural systems and human activity to greenhouse gas emissions. *Advances in Climate Change Research* 9, 243–252 (2018).
5. Nunes, L. J. R. The Rising Threat of Atmospheric CO2: A Review on the Causes, Impacts, and Mitigation Strategies. *Environments* 10, 66 (2023).
6. Liu, H. & Han, P. Renewable energy development and carbon emissions: The role of electricity exchange. *J Clean Prod* 439, 140807 (2024).
7. International Energy Agency, I. *World Energy Outlook 2023*. www.iea.org/terms (2023).
8. Josefine Fokuhl & Todd Gillespie. Germany revives coal as energy security trumps climate goals. *Bloomberg* (2022).
9. McKinsey. *Global Energy Perspective*. (2023).
10. McKinsey. Global energy perspective 2023: Oil outlook. https://www.mckinsey.com/industries/oil-and-gas/our-insights/global-energy-perspective-2023-oil-outlook (2024).
11. Thomas Hundertmark. 'You need to do the math and then explain the math': A talk with ExxonMobil's Darren Woods. *McKinsey* https://www.mckinsey.com/industries/oil-and-gas/our-insights/you-need-to-do-the-math-and-then-explain-the-math-a-talk-with-exxonmobils-darren-woods (2023).

12. Household air pollution. *World Health Organization,* https://www.who.int/news-room/fact-sheets/detail/household-air-pollution-and-health (2024).
13. Laura Cozzi, Daniel Wetzel, Gianluca Tonolo & Jacob Hyppolite II. For the first time in decades, the number of people without access to electricity is set to increase in 2022. (2022).
14. *TRACKING SDG 7*. https://trackingsdg7.esmap.org/downloads. (2024).
15. *Statistical Review of World Energy*. (2024).
16. McKinsey. From poverty to empowerment. https://www.mckinsey.com/featured-insights/sustainable-inclusive-growth/charts/from-poverty-to-empowerment (2023).
17. *GLOBAL METHANE ASSESSMENT Benefits and Costs of Mitigating Methane Emissions*.
18. *CARBON DIOXIDE CAPTURE AND STORAGE*.
19. Ritchie, H. & Rosado, P. Energy Mix - Explore global data on where our energy comes from, and how this is changing. https://ourworldindata.org/energy-mix (2020).
20. Payne, J. E., Vizek, M. & Lee, J. Stochastic convergence in per capita fossil fuel consumption in U.S. states. *Energy Econ* 62, 382–395 (2017).
21. Rick Carr, John England, KAte Hardin & Anshu Mittal. 2025 Oil and Gas Industry Outlook. https://www2.deloitte.com/us/en/insights/industry/oil-and-gas/oil-and-gas-industry-outlook.html (2024).
22. Petroleum and other liquids oil spot prices. https://www.eia.gov/dnav/pet/pet_pri_spt_s1_d.htm.
23. Oil & natural gas: supporting the economy, creating jobs, driving America forward. (2018).
24. Energy Information Administration, U. *Annual Energy Outlook 2023: Release Presentation*. www.eia.gov/aeo (2023).

25. Gong, X., Fu, C., Li, H. & Pirabi, M. The impact of U.S. political decisions on renewable and fossil energy companies in the era of the Paris Agreement. *Financ Res Lett* 69, 106165 (2024).
26. Bridget van Dorsten. Hydrogen: 5 things to look for in 2025. https://www.woodmac.com/news/opinion/hydrogen-2025-outlook/ (2024).
27. Council - McKinsey, H. *Hydrogen Insights 2024*. www.hydrogencouncil.com (2024).
28. Matti, S. Exploring Public Policy Legitimacy A Study of Belief-System Correspondence in Swedish Environmental Policy. in.
29. Poujade, R. & Frioux, S. Le premier ministère de l'Environnement (1971-1974): L'invention d'un possible. Vingtième Siècle. in *Revue d'histoire* vol. 113 51–54 (2012).
30. Central Intelligence Agency (CIA). Crude oil - exports. https://www.cia.gov/the-world-factbook/about/archives/2021/field/crude-oil-exports/country-comparison.
31. Norges Bank Investment Management. https://www.nbim.no/.
32. Reuters. Norway sovereign wealth fund commits $1 bln to renewable energy fund. https://www.reuters.com/business/energy/norways-sovereign-wealth-fund-commits-1-bln-renewable-energy-fund-2024-08-26/.
33. Kouveliotis-Lysikatos, I., Waernlund, A., Marin, M., Amelin, M. & Söder, L. Open source modelling and simulation of the nordic hydro power system. *Energies (Basel)* 14, (2021).
34. Le comité technique Euratom.
35. Orano. Niger Mining Sites. https://www.orano.group/en/nuclear-expertise/orano-s-sites-around-the-world/uranium-mines/niger/mining-sites.
36. *IRSN 2020*.

37. West, J. B. Henry Cavendish (1731-1810): hydrogen, carbon dioxide, water, and weighing the world. (2014) doi:10.1152/ajplung.00067.2014.-Henry.
38. Cruden, A. J. Preface and Context to Hydrogen and Fuel Cells. in *Comprehensive Renewable Energy* 1–27 (Elsevier, 2012). doi:10.1016/B978-0-08-087872-0.00401-7.
39. Schlapbach, L. & Züttel, A. *Hydrogen-Storage Materials for Mobile Applications*. www.nature.com (2001).
40. Nitsch, J., Berlin, S.-V., New, H., London, Y. & Tokyo, P. *Carl-Jochen Winter Hydrogen as an Energy Carrier Technologies, Systems, Economy With 188 Figures*.
41. Ne, J. B. S. H. *DA EDA LUS OR SCIEN CE & THE FUTU RE*.
42. Bockris, J. O. M. The hydrogen economy: Its history. *Int J Hydrogen Energy* 38, 2579–2588 (2013).
43. Bockris, J. O. A Hydrogen Economy. *Science (1979)* 176, 1323–1323 (1972).
44. Lawrence W. Jones. 1970_Towards a liquid hydrogen fuel economy. (1970).
45. Chu, Y. & Cui, H. *Annual Update on the Global Transition to Electric Vehicles: 2022*. http://www.ev-volumes.com/datacenter/. (2023).
46. *THE PARIS AGREEMENT ON CLIMATE CHANGE*. http://edgar.jrc.ec.europa.eu/overview.
47. Lin, R. H., Zhao, Y. Y. & Wu, B. D. Toward a hydrogen society: Hydrogen and smart grid integration. *Int J Hydrogen Energy* 45, 20164–20175 (2020).
48. Shigarov, A. B., Meshcheryakov, V. D. & Kirillov, V. A. Use of Pd membranes in catalytic reactors for steam methane reforming for pure hydrogen production. *Theoretical Foundations of Chemical Engineering* 45, 595–609 (2011).
49. Luo, M. *et al.* Review of hydrogen production using chemical-looping technology. *Renewable and Sustainable Energy Reviews* 81, 3186–3214 (2018).

50. WATANABE, F. *et al.* Carbon Formation and Active Site of Alumina Supported Platinum Catalyst in Steam Methane Reforming Containing Sulfur. *Journal of the Japan Petroleum Institute* 63, 89–95 (2020).
51. Go, K. S., Son, S. R., Kim, S. D., Kang, K. S. & Park, C. S. Hydrogen production from two-step steam methane reforming in a fluidized bed reactor. *Int J Hydrogen Energy* 34, 1301–1309 (2009).
52. Prins, M. J., Ptasinski, K. J. & Janssen, F. J. J. G. From coal to biomass gasification: Comparison of thermodynamic efficiency. *Energy* 32, 1248–1259 (2007).
53. González-Vázquez, M. P., Rubiera, F., Pevida, C., Pio, D. T. & Tarelho, L. A. C. Thermodynamic analysis of biomass gasification using aspen plus: Comparison of stoichiometric and non-stoichiometric models. *Energies (Basel)* 14, (2021).
54. Go, K. S., Son, S. R., Kim, S. D., Kang, K. S. & Park, C. S. Hydrogen production from two-step steam methane reforming in a fluidized bed reactor. *Int J Hydrogen Energy* 34, 1301–1309 (2009).
55. Oni, A. O., Anaya, K., Giwa, T., Di Lullo, G. & Kumar, A. Comparative assessment of blue hydrogen from steam methane reforming, autothermal reforming, and natural gas decomposition technologies for natural gas-producing regions. *Energy Convers Manag* 254, 115245 (2022).
56. Zapantis Alex. *BLUE HYDROGEN*. (2021).
57. Methane Pyrolysis: Unlocking the Potential of Turquoise Hydrogen. https://www.idtechex.com/en/research-article/methane-pyrolysis-unlocking-%20the-potential-of-turquoise-hydrogen/29395 (2023).
58. Sheil, A., Konarova, M., McConnachie, M. & Smart, S. "Selectivity and reaction kinetics of methane pyrolysis to produce hydrogen in catalytically active molten salts". *Appl Energy* 364, 123137 (2024).

59. Takeshi Amari, Nickolas J. Themelis & Iddo K. Wernick. Resource recovery from used rubber tires. *Resources Policy* 25, 179–188 (1999).
60. Siddiqui, H. *et al.* Comprehensive review of carbon materials as counter electrodes in dye-sensitized solar cells: Efficiency assessment and deposition methods. *Mater Sci Semicond Process* 172, 108074 (2024).
61. Dadsetan, M. *et al.* Characterization of carbon products from microwave-driven methane pyrolysis. *Carbon Trends* 12, 100277 (2023).
62. Klein, F. *et al.* Iron partitioning and hydrogen generation during serpentinization of abyssal peridotites from 15°N on the Mid-Atlantic Ridge. *Geochim Cosmochim Acta* 73, 6868–6893 (2009).
63. Kelley, D. S. *et al.* A Serpentinite-Hosted Ecosystem: The Lost City Hydrothermal Field. *Science (1979)* 307, 1428–1434 (2005).
64. Worman, S. L., Pratson, L. F., Karson, J. A. & Klein, E. M. Global rate and distribution of H_2 gas produced by serpentinization within oceanic lithosphere. *Geophys Res Lett* 43, 6435–6443 (2016).
65. Incer-Valverde, J., Korayem, A., Tsatsaronis, G. & Morosuk, T. "Colors" of hydrogen: Definitions and carbon intensity. *Energy Convers Manag* 291, 117294 (2023).
66. Małek, A., Dudziak, A., Caban, J. & Stoma, M. Strategic Model for Yellow Hydrogen Production Using the Metalog Family of Probability Distributions. *Energies (Basel)* 17, 2398 (2024).
67. Makky, A. Al, Kanjo, H. A., Salameh, T., Hamid, A. K. & Hussein, M. Performance analysis of yellow hydrogen production in the UAE. *Energy Conversion and Management: X* 26, (2025).
68. Droege T. What are the colors of hydrogen? *Williams Companies* https:// www.williams.com/2021/04/23/what-are-the-colors-of-hydrogen/ (2021).

69. Liponi, A., Pasini, G., Baccioli, A. & Ferrari, L. Hydrogen from renewables: Is it always green? The Italian scenario. *Energy Convers Manag* 276, 116525 (2023).
70. Ajanovic, A., Sayer, M. & Haas, R. The economics and the environmental benignity of different colors of hydrogen. *Int J Hydrogen Energy* 47, 24136–24154 (2022).
71. Zhang, Y., Huang, T. & Bompard, E. F. Big data analytics in smart grids: a review. *Energy Informatics* vol. 1 Preprint at https://doi.org/10.1186/s42162-018-0007-5 (2018).
72. Sharma, R., Gupta, D., Maseleno, A. & Peng, S. Introduction to the special issue on big data analytics with internet of things-oriented infrastructures for future smart cities. *Expert Syst* 39, (2022).
73. Sharma, R., Gavalas, D. & Peng, S.-L. Smart and Future Applications of Internet of Multimedia Things (IoMT) Using Big Data Analytics. *Sensors* 22, 4146 (2022).
74. Zheng, J., Wu, Z., Sharma, R. & Lv, H. Adaptive decision model of product team organization pattern for extracting new energy from agricultural waste. *Sustainable Energy Technologies and Assessments* 53, 102352 (2022).
75. Tracking Clean Energy Progress 2023. https://www.iea.org/reports/tracking-clean-energy-progress-2023 (2023).
76. Kumar, D., Rohit, S., Gwanggil, S., Raghvendra, J. & Editors, K. *Intelligent Systems Reference Library 247 Data Analytics for Smart Grids Applications-A Key to Smart City Development*.
77. Eltigani, D. & Masri, S. Challenges of integrating renewable energy sources to smart grids: A review. *Renewable and Sustainable Energy Reviews* vol. 52 770–780 Preprint at https://doi.org/10.1016/j.rser.2015.07.140 (2015).
78. Powell, J., McCafferty-Leroux, A., Hilal, W. & Gadsden, S. A. Smart grids: A comprehensive survey of challenges, industry applications,

and future trends. *Energy Reports* vol. 11 5760–5785 Preprint at https://doi.org/10.1016/j.egyr.2024.05.051 (2024).

79. Marocco, P., Gandiglio, M. & Santarelli, M. Optimal design of PV-based grid-connected hydrogen production systems. *J Clean Prod* 434, (2024).
80. Jordan, T. Hydrogen technologies. in *Hydrogen Safety for Energy Applications* 25–115 (Elsevier, 2022). doi:10.1016/B978-0-12-820492-4.00005-1.
81. Preston, N. *et al.* How can the integration of renewable energy and power-to-gas benefit industrial facilities? From techno-economic, policy, and environmental assessment. *Int J Hydrogen Energy* 45, 26559–26573 (2020).
82. Baufumé, S. *et al.* GIS-based scenario calculations for a nationwide German hydrogen pipeline infrastructure. *Int J Hydrogen Energy* 38, 3813–3829 (2013).
83. Okonkwo, E. C., Al-Breiki, M., Bicer, Y. & Al-Ansari, T. Sustainable hydrogen roadmap: A holistic review and decision-making methodology for production, utilisation and exportation using Qatar as a case study. *Int J Hydrogen Energy* 46, 35525–35549 (2021).
84. Rezaei, M., Khalilpour, K. R. & Mohamed, M. A. Co-production of electricity and hydrogen from wind: A comprehensive scenario-based techno-economic analysis. *Int J Hydrogen Energy* 46, 18242–18256 (2021).
85. Bristowe, G. & Smallbone, A. The Key Techno-Economic and Manufacturing Drivers for Reducing the Cost of Power-to-Gas and a Hydrogen-Enabled Energy System. *Hydrogen* 2, 273–300 (2021).
86. Tozlu, A. Techno-economic assessment of a synthetic fuel production facility by hydrogenation of CO2 captured from biogas. *Int J Hydrogen Energy* 47, 3306–3315 (2022).

87. Tozlu, A. Techno-economic assessment of a synthetic fuel production facility by hydrogenation of CO2 captured from biogas. *Int J Hydrogen Energy* 47, 3306–3315 (2022).
88. Bhandari, R. & Shah, R. R. Hydrogen as energy carrier: Techno-economic assessment of decentralized hydrogen production in Germany. *Renew Energy* 177, 915–931 (2021).
89. Hofrichter, A., Rank, D., Heberl, M. & Sterner, M. Determination of the optimal power ratio between electrolysis and renewable energy to investigate the effects on the hydrogen production costs. *Int J Hydrogen Energy* 48, 1651–1663 (2023).
90. Kitzing, L., Mitchell, C. & Morthorst, P. E. Wind Energy Policy. in *Comprehensive Renewable Energy* 721–731 (Elsevier, 2022). doi:10.1016/B978-0-12-819727-1.00160-6.
91. Hassan, Q. *et al.* Renewable energy-to-green hydrogen: A review of main resources routes, processes and evaluation. *Int J Hydrogen Energy* 48, 17383–17408 (2023).
92. Somma, M. Di *et al.* Integration of renewable energy source in transmission grids: issues and perspectives. in *2021 IEEE International Conference on Environment and Electrical Engineering and 2021 IEEE Industrial and Commercial Power Systems Europe (EEEIC / I&CPS Europe)* 1–8 (IEEE, 2021). doi:10.1109/EEEIC/ICPSEurope51590.2021.9584553.
93. Marouani, I. *et al.* Integration of Renewable-Energy-Based Green Hydrogen into the Energy Future. *Processes* 11, 2685 (2023).
94. Rampini, A. Idrogeno: prospettive e sviluppi.
95. Abe, R. Recent progress on photocatalytic and photoelectrochemical water splitting under visible light irradiation. *Journal of Photochemistry and Photobiology C: Photochemistry Reviews* vol. 11 179–209 Preprint at https://doi.org/10.1016/j.jphotochemrev.2011.02.003 (2010).

CHAPTER 2

Green hydrogen production

2.1 The water splitting reaction: the chemistry behind green hydrogen

The water splitting reaction (WSR) is a carbon-free method to produce one mole of hydrogen and one mole of oxygen from two moles of water.

$$2\,H_2O \rightarrow O_2 + 2\,H_2 \tag{15}$$

As a redox reaction, water splitting consists of two half-reactions: the oxygen evolution reaction (OER) and the hydrogen evolution reaction (HER). From a thermodynamic point of view, the WSR is a non-spontaneous reaction having a standard Gibbs free energy change of +237.178 kJ mol^{-1}. This implies that it must be run by providing the system with external energy. In this regard, a distinction must be made between primary and secondary energy sources. Primary energy sources are defined as all those energy sources that are present in nature in a form directly usable by humans, without the need to be subjected to industrial transformations or other intermediate processing. Primary energy sources can be non-renewable, such as crude oil, natural gas, coal, nuclear fuels, or renewables, such as solar, wind, hydroelectric, geothermal, biomass, tidal and wave energy.

Secondary energies derive from the transformation of primary energy forms. They include liquid fuels, such as gasoline and diesel, or electricity and heat. For hydrogen to be environmentally friendly, the primary source of energy used must be carbon-free and totally renewable.
Generally, water splitting process for green hydrogen production can occur through photolysis, thermolysis, or electrolysis when the source of energy is an electromagnetic radiation, heat or electricity respectively.

2.1.1 *Photocatalytic water splitting*

Photocatalytic splitting of water is an artificial form of photosynthesis that breaks down H_2O into its components H_2 and O_2 through the use of solar energy (photons) and a photocatalyst. As in photosynthesis where solar energy is converted into chemical energy in the form of glucose, during the photocatalytic splitting of water light energy is converted into chemical energy in the form of hydrogen. For the overall water splitting, however, several metal oxide-based photocatalytic systems have been reported to be active most of them need ultraviolet (UV) light ($\lambda < 400$ nm) because semiconductor materials have a wide bandgap. Since the visible region (400 nm $< \lambda <$ 800 nm) contains nearly half of the solar energy incident on the Earth's surface, photocatalytic water splitting requires efficient use of visible light to achieve large-scale H_2 production.
Three primary processes are involved in photocatalysis on semiconductor particles (Figure 25a):

1. Photons with energies higher than the semiconductor bandgap are absorbed, resulting in the creation of electron (e^-)-hole (h^+) pairs in the semiconductor particles, which are essential for driving the redox reactions.
2. Charge separation between electrons and holes and subsequent migration of these to the surface of the semiconductors particles before recombination occurs. Efficient charge separation is crucial for enhancing reaction efficiency.

3. Water oxidation (oxygen evolution reaction, OER) and proton reduction (hydrogen evolution reaction, HER). The holes in the valence band participate in the oxidation of water molecules (Equation 16), while the excited electrons in the conduction band reduce protons into hydrogen (Equation 17):

$$2\,H_2O + 4\,h^+ \rightarrow O_2 + 4\,H^+ \tag{16}$$

$$4\,H^+ + 4\,e^+ \rightarrow 2\,H_2 \tag{17}$$

Both these reactions typically require a co-catalyst like platinum or suitable surface modifications to improve efficiency.

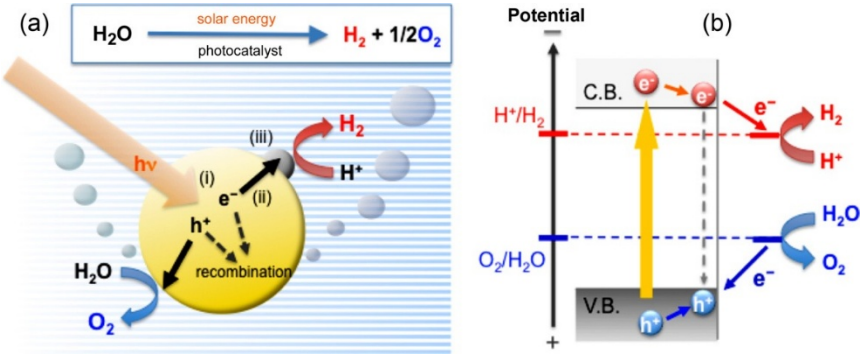


Figure 25. Schematic illustration of water splitting over semiconductor photocatalyst.[95]

It is also possible for electrons and holes to recombine with each other without taking part in any chemical reaction. As shown in Figure 25b, to split water using a heterogeneous semiconductor photocatalyst, the upper part of the valence band (VB) must be more positive than the oxidation potential of water to produce O_2, and the lower part of the conduction band (CB) must be more negative than the reduction potential of water to produce H_2.[95]

2.1.2 *Thermochemical water splitting*

In thermochemical water-splitting processes hydrogen is produced by a sequence of chemical reactions fueled by high-temperature heat (500 °C to 2000 °C). The process creates a closed cycle that uses only water and generates hydrogen and oxygen by reusing the chemicals used in each cycle.[96] In water thermolysis, the driving energy source can be purely thermal or hybrid, that is, thermal energy is associated with photonic or electrical energy. H_2 and O_2 can be produced from water in a single step. However, thermochemical cycles are suggested as a series of repeated reactions in which water is split using thermal energy at temperatures below 2000 °C, typically in two or more steps, due to undesirable thermodynamics and the extremely high temperature required for the single step.[97] To date, more than 200 possible thermochemical cycles have been identified, but only few of them are suitable for large-scale hydrogen production. Among these, the best known is the Sulphur-Iodine cycle (S-I), which uses the heat produced by nuclear reactions and can reach up to 900 °C (Figure 26).[98]

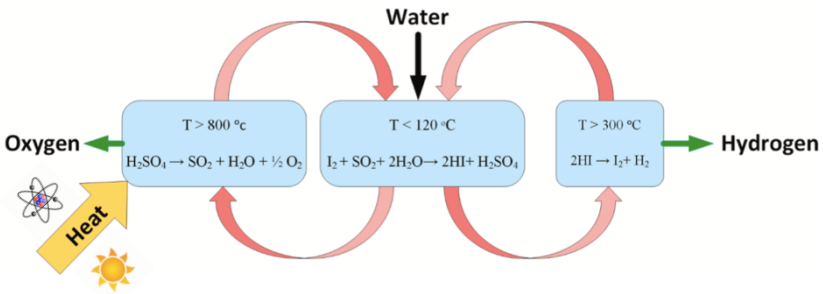


Figure 26. Schematic diagram for a three step S-I thermochemical cycle.[99]

Two moles of water vapor react with one mole of iodine and one mole of sulfur dioxide in the exothermic Bunsen reaction at temperature above 120 °C to form one mole of sulfuric acid and two moles of hydroiodic acid. Sulfuric acid and hydroiodic acid are separated and because of the endothermic decomposition they are treated at high temperatures,

respectively above 800 °C and 300 °C, giving oxygen and hydrogen as by-products and transformed into the starting reagents which react with water vapor to start the cycle again. Although the method is quite simple, it has some drawbacks, such as the high corrosiveness of the reagents and the loss of a significant amount of iodine during separation from H_2SO_4.

Alternative techniques that utilize both heat and an electrically driven reaction are hybrid thermochemical water splitting cycles. The advantage of hybrid processes is that two-step processes can be powered by moderately heated heat sources or nuclear waste heat and require much lower temperatures.[100]

In hybrid thermochemical water splitting (Figure 27), sulfuric acid undergoes a thermal degradation step that produces oxygen, followed by electrolysis of SO_2 that produces hydrogen and consumes electricity.

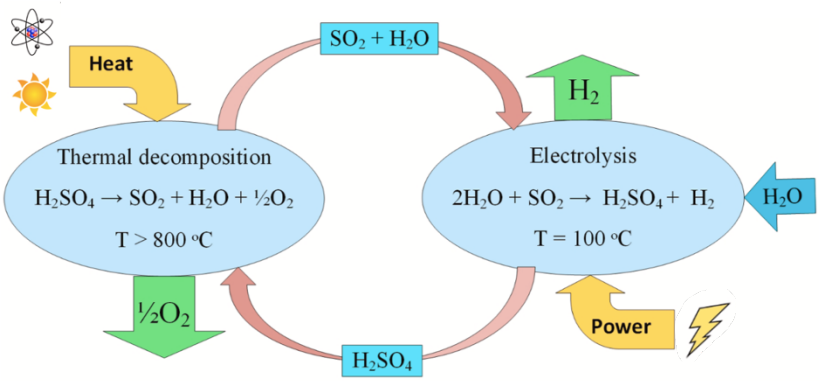


Figure 27. Schematic diagram for a hybrid sulfur thermochemical cycle.[99]

Sulfur dioxide electrolysis requires a voltage of roughly 0.17 V, which is significantly less than the voltage needed to electrolyze water (1.23 V).[101]

2.1.3 *Electrolytic water splitting*

The electrolysis of water is an electrochemical process to split water into oxygen and hydrogen. An electrolyzer unit, a typical device used for water electrolysis, is composed by:

1. A positive electrode (anode) and a negative electrode (cathode) usually separated by a permeable membrane.
2. An electrolyte allows the passage of ions between the electrodes, thus allowing the circulation of electric current in the circuit. It can be liquid, such as alkaline or acidic solutions, or solid, such as a proton exchange membrane (PEM).
3. An external electrical energy source that is transformed into chemical energy by a charge transfer reaction at the electrode-electrolyte interface.

Oxygen Evolution Reaction (OER) takes place at the anode while Hydrogen Evolution Reaction (HER) occurs at the cathode. Under standard conditions, namely, ion concentration 1 M, gas pressure 1 atm and temperature 25 °C (298 K), a redox couple have an intrinsic tendency to gain or lose electrons. Equations 18 and 19 show OER and HER in acidic media and their standard reduction potential.

$$2\,H_2O \rightarrow O_2 + 4\,e^- + 4\,H^+ \quad E^0 = 1.23\ \text{V versus SHE at pH 0} \tag{18}$$

$$2\,H^+ + 2\,e^- \rightarrow H_2 \quad E^0 = 0\ \text{V versus SHE at pH 0} \tag{19}$$

As above-mentioned, the WSR is a non-spontaneous reaction having a standard Gibbs free energy change of +237.178 kJ mol^{-1}. This is obviously also true from an electrochemical point of view, where a negative cell potential indicates the non-spontaneity of the reaction.

$$E^0_{\text{cell}} = E^0_{\text{cathode}} - E^0_{\text{anode}} = -1.23\ V \tag{20}$$

The Gibbs free energy for an electrochemical reaction is related to the standard cell potential by Equation 18:

$$\Delta G^0 = -nFE^0 \tag{21}$$

where:

ΔG^0: standard Gibbs free energy change (Joules)

n: number of electrons transferred ($4e^-$/mol)

F: Faraday's constant (96485 C mol^{-1})

E^0: standard cell potential (V)

Figure 28 shows a schematic representation of an electrolysis cell for water splitting in acidic media.

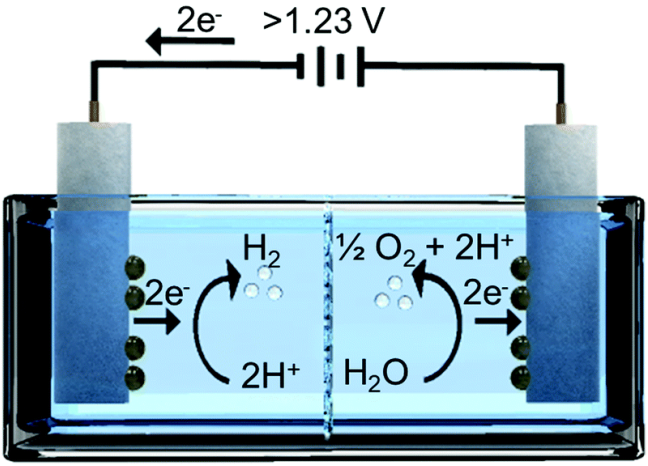


Figure 28. Electrolysis cell for water splitting reaction in acid media.[102]

Under non-standard conditions, electrode potential of an electrochemical cell is calculated by the Nernst equation (Equation 22), according to which, cell potential depends on ion nature, and the relative activities of the oxidized (Ox) and Reduced (Red) species in the system at equilibrium.

$$E = E^0 - \frac{RT}{nF} ln \frac{(Red)}{(Ox)} = E^0 - \frac{2.303RT}{nF} log \frac{(Red)}{(Ox)} \tag{22}$$

where:
E: cell potential (V)
E^0: standard cell potential (V)
R: universal gas constant (8.3145 J mol^{-1} K^{-1})
T: temperature (K)
n: number of electrons transferred
F: Faraday's constant (96485 C mol^{-1})
(Red): activity of the reduced specie
(Ox): activity of the oxidized specie

In water splitting reaction, the Nernst equation describes the shift in electrode potential with pH. Under standard conditions, Equation 22 can be simplified to Equation 23:

$$E = E^0 - \frac{0.059}{n}\log[\mathrm{H}^+] \tag{23}$$

For OER, as pH increases ($[\mathrm{H}^+]$ decreases), E decreases, meaning OER becomes thermodynamically more favorable in alkaline solution (Equation 24):

$$E = 1.23\ \mathrm{V} - 0.059\ \mathrm{pH} \tag{24}$$

For HER, as pH decreases ($[\mathrm{H}^+]$ increases), E decreases, meaning HER becomes thermodynamically more favorable in acidic solution (Equation 25):

$$E = -0.059\ \mathrm{pH} \tag{25}$$

The thermodynamic stability of chemical species in water as a function of pH and electrical potential (E) relative to the standard hydrogen electrode (SHE) is graphically represented in the Pourbaix diagram of water. The two lines related to the Equations (24) and (25) divide the Pourbaix diagram shown in Figure 29 into three zones. Above the upper line, water dissociates

with the development of oxygen and the production of acidity. Between the two lines is the zone of electrochemical stability of water. Below the lower line, water dissociates with the development of hydrogen and the production of alkalinity.

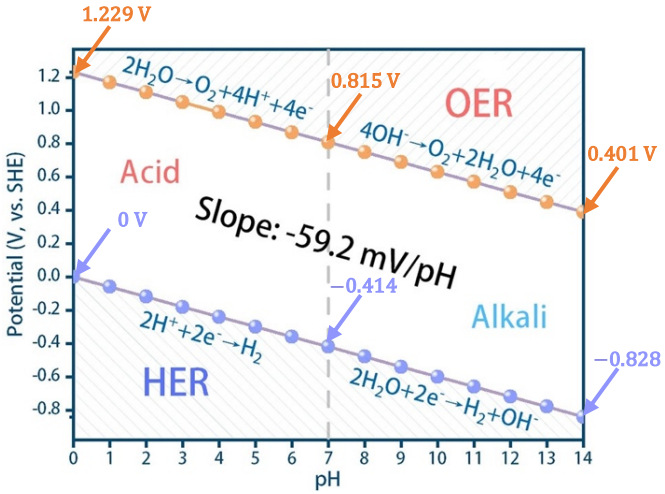


Figure 29. Pourbaix diagram and reaction processes of water showing the pH dependence of HER and OER.[103]

Equations 26 and 27 show HER and OER in neutral medium respectively.

$$4\ H_2O + 4\ e^- \rightarrow +2\ H_2 + 4\ OH^- \qquad E^0 = 0.414\ \text{V versus SHE at pH 7} \quad (26)$$

$$2\ H_2O \rightarrow O_2 + 4\ H^+ + 4\ e^- \qquad E^0 = -0.815\ \text{V versus SHE at pH 7} \quad (27)$$

Equations 28 and 29 show HER and OER in basic medium respectively.

$$2\ H_2O + 2\ e^- \rightarrow H_2 + 2\ OH^- \qquad E^0 = -0.828\ \text{V versus SHE at pH 14} \quad (28)$$

$$4\ OH^- \rightarrow O_2 + 2\ H_2O + 4\ e^- \qquad E^0 = 0.401\ \text{V versus SHE at pH 14} \quad (29)$$

However, a large overpotential (the difference between the applied potential and the thermodynamic potential) is usually required to achieve industrially relevant current density due to the slow kinetics of both half-reactions. This results in lower energy conversion efficiency.[104]

It is generally recognized that the formation of hydrogen on the cathode surface results from a multi-step two-electron transfer process both in acidic medium and alkaline medium while the formation of oxygen on the anode results from a multi-step four-electron transfer process both in acidic medium and alkaline medium.

Reaction mechanism in the electrocatalytic hydrogen evolution

The commonly accepted pathway for the evolution of hydrogen involves the Volmer reaction, followed either by the Heyrovsky or the Tafel reaction. In the Volmer reaction in acidic medium, a proton from the solution is combined with an electron from the electrocatalyst and adsorbed on the catalyst surface (Equation 30). In the Volmer-Heyrovsky pathway, H_2 is generated by the reaction of adsorbed hydrogen intermediates and protons in the acid electrolyte (Equation 31). Alternatively, in the Volmer-Tafel pathway the paired hydrogen intermediates directly combine on the surface of the electrocatalyst to evolve H_2 (Equation 32). Figures 30 represents the two possible pathways for hydrogen evolution reaction in acidic medium.

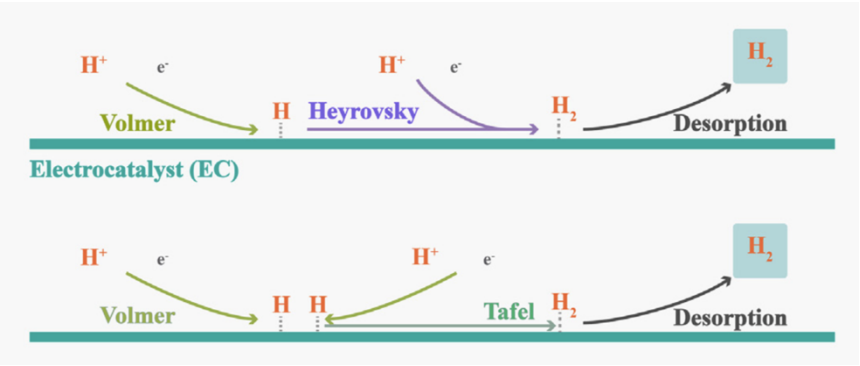


Figure 30. Two electron-transfer involved electrocatalytic hydrogen evolution mechanism in acidic medium.[105]

The same reactions occur in alkaline medium, with the difference that the protons come from the water with the release of hydroxyl ions (Equations 33-35). Figure 31 shows the two possible pathways for hydrogen evolution in alkaline medium.

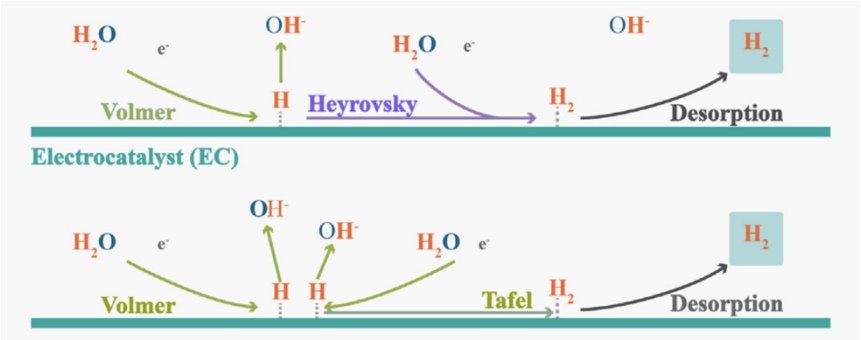


Figure 31. Two electron-transfer involved electrocatalytic hydrogen evolution mechanism in alkaline medium.[105]

All the above reactions involved in HER are reported in Table 7.

Table 7. Reaction mechanisms in the electrocatalytic hydrogen evolution in acidic and alkaline medium.[105]

Medium	Reaction	Name	#
Acidic	$H^+ + e^- + M \rightarrow M - H_{ads.}$	Volmer	(30)
	$M - H_{ads.} + H^+ + e^- \rightarrow M + H_2$	Heyrovsky	(31)
	$2\,M - H_{ads.} \rightarrow 2M + H_2$	Tafel	(32)
Alkaline	$H_2O + e^- + M \rightarrow M - H_{ads.} + OH^-$	Volmer	(33)
	$M - H_{ads.} + H_2O + e^- \rightarrow M + H_2 + OH^-$	Heyrovsky	(34)
	$2\,M - H_{ads.} \rightarrow 2M + H_2$	Tafel	(35)

Reaction mechanism in the electrocatalytic oxygen evolution

The energy efficiency of the entire water electrolysis process is hampered by the oxygen evolution reaction's relatively slow kinetics, due to multi-electron/proton processes. For acidic OER illustrated in Figure 32, a one-electron oxidation process is used to first adsorbe water molecules on the electrocatalyst's active sites producing adsorbed hydroxyl species (*OH) (Equation 36). After the oxidation of the *OH, oxo intermediates (*O) remain adsorbed on the catalyst (Equation 37). Oxo intermediates undergo two different pathways: (i) similarly to HER, they can react in a redox reaction with another water molecule from the solution to obtain peroxide intermediates (*OOH) (Equation 38), which are then oxidized to O_2 (Equation 39) or (ii) they can directly combine to another adsorbed oxo intermediate nearby (Equation 40). Each step of the reaction releases one electron, for a total of 4 electrons.

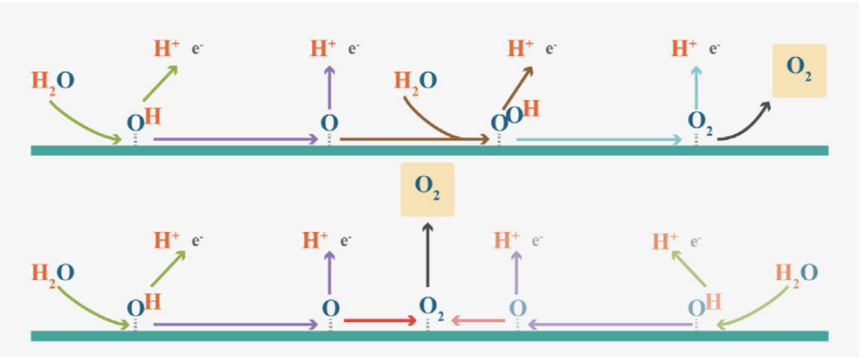


Figure 32. Four electron-transfer involved electrocatalytic oxygen evolution mechanism in acidic medium.

In Figure 33 the OER in alkaline medium is represented. A hydroxyl ion combines with an electron to be adsorbed on the catalyst's surface (Equaiton 41). It then reacts with another hydroxyl ion to form O* specie by releasing water (Equation 42). Subsequently, it can either (i) react with another OH^- obtaining a peroxide specie (*OOH) (Equation 43) that ultimately reacts with a OH^- evolving in oxygen (Equation 44), or (ii) it can combine with another adsorbed O* on the nearby site to evolve in oxygen (Equation 45).

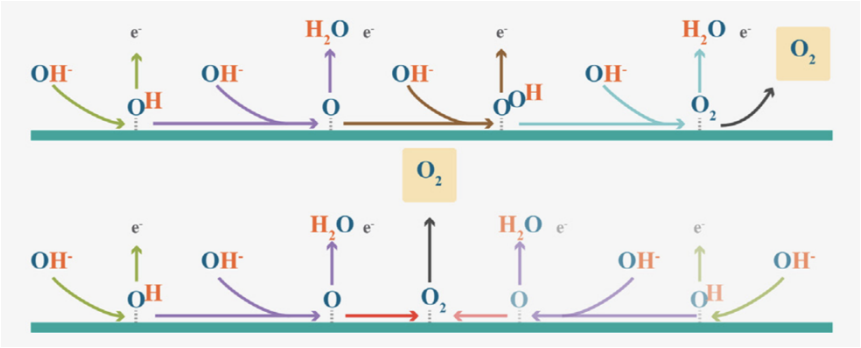


Figure 33. Four electron-transfer involved electrocatalytic oxygen evolution mechanism in alkaline medium.[105]

All the above reactions involved in OER are reported in Table 8.

Table 8. Reaction mechanisms in the electrocatalytic oxygen evolution in acidic and alkaline medium.[105]

Medium	Reaction	#
Acidic	$M + H_2O \rightarrow M - OH_{ads.} + H^+ + e^-$	(36)
	$M - OH_{ads.} \rightarrow M - O_{ads.} + H^+ + e^-$	(37)
	$M - O_{ads.} + H_2O \rightarrow M - OOH_{ads.} + H^+ + e^-$	(38)
	$M - OOH_{ads.} \rightarrow M + O_2 + H^+ + e^-$	(39)
	$2\,M - O_{ads.} \rightarrow 2\,M + O_2$	(40)
Alkaline	$M + OH^- \rightarrow M - OH_{ads.} + e^-$	(41)
	$M - OH_{ads.} + OH^- \rightarrow M - O_{ads.} + H_2O + e^-$	(42)
	$M - O_{ads.} + OH^- \rightarrow M - OOH_{ads.} + e^-$	(43)
	$M - OOH_{ads.} + OH^- \rightarrow M + O_2 + H_2O + e^-$	(44)
	$2\,M - O_{ads.} \rightarrow 2\,M + O_2$	(45)

2.2 Overview of current catalysts used for Hydrogen Production

2.2.1 *State-of-the-art catalyst: platinum and its properties*

In addition to being an uphill reaction, as indicated by the positive value of the Gibbs free energy (ΔG), electrolytic water splitting must overcome a substantial kinetic barrier. Catalysts play a crucial role in lowering the kinetic barrier. According to the Sabatier principle, the best catalyst for a particular reaction binds intermediates with a moderate degree of strength. This is frequently explained qualitatively in a straightforward manner: a balance must be struck between binding strongly enough to promote the reaction and weakly enough to allow the product to readily desorb (Figure 34).

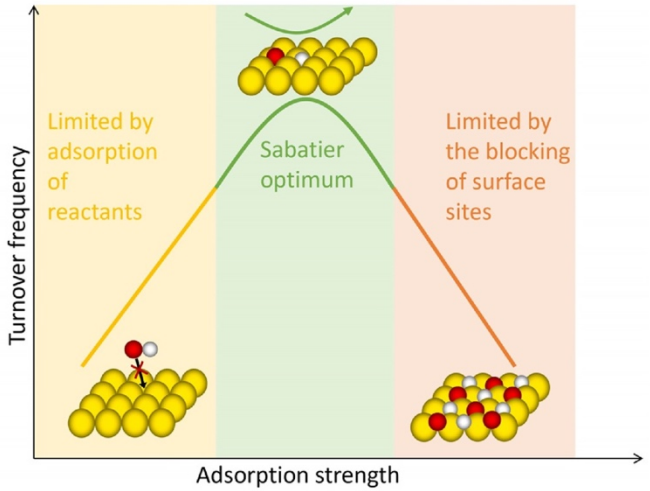


Figure 34. Diagram of the Sabatier principle. Slow product formation or desorption limits the reaction for strong-binding materials. Slow reactant activation or adsorption limits the reaction for weak-binding materials. The ideal catalyst has a medium binding strength.[106]

The development of density functional theory (DFT) in recent decades, had the Sabatier principle evolved from an empirical principle for comprehension to a predictive tool for screening and design of catalysts. The combination of experimental rates and DFT-calculated adsorption energies

frequently produces a volcano plot with low activity for very weak or very strong binding. This method can be applied to catalyst screening or rational design in order to identify the best value for the descriptor. This combination of DFT-calculated adsorption energies and experimental rates has been used to study a number of reactions. According to the Sabatier Principle, the efficiency of an HER catalyst is largely determined by the hydrogen adsorption free energy on the catalyst surface. The optimal catalyst should have a hydrogen adsorption free energy close to 0 eV, ensuring a balanced adsorption and desorption process. For instance, a plot resembling a volcano is produced when the catalytic activity for the HER is plotted against the hydrogen adsorption energies on metal determined by DFT. According to a simple kinetic model, in the left side of the volcano, corresponding to the strong binding region, we find catalysts that bind the adsorbed hydrogen too strongly, making the product desorption the rate-limiting step. The right side corresponds to the weak binding region, in which catalysts do not adsorb the intermediate efficiently. The most active catalysts are found at the peak, where the binding energy is optimized for both adsorption and desorption, meaning that the hydrogen adsorption free energy is 0 and leading to the best compromise to have an excellent activity. Figure 35 shows the catalysts activity plotted against the DFT-calculated metal-hydrogen bond strength, in which platinum (Pt) is placed at the peak of the volcano plot.[107]

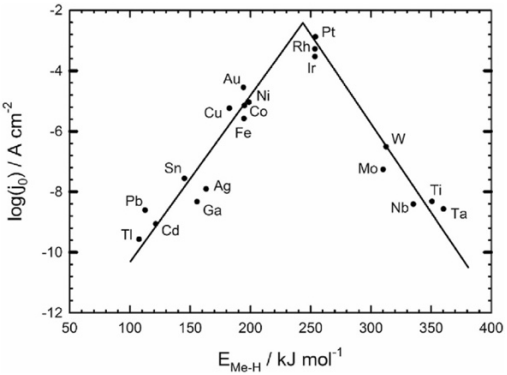


Figure 35. A volcano plot for the HER derived from the experimental current density and the DFT-calculated metal-hydrogen bond strength.

Not only for HER, but for many energy-related electrocatalytic systems, including the methanol oxidation reaction (MOR), oxygen reduction reaction (ORR) and ethanol oxidation reaction (EOR), platinum is the most extensively studied catalyst due to its inherent electrocatalytic activity and stability.[108–110] When assessing the catalytic performance, some important parameters are taken into account.

Overpotential

Under standard conditions, as previously mentioned in Equation 19, theoretical E_0 for HER vs SHE is 0. To overcome some unfavorable issues, such as kinetic energy barrier due to high ΔG_H and electrolyte resistance in three electrode measurement system, the practical procedure necessitates an overpotential (η), an extra voltage required in excess of the theoretical value needed to reach a specific current density (usually 10 mA/cm^2) to drive HER. Overpotential is calculated by Equation 46 as the difference between the experimental potential to and the standard potential. An excellent catalyst shows a high energy efficiency measured by a low overpotential.

$$\eta = E - E_0 \tag{46}$$

Platinum overpotential at 10 mA/cm^2 in acidic medium (0.5 M H_2SO_4) is comprised between 0 and 50 mV while in alkaline medium (1 M NaOH) is comprised between 50 and 100 mV.

Tafel slope

The Tafel slope gives an indication of the rate-limiting step and the mechanism of the reaction.
Overpotential and exchange current density are correlated by the Tafel slope in Equation 47:

$$\eta = b \cdot log\, j + a \tag{47}$$

where:
η: overpotential (V)
b: Tafel slope (mV/dec)
j: current density (A/cm^2)
a: Tafel intercept

Since a smaller overpotential is needed to increase the same current density, a smaller Tafel slope indicates a faster reaction kinetic. A Tafel slope of 30 mV/dec indicate that the process proceeds through the Volmer-Tafel path while a Tafel slope of 40 mV/dec indicate that the process proceeds through the Volmer-Heyrovsky mechanism. Both cases indicate that the adsorption of hydrogen on the catalyst surface is simple to carry out and that its desorption influences the HER reaction rate. When hydrogen is not readily adsorbed to the active sites on the catalyst surface, the Volmer step becomes the rate-limiting step reaching a Tafel slope of 120 mV/dec.[111,112]
In acidic medium, platinum has a Tafel slope of ~30 mV/dec, indicating that the Tafel step is the rate-limiting step. In alkaline medium, platinum shows a slightly higher Tafel slope (30-40 mV/dec) due to the additional water dissociation step required before hydrogen adsorption.

Turnover frequency (TOF)

The turnover frequency (TOF) in the HER process is the quantity of hydrogen molecules produced by each active site in a second. TOF is also able to assess each active site's inherent activity and effectiveness.[113] TOF is calculated based on Equation 48.[105]

$$TOF = \frac{I}{\alpha n F} \tag{48}$$

where:
I: current (A)
α: number of electrons transferred during HER
n: number of moles of active sites (mol)
F: Faraday constant (96485 C/mol)

Depending on conditions, the TOF of platinum varies from acidic medium (~1-10 s^{-1} at η =50 mV) to alkaline medium (~0.1-1 s^{-1} at η =50 mV) due to the slower kinetic for water dissociation.

Electrochemically Active Surface Area (ECSA)

The portion of the electrode material that is available to the electrolyte for charge transfer and/or storage is known as the electrochemically active surface area.[114] It is crucial for connecting an electrode's electrocatalytic performance to the inherent activity of the material being studied. A frequent method for estimating ECSA that is flexible and non-destructive is evaluating the double-layer capacitance (C_{dl}). In the non-faradic region, CV is carried out at varying scan rates in order to calculate C_{dl}. The current density variation ($\Delta J = Ja - Jc$) at a particular potential versus scan rate is linearly fitted to estimate C_{dl}. A higher C_{dl} value indicates a higher current density and more active sites exposed to the electrolyte. The calculation of ECSA is shown in Equation 49.

$$ECSA = \frac{C_{dl}}{C_s} \tag{49}$$

where:
C_{dl}: double-layer capacitance
C_s: specific capacitance

Another way to calculate ECSA is through the Randles-Sevcik equation (Equation 50). The Randles-Sevcik equation is a powerful tool in electrochemistry because it relates three key parameters: surface area, diffusion coefficient and redox specie concentration.[115]
In most cases, one of these three parameters will be unknown which opens a wide range of applications for this equation.

$$i_p = 0{,}4463nFAC\sqrt{\frac{nF\nu D}{RT}} \tag{50}$$

where:

i_p is the peak current of the redox reaction in the voltammogram (A)

n is the number of electrons of the reaction (1 for ferrocene)

F is Faraday's Constant (96485 C/mol)

A is the surface area of the working electrode (cm^2)

C is the concentration of the redox species (mol/cm^3)

v is the scan rate used to collect the voltammogram (V/s)

D is the diffusion coefficient of the redox species ($2{,}3 \cdot 10^{-5}$ cm^2/s for ferrocene)

R is the Gas Constant (8,314 J/molK)

T is the temperature (298,55 K)

Stability

For commercial application, stability or durability is a crucial metric to evaluate the performance of the electrocatalysts. The most widely used techniques to establish the catalyst's stability is cyclic voltammetry, chronoamperometry, and chronopotentiometry.[116] The stability is determined by comparing the overpotential value before and after the potential cycles using the Linear Sweep Voltammetry (LSV) curves at current density of 10 mA/cm^2.

Although platinum is a benchmark catalyst that shows excellent characteristics, it has drawbacks that prevent it from being produced on a large scale. Its scarcity results in a high cost on the market and the impossibility of creating a production chain of pure platinum-based electrolyzers for the development of hydrogen. Thus, current research is underway to find strategies to reduce the amount of metal used or replace it completely without sacrificing its excellent performance.

2.2.2 *Strategies for enhancing platinum catalyst efficiency in HER*

In order to reduce the amount of platinum, the overpotential requirement, minimize energy losses and simultaneously increase the overall energy conversion efficiency, intensive research has been conducted to study and

create a variety of electrocatalytic systems. The most commonly used strategies are listed below.

Nanostructuring

Nanoparticles are widely used as heterogeneous catalysts and many other fields such as energy conversion, storage, and biomedical drug delivery systems.[117,118] Regulating the dynamics of the nanostructure to achieve the desired catalytic activity is crucial for logical catalyst design.[119] Also, understanding and improving reaction on nanoparticles became more complex when unique physicochemical properties appeared at the nanoscale. After a so-called induction period, the reshaped nanocatalyst may show entirely different activity, either poisoned or promoted, due to the more flexible morphology of nanoparticles compared to chunky crystalline materials. Pt-based nanocatalysts come in a variety of architectures. When metal particles get smaller than 1 nm, their electronic characteristics should change significantly (Figure 36). The subnanometric metal particles should therefore interact with reactants in a different way and exhibit different reactivity in comparison to larger nanoparticles.

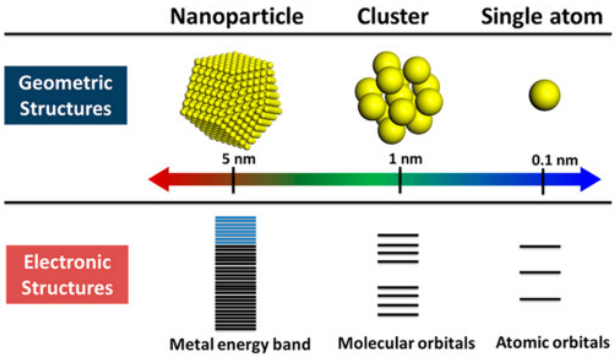


Figure 36. Geometric and electronic structure of nanoparticles, cluster and single atom.[120]

Chemical bonding can be used to stabilize atomic clusters and single-atom catalysts (SACs) on the support. While their electronic structure is closely linked to their electronic orbits and valance states, the geometric structure displays the coordination environments between a single atom and its

neighbors. The anchoring sites of support in the case of SACs are connected to the locations of individual atoms. Unique electronic structures are produced by the supports' unique location and chemical bonding.[121]

Alloying

Alloys are created when metals or metals are combined with other elements. These alloys have been extensively studied in electrocatalytic reactions, such as oxygen reduction reactions, CO_2 reduction reactions, nitrogen reduction reactions, hydrogen evolution reactions, and oxygen evolution reactions, and they have distinctive physical and chemical properties.[122] By optimizing the electron distribution towards a favorable adsorption/desorption behavior of the key intermediates, the components' synergy may speed up the reaction kinetics and improve electrocatalytic performance.[105]

Doping

Heteroatom doping has been shown to be a successful method for modifying the electronic structure, adding more active sites, and reducing the kinetic energy barriers.[123] With the exception of intrinsic characteristics, doping heteroatoms alters the elemental composition of catalysts, introducing charge redistribution and altering their surface and electronic characteristics. Doping is a capable and effective way to adjust catalysts' electrocatalytic activity toward HER and OER. Understanding the reaction path and function of the dopants in the CA is aided by both experimental research and DFT simulations. The concentration and locations of the dopants are determined using high-resolution imaging techniques. Metal and non-metal atom doping are the two general categories into which doping is divided. Heteroatom doping entails doping N, O, F, S, P, and B atoms, while transition metal atom doping includes doping Mn, Fe, Co, Ni, Cu, Zn, Mo, Pt, and Au atoms. It has been possible to successfully dope the carbon framework with both metal and non-metal atoms (graphene, CNTs, etc.). as well as catalysts based on transition metals.[123]

Vacancy-rich materials

Vacancies are the natural phenomenon of the crystal that exist above 0 K (absolute zero), and they cause imperfect distributions and arrangement of atoms in the crystal. By altering the density and distribution of vacancies in the crystals, one can modify their physical and chemical characteristics. It also has an impact on the crystals' free energy, enthalpy, and entropy. A variety of techniques, including plasma etching, thermal treatment, liquid exfoliation, chemical reductions, laser fragmentations, electrochemical methods, CVD methods, and others, have recently been used to purposefully create a vacancy.[124,125] The position and concentration of vacancies in the nanocrystals are determined using a variety of characterization techniques, including aberration-corrected transmission electron microscopy (TEM), high-angle annular dark-field scanning mode TEM (HAADF-STEM), positron annihilation spectroscopy, electron paramagnetic resonance spectroscopy, X-ray photoelectron spectroscopy, X-ray absorption fine structure spectroscopy, and others. Lately, the investigation into vacancies in electrocatalysts has gained significant importance and is a rapidly growing research field, as it aims to enhance the efficiency of the electrocatalyst for hydrogen evolution reaction (HER) and oxygen evolution reaction (OER).[126] In the context of transition metal catalysts (TMCs), three distinct categories of vacancies are generated, namely cationic, anionic, and a combination of both cationic and anionic vacancies. These vacancies play a crucial role in enhancing the performance of the electrocatalyst.[126] According to both theoretical and experimental research, vacancies in the electrocatalyst have a high exposed surface area, increase the density of exposed active sites, improve electrical conductivity by creating a new gap state, and reduce the energy barriers for the water adsorption/desorption pathway.[127,128] Vacancy-rich electrocatalysts created a new avenue for increasing electrocatalyst efficiency in the direction of HER and OER.

Carbon-based composite

For both academic research and industrial applications, composite catalysts are crucial.[129] Generally speaking, transition metal-based catalysts (TMCs) have fewer active sites, poor electrical conductivity, and accumulate during synthesis before dissolving during electrochemical reactions. Recently, solar cells, metal-air batteries, and water splitting have made extensive use of nanocarbon-based materials like graphene, carbon nanotubes (CNTs), mesoporous carbon, activated carbon, and so forth. Increased electrocatalytic activity could be greatly aided by the special qualities of nanocarbon materials, which include high surface area, superior electrical conductivity, tunable structure, high corrosion resistance, environmental friendliness, and novel physical and chemical properties.[130–132] TMCs have a special propensity to combine with nanocarbon-based materials to form composites, and the physicochemical properties of composites differ from those of their individual counterparts. The electrical conductivity is enhanced, and the number of active sites is increased by the synergistic interaction between nanocarbon and TMCs. These special qualities of the composite, in addition to the addition of chemical modification and processability, make it a perfect candidate for electrocatalytic activity toward HER and OER.[133,134] The carbon-based composite also lowers the composite's hydrogen adsorption Gibbs free energy (ΔG_{H^*}), according to theoretical research. Doping the nanocarbon's heteroatoms further reduces (ΔG_{H^*}). When dopant is present, the DOS of carbon shifts to the Fermi level and hydrogen adsorption strength, which lowers the ΔG_{H^*} value. On the other hand, the higher electrocatalytic activity is indicated by the lower ΔG_{H^*} value. Among the heteroatoms (N, P, B, S, and so forth. When it comes to electrocatalytic activity, the nitrogen-doped is far more active than the bare nanocarbon. The carbon-based composites are made using a variety of synthesis techniques, including low-temperature pyrolysis, electrochemical depositions, solvothermal, hydrothermal, and others.[135–137]

2.3 Exploration of an innovative supporting material: graphene

Graphene is a two-dimensional structure of sp^2 hybridized carbons, which form an extended crystal lattice with a honeycomb shape. Several layers of graphene, linked by van der Waals forces, form a 3D material called graphite, while a single sheet can be rolled up to form a nanotube or closed to form a fullerene (Figure 37).

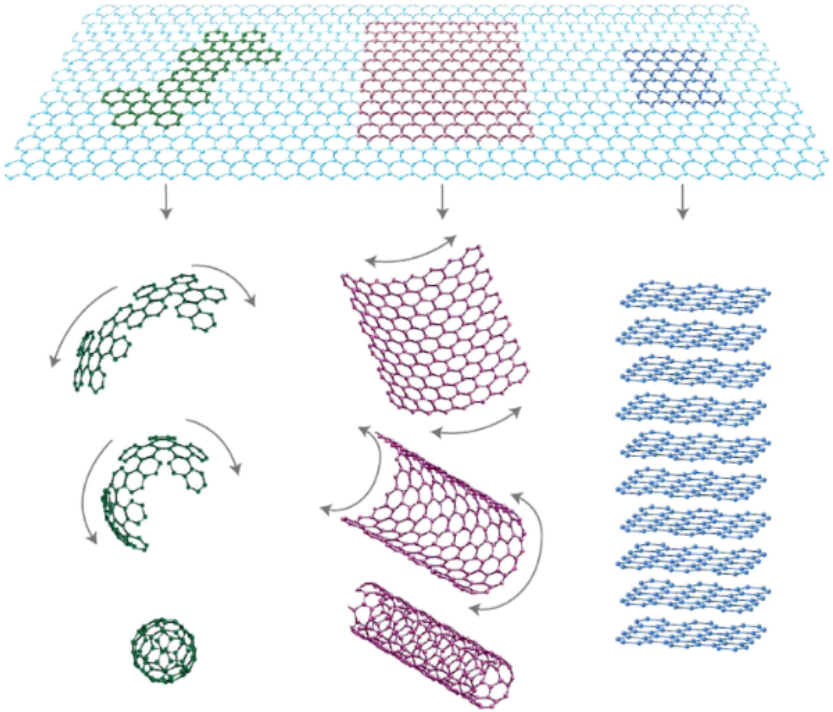


Figure 37. Representation of the structural relationship between graphene (top) and fullerenes (bottom left), carbon nanotubes (bottom center) and graphite (bottom right).[138]

An important feature of graphene, which explains part of its extraordinary physical characteristics, is the long-range π conjugation of the electrons found in the p atomic orbital, perpendicular to the plane.

Graphene is a material with exceptional physical properties. These properties, together with the abundance of low-cost graphite, have made graphene one of the most studied materials for application in countless innovative fields. Among its characteristics, the most interesting are high thermal conductivity, high electrical conductivity, particular hardness, excellent elasticity and flexibility, resistance similar to that of diamond combined with extreme lightness and the negligible Joule effect during current conduction. Some of these properties will be discussed.

Electrical conductivity

Even before graphene, carbon nanotubes were found to be excellent heat conductors,[139–141] with a theoretical and experimental λ (thermal conductivity) value calculated in the range 2000-6000 W mK^{-1}. Starting from 2008 in particular, these studies have focused on graphene, obtaining λ on average even higher than nanotubes. In 2008 A.A. Balandin and his group calculated the thermal conductivity of single layer graphene by heating a suspended graphene flake (Figure 38). The researchers obtained micrometric-sized fragments of monolayer graphene and positioned them on a channel obtained on the coating of a Si/SiO_2 wafer. The ends of the graphene fragment bound some graphitic material, which acted as a sink for the heat traveling from the laser source. A confocal Raman microscopy instrument was used, with which a 488 nm laser was irradiated on the suspended center of the graphene. In fact, the 488 nm radiation is strongly absorbed by graphene, allowing it to heat up. The temperature variation of the lattice was instead monitored by following the shift of the G peak by means of a 633 nm laser, which causes negligible heating. The result of these studies was that single layer graphene has a thermal conductivity in the range of 2000-5000 W mK^{-1}, depending on the amount of lattice defects.[142–144]

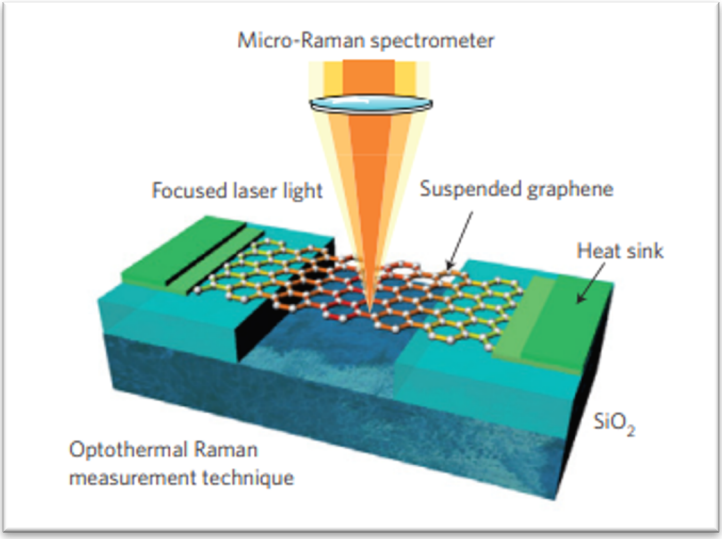


Figure 38. Representation of the experiment carried out by Balandin et al in 2008.[145]

Electronic mobility

The supposed high electronic mobility of graphene was suggested long before experiments could prove it.[146–148] The extraordinary electronic properties of graphene arise from its highly ordered lattice, which, in the absence of density defects, allows charge transport with negligible scattering. The first to make measurements of the electronic properties of few-layer graphene were Geim and Novoselov in 2004,[149] when they calculated electronic mobilities up to about 10,000 cm^2/Vs, although they emphasized that the mobility was limited by lattice defects. In 2008, Kim's group measured the carrier mobility of a single-layer graphene suspended between gold contacts. The suspended graphene was obtained on Si/SiO_2 wafers by removing the SiO_2 underlying the flake by immersion in an etching solution (buffered oxide etch). The mobility measured in this study was an extraordinary 230,000 cm^2/Vs.[150]

Flexibility and elasticity

The first experimental measurement of the mechanical properties of graphene was carried out by Frank's group,[151] on few-layer graphene fragments. Frank obtained grooves on the substrate, on which he deposited graphene to obtain the suspended material; after this, he measured the Young's modulus by means of force-displacement measurements with AFM. One year later, in 2008, Hone and Lee's group measured the elastic properties and the breaking strength of monolayer graphene suspended on a silicon substrate containing circular holes of 1 and 1.5 micrometers in diameter and 500 nm in depth (Figure 39).[152] Also, in this case the measurements were carried out with an AFM device, with diamond tips to avoid breakage.

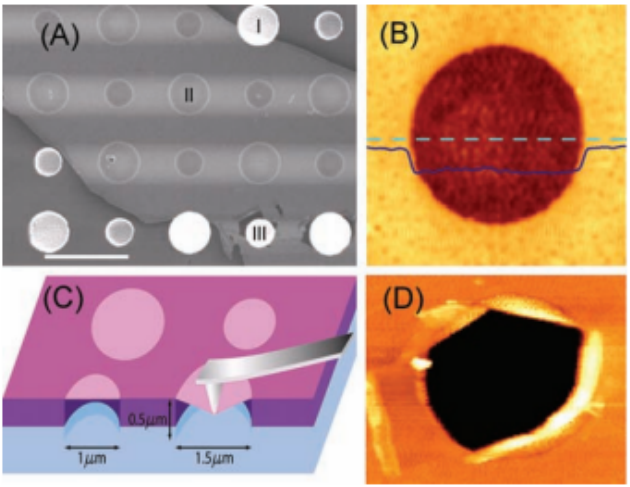


Figure 39. (A) SEM image of the perforated substrate overlaid by the monolayer graphene fragment (B) non-contact AFM image of a suspended membrane, with a height between the substrate and the graphene tip of 2.5 nm (C) schematic representation of the measurement (nanoidentation method) (D) AFM image of a perforated membrane.[153]

The study reports a Young's modulus of 1.0 TPa and a fracture strength of 130 GPa for a defect-free monolayer graphene. The authors of the study themselves defined graphene as "the strongest material ever measured".

Another study reports a Young's modulus value for graphene oxide reduced to 0.25 TPa; the measurement was obtained with a similar method to the previous one.[154,155]

2.3.1 *Graphene production methods*

The failure to produce mono- and few-layer graphene with a scalable method at industrial level has been, and continues to be, the main cause of the delay in the large-scale introduction of new technologies based on graphene. Figure 40 shows the two large groups of production methods of this crystalline lattice: bottom-up methods and top-down methods.

Bottom-up methods are those processes that lead to the formation of one or more layers of graphene starting from molecules containing carbon. An advantage of these production methods is that the graphene obtained often has a high surface area per fragment and few defects, while an important disadvantage is the often-extreme operating conditions and limited scalability. One of the most important bottom-up methods is certainly vapor flow deposition (CVD). Through the CVD technique it is possible to create single or very few-layer graphene (VFLG) with a relatively large area and a low concentration of lattice defects,[156–158] on various metal substrates, such as copper. The formation of the graphitic film occurs at temperatures of about 1000° C in the presence of organic gases, such as methane, which constitute the carbon source. Following the formation of the film on the metal substrate, the graphene must be transferred to another substrate, such as a silicon wafer, and this often leads to cracking or folding.[159] The resulting graphene is of high quality and with a high surface area, but the process is expensive due to the high energy consumption. Further challenges of the method are the necessary removal of the metal substrate, the difficulty in controlling the number of layers and doping, and the formation of grain boundaries, such as peripheral discontinuities in the crystal lattice. Another representative bottom-up method is the synthesis of graphene on SiC. It has been shown that a graphitic film can be obtained on both the silicon and carbon surfaces of a silicon carbide wafer. The process occurs by

sublimation of the silicon atoms, with formation of a graphitic surface.[156,160,161] The two main disadvantages of this technique are the high cost of the SiC wafers and the high operating temperatures, usually above 1000 °C.

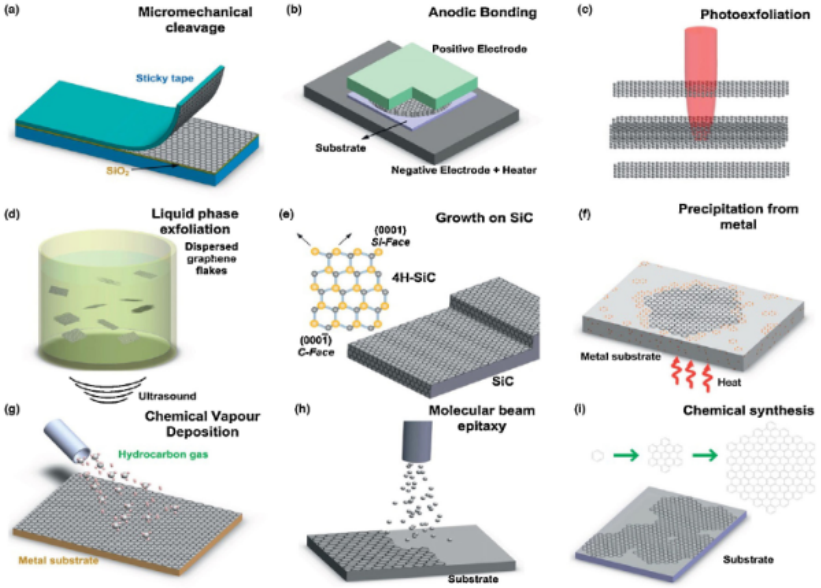


Figure 40. Main methods of graphene production: (a) micromechanical cleavage (scotch tape method), (b) anodic bonding, (c) photoexfoliation, (d) liquid phase exfoliation (LPE), (e) silicon carbide sublimation, (f) metal precipitation (by heating alloys with carbon), (g) vapor deposition (CVD), (h) molecular beam epitaxy, (i) chemical synthesis.[162]

Top-down methods represent those processes through which graphene fragments are isolated starting from graphitic material. Top-down methods have the advantages of obtaining higher yields and starting from a low-cost raw material such as graphite. Unfortunately, they have the disadvantage, with the exception of the method used by Geim and Novoselov in 2004, of producing graphenes of limited size and with a large variability in thickness. Top-down methods include the micromechanical cleavage method, also called Scotch tape method, and liquid-phase exfoliation. The first method was the one conceived by Geim and Novoselov in the study that earned them

the Nobel Prize in Physics in 2010.[163] The two scientists created square-shaped, micrometric-sized bas-reliefs on the surface of a piece of highly oriented pyrolytic graphite; they then bonded these bas-reliefs to a glass substrate using photoresist (a light-sensitive material used to form a "micro-modeled" coating on a surface), and then cleaved the graphite at the base, leaving only the square parts attached to the glass. The next step was to exfoliate the graphite material with several pieces of scotch tape, until thin films were obtained on the photoresist. After dissolving the photoresist in acetone, with dispersion of the graphite and graphene fragments at different thicknesses in the solvent, the process continues with the immersion of Si/SiO_2 wafers in the same solvent to mediate their adhesion to the fragments. The next step is represented by washing, useful to eliminate the thicker adhered graphite fragments. Another top-down method is the liquid phase exfoliation of graphite. Liquid phase exfoliation (LPE) of graphite is based on the interaction of the solvent (usually organic) with the graphite material; in fact, the solvent should loosen the van der Waals forces between the layers and, subsequently, stabilize them in suspension. Added to this effect is a mechanical force responsible for exfoliation, which can be applied by sonication or other methods (microfluidification, ball milling). The choice of solvent is based on its surface tension which, for maximum stabilization of graphene, should have values close to 40 mN/m.[164] Exfoliation in the liquid phase, in addition to organic solvents, can also be obtained with aqueous solutions containing surfactants or dispersion-stabilizing molecules.[165,166] A method related to the one just described, and also classifiable as LPE, is the one that exploits the oxidation of graphite to obtain oxidized graphite, more easily exfoliated by subsequent sonication in aqueous solution. Following exfoliation, the suspension is centrifuged, and the graphene oxide is reduced, even if partially, to reduced graphene oxide (rGO).

2.3.2 *Synthesis of Graphene Oxide: Modified Hummers Method*

Although graphite exfoliation is a simple method to obtain pristine graphene sheets, the distribution of monolayer and few-layer fragments is very heterogeneous and poorly stabilized in polar solvents such as water. To increase the stabilization of the sheets, a step preceding exfoliation is often necessary, the oxidation of graphite.[167–169] The Hummers method is the most known technique for oxidizing graphite to obtain graphene oxide (GO),[170] a material that is easily dispersible in water and other polar solvents. This process uses a combination of strong acid (sulfuric acid, H_2SO_4), and oxidizing agents (potassium permanganate, $KMnO_4$) to introduce oxygen-containing functional groups into the graphite structure. Hydrogen peroxide (H_2O_2) stops the reaction and reduces byproducts. The product is then washed with abundant water and hydrochloric acid (HCl). Traditional Hummers method involves the use of sodium nitrate ($NaNO_3$) to facilitate oxidation. Unfortunately, $NaNO_3$ gives rise to NO_2, a toxic gas that is easily absorbed through the lungs which can cause heart failure and, in extreme situations, death when inhaled. Hummers method has been adapted into the Modified Hummers Method to improve efficiency and reduce the formation of unwanted byproducts. In the synthesis, graphene is oxidized with a mixture of sulfuric acid (H_2SO_4), phosphoric acid (H_3PO_4), and potassium permanganate ($KMnO_4$). The reaction produces graphene oxide, which is a form of graphene with hydroxyl, epoxy, and carboxyl groups on its surface.

2.4 Aim of this work

The aim of this part of the project is to develop innovative composite materials with applications in catalysis, exploiting the exceptional properties of graphene and noble and non-noble metals. The metals chosen for this research are platinum, due to its excellent catalytic characteristics, copper, which can improve thermal stability and catalytic efficiency, reducing the sensitivity of platinum to degradation during utilization, and iron, which can improve the material's resistance to high temperature or aggressive environments, where iron can form protective oxides that

protect the catalyst. The use of a graphene-supported platinum-copper-iron nanoalloy combines the advantages of metal nanoparticles with the extraordinary properties of graphene, creating a highly functional, stable and versatile material. The main advantages of this combination follow below.

1) *Improved catalytic performance*

Platinum is known for its excellent catalytic properties, but its high cost can limit its application. Copper and iron can reduce costs, without significantly compromising performance, and improve efficiency in catalytic reactions.

Anchoring on graphene improves the dispersion of metal nanoparticles, increasing the active surface available for catalytic reactions and improving the stability of the catalyst. Graphene acts as a conductive support and helps in the uniform distribution of nanoparticles, improving the overall performance of the catalyst, particularly useful in applications such as hydrogen production or fuel cells.

2) *Increased stability and durability*

Graphene is known for its high thermal stability and chemical resistance. The combination of platinum-copper-iron nanoparticles with graphene makes the composite much more resistant to degradation and corrosion than traditional catalysts. Graphene protects the metal nanoparticles from losing activity during operation, increasing the longevity of the catalyst and reducing the need for replacement.

3) *Optimized electrical conductivity*

Graphene is an excellent electrical conductor, which means that a platinum-copper-iron nanoalloy supported on graphene will offer excellent conductivity. This is particularly useful in electrochemical devices, such as fuel cells, batteries and sensors, where it is essential to reduce electrical resistance and improve the efficiency of charge transfers. Graphene contributes to improved electronic transfer between the metals and the support, improving the performance of the devices.

4) *Increased active surface area*

Graphene is made up of a single film of carbon atoms and is therefore able to host a high number of active sites for the anchoring of metal nanoparticles. This increases the surface area available for catalytic reactions. Platinum, copper, and iron nanoparticles are more uniformly distributed on the graphene surface, creating a synergistic effect that can improve reaction efficiency compared to conventional catalysts.

5) *Control and tailoring of properties*

The use of metal nanoparticles on graphene allows for precise control and optimization of the catalyst properties. The size and distribution of the nanoparticles can be adjusted to improve the reactivity and stability of the system. The composition of the platinum-copper-iron alloy allows for the catalyst to be tailored for specific applications, improving selectivity and efficiency for certain chemical reactions, such as the oxygen reduction reaction in fuel cells or hydrogen synthesis.

6) *Cost reduction*

The use of copper and iron (both cheaper metals than platinum) lowers the cost of the nanoalloy compared to using platinum alone, without significantly compromising performance. Using graphene as a support helps reduce the amount of platinum needed, making the production of these catalysts more economical and scalable for industrial applications.

7) *Environmental sustainability*

The slight reduction in the amount of platinum by using copper and iron makes this combination more sustainable than using pure platinum.

Graphene is an abundant and relatively cheap material, helping to make the catalyst production process less impactful on the environment, especially when compared to more traditional production methods that use large amounts of noble metals.

8) *Versatility and advanced applications*

This graphene-based platinum-copper-iron nanoalloy can be used in a wide range of applications, including hydrogen production and fuel cells, catalysis

for oxidation and reduction reactions, electrochemical sensors, advanced batteries (e.g., lithium batteries or supercapacitors). The versatility of this material makes it promising for a variety of technology sectors, including renewable energy, electronics, and the chemical industry.

I conducted preliminary studies to investigate the method of graphene exfoliation in liquid phase and the control of nanoparticle growth through the use of nanoparticle systems. This step was fundamental to understand how to obtain a homogeneous distribution of nanoparticles on the graphene support and to optimize the synthesis of nanocomposites. In particular, the part of the work related to electrochemistry was carried out at the laboratory of Dr. Lichtenberger in the Department of Chemistry and Biochemistry at the University of Tucson, Arizona. Here, two main methods for the synthesis of nanocomposites have been studied. The first method, wet chemistry, has shown some difficulties related to the reproducibility of the results, the amount of material used and the greater complexity of the processes. Despite this, it has offered important ideas to improve the synthesis techniques. The second method, which I found particularly interesting, is that of electroreduction synthesis, a much greener, faster and more efficient approach, which minimizes the use of solvents and chemical reagents. A fundamental aspect on which I focused concerns the study of the deposition and growth of metal nanoparticles on two main supports: electrically reduced graphene oxide and reduced graphene oxide modified with aniline rings. Aniline is covalently linked to the graphene surface and acts as a “spacer” for an ordered arrangement of the nanoparticles on the graphene sheet. This innovative approach allows a more controlled distribution of the nanoparticles, thus improving the catalytic performance. However, further investigation is needed to refine synthesis methods and reach better results.

In conclusion, this work represents an important step in the development of metal nanocomposites on graphene, with the potential for significant applications in catalysis, energy and other technological fields. By using

sustainable and efficient methods such as electroreduction, is possible to obtain materials with high performance and low costs.

2.5 References

96. T-Raissi, A. Water Splitting: Thermochemical. in *Encyclopedia of Inorganic and Bioinorganic Chemistry* (Wiley, 2011). doi:10.1002/9781119951438.eibc0463.
97. E. Funk, J. Thermochemical hydrogen production: past and present. *Int J Hydrogen Energy* 26, 185–190 (2001).
98. Kubo, S. *et al.* A pilot test plan of the thermochemical water-splitting iodine–sulfur process. *Nuclear Engineering and Design* 233, 355–362 (2004).
99. Safari, F. & Dincer, I. A review and comparative evaluation of thermochemical water splitting cycles for hydrogen production. *Energy Convers Manag* 205, 112182 (2020).
100. *Light, Water, Hydrogen*. (Springer US, Boston, MA, 2008). doi:10.1007/978-0-387-68238-9.
101. Allen, J. A., Rowe, G., Hinkley, J. T. & Donne, S. W. Electrochemical aspects of the Hybrid Sulfur Cycle for large scale hydrogen production. *Int J Hydrogen Energy* 39, 11376–11389 (2014).
102. Ifkovits, Z. P., Evans, J. M., Meier, M. C., Papadantonakis, K. M. & Lewis, N. S. Decoupled electrochemical water-splitting systems: a review and perspective. *Energy Environ Sci* 14, 4740–4759 (2021).
103. Hu, T. *et al.* Progress in the Regulation of Electrode/Electrolyte Interfacial Reactions toward High-voltage Aqueous Hybrid Capacitors. *Batter Supercaps* 4, 717–732 (2021).
104. Liu, X., Chi, J., Dong, B. & Sun, Y. Recent Progress in Decoupled H 2 and O 2 Production from Electrolytic Water Splitting. *ChemElectroChem* vol. 6 2157–2166 Preprint at https://doi.org/10.1002/celc.201801671 (2019).
105. Fu, X., Shi, R., Jiao, S., Li, M. & Li, Q. Structural design for electrocatalytic water splitting to realize industrial-scale

deployment: Strategies, advances, and perspectives. *Journal of Energy Chemistry* 70, 129–153 (2022).

106. Stratton, S. M., Zhang, S. & Montemore, M. M. Addressing complexity in catalyst design: From volcanos and scaling to more sophisticated design strategies. *Surf Sci Rep* 78, 100597 (2023).
107. Wang, L. *et al.* Optimizing the volmer step by single-layer nickel hydroxide nanosheets in hydrogen evolution reaction of platinum. *ACS Catal* 5, 3801–3806 (2015).
108. Ren, F. *et al.* Clean Method for the Synthesis of Reduced Graphene Oxide-Supported PtPd Alloys with High Electrocatalytic Activity for Ethanol Oxidation in Alkaline Medium. *ACS Appl Mater Interfaces* 6, 3607–3614 (2014).
109. Zhao, Y. *et al.* Modulating Pt-O-Pt atomic clusters with isolated cobalt atoms for enhanced hydrogen evolution catalysis. *Nat Commun* 13, 2430 (2022).
110. Amini Horri, B. & Ozcan, H. Green hydrogen production by water electrolysis: Current status and challenges. *Curr Opin Green Sustain Chem* 47, 100932 (2024).
111. Zhao, G., Rui, K., Dou, S. X. & Sun, W. Heterostructures for Electrochemical Hydrogen Evolution Reaction: A Review. *Adv Funct Mater* 28, (2018).
112. Conway, B. E. & Tilak, B. V. Interfacial processes involving electrocatalytic evolution and oxidation of H2, and the role of chemisorbed H. *Electrochim Acta* 47, 3571–3594 (2002).
113. Hansen, J. N. *et al.* Is There Anything Better than Pt for HER? *ACS Energy Letters* vol. 6 1175–1180 Preprint at https://doi.org/10.1021/acsenergylett.1c00246 (2021).
114. Dupont, M., Hollenkamp, A. F. & Donne, S. W. Electrochemically active surface area effects on the performance of manganese dioxide for electrochemical capacitor applications. *Electrochim Acta* 104, 140–147 (2013).

115. Elgrishi, N. *et al.* A Practical Beginner's Guide to Cyclic Voltammetry. *J Chem Educ* 95, 197–206 (2018).
116. Şahin, M. E. An Overview of Different Water Electrolyzer Types for Hydrogen Production. *Energies (Basel)* 17, 4944 (2024).
117. Román-Leshkov, Y., Barrett, C. J., Liu, Z. Y. & Dumesic, J. A. Production of dimethylfuran for liquid fuels from biomass-derived carbohydrates. *Nature* 447, 982–985 (2007).
118. Wei, G. F. & Liu, Z. P. Restructuring and hydrogen evolution on Pt nanoparticle. *Chem Sci* 6, 1485–1490 (2015).
119. Helveg, S. *et al.* Atomic-scale imaging of carbon nanofibre growth. *Nature* 427, 426–429 (2004).
120. Wu, S. & Schmuki, P. Single Atom Cocatalysts in Photocatalysis. *Advanced Materials* 37, (2025).
121. Chen, Y. *et al.* Isolating Single and Few Atoms for Enhanced Catalysis. *Advanced Materials* 34, (2022).
122. Kim, C. *et al.* Alloy Nanocatalysts for the Electrochemical Oxygen Reduction (ORR) and the Direct Electrochemical Carbon Dioxide Reduction Reaction (CO2 RR). *Advanced Materials* 31, (2019).
123. Zhou, Q. *et al.* Innovative strategies in design of transition metal-based catalysts for large-current-density alkaline water/seawater electrolysis. *Materials Today Physics* 26, 100727 (2022).
124. Li, G., Blake, G. R. & Palstra, T. T. M. Vacancies in functional materials for clean energy storage and harvesting: the perfect imperfection. *Chem Soc Rev* 46, 1693–1706 (2017).
125. Xu, L. *et al.* Plasma-Engraved Co_3O_4 Nanosheets with Oxygen Vacancies and High Surface Area for the Oxygen Evolution Reaction. *Angewandte Chemie International Edition* 55, 5277–5281 (2016).
126. Xu, L. *et al.* Plasma-Engraved Co3O4 Nanosheets with Oxygen Vacancies and High Surface Area for the Oxygen Evolution Reaction. *Angewandte Chemie International Edition* 55, 5277–5281 (2016).

127. Bao, J. *et al.* Ultrathin Spinel-Structured Nanosheets Rich in Oxygen Deficiencies for Enhanced Electrocatalytic Water Oxidation. *Angewandte Chemie International Edition* 54, 7399–7404 (2015).
128. Tsai, C. *et al.* Electrochemical generation of sulfur vacancies in the basal plane of MoS2 for hydrogen evolution. *Nat Commun* 8, 15113 (2017).
129. Xie, Z. *et al.* An Overview of Recent Development in Composite Catalysts from Porous Materials for Various Reactions and Processes. *Int J Mol Sci* 11, 2152–2187 (2010).
130. Hao, C. *et al.* Interface-coupling of CoFe-LDH on MXene as high-performance oxygen evolution catalyst. *Mater Today Energy* 12, 453–462 (2019).
131. Lv, T., Liu, M., Zhu, D., Gan, L. & Chen, T. Nanocarbon-Based Materials for Flexible All-Solid-State Supercapacitors. *Advanced Materials* 30, (2018).
132. Borenstein, A. *et al.* Carbon-based composite materials for supercapacitor electrodes: a review. *J Mater Chem A Mater* 5, 12653–12672 (2017).
133. Liang, D. *et al.* MOFs-derived core-shell Co3Fe7@Fe2N nanopaticles supported on rGO as high-performance bifunctional electrocatalyst for oxygen reduction and oxygen evolution reactions. *Mater Today Energy* 17, 100433 (2020).
134. Xu, J., Wang, R., Chen, X., Zhou, R. & Zhang, J. Cu2SnS3 nanocrystals decorated rGO nanosheets towards efficient and stable hydrogen evolution reaction in both acid and alkaline solutions. *Mater Today Energy* 17, 100435 (2020).
135. Gong, M. *et al.* An Advanced Ni–Fe Layered Double Hydroxide Electrocatalyst for Water Oxidation. *J Am Chem Soc* 135, 8452–8455 (2013).
136. Kai, W. *et al.* Electrodeposition Synthesis of PANI/MnO2/Graphene Composite Materials and its Electrochemical Performance. *Int J Electrochem Sci* 12, 8306–8314 (2017).

137. Fu, Y. *et al.* NiCo Alloy Nanoparticles Decorated on N-Doped Carbon Nanofibers as Highly Active and Durable Oxygen Electrocatalyst. *Adv Funct Mater* 28, (2018).
138. Randviir, E. P., Brownson, D. A. C. & Banks, C. E. A decade of graphene research: production, applications and outlook. *Materials Today* 17, 426–432 (2014).
139. Berber, S., Kwon, Y.-K. & Tománek, D. Unusually High Thermal Conductivity of Carbon Nanotubes. *Phys Rev Lett* 84, 4613–4616 (2000).
140. Hone, J., Whitney, M. & Zettl, A. Thermal conductivity of single-walled carbon nanotubes. *Synth Met* 103, 2498–2499 (1999).
141. Fujii, M. *et al.* Measuring the Thermal Conductivity of a Single Carbon Nanotube. *Phys Rev Lett* 95, 065502 (2005).
142. Balandin, A. A. *et al.* Superior Thermal Conductivity of Single-Layer Graphene. *Nano Lett* 8, 902–907 (2008).
143. Ghosh, S. *et al.* Extremely high thermal conductivity of graphene: Prospects for thermal management applications in nanoelectronic circuits. *Appl Phys Lett* 92, (2008).
144. Balandin, A. A. Thermal properties of graphene and nanostructured carbon materials. *Nat Mater* 10, 569–581 (2011).
145. Balandin, A. A. Thermal properties of graphene and nanostructured carbon materials. *Nat Mater* 10, 569–581 (2011).
146. Allen, M. J., Tung, V. C. & Kaner, R. B. Honeycomb Carbon: A Review of Graphene. *Chem Rev* 110, 132–145 (2010).
147. Wallace, P. R. The Band Theory of Graphite. *Physical Review* 71, 622–634 (1947).
148. Slonczewski, J. C. & Weiss, P. R. Band Structure of Graphite. *Physical Review* 109, 272–279 (1958).
149. Novoselov, K. S. *et al.* Electric Field Effect in Atomically Thin Carbon Films. *Science (1979)* 306, 666–669 (2004).
150. Bolotin, K. I. *et al.* Ultrahigh electron mobility in suspended graphene. *Solid State Commun* 146, 351–355 (2008).

151. Frank, I. W., Tanenbaum, D. M., van der Zande, A. M. & McEuen, P. L. Mechanical properties of suspended graphene sheets. *Journal of Vacuum Science & Technology B: Microelectronics and Nanometer Structures Processing, Measurement, and Phenomena* 25, 2558–2561 (2007).
152. Lee, C., Wei, X., Kysar, J. W. & Hone, J. Measurement of the Elastic Properties and Intrinsic Strength of Monolayer Graphene. *Science (1979)* 321, 385–388 (2008).
153. Cao, K. *et al.* Elastic straining of free-standing monolayer graphene. *Nat Commun* 11, 284 (2020).
154. Zhu, Y. *et al.* Graphene and Graphene Oxide: Synthesis, Properties, and Applications. *Advanced Materials* 22, 3906–3924 (2010).
155. Gómez-Navarro, C., Burghard, M. & Kern, K. Elastic Properties of Chemically Derived Single Graphene Sheets. *Nano Lett* 8, 2045–2049 (2008).
156. Novoselov, K. S. *et al.* A roadmap for graphene. *Nature* 490, 192–200 (2012).
157. Reina, A. *et al.* Large Area, Few-Layer Graphene Films on Arbitrary Substrates by Chemical Vapor Deposition. *Nano Lett* 9, 30–35 (2009).
158. Li, X. *et al.* Large-Area Synthesis of High-Quality and Uniform Graphene Films on Copper Foils. *Science (1979)* 324, 1312–1314 (2009).
159. Avouris, P. & Dimitrakopoulos, C. Graphene: synthesis and applications. *Materials Today* 15, 86–97 (2012).
160. Forbeaux, I., Themlin, J.-M. & Debever, J.-M. Heteroepitaxial graphite on 6H−SiC (0001): Interface formation through conduction-band electronic structure. *Phys Rev B* 58, 16396–16406 (1998).
161. Emtsev, K. V. *et al.* Towards wafer-size graphene layers by atmospheric pressure graphitization of silicon carbide. *Nat Mater* 8, 203–207 (2009).

162. Zhong, Y. L., Tian, Z., Simon, G. P. & Li, D. Scalable production of graphene via wet chemistry: progress and challenges. *Materials Today* 18, 73–78 (2015).
163. Novoselov, K. S. *et al.* Electric Field Effect in Atomically Thin Carbon Films. *Science (1979)* 306, 666–669 (2004).
164. Shen, J. *et al.* Liquid Phase Exfoliation of Two-Dimensional Materials by Directly Probing and Matching Surface Tension Components. *Nano Lett* 15, 5449–5454 (2015).
165. Ciesielski, A. & Samorì, P. Grapheneviasonication assisted liquid-phase exfoliation. *Chem. Soc. Rev.* 43, 381–398 (2014).
166. Xu, Y., Cao, H., Xue, Y., Li, B. & Cai, W. Liquid-Phase Exfoliation of Graphene: An Overview on Exfoliation Media, Techniques, and Challenges. *Nanomaterials* 8, 942 (2018).
167. Dreyer, D. R., Ruoff, R. S. & Bielawski, C. W. From Conception to Realization: An Historial Account of Graphene and Some Perspectives for Its Future. *Angewandte Chemie International Edition* 49, 9336–9344 (2010).
168. Zhu, Y. *et al.* Graphene and Graphene Oxide: Synthesis, Properties, and Applications. *Advanced Materials* 22, 3906–3924 (2010).
169. Stankovich, S. *et al.* Synthesis of graphene-based nanosheets via chemical reduction of exfoliated graphite oxide. *Carbon N Y* 45, 1558–1565 (2007).
170. Hummers, W. S. & Offeman, R. E. Preparation of Graphitic Oxide. *J Am Chem Soc* 80, 1339–1339 (1958).

CHAPTER 3

Hydrogen production: experimental section

3.1 Graphene liquid phase exfoliation

3.1.1 *Introduction*

Among the simplest graphene production methods are the micromechanical cleavage method, also called Scotch-tape method, and liquid phase exfoliation. Liquid Phase Exfoliation (LPE) of graphite is based on the interaction of the solvent, generally organic, with the graphitic material. The solvent, in fact, would loosen the van der Waals forces between the layers and then stabilize them in suspension. Added to this effect is a mechanical force responsible for the exfoliation, which can be applied through sonication or other methods (microfluidification, ball milling). The choice of solvent is based on its surface tension which, for maximum stabilization of graphene, should have values close to 40 mN/m.[171]
Exfoliation in the liquid phase, in addition to organic solvents, can also be obtained with aqueous solutions containing surfactants or dispersion-stabilizing molecules.[172]

The aim of this work is to obtain graphene from the mechanical exfoliation of graphite in a solvent with a low boiling point, chloroform. The samples obtained were then deposited on SiO_2 wafers and analyzed by Raman spectroscopy.

3.1.2 *Materials and methods*

Exfoliations were obtained in glass tubes immersed in a sonicator bath. Each glass tube contained 50 mg of graphite powder (Alfa Aesar, purity 99.9995%, particle size 200 mesh) dispersed in 6 ml of chloroform (Sigma-Aldrich, GC grade purity). The sonicator had a nominal power of 580 W. UV-VIS analysis of the exfoliate was performed with a Jasco V-550 spectrophotometer. The substrate where graphene was transferred for Raman analyses was a silicon wafer (Si/SiO_2) with a 290 nm thick silicon dioxide coating, formed by thermal oxidation. Raman analyses were performed with an XploRA PLUS high-performance confocal Raman microscope (HORIBA), equipped with a CCD detector with cooling technology. LabSpec 6 software (HORIBA) was used to control the instrument, as well as to process the spectral data. All acquisitions were recorded using a 2400 lines/mm grating and a 532 nm wavelength laser. The instrument is equipped with three objectives of 10, 50 and 100x.

3.1.3 *Discussion and characterization*

Liquid phase exfoliation occurs inside an ultrasonic bath. Each glass tube contains 50 mg of graphite powder dispersed in 6 ml of chloroform. The sonicator was set to develop 100% power (580 W nominal), without temperature control, for exfoliation times ranging from 30 minutes to 2 hours. Once the sonication was completed, the dispersions were centrifuged at 4000 rpm for 20 min, and the supernatant was collected and analyzed with a UV-VIS spectrophotometer (Figure 41).

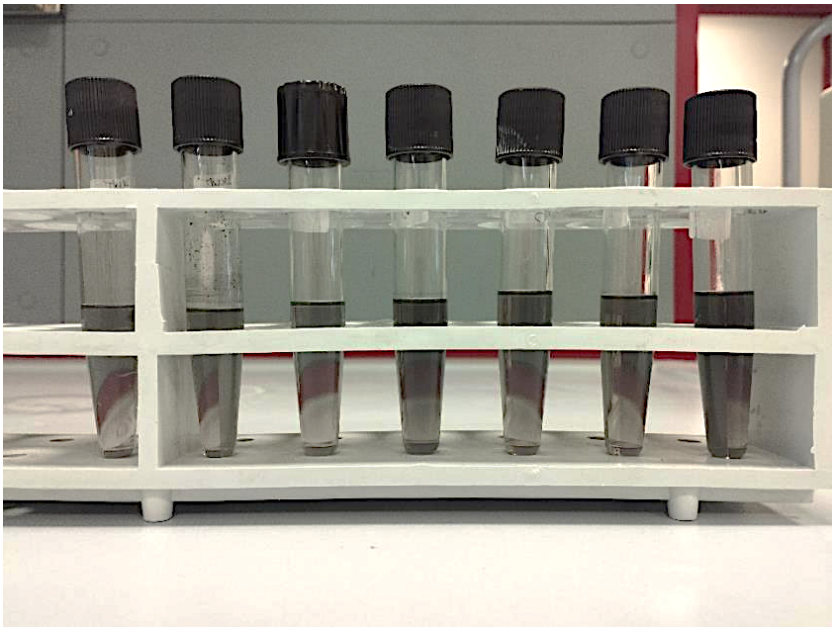


Figure 41. Supernatants obtained following centrifugation. The tubes are arranged in order of increasing sonication time, from left to right. The image shows the supernatants from exfoliations number 2-8. The darker suspension color in tubes 5-8 is due to the higher graphene concentration.

The exfoliations were performed in duplicate for a total of 8 dispersions. The graphene concentration was calculated from the absorbance using the Lambert-Beer law in Equation 51.

$$A_\lambda = \varepsilon^\lambda dc \tag{51}$$

where:
ε^λ: is the absorption coefficient at wavelength λ
d: optical path
c: concentration

The absorbance per optical path, A/d, of these dispersions was measured at 660 nm. The concentration c of graphitic material in the supernatants, coming from the centrifugation process, was determined by substituting ε^λ

with the value of 3620 mg/mL/m.[173] The concentrations calculated based on time are reported in Table 9 together with the other experimental parameters.

Table 9. Summary table of exfoliation results. Times marked with * represent exfoliations obtained with a solvent dilution method.

# Exfoliation	1	2	3	4
Temperature	26 -42 °C	26-41 °C	26-53 °C	26-54 °C
Time	30 min	30 min	60 min	60 min
Concentration	0.00680 mg/mL	0.00931 mg/mL	0.01034 mg/mL	0.01239 mg/mL
# Exfoliation	**5**	**6**	**7**	**8**
Temperature	26-62 °C	27-63 °C	26-62 °C	26-62 °C
Time	120 min	120 min	120 min*	120 min*
Concentration	0.02020 mg/mL	0.01613 mg/mL	0.01550 mg/mL	0.02212 mg/mL

As can be seen from Table 7, the sonication time correlates quite well with the concentration, however, the variability of the results is not negligible. Exfoliations 7 and 8 were carried out according to a solvent dilution method, 3 ml of chloroform was added to 50 mg of graphite and the resulting suspension was sonicated for 30 min. At the end of the first sonication, 1 ml of clean solvent was added and the sonicator was operated for another 30 min. This procedure was repeated four times for each of the two dispersions, for a total of 120 min and a final 6 ml of dispersion. Figure 42A shows an optical microscope image of a fragment obtained from the exfoliation of sample 8, while Figure 42B shows the relative Raman spectrum. From the analysis of the fragment under the optical microscope, it is clear that it is formed by a low number of layers, given the light color and the perimeter not particularly defined compared to the surrounding area. From the Raman spectrum, the D peak can be seen centered at 1351 cm^{-1} and the G peak at

1583 cm^{-1}. The defect content is $I_D/I_G = 0.279$, associated with high-quality graphene, and it is possible to identify the type of defects present through the $I_D/I_{D'}$ ratio, with the D' peak positioned at about 1620 cm^{-1}.

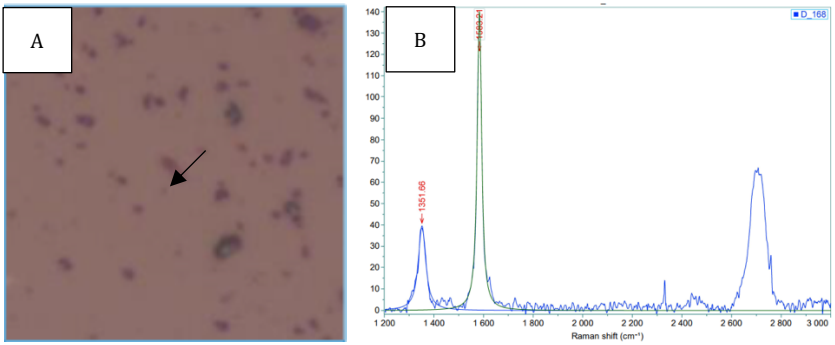


Figure 42. (a) Optical microscope image with 100X magnification centered on the analyzed fragment; (b) Raman spectrum related to the analyzed fragment.

The $I_D/I_{D'}$ ratio = 2.49 indicates that the D band is associated with perimeter defects. The amplitudes at half height of the G band (about 21.5 cm^{-1}) and of the 2D band (> 70 cm^{-1}) indicate a broadening due to the presence of defects; in fact, the sub-micrometric size of the fragment means that a good part of the perimeter is present in the laser focus at the time of acquisition. The shape of the 2D peak recalls that of a four-layer graphene but has a greater intensity and amplitude than typical ones, which could indicate the presence of a fragment underlying the one analyzed (in the absence of electronic coupling between the two) or of a folding.

3.1.4 *Conclusions*

This type of procedure was followed in an attempt to increase the amount of exfoliating energy per volume of solvent (E/V). The results in Table 7 show how the energy transferred from the sonicator to the test tub shows a great variability. The influencing variables that were recognized during this work are the position of the test tube, the water level in the bath, the temperature of the water. Starting from the graphene concentration in the dispersion, the percentage yield can be deduced. Considering the maximum concentration

reached between the above-mentioned tests, i.e., 0.022 mg/mL, multiplied by the volume of 6 ml, a yield of 0.132 mg is obtained. Having an initial concentration of 8.34 mg/mL of graphite, the percentage yield is 0.264% after 2 hours of sonication (in the literature a percentage yield value equal to 4% is reported with a sonication time of 460 hours).[173]

3.2 Synthesis of graphene oxide using Modified Hummers method and reduced graphene oxide

3.2.1 *Introduction*

Since graphene was discovered, research have been addressed to the study of this two-dimensional carbon material to learn more about its characteristics and properties and to develop better devices for a huge number of applications.[174] Due to its high mobility (200000 cm^2/vs),[175,176] Therefore, before exfoliation, graphite is often oxidized to obtain graphene oxide, which is much more reactive to nucleophilic additions, due to the presence of epoxy bridges and hydroxyl functions on its surface, or nucleophilic acyl substitutions on the carboxylic groups at the edges (Figure 43).

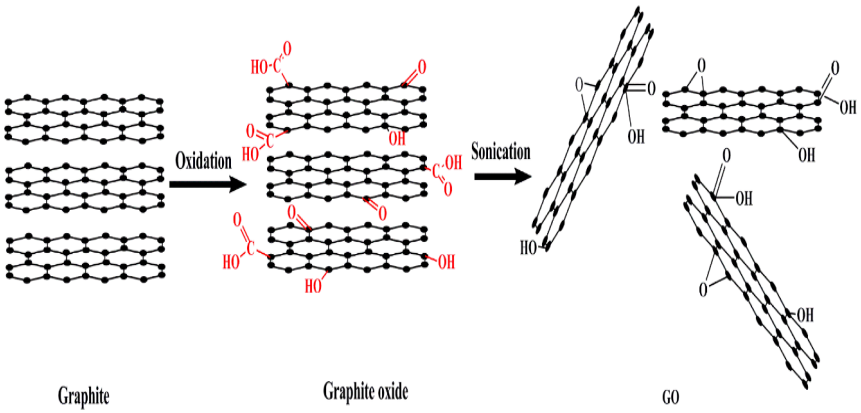


Figure 43. Synthesis of graphene oxide: after graphite's oxidation and subsequent exfoliation, the obtained graphene oxide is more stable in aqueous solvent.

Even if many sp^3 carbons are obtained during oxidation process, which significantly reduces graphene oxide's electrical conductivity making it an insulator, it can be reduced to reduced graphene oxide (rGO) that shows good conductivity properties, by chemical, thermal or electrochemical means to restore its sp^2 structure.[177]

The Raman technique has been used to monitor the evolution of the structure of the graphite upon chemical thermal reduction to rGO. In a Raman study, the primary Raman peaks in the graphene material's spectra are analyzed, along with their location, width, and most importantly, the relative intensity ratio I_D/I_G, where a higher ratio indicates a lower degree of oxidation.[178] The typical diagnostic peaks in a Raman spectrum of graphite are the D band at ~1350 cm^{-1}, the G band at ~1580 cm^{-1}, the G' band at ~2700 cm^{-1}, and the D' band at ~1620 cm^{-1}.[179]The D band is associated with defects and disorder in the crystal structure of carbon. This band shows up only in the presence of structural defects, such as vacancies or disorder, and depends on the scattering process mechanism involving the defect.[180] The intensity of the D band is an indicator of the number of defects in the graphite.

The G band is the main band of graphite and is associated with the carbon-carbon (C–C) vibration in the plane lines of graphene sheets. The G band originates from the stretching vibration of the sp^2 carbon atoms in the hexagonal lattice.[181,182188,189] The position and intensity of the G band generally remain constant for graphene and graphite and are indicators of a material with a relatively ordered structure. The G band is one of the distinguishing features of graphite and is located at about 1580 cm^{-1}, although it can shift slightly depending on the structure of the material and the presence of internal stresses.

The G' band is a second-order band that results from the combination of two phonons and provides information about the layered structure. Due to multiple layers in graphite, the G' band appears as a single broad band.[183]

The D' band is another defect band similar to the D, but it is generally weaker and occurs closer to the G band (at about 1620 cm^{-1}). It is also related to material disorganization, but its location and intensity depend on different types of defects and disruption of the crystal structure.

3.2.2 *Materials and methods*

The reagents and materials used in the above study were as follows: graphite derived from industrial waste material; sulfuric acid (H_2SO_4, 98%) purchased from VWR Chemicals (US); potassium permanganate (K_2MnO_4, 99.5%) powder supplied by CARLO ERBA Reagents S.r.l. (Italy); hydrogen peroxide (H_2O_2) 30% w/w supplied by Honeywell Fluka (US); Milli-Q water produced in the laboratory (Merck Millipore, Germany). Raman analyses were performed with an XploRA PLUS high-performance confocal Raman microscope (HORIBA), equipped with a CCD detector with cooling technology. LabSpec 6 software (HORIBA) was used to control the instrument, as well as to process the spectral data. All acquisitions were recorded using a 2400 lines/mm grating and a 532 nm wavelength laser. The instrument is equipped with three objectives of 10, 50 and 100x.

3.2.3 *Discussion and characterization*

The starting material used, graphite, was supplied as a company waste product, making the process also interesting with regards to a circular economy. Before obtaining it oxidation, the graphite was analyzed with Raman spectra (Figure 44). Then graphene oxide was produced from graphite powder by the modified Hummers method.[170] Briefly, 5 g of graphite powder is dispersed in 150 mL of concentrated H_2SO_4 is added to the solution. The concentrated H_2SO_4 is needed to deintercalate the graphite sheets and to promote oxidation. During this step, it is very important to keep the temperature under control to avoid excessively violent reactions. Next, 20 g of $KMnO_4$ are slowly added to the mixture, which causes the graphite to oxidize, transforming it into graphene oxide. During this step, the reaction generates heat, and it is essential to keep it under control to avoid uncontrolled exothermic reactions, running this phase in ice bath (0-5° C) for 6 hours. After the reaction, the mixture is diluted with 400 mL of water and then treated with 40 mL of hydrogen peroxide (H_2O_2) solution, which helps reduce the permanganate and stop the oxidation. This step produces graphene oxide (GO) in suspension. The produced graphene oxide is

subsequently purified by filtration, washing and drying to remove residual acids and by-products. The graphene oxide obtained can then be reduced to be used as reduced graphene oxide (rGO) either by $NaBH_4$, therefore a purely chemical reduction,[184] or by using high temperatures in an inert environment,[185] which will find greater use in the catalytic field.

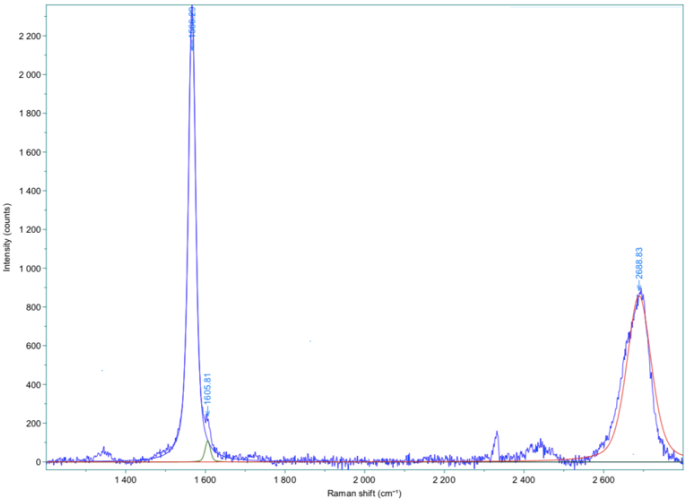


Figure 44. Raman spectrum of graphite. The graphite three main typical bands, D, G and 2D are observed. A multi-phonon response that arises from the combination of the longitudinal acoustic phonon and the D peak is represented by the weak Raman mode at about 2450 cm^{-1}.[186]

Figure 43 shows the Raman spectrum of graphite before its treatment. Because of the graphite edges, D band appears weak, while G band, the in-phase vibration of the lattice is much more intense. Bothe of the two bands are diagnostic of graphite.[187] The other characteristic G' peak of graphitic materials is also shown in the Raman spectrum. G' peak of graphite is formed by a two-peak line shape and it is slightly distinguishable. According to literature, The G' band, which is derived from bilayer graphene, is made up of an infinite number of peaks that are convolutions of peaks with frequencies that span the bottom to the top of the spectrum.[188195] The

analyzed graphite shows a good quality with few defects probably due to its previous treatment.

GO was also analyzed with Raman spectra. The typical bands and its appearance are shown in Figure 45.

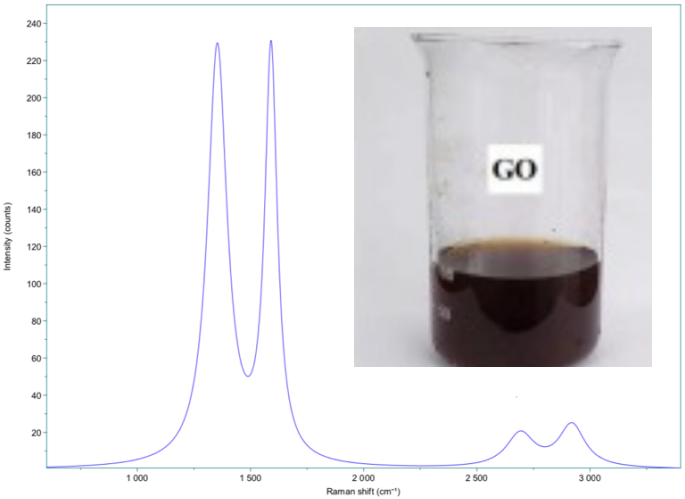


Figure 45. Raman spectra of graphene oxide. The typical bands, D, G and 2D are observed. When graphene oxide is dispersed in aqueous solvent, the suspension takes on a brownish color.

From a first organoleptic analysis, the graphene oxide in suspension takes on a brown color and appears uniformly dispersed thanks to the formation of hydrogen bridges with the aqueous solvent. A typical Raman spectrum confirms that the graphene oxide was successfully obtained. The increase in the intensity of the D band correlates with a higher degree of oxidation of graphene. In GO, the G' band appears wider than in non-oxidized graphite. This is due to the presence of oxidation, which alters the structure and reduces the symmetry of the material. The I_D/I_G ratio is diagnostic to evaluate the degree of oxidation. Compared to graphite, the higher ratio indicates more disorder and a higher degree of oxidation.

Finally, Figure 46 shows the rGO Raman analysis and its appearance. The reduced graphene oxide takes on a black color and it disperses more difficultly than GO due to the restoration of the sp^2 carbons.

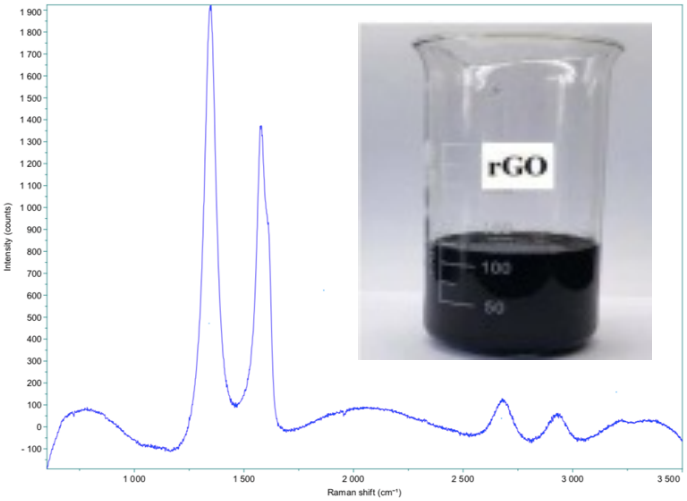


Figure 46. Raman spectra of reduced graphene oxide. The typical bands, D, G and 2D are observed. When reduced graphene oxide is dispersed in aqueous solvent, the suspension takes on a blackish color.

The diagnostic feature of reduced graphene is the increased I_D/I_G ratio. From the Raman analysis a ratio of 1.36 is found, meaning that the GO was successfully reduced.

3.2.4 *Conclusions*

Graphene oxide was produced according to the modified Hummers method using industrial graphite waste. These waste materials, which would otherwise be difficult to dispose of and would have a negative environmental impact, can be reused as raw material for the production of graphene oxide. This reduces the need to extract new graphite and minimizes the consumption of natural resources. Graphene oxide produced from industrial graphite waste has multiple applications in the scientific and industrial fields. One of the most promising uses is as a catalyst support, especially for electrochemical reactions such as HER and OER, which are key to sustainable energy production. After being reduced, graphene oxide (rGO) was selected as the supporting material for metallic nanoparticles.

3.3 Synthesis of Copper and Iron Nanoparticles and their size control using inverted micelles

3.3.1 *Introduction*

Metallic nanoparticles have been widely studied due to their large surface-to-volume ratio that makes them attractive to be used as highly efficient catalysts and with a large number of active atoms on their surfaces, including corners and edges.[189196]

The production methods of metallic nanoparticles can be classified into chemical methods, which include the use of polyol solvents, microemulsions, thermal decomposition and electrochemical synthesis and physical methods, including plasma method, chemical vapor deposition, microwave irradiation, sonochemical reduction and gamma radiation.[190197]

Nanoparticles are extremely versatile materials, whose wide range of applications covers the medical-pharmaceutical, environmental, electronic, mechanical and energy fields.[191198]

The aim of this work is to obtain nanoparticles with controlled and stable dimensions over time. In these preliminary tests only copper and iron particles are used. The alteration of the nanoparticles size in aqueous environment was observed over a 20-minute period and the same experiment was repeated using as solvent a nanoemulsion of inverse micelles composed of isooctane, water and AOT under the same conditions. The analyses were conducted with the dynamic light scattering (DLS) technique and were subsequently confirmed with the atomic force microscopy (AFM) technique.

3.3.2 *Materials and methods*

Nanoparticle sizes were measured using a 90Plus/BI-MAS ZetaPlus particle size analyzer (Brookhaven Instruments Corp., Holtsville, NY). ZetaPals Particle Sizing Software Ver. 3.86 was used to develop multimodal distributions. The Multimode 8 AFM atomic force microscope (Bruker, Billerica, Massachusetts, US) was used to determine the morphology of the

produced nanoparticles. The analysis was performed using the Nanoscope V controller in ScanAsyst in Air mode using SCANASYST-AIR silicon tips; these have a cantilever resonance frequency of 70 kHz, a nominal spring constant of 0.4 N/m and a curvature radius of 8 nm. Data processing was performed using Nanoscope Analysis 1.8 software.

3.3.3 *Discussion and characterization*

To a volume of 2.5 mL of Milli-Q water, 15 µL of copper (II) sulphate pentahydrate ($CuSO_4 \cdot 5H_2O$) at a concentration of 50 mM were added, reduced with 300 µL of 10 mM sodium borohydride ($NaBH_4$) and, subsequently, 15 µL of iron (II) sulphate eptahydrate ($FeSO_4 \cdot 7H_2O$) at a concentration of 50 mM reduced with 300 µL of 10 mM $NaBH_4$. The reaction was carried out under magnetic stirring and on ice, in order to avoid the onset of secondary reactions[192199] and to slow down the reaction rate of sodium boron hydride with the salts in solution to have greater control over the shape and size of the particles. Upon addition of the reducing agent, the previously transparent salt solution takes on a yellowish color, after the reduction of copper (Figure 47), and then gray, following the reduction of iron, which highlights the formation of metal nanoparticles.



Figure 47. Comparison of the reaction system before (clear solution) and after (yellow solution) the addition of 15 µL of 50 mM $CuSO_4 \cdot 5H_2O$ and 300 µL of 10 mM $NaBH_4$.

The nanoparticles were analyzed by Dynamic Light Scattering (DLS): two acquisitions lasting 5 minutes each were recorded 20 minutes apart. The results of the DLS analyses of the nanoparticles produced in an aqueous environment are reported in Figures 48 and 49.

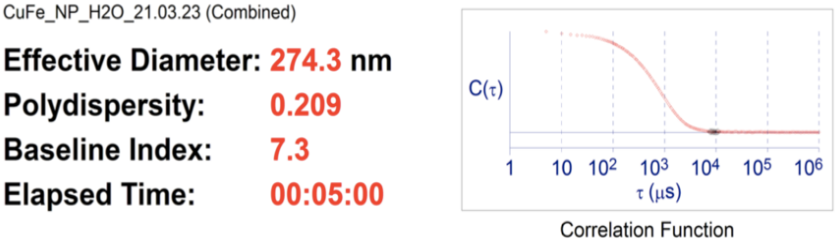


Figure 48. Dynamic Light Scattering (DLS) analysis result at t = 0 min: mean particle size of copper and iron in aqueous solution recorded over a time span of 5 min.

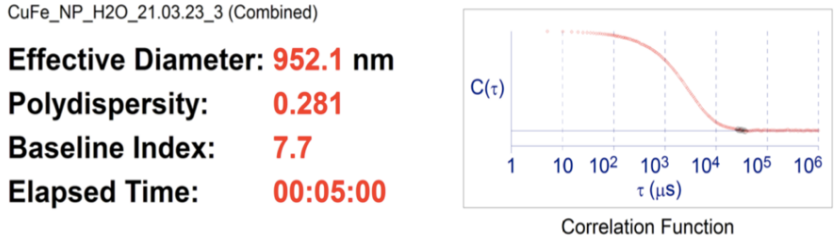


Figure 49. Dynamic Light Scattering (DLS) analysis result at t = 20 min: mean particle size of copper and iron in aqueous solution recorded over a time span of 5 min.

A similar test to the previous one was also conducted in a reverse micelle system. To a volume of 2.5 mL of isooctane and 0.1 M AOT, 20 µL of $CuSO_4 \cdot 5H_2O$ at a concentration of 0.05 M and 20 µL of $FeSO_4 \cdot 7H_2O$ at a concentration of 0.05 M were added, subsequently reduced with 80 µL of 0.1 M $NaBH_4$. The reaction was carried out on ice. A second DLS analysis was performed on the nanoparticles produced in the reverse micelle system (Figures 50 and 51).

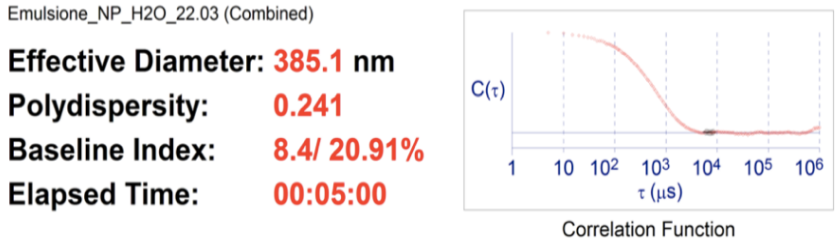


Figure 50. Dynamic Light Scattering (DLS) analysis result at t = 0 min: mean particle size of copper and iron in in the nanoemulsion system recorded over a time span of 5 min.

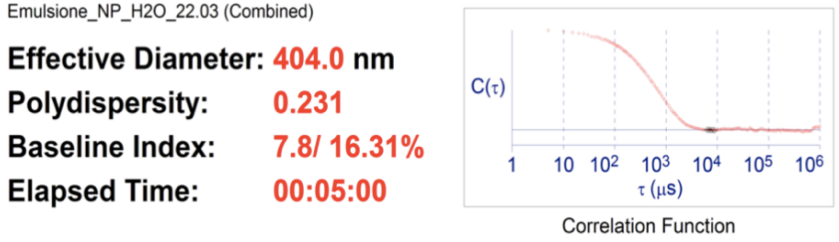


Figure 51. Dynamic Light Scattering (DLS) analysis result at t = 20 min: mean particle size of copper and iron in in the nanoemulsion system recorded over a time span of 5 min.

The data collected from an initial DLS analysis indicate a rapid and uncontrolled growth of nanoparticle dimensions in an aqueous environment, while the presence of inverse micelles favors a stabilization of particle growth over time.

Subsequent analyses were conducted with the Atomic Force Microscope (AFM) to observe the morphology and correspondence of the particle diameter evaluated with the previous DLS analyses. In this case, the analyses of the particles obtained in water at time t = 0 min and at time t = 5 min are reported because due to the evident final aggregation the instrument is unable to correctly analyze the sample. In Figure 52, an image of nanoparticles formed at time t = 0 min is reported, obtained by scanning an area of 5 μm^2 and setting 256 scan lines from which it can be deduced that

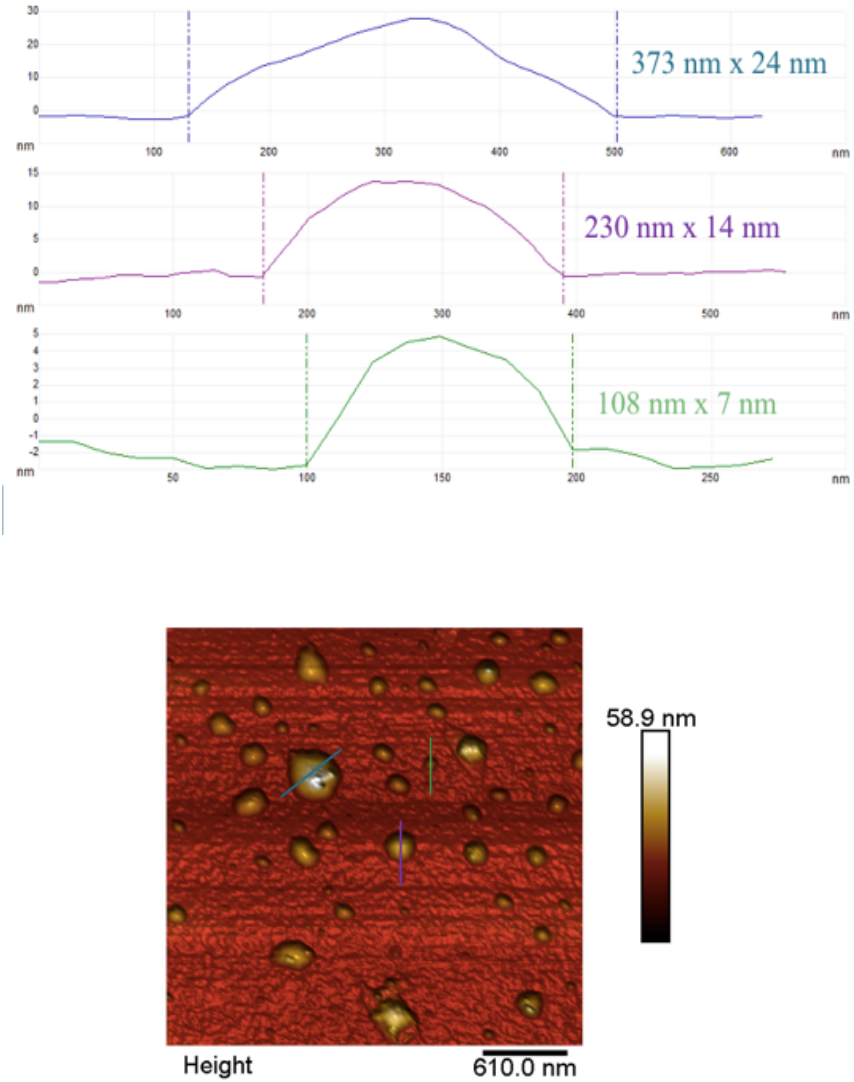


Figure 52. Size representation of some CuFe NPs particles and AFM image of CuFe NPs.

the particles have an average diameter of about 237 nm and an average height of about 15 nm, thus assuming a rather flattened shape.

Figure 53 shows an image of nanoparticles formed at time t = 5 min, in which it is possible to observe a strong aggregation that justifies the data obtained in the previous DLS analysis technique and which made AFM analysis impossible.

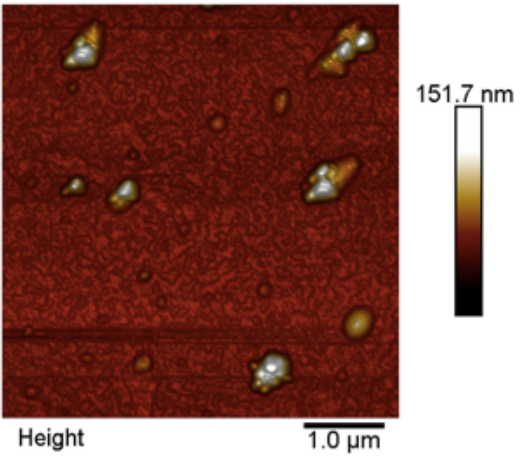


Figure 53. AFM image of highly aggregated CuFe NPs.

3.3.4 *Conclusions*

Synthesizing nanoparticles is a relatively simple process. There are numerous techniques to obtain nanostructured materials with high efficiency and reproducibility. However, one of the major challenges is ensuring that these nanoparticles remain stable over time, without aggregating or losing their functional properties. To overcome this problem, a commonly used method is the use of micellar systems. Micelles, structures formed by surfactants in solution, can act as nanoreactors, confining the growth of nanoparticles in a small space and thus controlling their size and morphology. However, this technique introduces new challenges. One of the main obstacles is the need to remove the surfactant after synthesis, a step that can be complex and sometimes compromise the stability of the nanoparticles themselves. For this reason, a more effective strategy is the

direct synthesis of nanoparticles on a graphene support. Graphene and its derivatives offer an ideal platform to anchor nanoparticles, preventing their aggregation and improving their dispersion. Furthermore, the interaction between the support and the nanoparticles can improve the electronic and catalytic properties of the system, making it more efficient in many applications.

3.4 Wet chemical synthesis of the trimetallic nanocomposite

3.4.1 *Introduction*

Green hydrogen is a clean and sustainable energy carrier, which can replace traditional fossil fuels that aggravate the greenhouse effect.[193] Therefore, it is crucial to identify effective routes for green hydrogen production through the optimization of electrochemical catalysts for the hydrogen evolution reaction (HER), the cathodic reaction in electrolysis.[194] Due to their strong catalytic capabilities, platinum catalysts have wide applications in HER.[195] However, their commercialization is severely limited by the skyrocketing cost of platinum, its scarce presence in nature and insufficient stability.[196] These drawbacks are efficiently overcome by developing platinum-derived alloy nanocatalysts (NCs) to reduce their loading or control their size, composition and/or morphology.[197]

The aim of this study is to reduce the amount of platinum used and evaluate the electrocatalytic activity of Cu/Fe/Pt nanoparticles deposited on reduced grefene oxide in an acidic environment with controlled pH through wet chemical synthesis method.

3.4.2 *Materials and methods*

The reagents and materials used in the above study were as follows: graphite derived from industrial waste material; sulfuric acid (H_2SO_4, 98%) purchased from VWR Chemicals (US); potassium permanganate (K_2MnO_4, 99.5%) powder supplied by CARLO ERBA Reagents S.r.l. (Italy); hydrogen peroxide (H_2O_2) 30% w/w supplied by Honeywell Fluka (US); milli-Q water produced in the laboratory (Merck Millipore, Germany); hexachloroplatinic(IV) acid hydrate ($H_2[PtCl_6] \cdot 6H_2O$) with a purity ≥ 99.9% supplied by Sigma-Aldrich (US); copper(II) sulfate pentahydrate ($CuSO_4 \cdot 5H_2O$) with a purity of 99.5% supplied by CARLO ERBA Reagents S.r.l. (Italy); iron(II) sulfate heptahydrate ($FeSO_4 \cdot 7H_2O$) with a purity ≥ 99.0% supplied by Sigma-Aldrich (US); sodium borohydride ($NaBH_4$) powder with a purity of ≥ 98.0% in powder supplied by Sigma-Aldrich (US).

For the filtration of the composites, paper filter Whatman 541, pore size 22μm Ø, was used. For the electrochemical experiments, potassium chloride (KCl), potassium ferricyanide $K_3[Fe(CN)_6]$ (sigma-Aldrich), sodium acetate 99.99% (Alfa Aesar), acetic acid 99.99% (Alfa Aesar) were used. All electrochemical experiments were conducted at the University of Arizona, Tucson (USA). A Gamry Reference 3000 potentiostat and a standard three-electrode system were used. The uncompensated resistance (R_u) was measured with the potentiostat by electrochemical impedance spectroscopy. The solution resistance was compensated to 80% of the measured R_u using positive feedback iR compensation. Potentials in aqueous solution were referenced to the standard hydrogen electrode (SHE) using the standard conversion from the Ag/AgCl reference electrode potential. The counter electrode used was a 5 mm diameter and 10 mm long Glassy Carbon Rod (GCR) (Alfa Aesar). All solutions were bubbled with argon for 10 min before performing electrochemical tests. For cyclic voltammetry (CV) experiments, a Glassy Carbon Disk (BASi) with a geometric surface area (Ageo) of 0.071 cm^2 was used as the working electrode, on which 5 μl of an aqueous suspension of each tested composite at a concentration of 0.1 mg/ml were deposited by drop-casting.

3.4.3 *Discussion and characterization*

The experiment that is the subject of this section 3.4 is briefly outlined and is represented in Figure 53. More detailed information is given below.

Graphene oxide was produced from graphite powder by the modified Hummers method.[170] Hexachloroplatinic(IV) acid hexahydrate ($H_2[PtCl_6] \cdot 6H_2O$) was chosen as a platinum precursor and was treated with $NaBH_4$ in a co-reduction reaction together with graphene oxide to obtain platinum nanoparticles anchored on reduced graphene oxide, denoted by Pt@rGO or Pt_{100}@rGO. An initial amount corresponding to 10% by mass of platinum with respect to the composite of platinum and reduced graphene oxide, was chosen. Pt was then combined with copper (Cu) and iron (Fe) in two bimetallic compounds (PtCu@rGO and PtFe@rGO) in which platinum

amount is halved, and a trimetallic compound (PtCuFe@rGO), where Pt is reduced to a third.

Two procedures were followed. In the first procedure all the precursors are weighed and added to the graphene oxide suspension in powder form. Sodium borohydride ($NaBH_4$) at a concentration of 0.1 M or 0.2 M was chosen as the reducing agent. This first experiment was necessary to adjust the quantities of the total material used in the experiment to obtain enough product to be analyzed in the electrochemical analysis phase. For this reason, there were variations in the preparation of the samples. For a better clarity the amounts of graphene oxide, metals and reducing agent are outlined in Table 10.

Table 10. Amount of the graphitic and metallic materials calculated to obtain each sample.

Sample	Theoretical total mass (mg)	Total volume (mL)	GO mass (mg)	Pt mass (mg)
Pt@rGO	25	25	22,5	2,5
PtCu@rGO	100	100	90	5
PtFe@rGO	100	100	90	5
PtCuFe@rGO	50	50	45	1.67

Sample	Pt moles (mol)	Cu moles (mol)	Fe moles (mol)	$NaBH_4$ volume (mL) and concentration (M)
Pt@rGO	$1.28 \cdot 10^{-5}$			10 (0.1)
PtCu@rGO	$2.56 \cdot 10^{-5}$	$2.56 \cdot 10^{-5}$		10 (0.2)
PtFe@rGO	$2.56 \cdot 10^{-5}$		$2.56 \cdot 10^{-5}$	10 (0.2)
PtCuFe@rGO	$8.53 \cdot 10^{-5}$	$8.53 \cdot 10^{-5}$	$8.53 \cdot 10^{-5}$	50 (0.1)

The preparation of Pt@rGO is described as follow: 22.5 mg GO is dispersed in 25 mL deionized (DI) water. After being sonicated for 15 min, it is transferred in a 100 mL reaction flask and 6.63 mg of $H_2[PtCl_6] \cdot 6H_2O$ is added to the suspension (Figure 54A). Nitrogen is gurgled for 15 min in the

suspension before reducing agent is added. 10 mL of 0.1 M $NaBH_4$ is prepared with cold water to slow down the reaction with water, then it is added dropwise to the suspension with a syringe through a polymer septum.

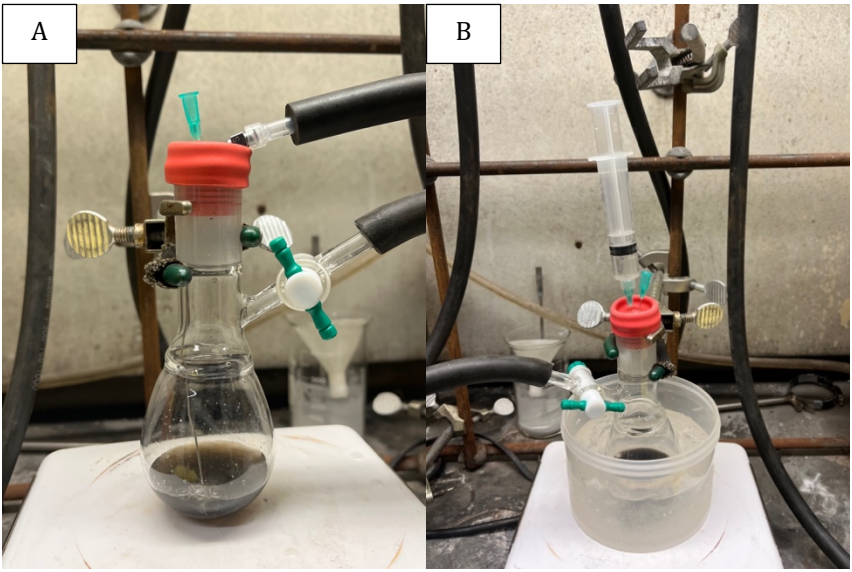


Figure 54. (A) After sonication, GO and Pt precursor are inserted in a 100 mL reaction flask and saturated with nitrogen for 15 min before (B) adding $NaBH_4$ in the suspension.

The reaction is run under stirring at 1000 rpm for 2 hours. The obtained composite is centrifuged in a 50 mL centrifuge tube for 15 min at 9000 rpm, then washed with ethanol three times in centrifuge for 15 min at 9000 rpm. Finally, the dispersion was dried under vacuum at 45 °C. After drying, the amount of composite was very small. A similar procedure was followed to obtain PtCu@rGO and PtFe@rGO but 100 mg of total mass of the composite in 100 mL was chosen and $NaBH_4$ concentration was raised to 0.2 M. After reacting for two hours, the suspensions obtained appeared as in the photos in Figure 55. It was observed that the PtFe@rGO composite exhibits magnetic properties in proximity to the stirring bar due to the presence of metallic iron.

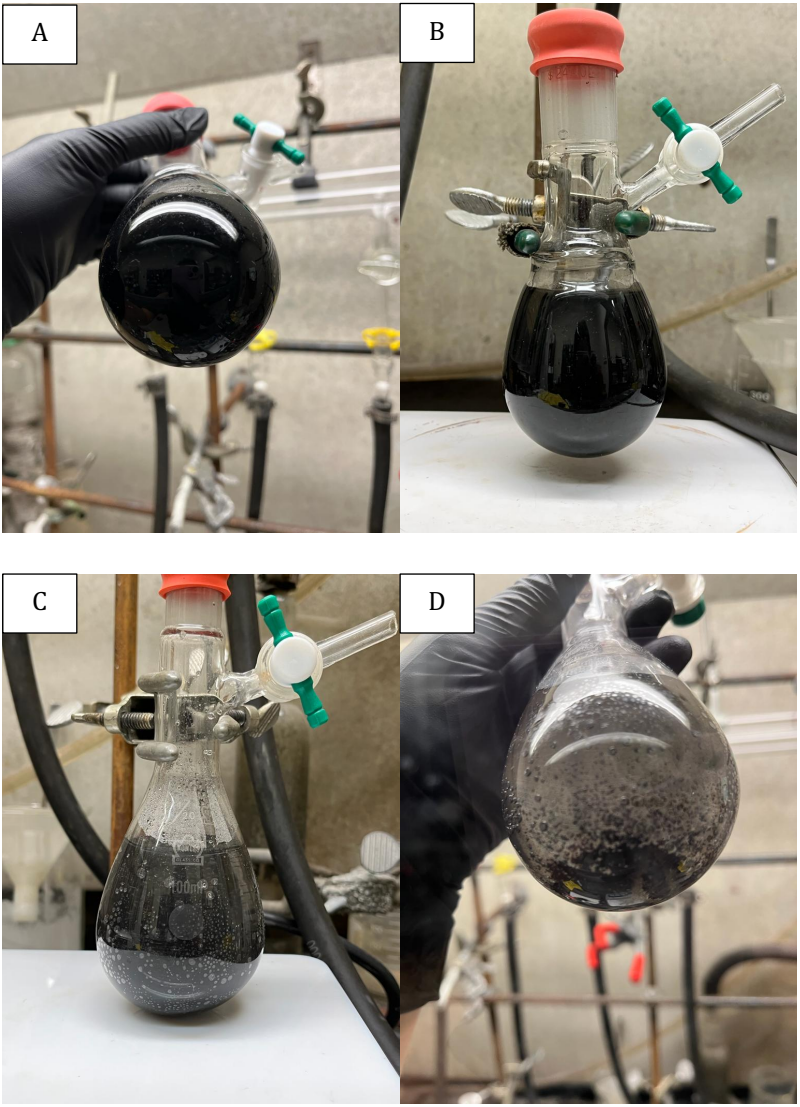


Figure 55. (A-B) PtCu@rGO aqueous suspension (C-D) PtFe@rGO aqueous suspension. While the first appears homogenous, the latter shows magnetic behavior, so the composite is attracted to the magnetic stirring bar.

To improve the reaction yield, the quantities used in synthesizing the trimetallic composite are varied again. 45 mg of GO are suspended in 50 mL, to which the three precursors of Pt, Cu and Fe are added in the right quantities to obtain three equal molar parts from the total mass of 5 mg of metals. To this volume, 50 mL of 0.1 M $NaBH_4$ are added.

After being collected, all the composites thus prepared were prepared as suspensions in 18.2 Ω water at a concentration of 0.1 mg/mL each. The dispersions were sonicated for 10 minutes to obtain a homogeneous suspension. 5 μL of each dispersion were drop-casted on the surface of a Glassy Carbon Electrode 3mm Ø and dried in oven at 40 °C.

The Electrochemically active surface area (ECSA) of the modified electrodes was evaluated through the Randles-Sevcik equation (Equation 50).

10 mL of a 1 mM ferricyanide $[Fe(CN)_6]^{3-}$ 0.1 M KCl aqueous solution was used respectively as redox specie and supporting electrolyte. The electrochemical cell was assembled as follow:

- drop-casted composite on Glassy Carbon Disk 3mm Ø (GCD) as working electrode (WE)
- Glassy Carbon Rod 5 mm Ø (GCR) as counter electrode (CE)
- Ag/AgCl (Saturated KCl) as reference electrode (RE)

The solution was saturated with argon during 10 minutes before starting the experiment. Several voltammograms were recorded at increasing scan rates (100, 900, 2500, 4900, 8100, 12100, and 16900 mV/s) from 0.5 V to –0.5 V starting from the negative (cathodic) direction (Figure 56). The negative peak current, i_p (y), of each scan was plotted versus the scan rate square root, $\sqrt{\nu}$ (x), to obtain a linear regression (Figure 57). The ECSA values obtained are reported further on in Table 9.

Preliminary cyclic voltammetry analyses are represented in Figures 58 and 59 the cyclic voltammograms obtained on the Pt@rGO sample are represented, respectively from 0 V to –1.5 V and 0 V to –1.6 V vs Ag/AgCl.

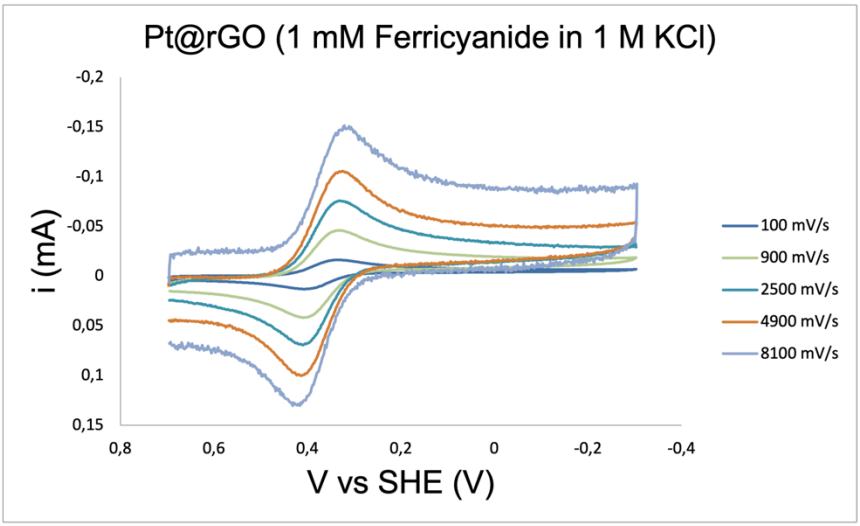


Figure 56. Cyclic voltammograms of a glassy carbon electrode immersed in an argon-saturated solution of 1 mM $K_3[Fe(CN)_6]$ in 0.1 M acetate buffer (pH 4) and 0.1 M KCl, collected at increasing scan rates (100-900-2500-4900-8100 mV/s, respectively). Cyclic voltammograms start with the cathodic scan from 0.5 V to −0.5 V vs Ag/AgCl (Sat'd KCl).

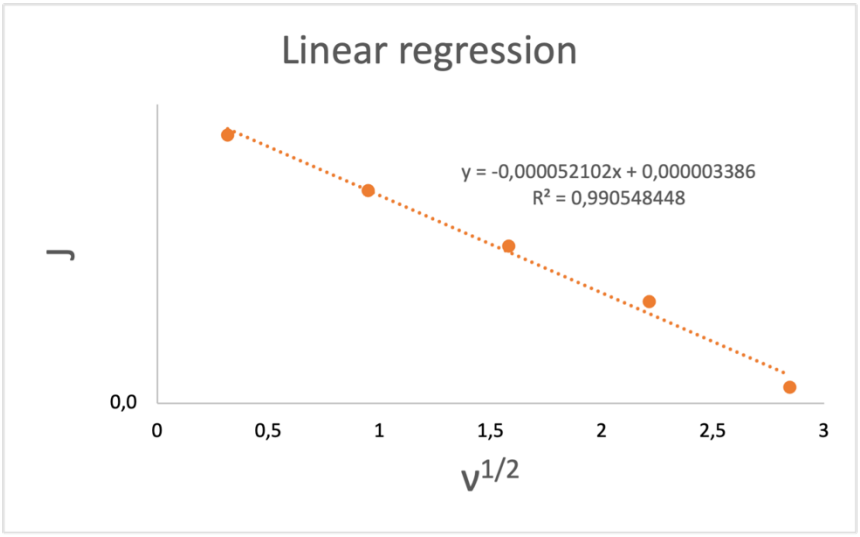


Figure 57. Linear regression obtained from the plot of the peak current (ip) in the cathodic scan as a function of the square root of the scan rate ($v^{1/2}$).

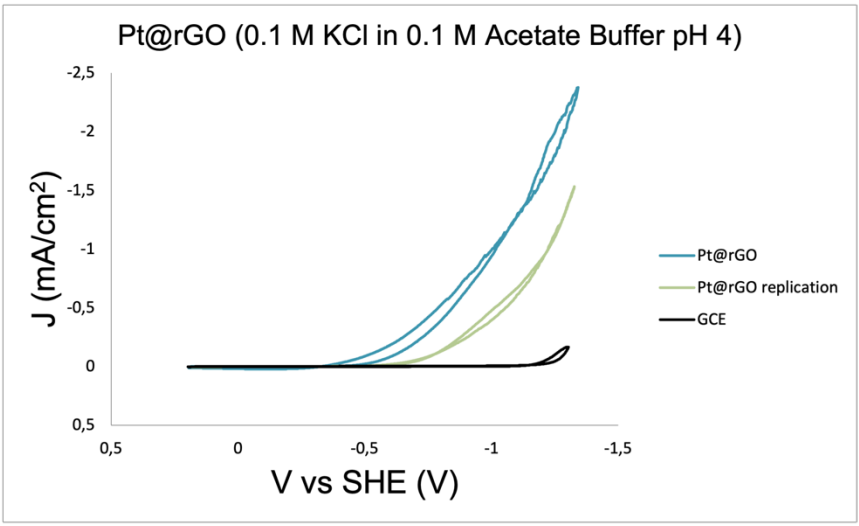


Figure 58. Cyclic voltammograms of Pt@rGO-GCE immersed in an argon-saturated solution of 0.1 M KCl in 0.1 M acetate buffer (pH 4), collected at a scan rate of 100 mV/s. Cyclic voltammograms start with the cathodic scan from 0 V to −1.5 V vs Ag/AgCl (Sat'd KCl).

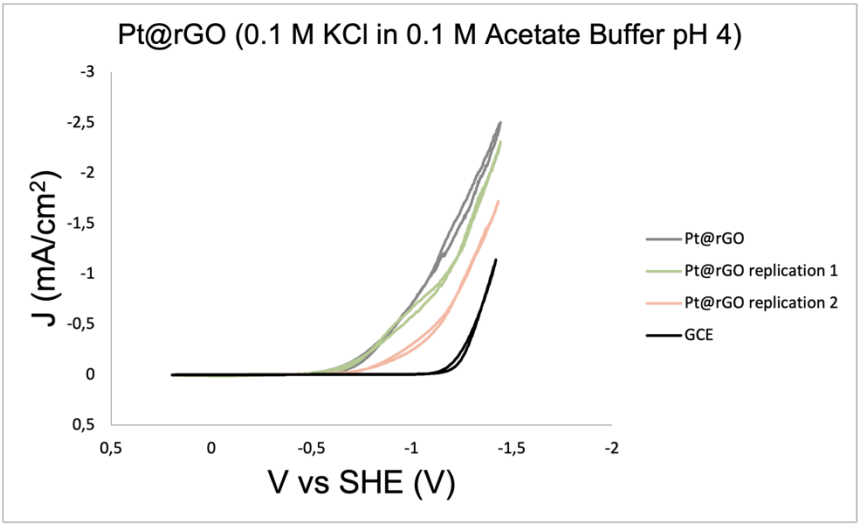


Figure 59. Cyclic voltammograms of Pt@rGO-GCE immersed in an argon-saturated solution of 0.1 M KCl in 0.1 M acetate buffer (pH 4), collected at a scan rate of 100 mV/s. Cyclic voltammograms start with the cathodic scan from 0 V to −1.6 V vs Ag/AgCl (Sat'd KCl).

In both cases, a loss of current density developed in the replicates is noted. This phenomenon is widely reported in the literature[198–202] and it is associated to the migration and agglomeration of the nanoparticles and the consecutive loss of ECSA. When platinum (Pt) or a related noble metal is dispersed on a high-surface carbon support with a high specific surface area for the catalyst reaction, the nanoscopic particles are susceptible to several degradation phenomena that are triggered by the presence of electric potential, high temperature, and humidity in the catalyst layer.[198]

Two very different mechanisms of catalyst degradation result from these harmful conditions. Pt dissolution powers the first mechanism, known as Ostwald ripening, and is more pronounced for smaller particles than for larger ones due to surface energy effects. As a result, Pt is dispersed from smaller particles and redeposited onto larger Pt particles, increasing the catalyst layer's particle size overall.[203] However, the corrosion of carbon support, which is also important in the catalyst environment, causes the particles to migrate, separate from their support, and possibly clump together.[199] Both Ostwald ripening and particle agglomeration cause the catalyst layer's mean particle size to gradually increase, which lowers the specific surface area, ECSA, and the catalyst efficiency.[204]

Because of the concomitant hydrogen evolution on the surface of the catalyst, it is also notable that the curves related to the Pt@rGO composite appear jagged. Bubble arising at the electrode can cause unwanted blocking of the electrocatalyst surface and ionic conductive pathways in the electrolyte, leading to losses of energy.[205–207] Figure 60 shows the evolution of the hydrogen bubbles on the bare glassy carbon electrode (GCE) and the evolution of the hydrogen bubbles on the glassy carbon electrode modified with drop-casted Pt@rGO when a potential of −1.6 V vs Ag/AgCl (Sat'd KCl) is applied. It is possible to notice how the hydrogen bubbles developed on the Pt@rGO-modified electrode appear larger, justifying both the current loss from the first cycle to the following ones and the jagged curves.

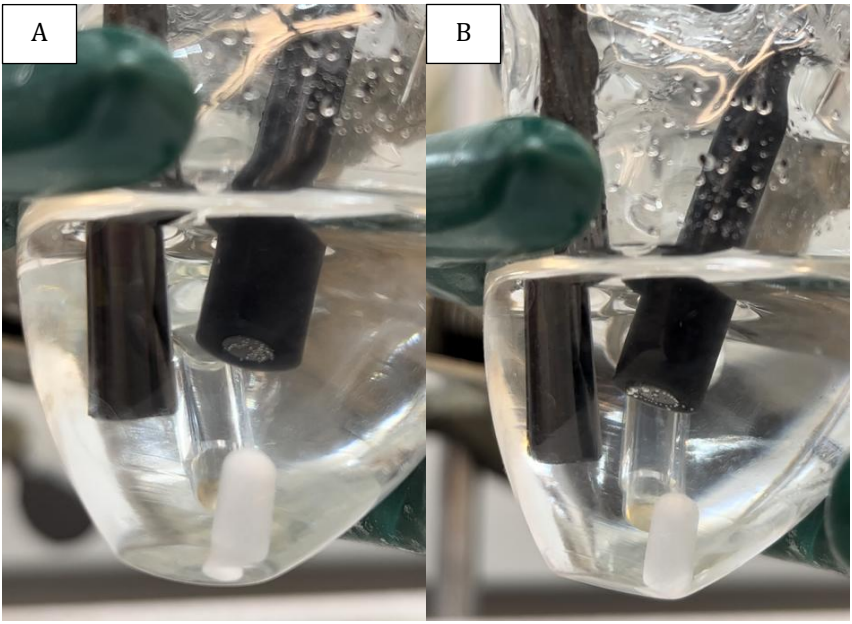


Figure 60. (A) Hydrogen bubbles on bare glassy carbon electrode and (B) hydrogen bubbles on Pt@rGO-GCE at −1.6 V vs Ag/AgCl (Saturated KCl). Bubbles on Pt@rGO-GCE are bigger causing the jagged cyclic voltammetry curves.

The graph in Figure 61 shows a comparison of cyclovoltammograms of the samples under examination. The data obtained do not seem to show clear differences in the current density developed in the potential window between 0 and −1.5 V vs Ag/AgCl (Sat'd KCl) between the Pt@rGO, PtFe@rGO and PtCu@rGO samples. Furthermore, the trimetallic composite, contrary to what reported in the literature, appears to be less efficient than the others. This poor comparability of the data has been attributed to the chosen preparation procedure. In fact, the addition of the precursors in powder form has not proven to be an easily reproducible method.
For this reason, the experiments described so far were repeated following a synthesis procedure that involves the addition of the metal precursors in the form of aqueous solutions.

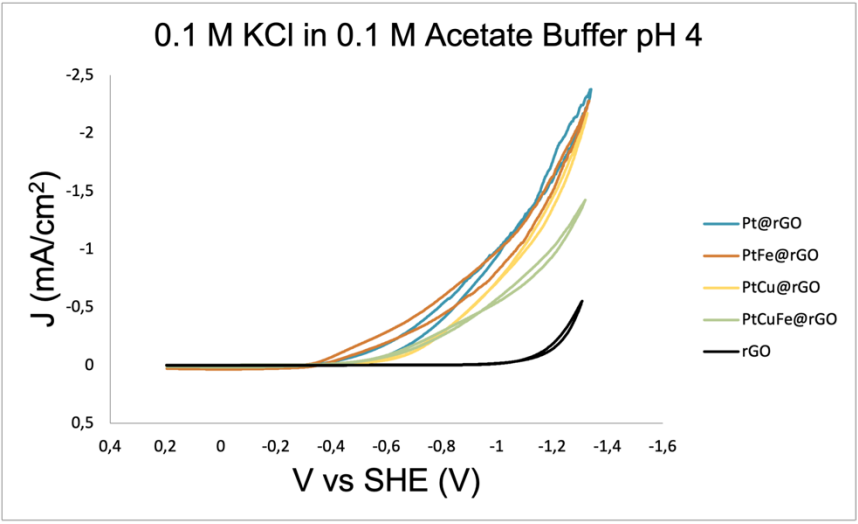


Figure 61. Compared cyclic voltammograms of Pt@rGO (blue line), PtFe@rGO (orange line), PtCu@rGO (yellow line), PtCuFe@rGO (green line), and rGO (black line) immersed in an argon-saturated solution of 0.1 M KCl in 0.1 M acetate buffer (pH 4), collected at a scan rate of 100 mV/s. Cyclic voltammograms start with the cathodic scan from 0 V to −1.5 V vs Ag/AgCl (Sat'd KCl).

In this second procedure, three stock solution were prepared in the following concentrations:

- 10 mM $H_2[PtCl_6] \cdot 6H_2O$
- 50 mM $CuSO_4 \cdot 5H_2O$
- 50 mM $FeSO_4 \cdot 7H_2O$

To obtain the monometallic sample, denoted as Pt_{100}@rGO, 45 mg of graphene oxide powder was dispersed in DI water by sonication. Subsequently, a volume of 10 mM $H_2[PtCl_6] \cdot 6H_2O$ containing 5 mg of platinum was added. The suspension was transferred to a 100 mL round bottom flask placed on ice, saturated with nitrogen, and stirred at 600 rpm for 2 hours. 50 mL of 0.1 M $NaBH_4$ is prepared with cold water to slow down the reaction between $NaBH_4$ and water, then it is added dropwise to the suspension using a syringe through the polymer septum. After two hours, the suspension obtained is filtered with a paper filter and dried overnight in

an oven at 40 °C. A similar procedure was followed to obtain two other samples in which half of the total moles of platinum was replaced with equal numbers of moles of copper and iron, respectively indicated with $Pt_{50}Cu_{50}$@rGO and $Pt_{50}Fe_{50}$@rGO. Finally, in the last sample, the mass of platinum is reduced to one third of the initial mass and the remaining two thirds are replaced with equal numbers of moles of copper and iron, indicated with $Pt_{33}Cu_{33}Fe_{33}$@rGO. Once the samples were collected, they were drop-casted on the GCE surface with the same procedure used for the previous samples. Their ECSA was evaluated using the Randles-Sevcik equation and the collected data are shown in Table 11. For comparison, monometallic Pt_{50}@rGO and Pt_{33}@rGO are also synthesized.

Table 11. ECSA of each sample, obtained with the Randles-Sevcik equation.

Procedure	Sample	ECSA
	GCD	0.057 cm^2
	rGO	0.048 cm^2
Metal precursors in powder form	Pt@rGO	0.049 cm^2
	PtCu@rGO	0.081 cm^2
	PtFe@rGO	0.058 cm^2
	PtCuFe@rGO	0.078 cm^2
Metal precursors in solution form	Pt_{100}@rGO	0.070 cm^2
	$Pt_{50}Cu_{50}$@rGO	0.079 cm^2
	$Pt_{50}Fe_{50}$@rGO	0.053 cm^2
	$Pt_{33}Cu_{33}Fe_{33}$@rGO	0.065 cm^2
	Pt_{50}@rGO	0.086 cm^2
	Pt_{33}@rGO	0.072 cm^2

The graphs obtained from the cyclic voltammetry scans of the composites Pt_{100}@rGO, $Pt_{50}Cu_{50}$@rGO, $Pt_{50}Fe_{50}$@rGO and $Pt_{33}Cu_{33}Fe_{33}$@rGO deposited on bare GCD are in Figures 62, 63, 64, 65 respectively and 66.

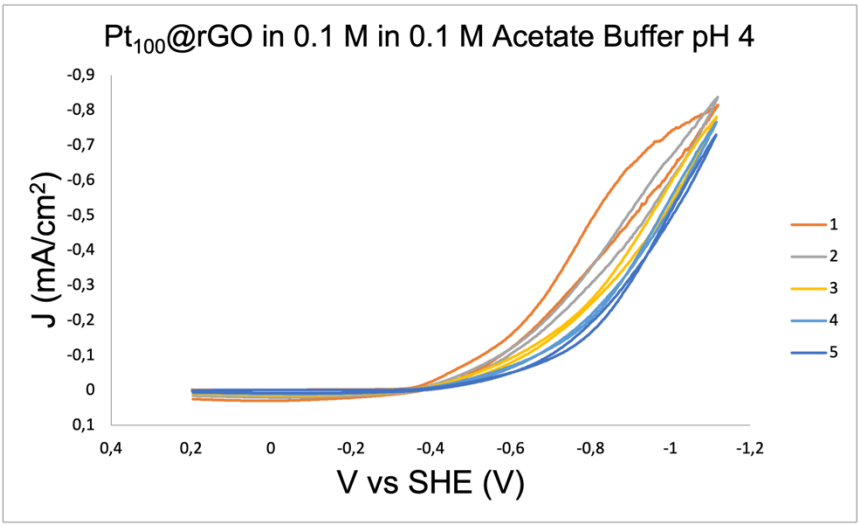


Figure 62. Five consecutive cyclic voltammograms of Pt_{100}@rGO-GCE immersed in an argon-saturated solution of 0.1 M KCl in 0.1 M acetate buffer (pH 4), collected at a scan rate of 100 mV/s. Cyclic voltammograms start with the cathodic scan from 0 V to −1.3 V vs Ag/AgCl (Sat'd KCl).

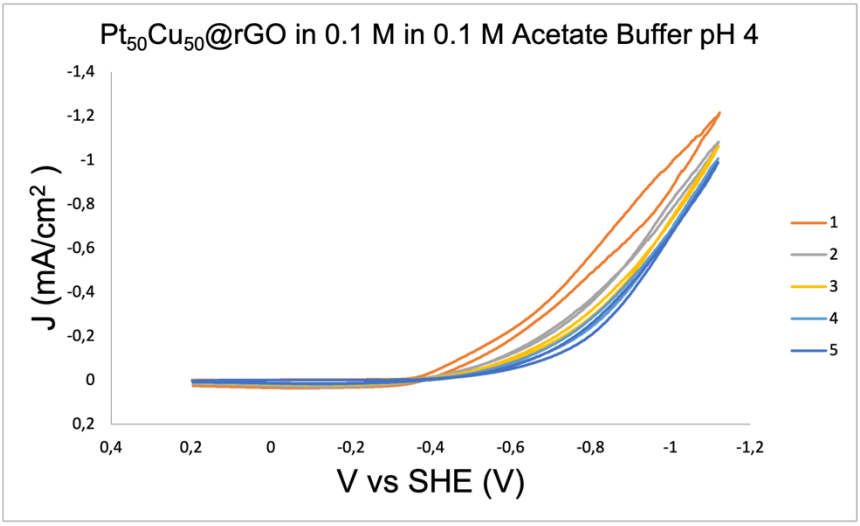


Figure 63. Five consecutive cyclic voltammograms of $Pt_{50}Cu_{50}$@rGO-GCE immersed in an argon-saturated solution of 0.1 M KCl in 0.1 M acetate buffer (pH 4), collected at a scan rate of 100 mV/s. Cyclic voltammograms start with the cathodic scan from 0 V to −1.3 V vs Ag/AgCl (Sat'd KCl).

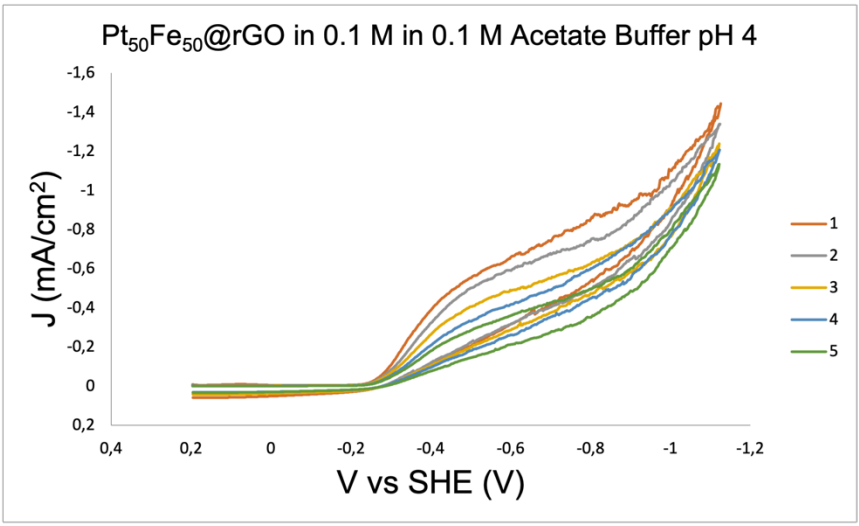


Figure 64. Five consecutive cyclic voltammograms of $Pt_{50}Fe_{50}$@rGO-GCE immersed in an argon-saturated solution of 0.1 M KCl in 0.1 M acetate buffer (pH 4), collected at a scan rate of 100 mV/s. Cyclic voltammograms start with the cathodic scan from 0 V to −1.3 V vs Ag/AgCl (Sat'd KCl).

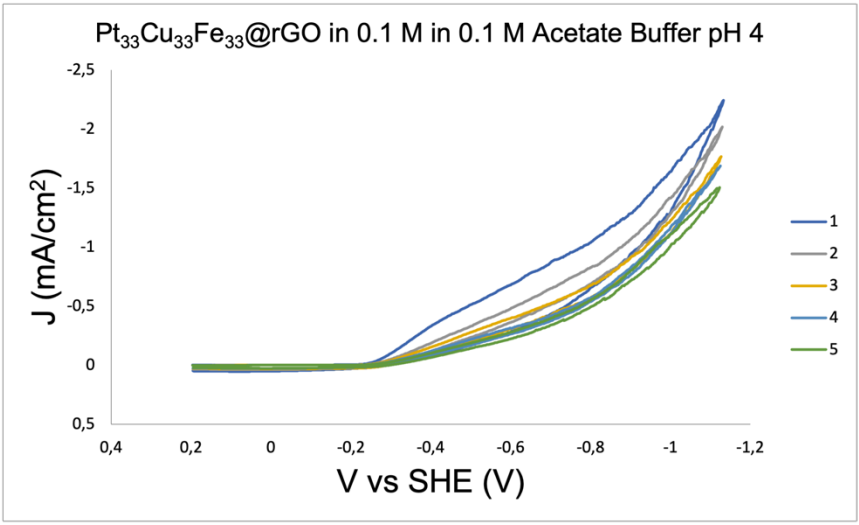


Figure 65. Five consecutive cyclic voltammograms of $Pt_{33}Cu_{33}Fe_{33}$@rGO-GCE immersed in an argon-saturated solution of 0.1 M KCl in 0.1 M acetate buffer (pH 4), collected at a scan rate of 100 mV/s. Cyclic voltammograms start with the cathodic scan from 0 V to −1.3 V vs Ag/AgCl (Sat'd KCl).

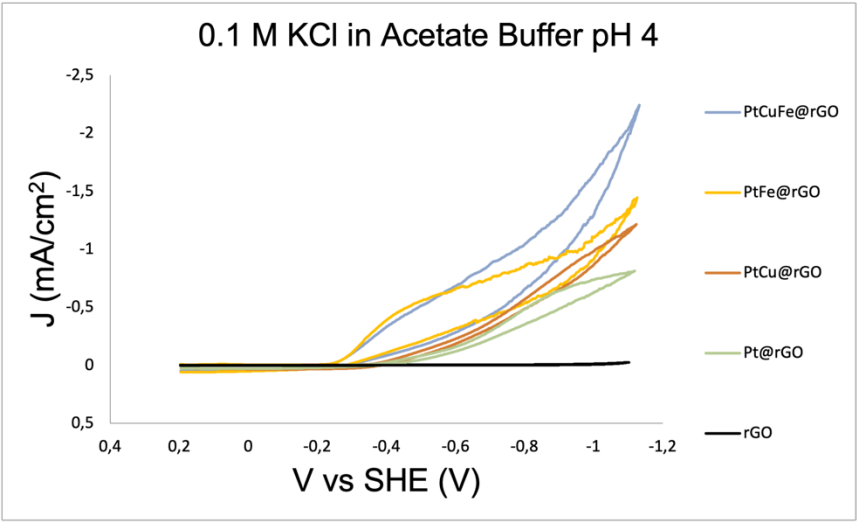


Figure 66. Compared cyclic voltammograms of $Pt_{33}Cu_{33}Fe_{33}$@rGO (blue line), $Pt_{50}Fe_{50}$@rGO (yellow line), $Pt_{50}Cu_{50}$@rGO (orange line), Pt_{100}@rGO (green line), and rGO (black line) immersed in an argon-saturated solution of 0.1 M KCl in 0.1 M acetate buffer (pH 4), collected at a scan rate of 100 mV/s. Cyclic voltammograms start with the cathodic scan from 0 V to −1.3 V vs Ag/AgCl (Sat'd KCl).

The concentration of platinum in the different catalysts plays a crucial role, since a higher current density is recorded when its concentration is halved and tri-halved respectively in the bimetallic and trimetallic composites. In Figure 67 cyclic voltammograms recorded on Pt_{100}@rGO, Pt_{50}@rGO and Pt_{33}@rGO are compared. The increased current density as the initial precursor concentration decreases is in line with information reported in literature. The higher current density was ascribed to a higher ECSA: this phenomenon can be directly linked to the initial concentration of platinum used in the synthesis, which influences the shape of the nanoparticles, and therefore to the active catalytic surface available for the reaction.[208]

The potential window explored, from 0 V to –1.3 V, was chosen to avoid reaching the potential necessary for the direct reduction of rGO, otherwise it would not be possible to distinguish the direct reduction of water from the reduction of the analyzed catalyst. The reduction of the oxygenated

functional groups of GO, in fact, generally occurs between –1.1 and –1.5 V, a range that corresponds to the reaction of the groups respectively on the surface and on the perimeter of the graphene oxide.[209]

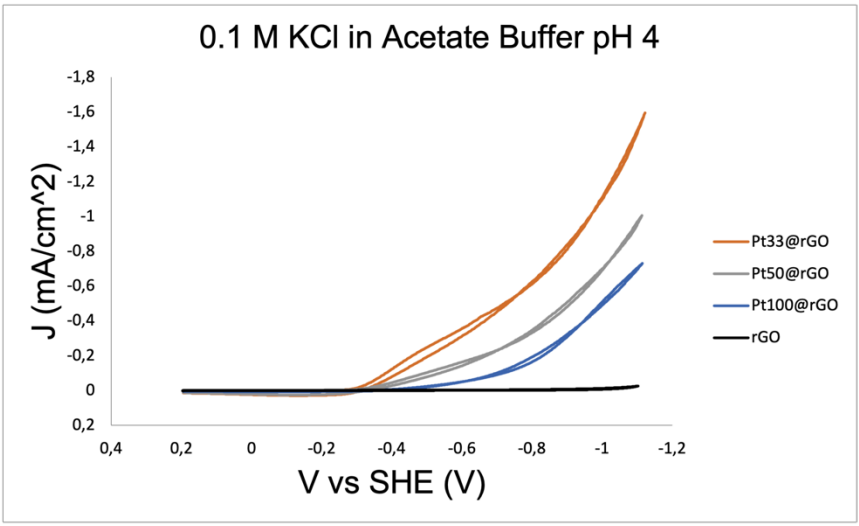


Figure 67. Compared cyclic voltammograms of Pt_{33}@rGO (orange line), Pt_{50}@rGO (gray line), Pt_{100}@rGO (blue line), and rGO (black line) immersed in an argon-saturated solution of 0.1 M KCl in 0.1 M acetate buffer (pH 4), collected at a scan rate of 100 mV/s. Cyclic voltammograms start with the cathodic scan from 0 V to −1.3 V vs Ag/AgCl (Sat'd KCl).

However, when comparing bi- and trimetallic samples with monometallic platinum samples, it seems evident that the addition of non-noble metals leads to increases in the developed current density (Figure 68). However, when comparing the bi- and trimetallic samples with the monometallic samples of platinum, it seems evident that the addition of non-noble metals leads to increases in the developed current density. Furthermore, it can be noted that the onset potential decreases when copper and iron are present.

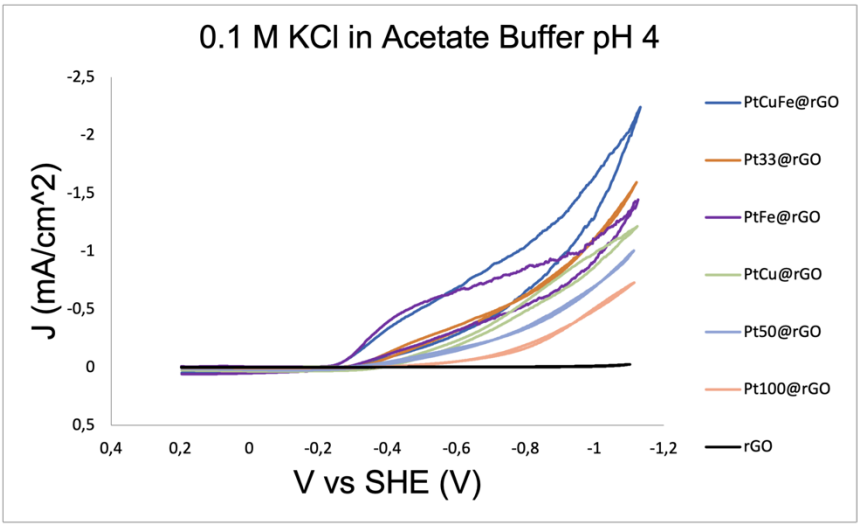


Figure 68. Compared cyclic voltammograms of PtCuFe@rGO (dark blue line), Pt_{33}@rGO (orange line), PtFe@rGO (purple line), PtCu@rGO (green line), Pt_{50}@rGO (light blue line), Pt_{100}@rGO (light pink line), and rGO (black line) immersed in an argon-saturated solution of 0.1 M KCl in 0.1 M acetate buffer (pH 4), collected at a scan rate of 100 mV/s. Cyclic voltammograms start with the cathodic scan from 0 V to −1.3 V vs Ag/AgCl (Sat'd KCl).

3.4.4 *Conclusions*

The techniques used to obtain nanoparticles can be considered green synthesis methods, with rather rapid times. It has been observed that the decrease in the amount of platinum leads to an increase in the current density developed, both in the presence of other non-noble metals and not. Two possible explanations have been given for these results: (1) the initial concentration of platinum added, for the same volume of the reaction flask, affects the shape and the extension of the surface of the nanoparticles formed; (2) the addition of non-noble metals has a synergistic effect with platinum, improving the performance of the catalyst anchored on rGO.
However, the sample preparation methods through the addition of metal precursors in the form of powders and drop-casting on the electrode, are not easily reproducible and give rise to results with significant uncertainty.

3.5 Electrochemical reduction of graphitic support and Pt, Cu, and Fe nanoparticles

3.5.1 *Introduction*

Anchoring metal nanoparticles on the surface of reduced graphene oxide represents a highly promising approach to improve catalytic performance, not only in the hydrogen evolution reaction (HER), but also in a number of other advanced catalytic applications. The combination of reduced graphene oxide (rGO) and metal nanoparticles is an ideal system to optimize the activity and stability of catalysts, thanks to the ability of graphene to provide an electrically active surface and at the same time improve the dispersion and stability of metal nanoparticles. This type of support contributes to an efficient charge distribution and to the improved interaction between the reagents and the nanoparticles themselves, making it possible to use such systems in critical reactions such as HER.

There are several methods to achieve the anchoring of metal nanoparticles on the graphene support, each with its advantages and limitations. Among the most common methods we find the chemical method, the thermal method and the electrochemical method. The chemical co-reduction method, described in paragraph 3.4, involves a series of critical steps, such as the preparation of precursor solutions and the management of reduction conditions, which can negatively affect the reproducibility of experiments. Typically, the reduction process of graphite oxide does not completely remove oxygen-containing functional groups from graphite oxide sheets. Therefore, variations in the reduction degree of rGO have a direct impact on its characteristics.[210] The reduction of nanoparticles requires careful control of the reaction conditions which affect the shape of the nanoparticles and consequently their surface. Variations in synthesis conditions, graphene quality and stability of metal precursors can cause inhomogeneity in the final result, reducing the reliability and consistency of nanoparticles anchored on the graphene surface.

On the contrary, the electrochemical method emerges as an innovative approach, which offers significant advantages in terms of environmental sustainability and reproducibility. This method, in fact, exploits the application of an electric potential to reduce metals directly on the surface of the reduced graphene oxide, avoiding the use of complex or potentially dangerous chemical reagents. The electrochemical reduction of metal nanoparticles allows for precise control over the size and distribution of nanoparticles. Furthermore, being a process that occurs in aqueous solution, the electrochemical method is environmentally friendly, reducing the use of organic solvents and other harmful chemical reagents, thus characterizing itself as an eco-efficient process.

The main objective of this study was to identify an optimal potential window, which allows both the reduction of the graphene support and of the metals involved. The choice of the electric potential was crucial to establish whether co-reductions are possible and in what order to proceed with the reduction and electrodeposition of all the elements that make up the composite.

3.5.2 *Materials and methods*

The reagents and materials used in the above study were as follows: graphite derived from industrial waste material, hexachloroplatinic(IV) acid hydrate ($H_2[PtCl_6] \cdot 6H_2O$) with a purity ≥ 99.9% supplied by Sigma-Aldrich (US), copper(II) sulfate pentahydrate ($CuSO_4 \cdot 5H_2O$) with a purity of 99.5% supplied by CARLO ERBA Reagents S.r.l. (Italy), iron(II) sulfate heptahydrate ($FeSO_4 \cdot 7H_2O$) with a purity ≥ 99.0% supplied by Sigma-Aldrich (US); sodium borohydride ($NaBH_4$) powder with a purity of ≥ 98.0% in powder supplied by Sigma-Aldrich (US), milli-Q water produced in the laboratory (Merck Millipore, Germany), potassium chloride (KCl), sodium acetate 99.99% (Alfa Aesar), acetic acid 99.99% (Alfa Aesar) were used. All electrochemical experiments were conducted at the University of Arizona, Tucson (USA). A Gamry Reference 3000 potentiostat and a standard three-electrode system were used. The uncompensated resistance (R_u) was

measured with the potentiostat by electrochemical impedance spectroscopy. The solution resistance was compensated to 90% of the measured R_u using positive feedback iR compensation. Potentials in aqueous solution were referenced to the standard hydrogen electrode (SHE) using the standard conversion from the Ag/AgCl (Sat'd KCl) reference electrode potential. The counter electrode used was a 5 mm diameter and 10 mm long Glassy Carbon Rod (GCR) (Alfa Aesar). All solutions were argon-saturated for 10 min before performing electrochemical tests. For cyclic voltammetry (CV) experiments, a Glassy Carbon Disk (BASi) with a geometric surface area (Ageo) of 0.071 cm^2 was used as the working electrode.

3.5.3 *Discussion and characterization*

For the electroreduction of the graphene support, an aqueous suspension of graphene oxide (GO) was prepared at a concentration of 0.1 mg/mL, a value that allows to obtain a stable dispersion of graphene oxide in solution, ensuring that the particles are sufficiently dispersed and not agglomerated, a fundamental condition for a good exfoliation. The suspension is subjected to 15 minutes of sonication. From the prepared suspension, a drop of 5 μL was taken, an optimal quantity to ensure a uniform and controlled coverage of the surface of the working electrode. The drop was carefully positioned on the surface of a glassy carbon electrode (CGE) of 3 mm Ø diameter. After slowly drying in oven at 40 °C to prevent the coffee-ring effect,[211] the modified electrode was used as working electrode in the three-electrode setup. 10 mL of 0.1 M KCl aqueous solution was used as supporting electrolyte. The electrochemical cell was assembled as follow:

- drop-casted GO on GCE 3mm Ø as working electrode (WE)
- Glassy Carbon Rod 5 mm Ø (GCR) as counter electrode (CE)
- Ag/AgCl (Saturated KCl) as reference electrode (RE)

The solution was saturated with argon during 10 minutes before starting the experiment. Five consecutive cyclic voltammograms (CVs) of GO electrochemical reduction processes, recorded at a scan rate of 100 mV/s, from 0 V to −2 V starting from the negative (cathodic) direction, are

displayed in Figure 69. With broad reduction peaks at −0.8 V and −1.5 V, respectively, the obtained CVs demonstrate that the first voltammetric cycle eliminated the larger reduction portion of oxygen-containing functional groups. The weak oxygen-containing functional groups on the basal plane of GO sheets within the non-covalent interaction are reduced, as indicated by the reduction peak at lower potential. However, the reduction of the strong oxygen-containing functional groups at the edges and defects of the GO sheets is responsible for the wider reduction peak at −1.5 V. The weak oxygen-containing functional groups on the basal plane, which were largely eliminated in the first voltammetric cycle, and the strong oxygen-containing functional groups that were progressively eliminated from the edges and defects of the GO sheets are the reasons why the remaining voltammetric cycles lack a sharp reduction peak and only have a broader reduction peak at higher potential.[210,212,213]

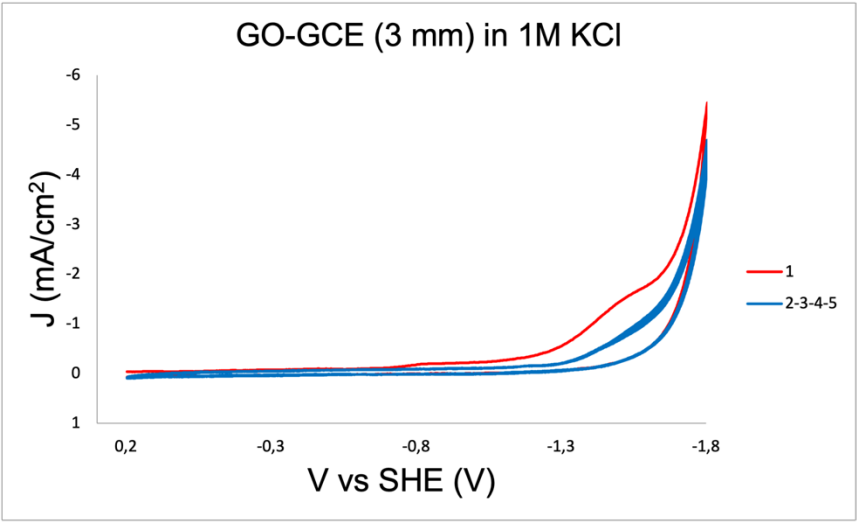


Figure 69. Five consecutive cyclic voltammograms of a saturated argon solution containing 0.1 M KCl in 0.1 M Acetate buffer (pH 4) and recorded on a 3 mm Ø glassy carbon electrode, GCE; The experiment starts from the negative scan (cathodic curve) from 0 V to −2 V vs Ag/AgCl (Sat'd KCl) with a scan rate of 100 mV/s.

For the electroreduction of metal nanoparticles, consecutive cyclovoltammetries were performed on each metal, without ever polishing the electrode in order to observe an initial deposition of particles at the first scan and continue with the nucleation and agglomeration in the subsequent scans. 10 cyclic voltammograms were recorded in 1 mM H_2PtCl_6 aqueous solution. 0.1 M KCl was chosen as supporting electrolyte and 0.1 M acetate buffer (pH 4) was selected as source of H^+. The experiment starts from the negative scan (cathodic curve) from 0.6 V to −0.5 V vs Ag/AgCl (Sat'd KCl) at a scan rate of 50 mV/s (Figure 70).

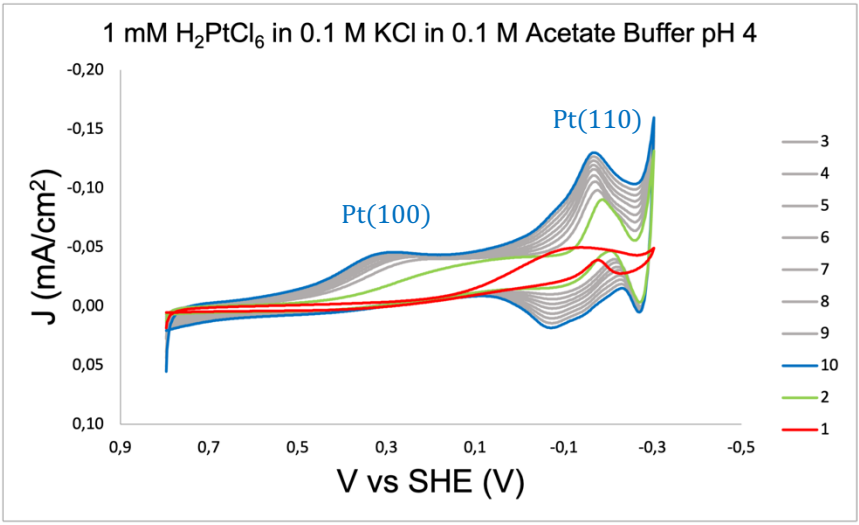


Figure 70. Ten consecutive cyclic voltammograms of a saturated argon solution containing 1 mM H_2PtCl_6 in 0.1 M KCl in 0.1 M Acetate buffer (pH 4) and recorded on a 3 mm Ø glassy carbon electrode, GCE; The experiment starts from the negative scan (cathodic curve) from 0.6 V to −0.5 V vs Ag/AgCl (Sat'd KCl); scan rate: 50 mV/s.

The first cyclic voltammogram is represented by a red line. A broad peak current in the cathodic curve around −0.1 V and two broad peaks in the anodic curve around −0.2 V and −0.1 V respectively, are observed. In the second cyclic voltammogram (green line) a broad peak current (0.2 V) and a sharp peak current (−0.2 V) are obtained during the cathodic scan. A sharp peak current (−0.3 V) and a broad peak current (−0.1 V) are present in the

anodic direction scan. In agreement with the data found in literature, the values of the two peaks in the cathodic curve correspond to the adsorption of hydrogen on two different crystalline structures of platinum while the two peaks in the anodic curve correspond to the desorption of hydrogen.[214] The peaks at lower and higher potentials, can be interpreted as the adsorption/desorption of hydrogen in the (110) and (100) planes of Pt, which are attributed to the weakly and strongly bonded H, respectively.

The same experiment was repeated for copper. Figure 71 shows 10 cyclic voltammograms recorded in 1 mM $CuSO_4$ aqueous solution. 0.1 M KCl was chose as supporting electrolyte and 0.1 M acetate buffer (pH 4) was selected as source of H^+. The experiment starts from the negative scan (cathodic curve) from 0.5 V to –0.9 V vs Ag/AgCl (Sat'd KCl) at a scan rate of 50 mV/s.

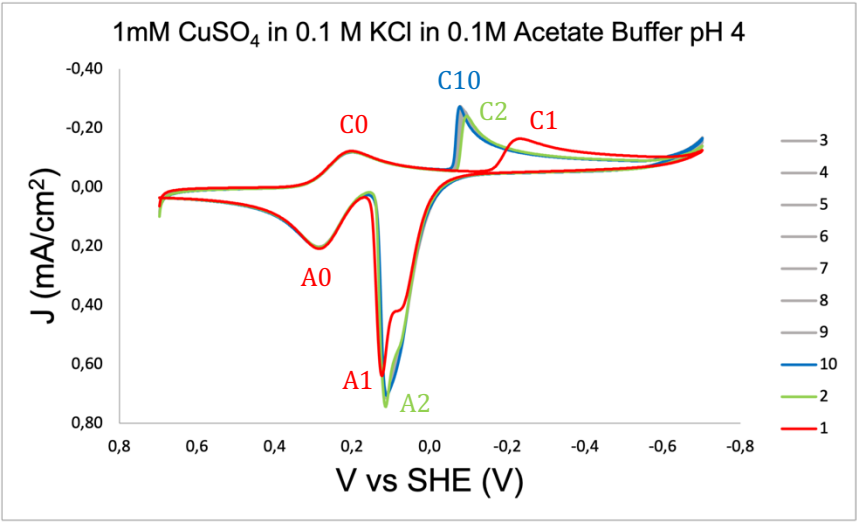


Figure 71. Ten consecutive cyclic voltammograms of a saturated argon solution containing 1 mM $CuSO_4$ in 0.1 M KCl in 0.1 M Acetate buffer (pH 4) and recorded on a 3 mm Ø glassy carbon electrode, GCE; The experiment starts from the negative scan (cathodic curve) from 0.5 V to −0.9 V vs Ag/AgCl (Sat'd KCl); scan rate: 50 mV/s.

The reduction of Cu^{2+} to Cu^0 occurs in two steps. Two well-defined pairs of reduction oxidation peaks on both the oxidative and reductive scans were observed. The first pair of oxidation/reduction peaks at 0.28 and 0.2 V

(A0/C0) correspond to the Cu^{2+}/Cu^{+} redox couple. Since both species are solubilized during the reduction and subsequent oxidation, these signals remain overlapped during the ten cycles.

The second redox couple located at 0.12 and −0.25 V (A1/C1) in the first scan, and 0.11 and −0.11 V in the second scan (A2/C2) corresponds to the Cu^{+}/Cu^{0} reduction/oxidation processes.[215,216]

The shift from C1 to peak C2 and C10 indicates that the deposition of copper nanoparticle occurred on the electrode surface. The shift from C1 to C10 was attributed to the dissolution and reformation of copper nanoparticles during cycling, which leads to a change in particle size and distribution, causing non-superimposable current peaks. Since both the formation potential of the metallic Pt and metallic Cu is around −0.4 V vs Ag/AgCl (Sat'd KCl), both metals can be electroplated simultaneously.

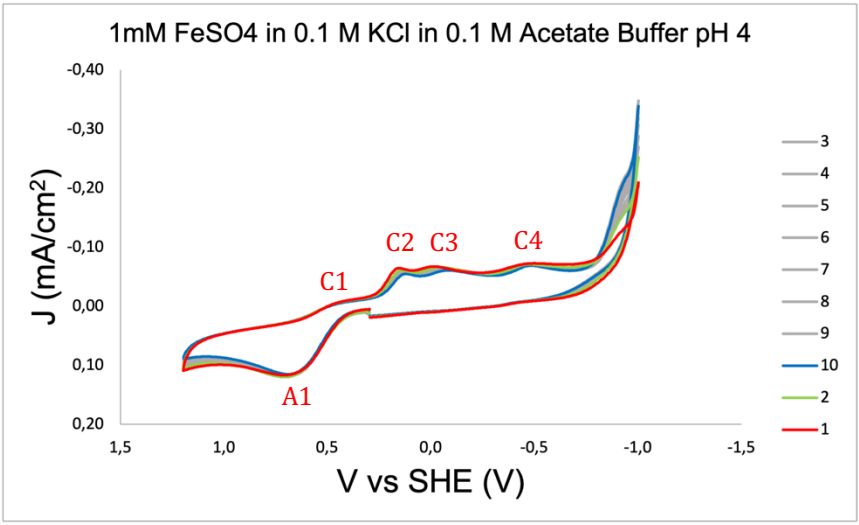


Figure 72. Ten consecutive cyclic voltammograms of a saturated argon solution containing 1 mM $FeSO_4$ in 0.1 M KCl in 0.1 M Acetate buffer (pH 4) and recorded on a 3 mm Ø glassy carbon electrode, GCE; The experiment starts from the positive scan (anodic curve) from 0.1 V to 1 V to −1.2 V vs Ag/AgCl (Sat'd KCl); scan rate: 50 mV/s.

The same experiment was repeated for iron. Figure 72 shows 10 cyclic voltammograms recorded in 1 mM $FeSO_4$ aqueous solution. 0.1 M KCl was

chose as supporting electrolyte and 0.1 M acetate buffer (pH 4) was selected as source of H^+. The experiment starts from the positive scan (anodic curve) from 0.1 V to 1 V and to −1.2 V vs Ag/AgCl (Sat'd KCl) at a scan rate of 50 mV/s. The CV shows several reduction processes (C1 to C4) in the cathodic scan and, after the oxidation of Fe^{2+} to Fe^{3+} (A1) in the first anodic scan of the CV. The reduction waves C3 at -0.04 V and C4 at −0.44 V are attributed, respectively, to the reduction of Fe^{3+} to Fe^0 and $Fe2^+$ to Fe^0. No iron compounds have been found in the literature that have a reduction potential corresponding to the C1 and C2 wave, therefore it has been hypothesized that it is a signal due to impurities present in the sample.

3.5.4 *Conclusions*

The electrochemical reduction of graphene oxide (GO) was successfully achieved in this study, as confirmed by data collected from the literature.[209] By applying a potential of −1.5 V vs Ag/AgCl (Sat'd KCl), graphene oxide was reduced to reduced graphene oxide (rGO), a crucial step to obtain a stable and functional support for the deposition of metal nanoparticles. This reduction is a key process to improve the properties of graphene, making it suitable for catalytic applications, where the electrically active surface plays a fundamental role in the efficiency of the reactions.

As for the deposition of metal nanoparticles, the scanning window chosen for platinum, ranging from +0.6 V to −0.5 V, proved to be suitable for the agglomeration of nanoparticles on the graphene support. This potential range allowed a controlled growth of platinum nanoparticles on the surface of reduced graphene oxide (rGO). Copper, on the other hand, was deposited in a scanning window ranging from +0.5 V to −0.9 V, a range in which the reduction of copper occurs favorably. However, for iron, which has a more negative reduction potential than the HER, it was necessary to reach a potential of −1.2 V to achieve efficient deposition of iron nanoparticles.[217]

In light of these results, it was decided to proceed with a three-step strategy for the subsequent experiments. In the first step, an electrodeposition of the graphene support (rGO) on the bare GDE will be performed at −1.5 V. The

obtained electrochemically reduced graphene oxide (erGO) constitutes the basis for the anchoring of the metal nanoparticles. Subsequently, in the second step, the deposition of iron nanoparticles will be carried out at −1.2 V, followed by a simultaneous co-deposition of copper and platinum nanoparticles at −0.4 V. This deposition sequence was designed to ensure optimal control over the distribution and size of the nanoparticles, as well as to maximize the catalytic performance of the final material.

3.6 Electroreduced platinum nanoparticles anchored on reduced graphene oxide functionalized with para-aminophenyl groups for hydrogen evolution reaction

3.6.1 *Introduction*

Hydrogen evolution reaction (HER) plays a critical role in the generation of green hydrogen fuel. Platinum (Pt)-based catalysts can effectively improve HER by reducing the activation energy and substantially increasing the reaction rate. Although platinum-based materials are considered as the cutting-edge electrocatalysts for HER, the high cost and scarcity in nature hinder their large-scale use in industrial implementation.

Due to its novel properties, such as high electrical conductivity and large specific surface area, graphene is a suitable supporting material for the design of electrocatalysts. Therefore, the exploration of platinum-based catalysts anchored on reduced graphene oxide with low metal content, improved stability, and increased hydrogen production has become the focus of HER reaction research.[218] However, particle migration and coalescence kinetics (PMC) of a supported metal are the major deactivation mechanisms that limit the successful industrialization of graphene-anchored nanoparticles. The aim of the present work is to obtain nanoparticles with controlled size and prevent their migration and coalescence on the support surface. Covalently bonded *p*-aminophenyl (*p*-NH_2-Ph) groups on the graphene surface are used as "spacers" to coordinate the nanoparticles and prevent their migration and coalescence during the HER reaction by establishing an electrostatic interaction between the positive amino group and the negatively charged platinum particles.[219] In these experiments, graphene oxide was modified with *p*-aminophenyl groups and then electrochemically reduced. Subsequently, platinum nanoparticles were nucleated on the graphene support by electrochemical means and their electrochemically active surface area was evaluated. The same experiment was performed on an unmodified glassy carbon working electrode (GCE) and on a glassy carbon working electrode on which graphene oxide was electrically deposited and reduced (erGO-GCE).

3.6.2 *Materials and methods*

The reagents and materials used in the above study were as follows: graphite derived from industrial waste material; sulfuric acid (H_2SO_4, 98%)

purchased from VWR Chemicals (US); potassium permanganate (K_2MnO_4, 99.5%) powder supplied by CARLO ERBA Reagents S.r.l. (Italy); hydrogen peroxide (H_2O_2) 30% w/w supplied by Honeywell Fluka (US); Milli-Q water produced in the laboratory (Merck Millipore, Germany); chloroplatinic acid hexahydrate ($H_2[PtCl_6] \cdot 6H_2O$) with a purity ≥ 99.9% supplied by Sigma-Aldrich (US); para-phenyldiamine 98% from Sigma-Aldrich (US); sodium nitrite from Sigma-Aldrich (US); nitric acid 70% v/v from Sigma-Aldrich (US).

All electrochemical experiments were performed with a Gamry Reference 3000 potentiostat and a standard three-electrode system, in which a glassy carbon electrode (3 mm ∅) is used as the working electrode, an Ag/AgCl (saturated KCl) reference electrode and a carbon rod (5 mm ∅) as the counter electrode. Potentials in aqueous solutions are referenced to the standard hydrogen electrode (SHE) using the standard conversion of +0.197 V from the Ag/AgCl (saturated KCl) electrode potential. The modification of the working electrodes was performed as follows: 10 mL of aqueous graphene oxide (GO) and 10 mL of modified reduced graphene oxide (NH_2-mrGO), both at a concentration of 0.5 mg/mL, were sonicated for 1 hour. 5 μL were taken from each of the two suspensions, a volume suitable to cover the surface of the working electrodes (geometric surface 0.071 cm^2). Once dried in an uncontrolled atmosphere oven, they were inserted one at a time into a 0.1 M KCl saline solution and were subjected to chronoamperometry at a constant potential of −1.5 V for 5 minutes. The nucleation of platinum nanoparticles occurs through 12 consecutive cyclic voltammetries, at the end of which the electrochemically active surface area is evaluated by means of the Randles-Sevcik equation in a 1 mM solution of potassium ferricyanide as redox species and 0.1 M KCl as supporting electrolyte, obtaining a linear regression at different scanning speeds (100-900-2500-4900-8100 mV/s).

3.6.3 *Discussion and characterization*

The functionalization of graphene oxide was performed according to the procedure reported by Le Xin et al.[220] Graphene oxide (GO) is prepared according to the modified Hummers method,[170] then it is partially reduced by adding $NaBH_4$ to 100 mL of previously sonicated GO aqueous dispersion (1 mg/mL). The suspension is heated to 80 °C and stirred for 1 h (Figure 73). The mild reduced graphene oxide (mrGO) is collected and washed several times with deionized water. Subsequently, the mrGO is dispersed again in water, followed by the addition of para-phenylenediamine, 70% HNO_3 and $NaNO_2$ in the molar ratios 1 : 1 : 1. The suspension is maintained at 60 °C for 4 h. The modified graphene (NH_2-mrGO) is collected and washed several times with a hydroalcoholic mixture.

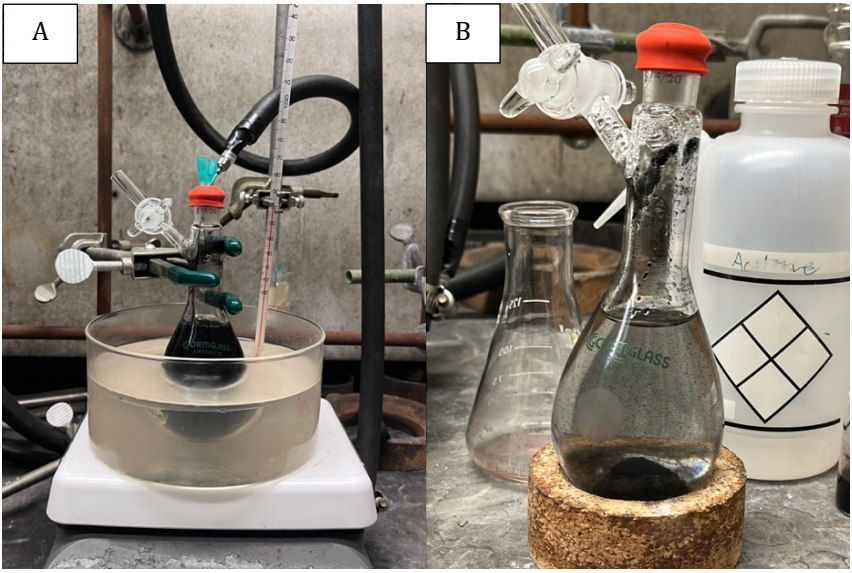


Figure 73. (A) GO before adding reducing agent and (B) the obtained mrGO.

The modified graphene support was analyzed by infrared spectroscopy (Figure 74). The IR spectrum reveals several key vibrational features that confirm the successful attachment of the amine group and provide insights into its interaction with the surface. The N-H stretching vibrations appear as two distinct bands in the 3300-3500 cm^{-1} region (3328 and 3198 cm^{-1}, respectively), corresponding to asymmetric and symmetric stretching

modes. Additionally, the N-H scissoring mode is observed about 1600 cm^{-1}, further confirming the presence of primary amine functionalities. The out-of-plane wagging and twisting modes of the amine group appear at 819 cm^{-1} region, indicating the potential influence of surface interactions on the molecular conformation. The characteristic C=C stretching vibrations of the aromatic ring are observed at 1502 cm^{-1}.

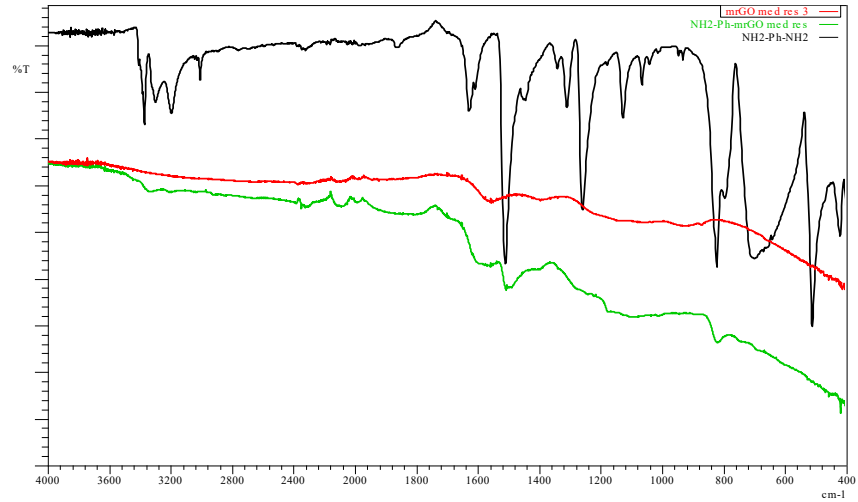
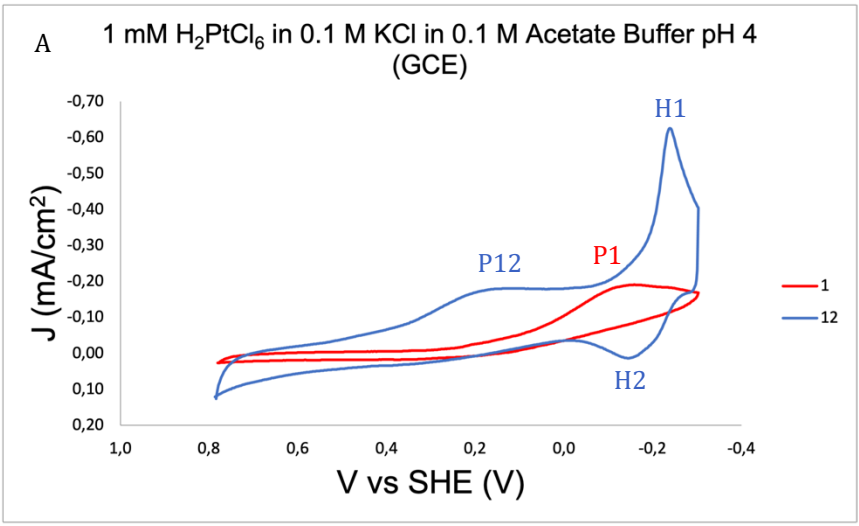
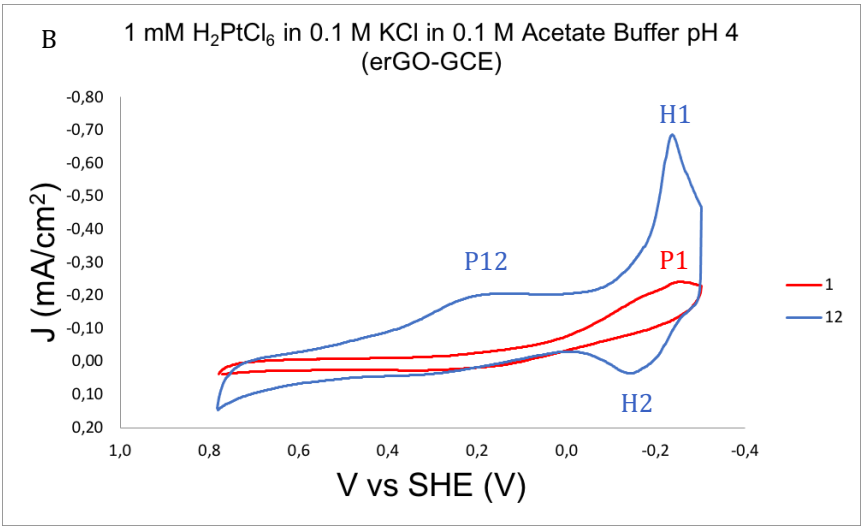


Figure 74. Infrared spectra of the *p*-phenylediamine (black line), mild reduced graphene oxide (red line), and the synthesized NH_2-mrGO (green line).

Subsequently, two glassy carbon electrodes were coated. One was coated with GO (GO-GCE), while the other was coated with mrGO modified with *p*-aminophenyl groups, by drop-casting (NH_2-mrGO-GCE). Both electrodes were subjected to chronoamperometry where a potential of −1.5 V vs Ag/AgCl (Sat'd KCl) was applied for 300 seconds. Platinum nanoparticles were then anchored on a bare electrode, Pt-GCE, and on the two coated electrodes, Pt@erGO-GCE and Pt@NH_2-erGO-GCE. 12 cyclic voltammograms in the scan window from +0.6 V to −0.5 V were recorded on each. Figure 75 shows the first and last cycle performed on the three electrodes: (A) glassy carbon electrode, GCE; (B) glassy carbon electrode modified with electrically reduced graphene oxide, erGO-GCE; (C) glassy carbon electrode

modified with electrically reduced NH_2-graphene oxide, NH_2-erGO-GCE. The significant increase in cathodic current at the H1 peak was assigned to the adsorption of hydrogen ions on the surface of platinum nanoparticles. The H2 peak during the anodic scan was attributed to the oxidation and desorption of H^+ ions from the platinum surface. The onset of cathode current at about 0.30 V in the first cycle and the subsequent reduction peak around −0.2 V were attributed to the reduction of H_2PtCl_6 to Pt^0 in agreement with the reduction peak of the H_2PtCl_6/Pt^0 redox couple in acidic medium. After twelve cycles this peak is shifted to a higher potential. The peak shift from −0.2 V to +0.2 V from the first to the last scan is due to the presence of platinum nanoparticles on the surface of the glassy carbon electrode. The nucleation of platinum particles in the first scan creates a more favorable surface for platinum deposition than the bare glassy carbon electrode. The shift of the P1 peak and the current observed for the H2 peak indicate the growth of platinum nanoparticles suggesting a diffusion-limited process.


A
1 mM H_2PtCl_6 in 0.1 M KCl in 0.1 M Acetate Buffer pH 4
(GCE)
H1
P12
P1
H2
J (mA/cm²)
V vs SHE (V)
1
12


B
1 mM H_2PtCl_6 in 0.1 M KCl in 0.1 M Acetate Buffer pH 4
(erGO-GCE)
H1
P12
P1
H2
J (mA/cm²)
V vs SHE (V)
1
12

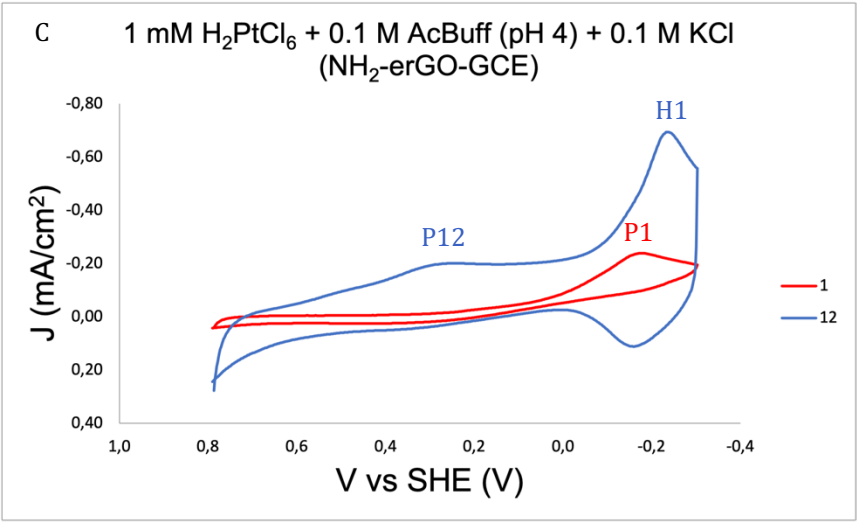


Figure 75. First and twelfth cyclic voltammograms of a saturated argon solution containing 1 mM H_2PtCl_6 in 0.1 M KCl in 0.1 M Acetate buffer (pH 4) and recorded on: (A) glassy carbon electrode, GCE; (B) glassy carbon electrode modified with electrically reduced graphene oxide, erGO-GCE; (C) glassy carbon electrode modified with electrically reduced graphene oxide, NH_2-erGO-GCE. Scan rate: 50 mV/s.

This hypothesis was confirmed by investigating the dependence of the P1 peak on the scan rate. The waves in Figure 73 show the shift towards a higher potential of the P1 peak with decreasing scan rate, indicating that the formation of platinum nanoparticles is irreversible. Furthermore, the peak current decreased with decreasing scan rate. A plot of the peak current as a function of the square root of the scan rate is also present in Figure 76. A linear relationship between the peak current and the square root of the scan rate was clearly observed, indicating that the platinum reduction reaction is diffusion-limited.

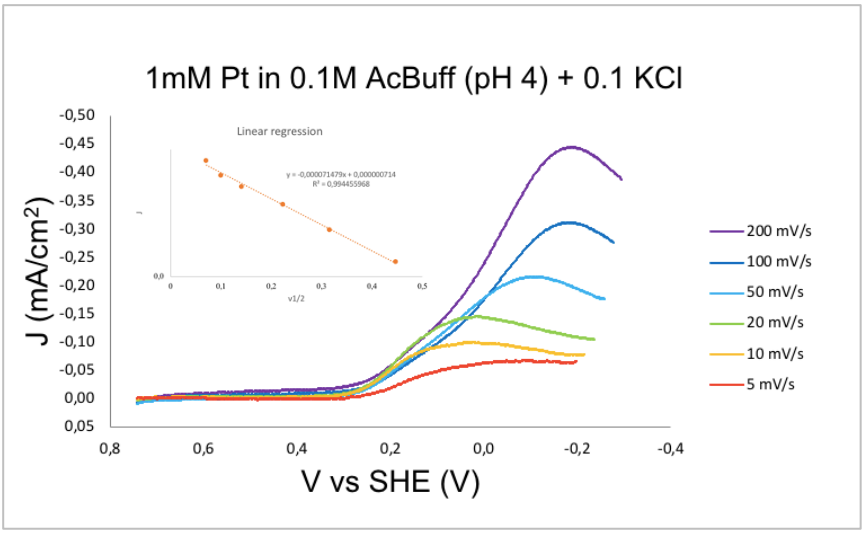


Figure 76. Cyclic voltammograms of the first cathodic scan of a glassy carbon electrode immersed in an argon-saturated solution of 1 mM H_2PtCl_6 in 0.1 M acetate buffer (pH 4) and 0.1 M KCl, collected at various scan rates (5-10-20-50-100-200 mV/s, respectively) and plot of the peak current (ip) as a function of the square root of the scan rate ($\nu^{1/2}$).

The anchoring of platinum particles on the different electrodes is followed by the evaluation of the electrically active surface area using the Randles-Sevcik equation[221] in Equation 50. The scan plots are reported in Figure 77, 78, and 79.

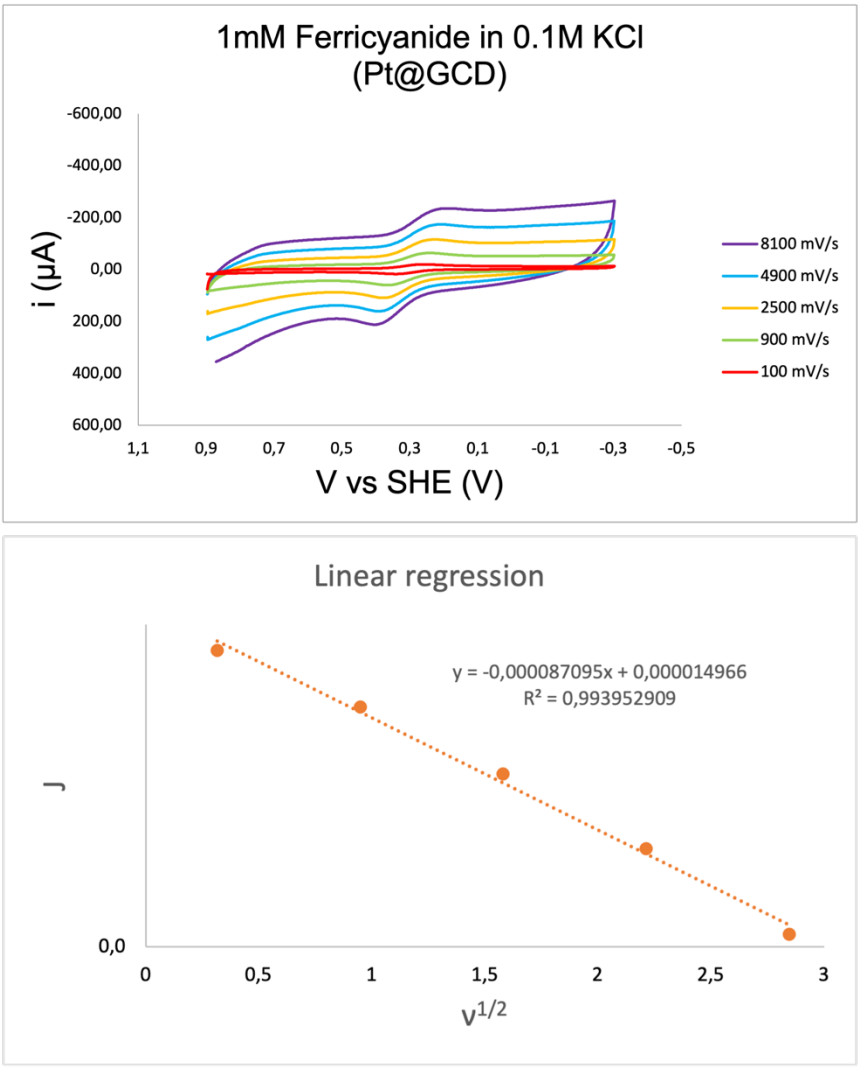


Figure 77. Cyclic voltammograms recorded on platinum nanoparticles anchored on a glassy carbon electrode (3 mm ∅). The scan started with the cathodic curve from +0.7 V to −0.5 V vs Ag/AgCl (Sat'd KCl); scan rates 100-900-2500-4900-8100 mV/s in saturated argon solution of 1 mM potassium ferricyanide and 0.1 M KCl.

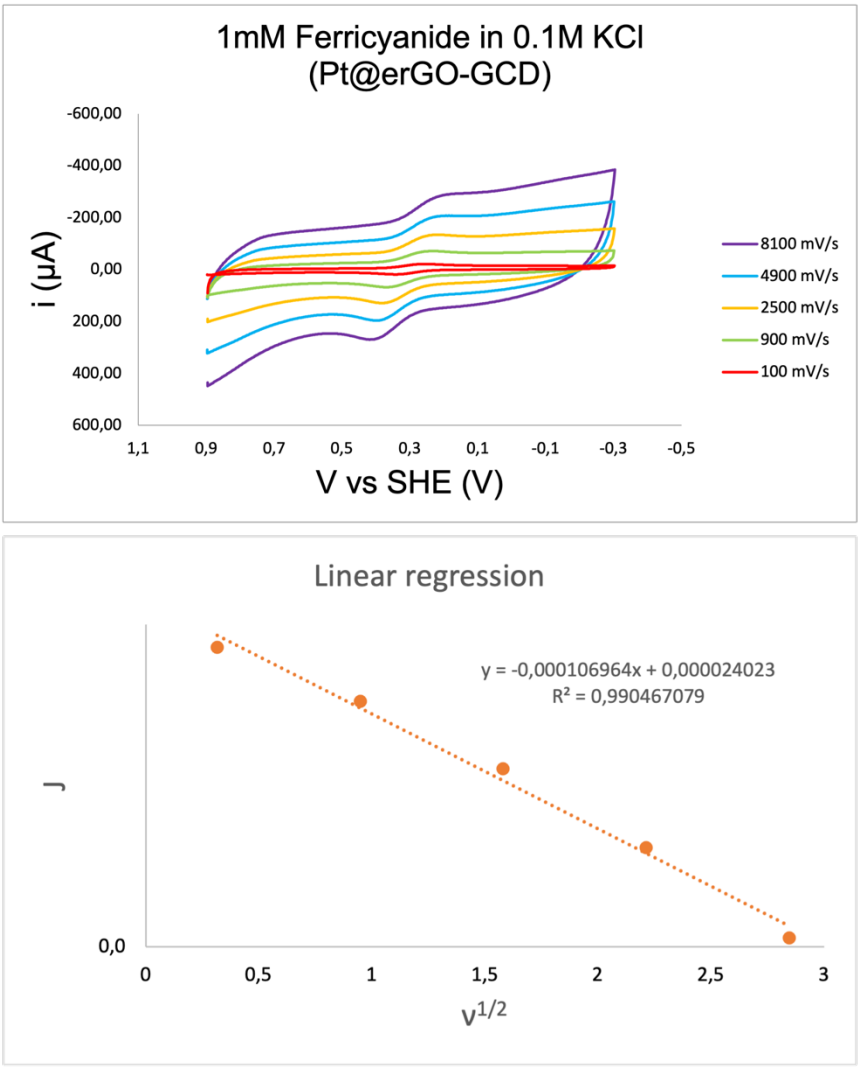
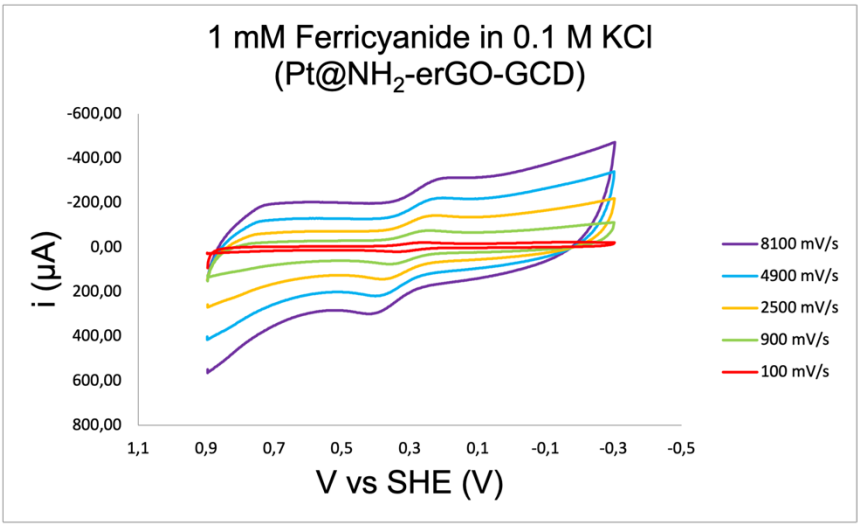


Figure 78. Cyclic voltammograms recorded on a glassy carbon electrode (3 mm Ø) modified with platinum nanoparticles anchored on erGO-GCD. The scan started with the cathodic curve from +0.7 V to −0.5 V vs Ag/AgCl (Sat'd KCl); scan rates 100-900-2500-4900-8100 mV/s in saturated argon solution of 1 mM potassium ferricyanide and 0.1 M KCl.



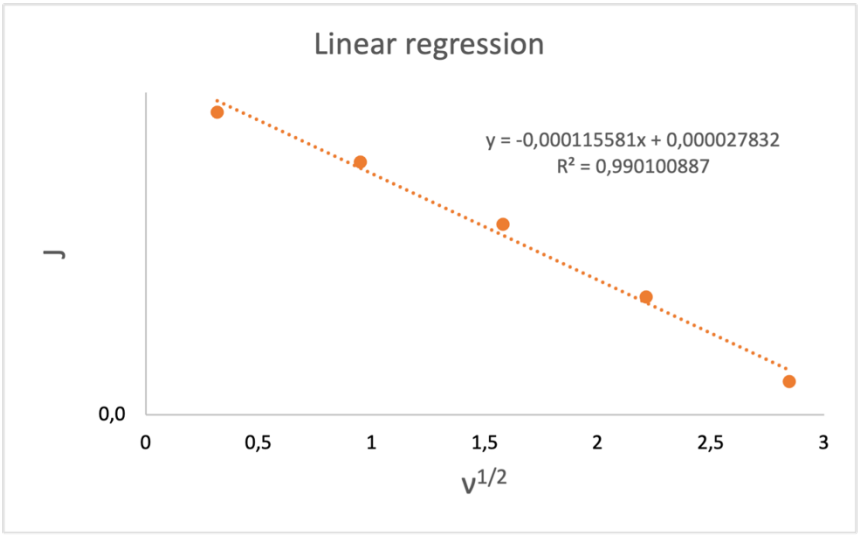


Figure 79. Cyclic voltammograms recorded on a glassy carbon electrode (3 mm ∅) modified with platinum nanoparticles anchored on NH_2-erGO-GCD. The scan started with the cathodic curve from +0.7 V to −0.5 V vs Ag/AgCl (Sat'd KCl); scan rates 100-900-2500-4900-8100 mV/s in saturated argon solution of 1 mM potassium ferricyanide and 0.1 M KCl.

The electrochemically active surface areas obtained are reported in Table 12.

Table 12. Values of the electrochemically active surface areas evaluated on the different samples.

#	Sample	ECSA
1	Bare glassy carbon electrode (GCE)	0.065 cm^2
2	Pt on GCE	0.114 cm^2
3	Pt on erGO-GCE	0.147 cm^2
4	Pt on NH_2-erGO-GCE	0.159 cm^2

In line with expectations, compared to sample 1, sample 2 has a larger surface area due to the presence of platinum nanoparticles. The reduced graphene oxide support is added to sample 3, which is assumed to facilitate the anchoring of the nanoparticles and limit their migration and coalescence, a phenomenon even more evident in sample 4 in which the *p*-aminophenyl groups were added.

3.6.4 *Conclusions*

The deposition of platinum particles on the bare electrode occurs through the electrochemical reduction of platinum in the oxidation state (Pt^{4+}) to metallic platinum (Pt^0). As the process progresses, the platinum reduction peak appears at lower and lower potentials, indicating that platinum is being progressively reduced on the electrode surface, forming metallic nanoparticles. During the deposition process, the hydrogen absorption peak becomes more and more evident. This phenomenon suggests that platinum particles are creating more active sites on the electrode surface, which can interact with hydrogen. These active sites are crucial for catalytic applications, as they are responsible for adhesion and reaction with reagents, such as hydrogen in hydrogen evolution reactions (HER).

The linear dependence on the square root of the scan rate was evaluated. The fact that the peak platinum reduction current shows a linear

dependence on the square root of the scan rate suggests that the platinum nanoparticle deposition process is diffusive (limited by the diffusion of Pt^{4+} ions towards the electrode). This feature indicates that the deposition process is irreversible, with the nanoparticles stably anchoring on the electrode surface, without an easy return to their oxidized state. The use of graphene supports such as reduced graphene oxide (erGO) and reduced graphene oxide modified with *p*-aminophenyl groups (NH_2-erGO) significantly improves the electrochemical properties of the catalyst. Graphene supports increase the available electrically active surface, improving the interaction capacity between the catalyst (Pt) and the reagents. Furthermore, functional groups such as aminophenyls on the surface of reduced graphene oxide can promote greater stability and better control over the migration and coalescence processes of platinum nanoparticles. In other words, these supports help prevent the aggregation of platinum particles, maintaining their catalytic activity.

The use of graphene supports not only increases the active surface area but could also improve the electronic conductivity and long-term stability of the platinum catalyst. This is particularly important in electrochemical reactions such as the hydrogen evolution reaction (HER) or other catalysis applications, where the lifetime and performance of the catalyst are crucial. This experimental approach highlights the importance of the interaction between platinum and graphene supports, as well as the control over the size of the nanoparticles and their distribution on the electrode surface. The result is a more active and stable catalyst, ideal for electrochemical reactions where platinum plays a crucial role.

3.7 Electrochemical deposition of the trimetallic nanocomposite

3.7.1 *Introduction*

The aim of this study is to deposit the three metals as nanoparticles on graphene oxide, based on the data obtained in the paragraph 3.5 of this section. I therefore proceeded to deposit a layer of iron nanoparticles at a fixed potential of −1.2 V, followed by the simultaneous deposition of Pt and Cu nanoparticles at a fixed potential of −0.4 V.

In addition to the electrochemical experiments, it was deemed necessary to develop a strategy that would allow us to analyze the samples using advanced techniques, such as Raman spectroscopy and atomic force microscopy (AFM). Considering the practical impossibility of directly analyzing the working electrode in this experiment, we opted for an alternative solution: the electrodeposition of the composites on removable nickel plates.

Nickel was chosen for its excellent electrical conductivity properties, but also for its ductility, which allows it to be easily shaped. In particular, nickel is malleable enough to be bent around a copper wire, which is then connected to the potentiostat to ensure the correct current flow during the experiment. Thanks to this strategy, it was possible to obtain nickel plates treated in an appropriate way for the analysis. The platelets were analyzed using Raman spectroscopy and AFM microscopy techniques, thus providing valuable data on the structure and properties of the deposited composites.

3.7.2 *Materials and methods*

For the preparation of the working electrode, 99.6% pure nickel plates (0.15 x 6 x 50 mm) were used. All electrochemical experiments were performed with a Gamry Reference 3000 potentiostat and a standard three-electrode system, in which a glassy carbon electrode (3 mm ∅) or Ni-Cu wire are used as the working electrode, an Ag/AgCl (saturated KCl) reference electrode and a carbon rod (5 mm ∅) as the counter electrode. Potentials in aqueous solutions are referenced to the standard hydrogen electrode (SHE) using the

standard conversion of +0.197 V from the Ag/AgCl (saturated KCl) electrode potential.

Raman spectroscopy was performed using a Horiba LabRAM Plus Raman spectrometer. A sample area of 1600 μm^2 was scanned using the spectrometer's Swift mode, with an acquisition time of 1 second and 1 accumulation per point and further, to minimize thermal effects on the sample, the laser power was set to 10% of its maximum output, as commonly reported in the literature. The analysis employed a 50× objective lens and a grating with a resolution of 1800 lines/mm. Raman far point spectra were subsequently acquired with an acquisition time of 10 seconds and 10 accumulations. For this phase of the analysis, the laser power was further reduced to 1% to avoid heating and degradation of the sample.

The Multimode 8 AFM atomic force microscope (Bruker, Billerica, Massachusetts, US) was used to determine the morphology of the produced nanoparticles. The analysis was performed using the Nanoscope V controller in ScanAsyst in Air mode using SCANASYST-AIR silicon tips; these have a cantilever resonance frequency of 70 kHz, a nominal spring constant of 0.4 N/m and a curvature radius of 8 nm. Data processing was performed using Nanoscope Analysis 1.8 software.

3.7.3 *Discussion and characterization*

Figure 80 depicts a typical electrodeposition of Pt nanoparticles on bare glassy carbon electrode. 0.1 M acetate buffer pH 4 was used as electrolyte and proton source, while 0.1 M KCl was used as supporting electrolyte. In the cathodic scan a signal is shown around –0.13 V related to the adsorption of H* on the Pt surface and a consecutive hydrogen evolution occurs right after. The desorption peak is visible in the anodic scan. The change in the slope of the current in the water reduction zone change suggests that new Pt nanoparticles are added to the electrode surface in each cycle.

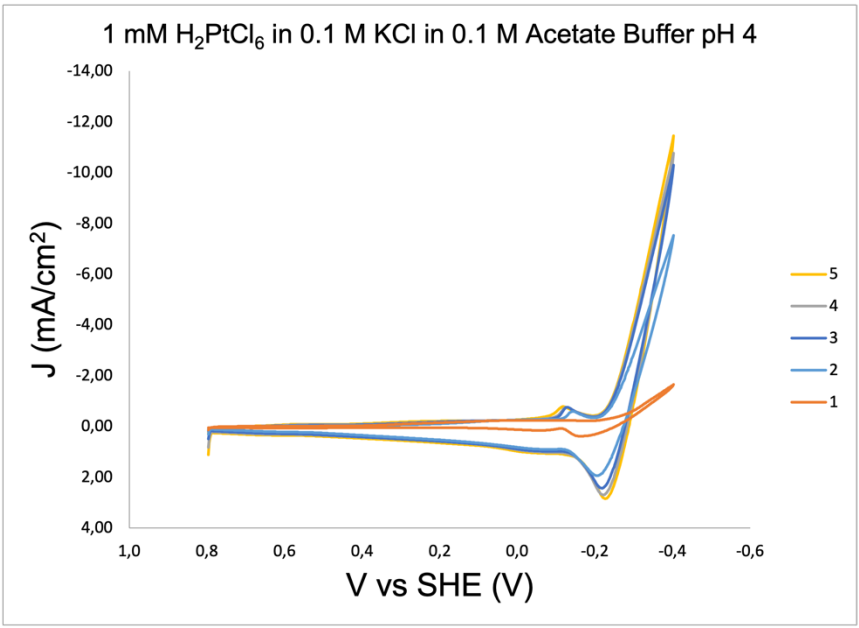


Figure 80. Cyclic voltammograms recorded on a bare glassy carbon electrode (3 mm ∅) soaked in saturated argon solution of 1 mM H_2PtCl_6 in 0.1 M KCl in 0.1 M acetate buffer (pH 4) bath. The scans started with the cathodic curve from +0.6 V to −0.6 V vs Ag/AgCl (Sat'd KCl); scan rates 50 mV/s.

A similar experiment was done on a glassy carbon electrode on which iron nanoparticles were previously electrodeposited. According to experiments in section 3.5, Fe was deposited on GCE through chronoamperometry, applying a constant potential of –1.2 V vs Ag/AgCl (Sat'd KCl) for 60 seconds. The modified electrode was then soaked in a platinum and copper bath containing 1 mM H_2PtCl_6 and 5 mM $CuSO_4$ in 0.1 M KCl in 0.1 M acetate buffer pH 4. Five consecutive cyclic voltammograms were recorded (Figure 81). It is possible to observe the oxidation peak of Cu^+/Cu^0 tends to reduce significantly. This behavior has been attributed to the formation of the alloy between copper and platinum: the simultaneous deposition of the two metals forms a more stable structure on the electrode surface compared to the single metal. In the cathodic curve (negative scan) it is possible to note how the two reduction peaks of the first cycle move towards more positive

potentials up to the fifth cycle. In the anodic curve (positive scan) it is possible to observe the oxidation peak of Cu^0 to Cu^+ tends to reduce significantly. This behavior has been attributed to the formation of the alloy between copper and platinum: the simultaneous deposition of the two metals forms a more stable structure on the electrode surface compared to the single metal. It is also noteworthy that from the third voltammogram cycle the current density developed is clearly greater by about 10 mA/cm^2.

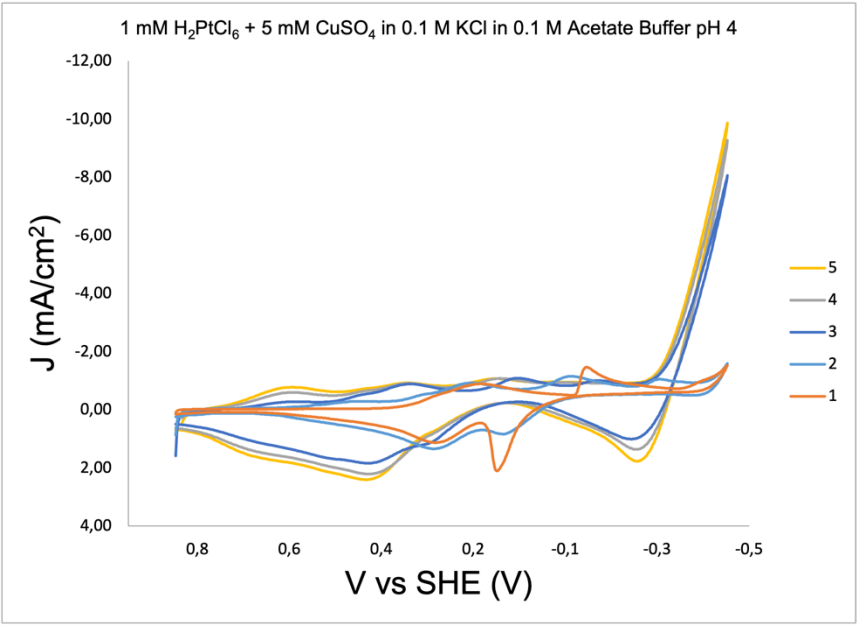


Figure 81. Cyclic voltammograms recorded on a bare glassy carbon electrode (3 mm ∅) soaked in saturated argon solution of 1 mM H_2PtCl_6 + 5 mM $CuSO_4$ in 0.1 M KCl in 0.1 M acetate buffer (pH 4) bath. The scans started with the cathodic curve from +0.6 V to −0.6 V vs Ag/AgCl (Sat'd KCl); scan rates 50 mV/s.

Since the reduction potential of Fe is more negative than that of HER, the idea of electrochemical co-reduction of the three metals was discarded. Therefore, I proceeded to coat the electrode surface with a layer of Fe nanoparticles on which Pt and Cu particles were co-deposited simultaneously. For a data comparison, Figure 82 shows the cyclovoltammograms obtained in a scanning window from 0.6 to –0.52 V vs

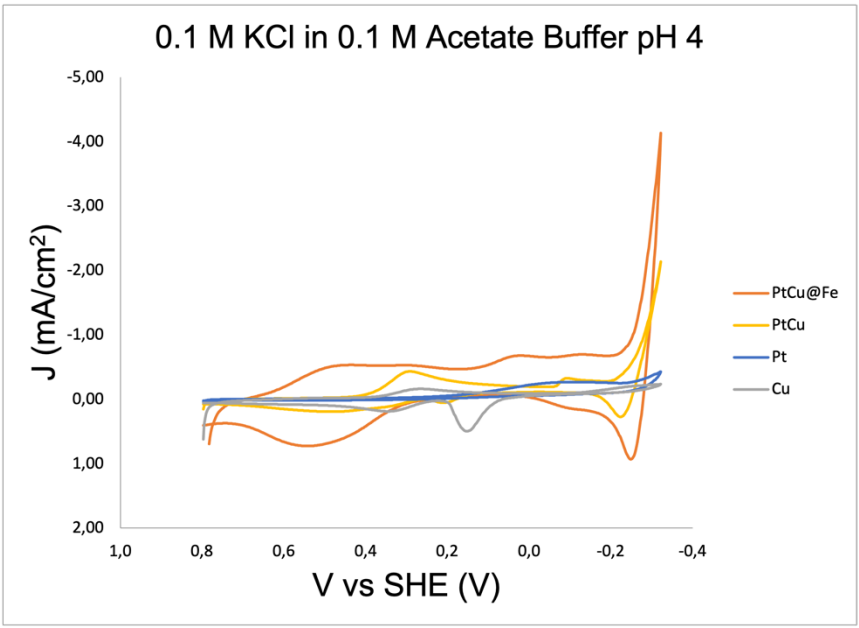


Figure 82. Cyclic voltammograms recorded on a bare glassy carbon electrode (3 mm Ø) soaked in saturated argon solution of 0.1 M KCl in 0.1 M acetate buffer (pH 4) of: 1 mM $H_2PtCl_6 \cdot 6H_2O$ (blue line), 1mM $CuSO_4 \cdot 5H_2O$ (gray line), 1 mM $H_2PtCl_6 \cdot 6H_2O$ and 1mM $CuSO_4 \cdot 5H_2O$ (yellow line), and a cyclic voltammogram recorded on a bare glassy carbon electrode coated with Fe nanoparticles, soaked in saturated argon solution of 0.1 M KCl in 0.1 M acetate buffer (pH 4) of 1 mM $H_2PtCl_6 \cdot 6H_2O$ and 1mM $CuSO_4 \cdot 5H_2O$ (orange line). The scans started with the cathodic curve from +0.6 V to −0.52 V vs Ag/AgCl (Sat'd KCl); scan rates 50 mV/s.

Ag/AgCl (Sat'd KCl) of the Cu deposition on bare GCE, of the Pt deposition on bare GCE, of the co-deposition of both metals on bare GCE, and finally of the co-deposition of both metals on the GCE coated with Fe nanoparticle.

It can be noted that in the curve relating to the deposition of Pt and Cu on Fe (orange line) both the current peaks in the cathodic and anodic direction appear broader, due to the involvement of more species in the redox reactions. It could be hypothesized that the presence of iron nanoparticle nuclei on the electrode facilitates the agglomeration of the other metals. The increased current density with a lower slope during water catalysis confirms the synergism between the particles of different nature.

To prepare the working electrode, nickel plates were bent around a copper wire (Figure 83). This strategy was necessary in order to remove the plates after the electrodeposition of the materials for analysis. The plates were first polished with 0.25-micron diamond powder. For the deposition of the graphene substrates, erGO and NH_2-erGO, 0.5 mg/mL suspensions were prepared and sonicated for 1 hour. 20 µL of each suspension were deposited on one half of a nickel plate and dried in an oven. The other edge of the plate was bent onto the copper wire. Half of the plate was immersed in a 0.1 M KCl solution on which a chronoamperometry was performed at a fixed potential of –1.5 V for 300 seconds, for each graphene supports (Figure 84 and 85). Subsequently, iron was deposited by electrodepositing from a 1 mM $FeSO_4$ solution in 0.1 M KCl in 0.1 M acetate buffer (pH 4) and for 60 seconds. Finally, on the resulting plate, platinum and copper nanoparticles were co-deposited from a 1 mM Pt and 1 mM Cu solution at a fixed potential of –0.4 V for 60 seconds. A similar process was followed to obtain Pt monometallic (Pt@erGO-Ni-Cu and Pt@NH_2-erGO-Ni-Cu) and bimetallic (PtCu@erGO-Ni-Cu and PtCu@NH_2-erGO-Ni-Cu) samples.

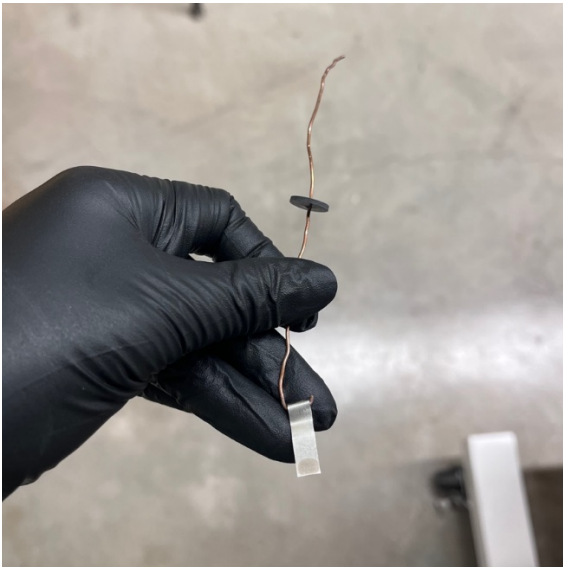


Figure 83. The Ni-Cu wire used as working electrode.

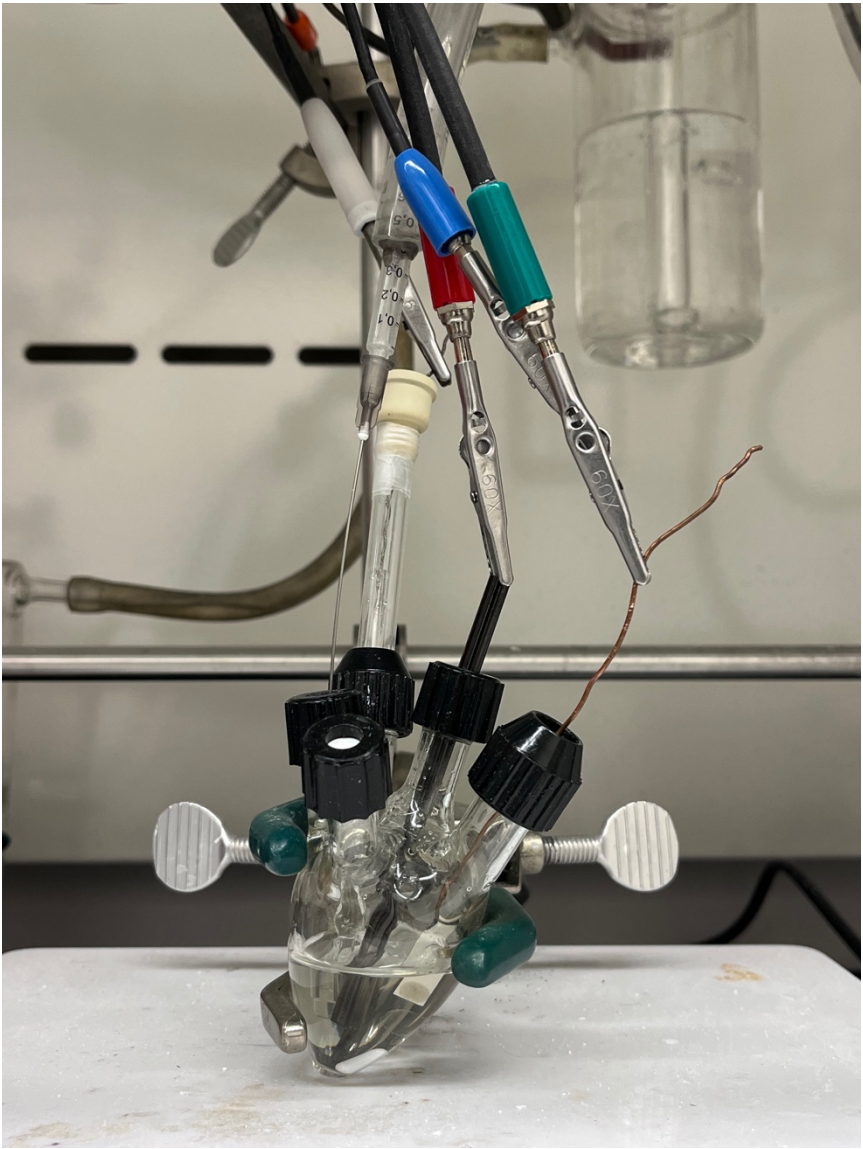


Figure 84. Three-electrode setup using Ni-Cu wire as working electrode.



Figure 85. Electrodeposition of the graphitic supports on the Ni plate at −1.5 V.

Raman spectroscopy is an essential technique for studying graphene derivatives, as these materials exhibit a distinctive fingerprint characterized by two broad peaks. The D peak, which signals the presence of defects such as vacancies and sp^3 carbon atoms, originates from transverse optical (TO) phonon modes near the K points in the Brillouin zone. The G peak, on the other hand, is associated with the doubly degenerate E_2g phonon mode, representing a C=C stretching vibration.[222] Another important Raman feature for assessing the oxidation state of graphene derivatives is the relationship between the full width at half-maximum (FWHM) of the D peak and the reduction degree of graphene oxide (GO). Additionally, the I_D/I_G ratio, representing the intensity ratio between the D and G peaks, provides insights into the number of defects in the graphene lattice.[223] Lee et al. demonstrated a correlation between the I_{D^*}/I_G ratio and the oxidation state of a sample, using XPS spectra to track changes with temperature. The D* peak, located around 1150 cm^{-1}, is attributed to residual oxygen-containing groups.[224] The I_D/I_G ratio is reported in Table 13.

Table 13. I_D/I_G ratio and the relative D peak Full Widht at half maximum (FWHM).

Sample	I_D/I_G	W (FWHM)
GO	1.11	110.92 cm^{-1}
erGO	1.25	84.67 cm^{-1}
NH_2-erGO	0.81	110.23 cm^{-1}
Pt@erGO	1.23	83.43 cm^{-1}
PtCu@erGO	1.19	94.87 cm^{-1}
PtCuFe@erGO	1.06	86.14 cm^{-1}
Pt@NH_2-erGO	0.61	107.15 cm^{-1}

The analysis of the I_D/I_G ratios and D peak FWHM for various samples suggests significant structural changes due to electrodeposition. A higher I_D/I_G ratio typically indicates an increase in defects or disruptions in the

graphene lattice. Raman mapping images are shown in Figures 86, 87, 88, 89 and 90. Most samples exhibit an increase in defects, which is reflected by elevated I_D/I_G ratios. This is particularly evident in the samples erGO, PtCu@erGO, and Pt@erGO, where the I_D/I_G ratios are higher compared to others, suggesting that electrodeposition tends to introduce more lattice defects in these materials.

However, the sample Pt@NH_2-erGO stands out with a notably lower I_D/I_G ratio, which could suggest fewer defects or possibly a more stable lattice structure after electrodeposition. This sample may have undergone a different structural modification compared to the others, leading to reduced defects.

The narrowing of the D peak FWHM in some samples, particularly erGO, Pt@erGO, and PtCu@erGO, further supports the idea of structural improvement with reduced defect density in these materials. A narrower FWHM indicates less broadening of the D peak, suggesting fewer defects and a more ordered structure. Conversely, the wider FWHM observed in samples like GO and NH_2-erGO correlates with higher defect levels.

In contrast, the PtCuFe@erGO sample could not be analyzed, limiting our ability to draw further conclusions about its structural characteristics. Further analysis of this sample is required to understand its structural behavior fully.

In summary, while electrodeposition generally leads to more defects in the lattice structure (as indicated by higher I_D/I_G ratios), certain samples, such as Pt@NH_2-erGO, show a unique behavior with fewer defects. The relationship between defect density and peak characteristics provides valuable insight into the materials' structural evolution during electrodeposition, helping to guide future material optimization strategies.

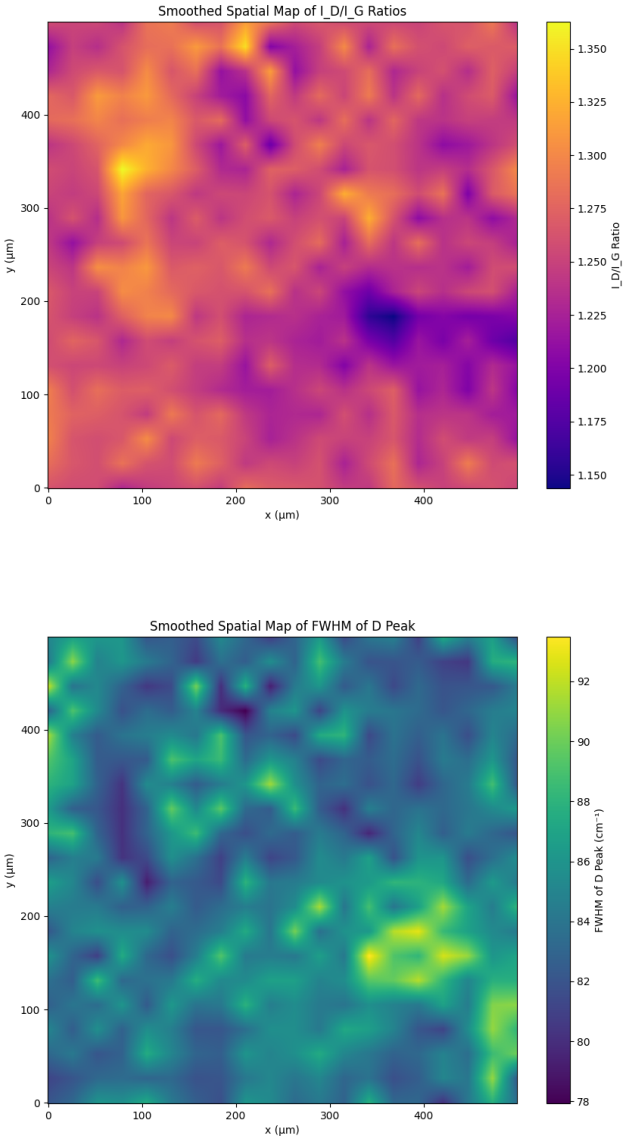


Figure 86. Raman mapping of erGO. (A) ID/IG ratio and (B) D band width.

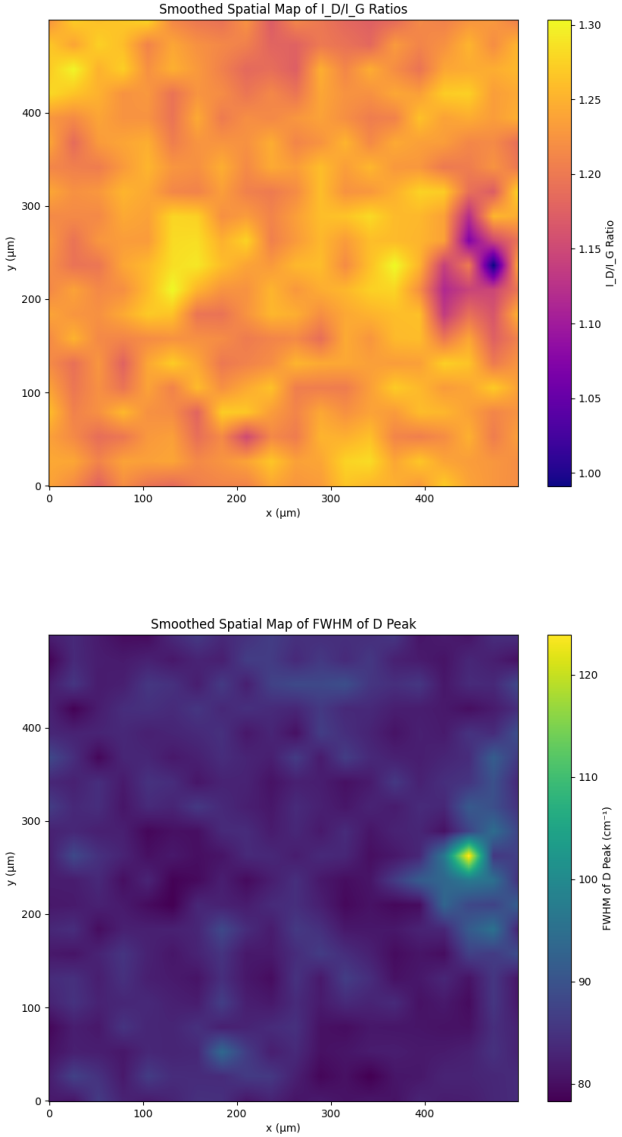


Figure 87. Raman mapping of Pt@erGO. (A) ID/IG ratio and (B) D band width.

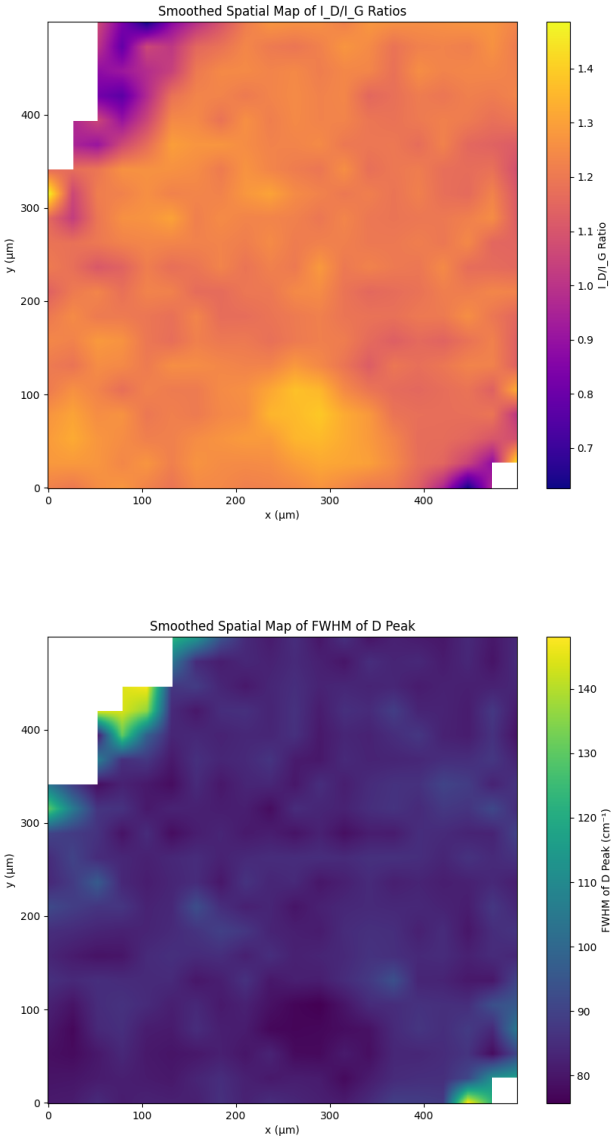


Figure 88. Raman mapping of PtCu@erGO. (A) ID/IG ratio and (B) D band width. Blank spots correspond to areas with no relevant sample (the same applies hereafter).

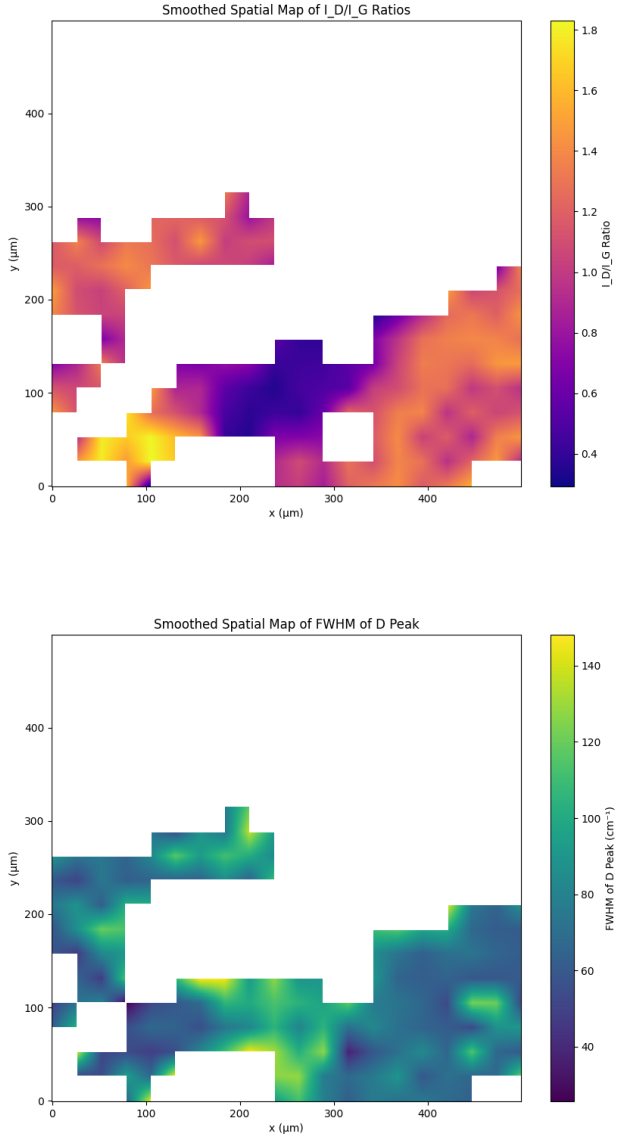


Figure 89. Raman mapping of PtCuFe@erGO. (A) ID/IG ratio and (B) D band width.

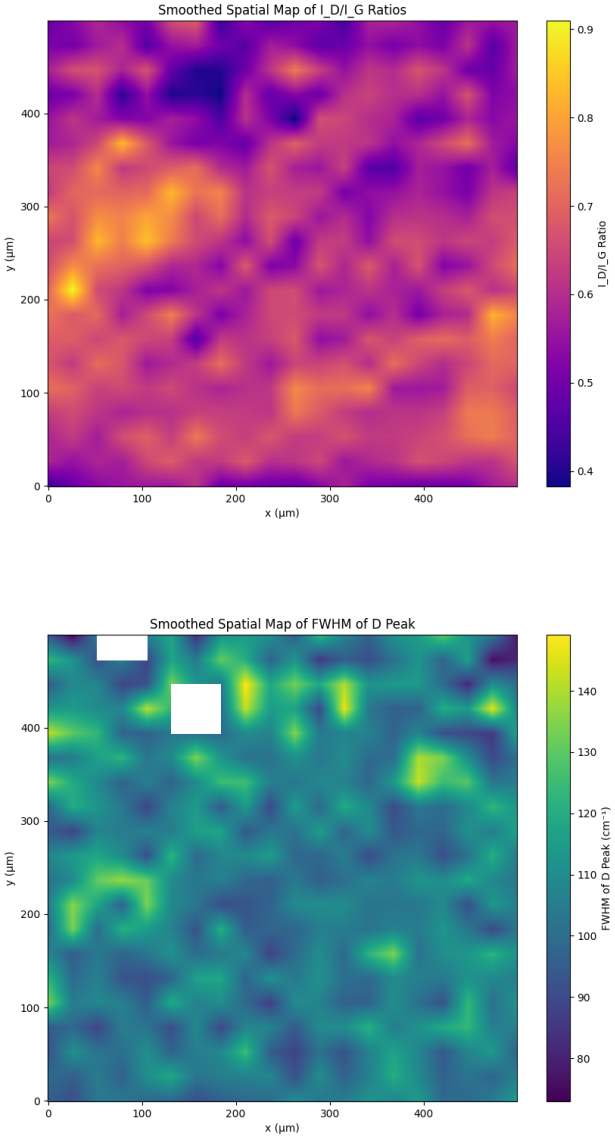


Figure 90. Raman mapping of Pt@NH_2-erGO. (A) ID/IG ratio and (B) D band width.

Raman mapping analysis of the samples reveals intriguing patterns related to the reduction and defect distribution within the graphene-based materials. For most of the samples, a strong correlation emerges between regions exhibiting a lower I_D/I_G ratio and a broadening of the D peak. This observation suggests that these areas have undergone less reduction and are associated with fewer defects. Conversely, regions with a narrower D peak and an increased I_D/I_G ratio indicate a higher degree of reduction, typically accompanied by a higher defect density. These trends underline the primary effect of electroreduction, which is characterized by the narrowing of the D peak and a corresponding increase in the I_D/I_G ratio, signifying enhanced reduction.

Interestingly, the NH_2-erGO sample exhibits a distinct behavior compared to the other samples. Despite showing a reduced oxidation degree, there is evidence of defect healing in the material. This anomaly might be attributed to the functionalization introduced by the amino groups, which could facilitate local structural rearrangements or chemical interactions that mitigate defect formation. Further investigation is required to confirm this hypothesis and to elucidate the precise mechanisms driving this unique behavior.

AFM analyses were performed to establish the PtCu nanoparticles size on bare nickel plate, PtCu@Ni-Cu_{wire} (Figure 91), erGO on nickel plate, PtCu@erGO-Ni-Cu_{wire} (Figure 92), and NH_2-erGO on nickel plate, PtCu@NH_2-erGO-Ni-Cu_{wire} (Figure 93). The PtCu@Ni-Cu_{wire} sample, in the absence of graphene support, shows nanoparticles of irregular size without an ordered deposition on the plate. From the results obtained the presence of the erGO support is essential for the anchoring of the PtCu nanoparticles. In fact, the PtCu@erGO-Ni-Cu_{wire} sample appears homogeneously covered with cluster-shaped nanoparticles with an average size of 30 nm. The distance of the nanoparticles is more regular than the PtCu@Ni-Cu_{wire} sample. The data obtained for the PtCu@NH_2-erGO-Ni-Cuwire sample, however, are not in line with expectations: the analyzed sample shows areas of very low concentration of nanoparticles and areas of high agglomeration of metals.

This result was attributed to the high concentration of electrodeposited support on the surface of the nickel plate, a characteristic that is instead optimal for a good Raman analysis.

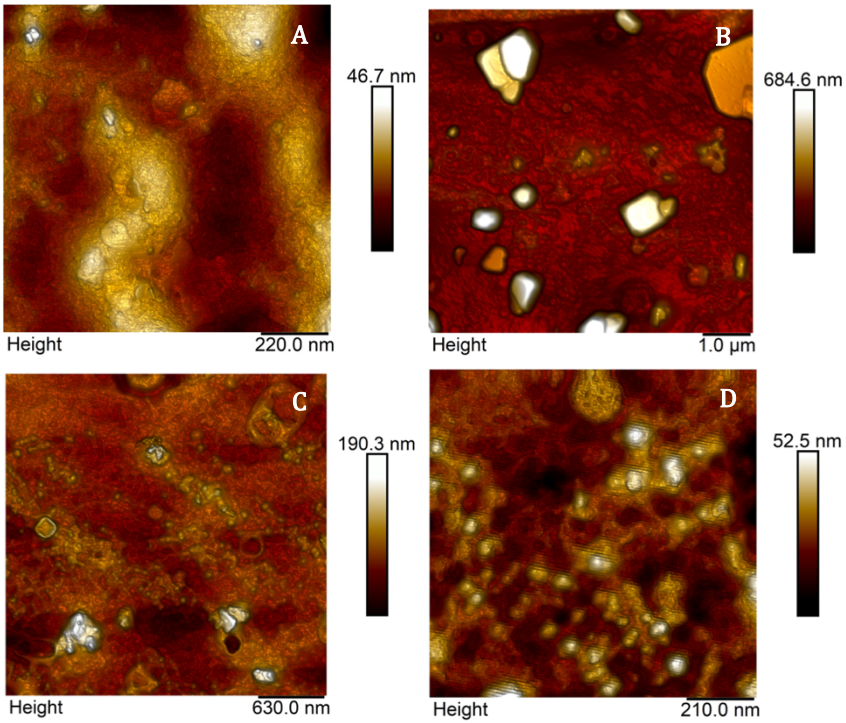


Figure 91. Atomic force microscope (AFM) images of (A) bare nickel plate and (B, C, D) PtCu nanoparticles on nickel plate.

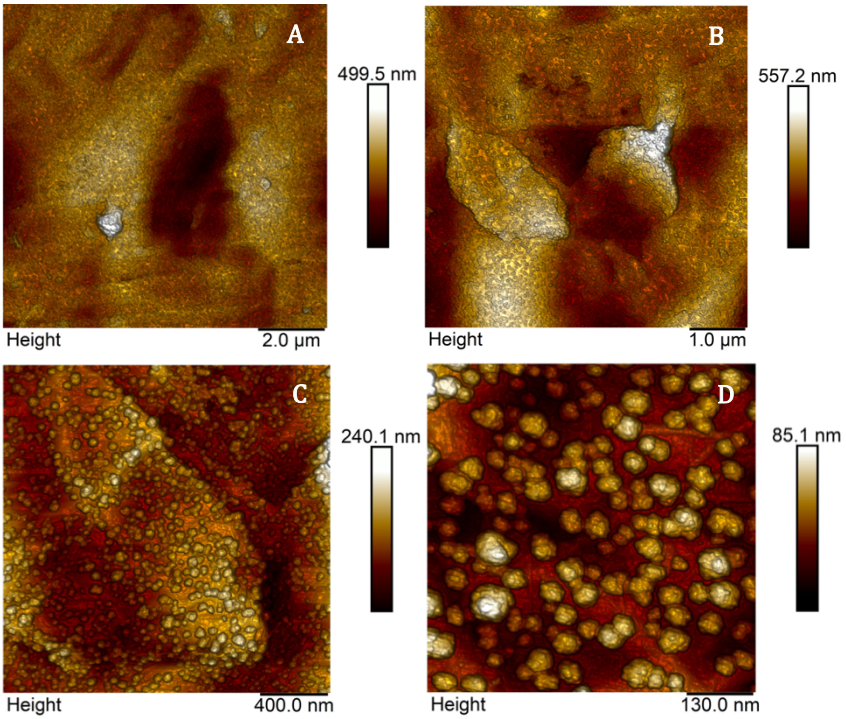


Figure 92. Atomic force microscope (AFM) images of (A, B, C, D) of PtCu@erGO nanoparticles on nickel plate.

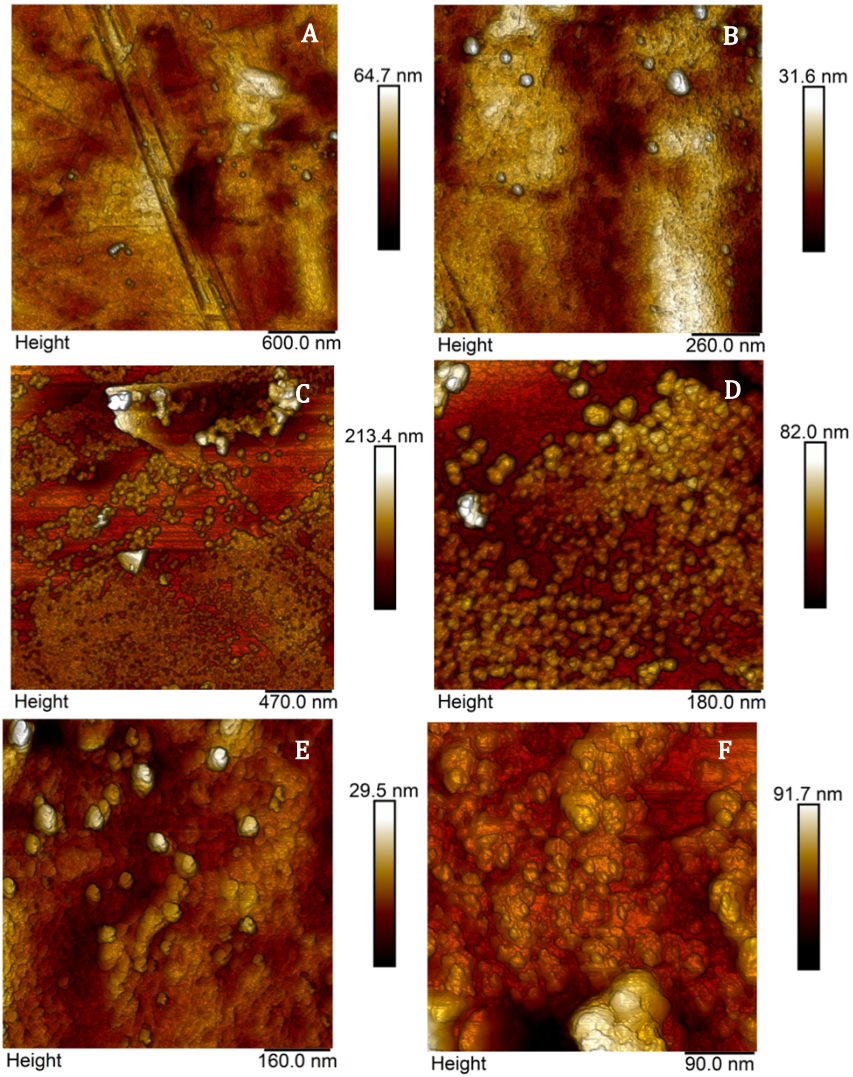


Figure 93. Atomic force microscope (AFM) images of (A, B, C, D, E, F) PtCu@NH_2-erGO nanoparticles on nickel plate.

3.7.4 *Conclusions*

Electrodeposition of metal nanoparticles on graphene supports has proven to be a rapid and eco-friendly method for the synthesis of nanocatalysts for the hydrogen evolution reaction (HER). In particular, the co-electrodeposition of platinum (Pt) and copper (Cu) on iron nanoparticles was successfully performed, leading to an improvement in the catalytic performance compared to the use of single metals, confirming the effectiveness of this combination in terms of catalytic activity.

Raman analyses of the samples revealed peaks indicating the degree of defects present in the graphene support, thus providing a confirmation of the structural modification occurred during the electrodeposition process. These results are significant, as they suggest that the presence of defects in graphene may favor the growth and dispersion of metal nanoparticles, improving the reactivity of the material for HER.

However, despite the progress, the concentration at which the samples were prepared was not suitable for a correct AFM analysis on the NH_2-erGO sample. This limited the ability to obtain detailed information on the morphology and distribution of the nanoparticles, a crucial aspect to fully understand the behavior of the material at the nanometric level.

The results obtained suggest that it is necessary to revise the initial concentrations of graphene material and metal precursors, as well as to reduce the electrodeposition times. These adjustments would allow a more accurate control over the particle growth and the final properties of the material, paving the way for possible improvements in the performance of nanocatalysts for HER.

3.8 References

171. Shen, J. *et al.* Liquid Phase Exfoliation of Two-Dimensional Materials by Directly Probing and Matching Surface Tension Components. *Nano Lett* 15, 5449–5454 (2015).
172. Khan, U., O'Neill, A., Lotya, M., De, S. & Coleman, J. N. High-Concentration Solvent Exfoliation of Graphene. *Small* 6, 864–871 (2010).
173. Khan, U., O'Neill, A., Lotya, M., De, S. & Coleman, J. N. High-Concentration Solvent Exfoliation of Graphene. *Small* 6, 864–871 (2010).
174. Novoselov, K. S. *et al.* Electric Field Effect in Atomically Thin Carbon Films. *Science (1979)* 306, 666–669 (2004).
175. Bolotin, K. I. *et al.* Ultrahigh electron mobility in suspended graphene. *Solid State Commun* 146, 351–355 (2008).
176. Morozov, S. V. *et al.* Giant Intrinsic Carrier Mobilities in Graphene and Its Bilayer. *Phys Rev Lett* 100, 016602 (2008).
177. Eda, G., Mattevi, C., Yamaguchi, H., Kim, H. & Chhowalla, M. Insulator to Semimetal Transition in Graphene Oxide. *The Journal of Physical Chemistry C* 113, 15768–15771 (2009).
178. Sahoo, M., Antony, R. P., Mathews, T., Dash, S. & Tyagi, A. K. Raman studies of chemically and thermally reduced graphene oxide. in 1262–1263 (2013). doi:10.1063/1.4791511.
179. Malard, L. M., Pimenta, M. A., Dresselhaus, G. & Dresselhaus, M. S. Raman spectroscopy in graphene. *Phys Rep* 473, 51–87 (2009).
180. Dzukarnain, M. Z. B., Takami, T., Imai, H. & Ogino, T. Highly conductive, monolayer and large-area reduced graphene oxide films fabricated by electrical connection at the two-dimensional boundaries between the tiled graphene oxide flakes. *Thin Solid Films* 615, 247–255 (2016).
181. Ferrari, A. C. *et al.* Raman Spectrum of Graphene and Graphene Layers. *Phys Rev Lett* 97, 187401 (2006).

182. Roslan, M. S., Chaudary, K. T., Haider, Z., Zin, A. F. M. & Ali, J. Effect of magnetic field on carbon nanotubes and graphene structure synthesized at low pressure via arc discharge process. in 030025 (2017). doi:10.1063/1.4978843.
183. Wang, X., Christopher, J. W. & Swan, A. K. 2D Raman band splitting in graphene: Charge screening and lifting of the K-point Kohn anomaly. *Sci Rep* 7, 13539 (2017).
184. Shin, H. *et al.* Efficient Reduction of Graphite Oxide by Sodium Borohydride and Its Effect on Electrical Conductance. *Adv Funct Mater* 19, 1987–1992 (2009).
185. Sengupta, I., Chakraborty, S., Talukdar, M., Pal, S. K. & Chakraborty, S. Thermal reduction of graphene oxide: How temperature influences purity. *J Mater Res* 33, 4113–4122 (2018).
186. Lee, T., Mas'ud, F. A., Kim, M. J. & Rho, H. Spatially resolved Raman spectroscopy of defects, strains, and strain fluctuations in domain structures of monolayer graphene. *Sci Rep* 7, 16681 (2017).
187. Kudin, K. N. *et al.* Raman Spectra of Graphite Oxide and Functionalized Graphene Sheets. *Nano Lett* 8, 36–41 (2008).
188. Cançado, L. G., Reina, A., Kong, J. & Dresselhaus, M. S. Geometrical approach for the study of G′band in the Raman spectrum of monolayer graphene, bilayer graphene, and bulk graphite. *Phys Rev B* 77, 245408 (2008).
189. Long, N. V. *et al.* The synthesis and characterization of platinum nanoparticles: a method of controlling the size and morphology. *Nanotechnology* 21, 035605 (2010).
190. Cele, T. Preparation of Nanoparticles. in *Engineered Nanomaterials - Health and Safety* (IntechOpen, 2020). doi:10.5772/intechopen.90771.
191. Khan, I., Saeed, K. & Khan, I. Nanoparticles: Properties, applications and toxicities. *Arabian Journal of Chemistry* 12, 908–931 (2019).

192. Banne, S. V., Patil, M. S., Kulkarni, R. M. & Patil, S. J. Synthesis and Characterization of Silver Nano Particles for EDM Applications. *Mater Today Proc* 4, 12054–12060 (2017).
193. Esposito, D. V., Hunt, S. T., Kimmel, Y. C. & Chen, J. G. A New Class of Electrocatalysts for Hydrogen Production from Water Electrolysis: Metal Monolayers Supported on Low-Cost Transition Metal Carbides. *J Am Chem Soc* 134, 3025–3033 (2012).
194. Ahn, H. S. & Bard, A. J. Electrochemical Surface Interrogation of a MoS_2 Hydrogen-Evolving Catalyst: In Situ Determination of the Surface Hydride Coverage and the Hydrogen Evolution Kinetics. *J Phys Chem Lett* 7, 2748–2752 (2016).
195. Bai, S. *et al.* Surface Polarization Matters: Enhancing the Hydrogen-Evolution Reaction by Shrinking Pt Shells in Pt–Pd–Graphene Stack Structures. *Angewandte Chemie International Edition* 53, 12120–12124 (2014).
196. Guo, S., Dong, S. & Wang, E. Pt/Pd bimetallic nanotubes with petal-like surfaces for enhanced catalytic activity and stability towards ethanol electrooxidation. *Energy Environ Sci* 3, 1307 (2010).
197. Safavi, A. & Farjami, F. Electrodeposition of gold–platinum alloy nanoparticles on ionic liquid–chitosan composite film and its application in fabricating an amperometric cholesterol biosensor. *Biosens Bioelectron* 26, 2547–2552 (2011).
198. Kregar, A., Kravos, A. & Katrašnik, T. Methodology for Evaluation of Contributions of Ostwald Ripening and Particle Agglomeration to Growth of Catalyst Particles in PEM Fuel Cells. *Fuel Cells* 20, 487–498 (2020).
199. Rinaldo, S. G. *et al.* Theoretical analysis of electrochemical surface-area loss in supported nanoparticle catalysts. *Phys. Chem. Chem. Phys.* 16, 26876–26886 (2014).
200. Guo, F. *et al.* Recent Advances in Ultralow-Pt-Loading Electrocatalysts for the Efficient Hydrogen Evolution. *Advanced Science* 10, (2023).

201. Liu, L. & Corma, A. Metal Catalysts for Heterogeneous Catalysis: From Single Atoms to Nanoclusters and Nanoparticles. *Chem Rev* 118, 4981–5079 (2018).
202. Xu, H., Shang, H., Wang, C. & Du, Y. Ultrafine Pt-Based Nanowires for Advanced Catalysis. *Adv Funct Mater* 30, (2020).
203. Baldan, A. Review Progress in Ostwald ripening theories and their applications to the γ′-precipitates in nickel-base superalloys Part II Nickel-base superalloys. *J Mater Sci* 37, 2379–2405 (2002).
204. de Bruijn, F. A., Dam, V. A. T. & Janssen, G. J. M. Review: Durability and Degradation Issues of PEM Fuel Cell Components. *Fuel Cells* 8, 3–22 (2008).
205. Thorne, R. J. *et al.* Bubble Evolution and Anode Surface Properties in Aluminium Electrolysis. *J Electrochem Soc* 162, E104–E114 (2015).
206. Vogt, H. The Quantities Affecting the Bubble Coverage of Gas-Evolving Electrodes. *Electrochim Acta* 235, 495–499 (2017).
207. Kiros, Y. & Bursell, M. Low Energy Consumption in Chlor-alkali Cells Using Oxygen Reduction Electrodes. *Int J Electrochem Sci* 3, 444–451 (2008).
208. Lagarteira, T. *et al.* The role of Pt loading on reduced graphene oxide support in the polyol synthesis of catalysts for oxygen reduction reaction. *Int J Hydrogen Energy* 45, 20594–20604 (2020).
209. AL-Gahouari, T. *et al.* Controlling reduction degree of graphene oxide-based electrode for improving the sensing performance toward heavy metal ions. *Applied Physics A* 127, 170 (2021).
210. Punckt, C. *et al.* The effect of degree of reduction on the electrical properties of functionalized graphene sheets. *Appl Phys Lett* 102, (2013).
211. Kaliyaraj Selva Kumar, A., Zhang, Y., Li, D. & Compton, R. G. A mini-review: How reliable is the drop casting technique? *Electrochem commun* 121, 106867 (2020).

212. Gupta, B. *et al.* Role of oxygen functional groups in reduced graphene oxide for lubrication. *Sci Rep* 7, 45030 (2017).
213. Bellunato, A., Arjmandi Tash, H., Cesa, Y. & Schneider, G. F. Chemistry at the Edge of Graphene. *ChemPhysChem* 17, 785–801 (2016).
214. Fei, H. *et al.* Extending MoS2-based materials into the catalysis of non-acidic hydrogen evolution: challenges, progress, and perspectives. *Materials Futures* 2, 022103 (2023).
215. Hussain, N., Saikia, U. & Puzari, P. Creatinine-copper interaction: electrochemical and spectroscopic insight, and an innovative verification of a molecularly imprinted creatinine sensor design. *J Appl Electrochem* (2025) doi:10.1007/s10800-025-02278-1.
216. Mihai, G. V., ROŞOIU Sabrina, Costovici, S., Anicai, L. & Enachescu, M. Synthesis of copper nanowire using water and ionic liquid electrolytes for electrochemical detection. *UPB Scientific Bulletin, Series B: Chemistry and Materials Science.* 81, (2019).
217. Osseo-asare, K., Deelo, M. E. & Weil, K. Electrodeposition of Iron in Aqueous Ferrous Sulfate Solution:Role of Ammonium Ion. *ECS Trans* 2, 293–302 (2006).
218. Shahazi, R. *et al.* Carbon nanomaterials for efficient oxygen and hydrogen evolution reactions in water splitting: A review. *Characterization and Application of Nanomaterials* 7, 8543 (2024).
219. Xin, L. *et al.* Understanding Pt Nanoparticle Anchoring on Graphene Supports through Surface Functionalization. *ACS Catal* 6, 2642–2653 (2016).
220. Yu, H., Zhang, B., Bulin, C., Li, R. & Xing, R. High-efficient Synthesis of Graphene Oxide Based on Improved Hummers Method. *Sci Rep* 6, 36143 (2016).
221. Elgrishi, N. *et al.* A Practical Beginner's Guide to Cyclic Voltammetry. *J Chem Educ* 95, 197–206 (2018).
222. Hong, J. *et al.* Origin of New Broad Raman D and G Peaks in Annealed Graphene. *Sci Rep* 3, 2700 (2013).

223. Ferrari, I. *et al.* Understanding the nature of graphene oxide functional groups by modulation of the electrochemical reduction: A combined experimental and theoretical approach. *Carbon N Y* 203, 29–38 (2023).

224. Lee, A. Y. *et al.* Raman study of D* band in graphene oxide and its correlation with reduction. *Appl Surf Sci* 536, 147990 (2021).

CHAPTER 4

Hydrogen storage

4.1 Overview of the traditional storage methods

Hydrogen storage represents one of the most significant challenges in the development of, for example, fuel cell vehicles (FCVs). This challenge mainly stems from the low energy density of hydrogen, which makes it difficult to store enough fuel on board to ensure adequate autonomy without having to resort to excessively large tanks. To overcome these obstacles, it is essential to develop hydrogen storage systems that are both volumetrically and gravimetrically efficient: the materials used must consequently possess specific characteristics, such as low cost, light weight, excellent adsorption, and desorption capacities, and recyclability.[225]

As depicted in Figure 94, there are currently two main categories of hydrogen storage systems: physical-based and material-based storage.

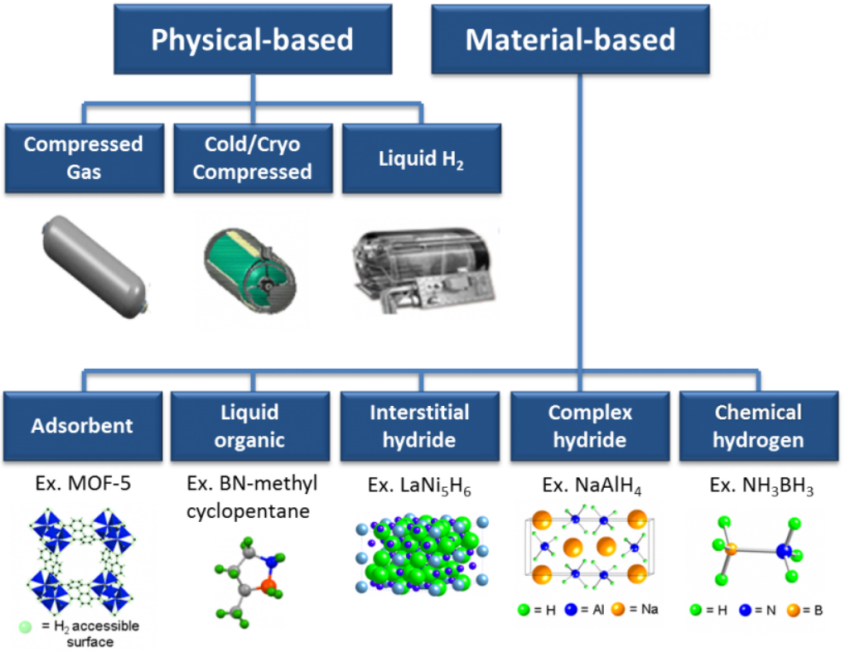


Figure 94. Different hydrogen storage methods.[226]

4.1.1 *Physical-based storage*

Physical storage of hydrogen can be either in the form of a compressed gas or a liquid. High-pressure tanks (350-700 bar) are the most mature and widespread solution for physical hydrogen storage in vehicles, although they still present challenges in terms of gravimetric and volumetric density, as well as cost.

Liquid hydrogen storage, on the other hand, requires cryogenic temperatures, as the boiling point of hydrogen is extremely low, but this solution is less common for automotive applications due to the energy required to maintain such temperatures.

A promising alternative is represented by hydrogen storage materials, which include sorbents, metal hydrides and chemical hydrogen storage materials. These materials can offer higher storage densities at low pressures, but research is still ongoing to overcome challenges related to

adsorption/desorption kinetics, storage capacity, and material regeneration.

Physical Storage of Hydrogen in Compressed Gas

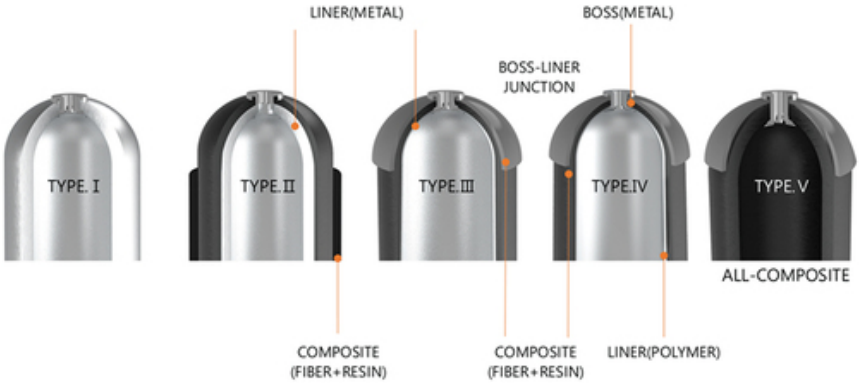


Figure 95. Different types of containers for the physical storage of compressed gaseous hydrogen.[227]

Figure 95 shows the types of containers for the physical storage of compressed hydrogen gas; the choice of container type depends on a trade-off between cost, weight, and operating pressure. While Type I and II containers offer a more economical and robust solution, Type III and IV containers, with their advanced composite materials, significantly reduce weight but at a higher cost. Type V is an emerging innovation that may offer advantages in terms of weight and volume reduction but is currently limited by a low operating pressure.

- Type I: These containers are made entirely of metal, typically steel or aluminum, and are the most common and cost-effective solution. However, they are also the heaviest, weighing approximately 3.0 lb per liter, and can withstand pressures up to 50 MPa.[228]
- Type II: These are steel containers wrapped in a fiberglass composite. This configuration allows for even distribution of structural stress between the steel and the composite, resulting in containers that are

30–40% lighter than Type I containers, yet 50% more expensive. These containers can withstand the highest pressures of all types.[228]

- Type III: These containers consist of a metal liner, usually aluminum, wrapped in a carbon fiber composite. Most of the structural load is carried by the composite frame, with the metal liner acting as a seal and supporting only up to 5% of the mechanical stress. They are effective at operating pressures of 45 MPa but fail aging tests at 70 MPa. They offer a weight of 0.75–1 pound per liter, about half the weight of Type II, but at twice the cost.[227]
- Type IV: Completely composite, with an inner polymer liner (e.g., high-density polyethylene) and a structural shell of carbon fiber or carbon-glass composites. These vessels are the lightest, but also the most expensive, and can handle pressures up to 100 MPa.[227]
- Type V: A pre-commercial innovation is the all-composite vessel without liner, introduced by Composites Technology Development Inc. in 2010. These vessels are 20% smaller than Type IV vessels and operate at a significantly lower pressure of 1.37 MPa, making them less suitable for practical use outside the laboratory due to the reduced pressures.[227]

Liquid/Cryogenic Hydrogen Storage

Hydrogen liquefaction occurs at very low temperatures, around −250 °C, and maintaining hydrogen at these temperatures is the most significant challenge in cryogenic storage. Liquefaction is time-consuming and resource-intensive and can result in a loss of up to 40% of the energy content of the hydrogen, compared to only 10% loss for hydrogen stored under pressure.[229] A cryogenic vessel can carry about 5000 kg of hydrogen, about five times the amount that can be transported with compressed gas tube trailers. In terms of safety, cryogenic vessels have an additional layer of insulation (vacuum jacket) that prevents accidents.[230] At cryogenic temperatures, hydrogen requires little energy for adiabatic expansion, which means that a major explosion will not occur if the vessel leaks or ruptures, until the gas is ignited. The low temperatures of the leaked

hydrogen can cause crippling and failure of nearby valves or pressure relief devices that are not accustomed to operating in such extreme conditions.[231]

Cryo-compressed hydrogen storage

In the cryo-compressed hydrogen storage method, hydrogen reaches a supercritical cryogenic gas state that is compressed to around –233 °C.[232] This method has shown promise in terms of storage density, safety and refueling efficiency: the storage density is high, around 80 g/L, which is around 10 g/L higher than normal cryogenic storage.[232] Advantages also include fast and efficient refueling and a high degree of safety due to the use of a vacuum envelope. This storage process can achieve good results in terms of gravimetric and volumetric capacity of the system and H_2 depletion during latency; however, the cost and supply of facilities remain significant obstacles.[232]

4.1.2 Material-based hydrogen storage

Material-based hydrogen storage is a key research area for the development of sustainable energy technologies. This field focuses mainly on two approaches: chemical adsorption and physical adsorption.

Chemical Adsorption

Chemical adsorption involves breaking hydrogen molecules into atoms that chemically bond to the molecular backbone of a catalyst. Metal hydrides are among the most studied materials for this purpose, offering high storage density.[233] However, the main challenges for chemical adsorption materials include reducing costs, weight, and operating temperature, as well as improving charge-discharge kinetics and minimizing the production of unwanted gases during the desorption process. A promising option in this area are Liquid Organic Hydrogen Carriers (LOHCs), which store hydrogen through reversible chemical bonds, offering simple operation at room temperature and a reduced environmental impact.[234]

Physical Adsorption

Physical adsorption uses porous materials such as Metal-Organic Frameworks (MOFs) and porous carbon structures to store hydrogen at high densities.[235] They are characterized by large surface area and low hydrogen binding energy and allow for rapid charging and discharging. Despite the progress, challenges remain to increase the volumetric and gravimetric hydrogen storage density and improve the operating efficiency at higher temperatures and pressures.

4.1.3 Emerging Technologies

Magnesium-based alloys

Due to their abundance, low cost, light weight, and high hydrogen storage capacity, they are promising materials for use in this field. However, the limited cycle life of Mg-based alloys is a significant obstacle to their practical use. In this regard, various efforts have been made to improve their cyclic stability; an effective approach to improve the corrosion performance of alloy electrodes is the introduction of one or more elements in multicomponent composites. Indeed, a remarkable increase in electrochemical performance was demonstrated with $Mg_{0.80}Ti_{0.15}$, $Al_{0.05}Zr_{0.05}Ni_{0.95}$, reaching a hydrogen storage capacity of 420 mAh/g and 90% capacity retention after 20 cycles, compared to the base MgNi alloy (495 mAh/g and 35% capacity retention after 20 cycles).[236]

Nanostructured metal oxides

These materials have been the subject of increasing interest due to their eco-friendly synthesis. For example, date extract was used to synthesize $Nd_2Sn_2O_7$ nanostructures in a novel and eco-friendly method, observing superior electrochemical hydrogen storage performance of about 14.8 wt% at room temperature due to the easy diffusion through a mesoporous, irregular, and uniform structure.[237] Furthermore, $Pr_2Ce_2O_7$ nanostructures were synthesized using banana extract, and it was found that the presence of a large amount of natural and harmless carbohydrates in banana extract,

such as fructose, sucrose, and glucose, can act as a surfactant and prevent aggregation, leading to the formation of very small and homogeneous $Pr_2Ce_2O_7$ nanoparticles. The discharge capacity achieved was about 9.6 wt% after 20 cycles.[238]

Perovskite oxides

As a class of potentially useful materials for hydrogen storage. These materials, which have a general formula ABX_3, corresponding to the crystalline prototype of $CaTiO_3$, have been explored as hydrogen storage materials over the past decade. In particular, the compounds $MgTiO_3H_x$ and $CaTiO_3H_x$ (where $x = 0$, 3, 6, and 8) were examined, and it was found that only $CaTiO_3H_6$ showed a good hydrogen storage capacity, equal to 4.27 wt%. [239] In addition, the compound $LaCrO_3H_x$ was studied, which showed a hydrogen storage capacity of 1.4 wt% at room temperature and 4% at a moderate temperature of 60 °C.[240] This behavior makes it a promising candidate for future hydrogen storage applications, such as in the transportation sector.

Clathrate hydrates

Clathrate hydrates, which will be discussed in depth in the next chapter, are emerging as a potential hydrogen storage method, gaining global attention due to their technological benefits. Indeed, these compounds offer several advantages:

- they require only minimal energy for their dissociation, allowing for the rapid release of stored hydrogen with slight adjustments in pressure and temperature conditions outside the stability zone of the hydrate crystals;
- the hydrate technology is environmentally friendly, as the crystals consist mainly of water molecules;
- they have the potential to store up to 4.2% by mass of molecular hydrogen, which while not very high, is still far greater than many other materials;[241]

Despite these advantages, there are challenges associated with their use as a storage medium, in particular the high pressure required for the formation of pure H_2 hydrate crystals, which for example at a temperature of 273 K requires a pressure of 200 MPa.[242] Although the use of promoters can reduce the pressure required for their formation, none of them has so far allowed this method to meet the technical objectives necessary for its potential use in hydrogen transport and storage.

4.2 Innovative storage methods: high-efficiency molecular matrices

4.2.1 Clathrate hydrate: "the burning ices"

Clathrate hydrates are non-stoichiometric crystalline inclusion compounds, very similar to ice, in which water molecules form a cage structure that traps gas molecules inside them (to date, 130 gas molecules are known that can form clathrate hydrates).[243]

These compounds generally form at low temperatures and high pressures and are held together by weak interactions between the water molecules that make up the various cages and the molecules hosted inside them (there are therefore the so-called guest-host interactions). The water molecules are linked together by hydrogen bonds.

Hydrates are also known as "burning ice", although this expression refers to methane hydrates, which form under drastic conditions of pressure and temperature; when these conditions are lacking, the clathrate cage breaks down, allowing the methane to escape. By subsequently setting fire to the hydrate, as can be seen in Figure 96, a real flame develops, testifying to the release of methane, a highly flammable gas.



Figure 96. A burning methane clathrate.[244]

Hydrates are very versatile compounds that could play a key role in several future energy and environmental technologies; in addition to H_2 storage, their potential uses are truly remarkable, including:

- Storage of CO_2, produced by industrial processes, in the seabed;[245] hydrates, as has been said, are formed under high pressure conditions, which can be found in the depths of the oceans, and can therefore be used as CCS, always paying attention to their stability so as not to cause unwanted release of trapped carbon dioxide, and a consequent negative impact on the marine ecosystem.
- Biogas purification, a mixture of various types of gas, mainly methane and carbon dioxide, produced by bacterial fermentation in anaerobic conditions (absence of oxygen) of organic plant or animal waste.[246] Useful waste can have several origins: waste from the agro-industry (chopped corn, sorghum or other crops), from the food industry (waste flour or expired products), from the livestock industry (animal waste or carcasses); crops specifically grown for the purpose of being harvested and chopped to produce "biomass" can also be used, such as corn, sweet

sorghum, wheat, common cane, beets. However, the biogas produced by the anaerobic digestion of organic waste contains, in addition to methane, also impurities such as CO_2 and water. By bubbling the raw biogas in water, hydrated clathrates can be formed that selectively trap impurities in their structure, allowing purified methane to be obtained.

- Clathrate hydrates can also serve as a system to safely store and transport large quantities of natural gas, since one m^3 of hydrate can in fact contain about 180 m^3 of methane;[247] this would allow the same amount of gas to be stored as a pipeline in much less space and at lower costs. Furthermore, the gas thus stored would be much safer, not being flammable or explosive as in the free state.
- Gas hydrates, thanks to their high formation/dissociation enthalpy and moderate formation conditions (phase change above 0 °C), offer a higher heat capacity and energy efficiency than traditional materials such as ice; for example, the dissociation enthalpy of CO_2 hydrate is sufficiently high (500 kJ/kg) compared to the dissociation enthalpy of ice (333 kJ/kg), indicating that hydrates have a higher thermal storage capacity and energy conversion efficiency. These characteristics could lead to a potential application in the food sector, for example with the rapid cooling of food.[248]
- Seawater desalination: it is a concept first proposed in the 1940s and which received considerable attention in the 1960s and 1970s, which exploits the selective ability of hydrates to trap gas molecules, such as methane or carbon dioxide, leaving fresh water behind. This process has been studied to produce drinking water from seawater and for the treatment of high salinity waters.

4.2.2 History of the clathrate hydrates

The discovery of gas hydrates is due to Sir Humphrey Davy, when in 1810 he coined the term "gas hydrate" after having noticed that a heterogeneous solution of chlorine gas and H_2O formed a solid on top of a layer of ice.[243] In fact, already in 1778 Priestley observed compounds that could have been

clathrate hydrates, but the lack of sufficient evidence makes this discovery unclear and therefore an attribution prior to that of Davy.[249] Later, in 1823, Michael Faraday made an important step forward, formulating the first chemical formula of a gas hydrate and laying the foundations for a more systematic understanding of these compounds.[243] This was a turning point, as it provided researchers with a common language and a conceptual framework to explore gas hydrates more rigorously. An important step was the development of an apparatus by Cailletet in 1878 for high-pressure, low-temperature studies, which allowed investigation of the stability conditions of hydrates, carried out by Villard and De Forcrand.[243] This led to the mapping of equilibrium lines between the various phases and thus to the obtaining of phase diagrams and to the understanding of the processes of dissociation of hydrates. Over time, gas hydrates proved to be not only a fascinating scientific phenomenon but also a practical problem: in 1934, Hammerschmidt noted that these compounds clogged gas pipelines such as the one in Figure 97, thus drawing the attention of industry to the technical challenges they presented.[250]



Figure 97. A gas pipeline clogged with hydrates.

The discovery that very small guests, such as hydrogen and methane, formed Structure II was of considerable importance: using powder neutron diffraction (PXRD) to test the integrity of a sample of methane hydrate, John Tse found that the model fit Structure II.

The determination of crystal structures by X-ray diffraction in 1951[251] made possible the next revolutionary development in hydrate science, the solid-solution thermodynamic model presented by Van der Waals and Platteeuw in 1959.

The discovery of gas hydrates in nature occurred in 1964, when they were identified while drilling a well in Siberia. This event opened people's eyes to the presence and distribution of hydrates in the natural world, suggesting that they may be much more widespread than previously thought.

In the 1970s, the discovery of gas hydrates in ocean sediments further expanded our knowledge of these compounds, revealing that they were also abundant in marine environments. This discovery raised new questions about their formation, stability, and impact on the environment.

The collection of the first gas hydrate samples from marine sediments in the 1980s was another significant step forward. These samples allowed scientists to study the composition and structure of hydrates up close, providing new insights and stimulating further research.

In 1987, the discovery of the H structure,[252] which water formed with numerous guests, many of them hydrocarbons, was made possible by the convergence of several techniques and ideas, which led to new insights into the dynamics and disorder of guests and water molecules, thus providing further insights into guest-host interactions and how these ones influence the properties of hydrates.

In the 1990s, the Ocean Drilling Program began actively searching for sites where hydrates were present. This interest demonstrates how the scientific and industrial community has recognized the importance of gas hydrates, both as a potential energy resource and for their role in climate change and in the stability of submarine slopes.

In recent decades, gas hydrates have remained compounds of great scientific interest, which certainly require further studies and research to fully understand them.

4.2.3 The main structures of gas hydrates

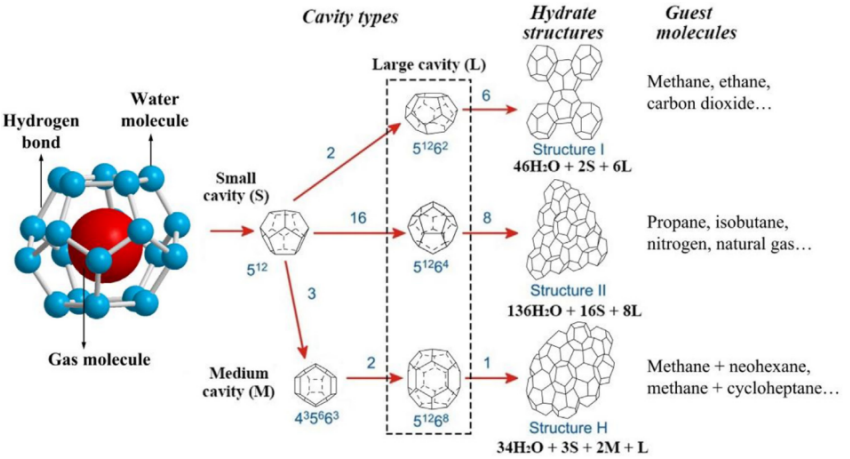


Figure 98. Schematic representation of the clathrate hydrates' structures.[243]

In Figure 98, three basic crystal structures for gas hydrates are represented: structure I (sI), structure II (sII), and structure H (sH). Each of these structures is characterized by a unique configuration of cages that house the gas molecules.

- Structure I, for example, has two types of cages: a small pentagonal dodecahedral cage (S), with 12 pentagonal faces, and a large tetrakaidecahedral cage (L), with 12 pentagonal faces and 2 hexagonal faces. It contains a total of 46 water molecules.[243]
- Structure II contains 136 water molecules and adds further complexity with its large hexadecahedral cage, which includes 12 pentagonal faces and 4 hexagonal faces.[243] The formation of a specific gas hydrate structure depends largely on the size of the guest molecule. For example, methane (CH_4) can fit into both the small and large cages of structure I, while propane (C_3H_8) is too large for the large cage of structure I, but fits

well into the large cage of structure II.[243] Hydrogen alone forms hydrates with the sII structure, and can occupy both the small (up to 2 H_2 molecules) and large cages (up to 4 H_2 molecules).[253]

- The unit cell of the sH structure, which has hexagonal symmetry, contains 36 water molecules and includes three small cages with 12 pentagonal faces, two irregular dodecahedra with 3 square, 6 pentagonal, and 3 hexagonal faces (medium cages), and one large icosahedral cage with 12 pentagonal and 8 hexagonal faces.[243] Typically, sH hydrate is formed with two types of guest molecules: a larger molecule with dimensions between 7.5 and 9 Å occupies the L cages, while small "help gas" molecules occupy the S cages.[243]

Semi-clathrate hydrates

Semi-clathrate hydrates are a particular type of hydrate in which the structure is composed of ionic bonds instead of only hydrogen bonds as in classical clathrate hydrates. This structural difference is due to the presence of guest molecules, generally quaternary ammonium salts, which interact ionically with the water molecules of the lattice.[243]

Mixed hydrates

When there is a mixture with more than one component capable of forming hydrates, we speak of mixed hydrates, in which each of these components will enter, based on its size, into certain specific types of cages of a structure; generally, the larger molecules in a multicomponent mixture occupy the larger cages, and the smaller ones the S cages.[243] In particular, if there are two components, for example hydrogen and THF, we have a binary hydrate, when instead the components are three, we speak of a ternary hydrate and so on.

4.3 Formation and stabilization of clathrate hydrates

The process of formation of hydrates depends essentially on the nature of the host molecule, which influences both the temperature and the pressure necessary for this event.

The thermodynamic aspects of the formation of clathrate hydrates have been well studied and understood, and various models have been hypothesized over the years.

4.3.1 Van der Waals and Platteeuw thermodynamic model

The Van der Waals and Platteeuw (vdW-P) model is a widely used statistical thermodynamic model, developed to correlate, and predict the conditions of hydrate formation.[254]
It is based on some simplifying assumptions:

1. Each hydrate cavity can accommodate only one gas molecule.
2. The trapped molecules do not distort the cavity.
3. The interactions between the trapped molecules can be neglected.
4. A spherical symmetry of the cage is assumed.

In Equation 52 is given the equilibrium between full cage and empty cage:

$$C(avity)_m + G(uest)_j \overset{C_{mj}^{(1)}}{\longleftrightarrow} C_m G_j \tag{52}$$

where:
C: is the m-type cage occupied by guest j
C_{mj}: is the constant governing the entry of the guest into the cage.

The vdW-P model provides an equation for the change in the chemical potential of water in the clathrate caused by the entrapment of guest molecules:

$$\Delta\mu_W^H(T,P) = -RT\sum_m \nu_m \ln\left(1 - \sum_j \theta_{mj}\right) \tag{53}$$

Where:
$\Delta\mu_W^H$: is the change in the chemical potential of water in the clathrate before and after guest enclathration;

R: is the gas constant (J $K^{-1}mol^{-1}$)

T: is the temperature (K)

P: is the pressure (Pa)

ν_m: is the number of m-type cavities per water molecule in the clathrate lattice

θ_{mj}: is the fraction of m-type cavities occupied by guest j

The fraction of m-type cavities occupied by guest j is calculated with a Langmuir adsorption relation, assuming one guest per cavity:

$$\theta_{mj}(T,P,y) = \frac{C_{mj}(T) f_j(T,P,y)}{1 + \sum_{i=1}^{ncomp} C_{mi} f_i(T,P,y)} \tag{54}$$

where:

θ_{mj} is the fraction of m-type cavities occupied by guest j

C_{mj} is the Langmuir constant for guest j in the m-type cavity

fj: is the fugacity of guest j in the liquid phase, which is typically calculated using certain equations of state such as the PC-SAFT EOS (Perturbated chain statistical associating fluid equation of state)[254] or the CPA-EOS (Cubic-Plus associated equation of state, often useful for multicomponent systems).[255]

The Langmuir constant C_{mj} is instead calculated with a simple integration:

$$C_{mj} = \frac{4\pi}{kT} \int_0^{Rcell} \exp(-W(r)/kT)\, r^2 dr \tag{55}$$

where:

k: is the Boltzmann constant

T: is the temperature

W(r): is the spherically symmetric cell potential

Rcell: is the radius of the clathrate cavity

To calculate W(r), potential functions such as the Lennard-Jones or Kihara function are used (preferred in case of multiple cage occupancy).[256,257]
Despite the limitations due to its simplifying assumptions, the vdW-P model is often used for estimating the formation conditions of clathrate hydrates and is incorporated into some commercial process simulators.[258] However, in some cases the standard vdW-P model cannot be applied due to its simplifying assumptions, particularly when there is experimental evidence indicating that in clathrate hydrates with small guest molecules such as H_2, He, N_2 or Ar, multiple molecules can be trapped in each cavity.[254] This multiple occupancy is relevant for some practical applications, such as increasing storage capacity if multiple occupancy occurs.

4.3.2 Kinetic model

The achievement of a kinetic model of gas hydrates represents a fundamental field of study to understand the mechanisms that regulate their formation and dissolution. Despite the importance of these processes, current knowledge on the kinetics of hydrate formation is still limited mainly due to two factors: the intrinsic complexity of the hydrate formation process and the relative novelty of the applicative interest towards the kinetic effects related to hydrates.
The formation of gas hydrates is a process that takes place in several phases, starting with nucleation, that is, the formation of initial aggregates of hydrates of dimensions large enough not to be destroyed by the thermal motions of the molecules, but rather to grow until they form crystals.[243] This process can occur homogeneously, with nuclei formed exclusively by the chemical species that compose the hydrates (water and gas), or heterogeneously, with the intervention of external factors such as rough surfaces or inorganic deposits that act as nucleation sites. It is interesting to note that nucleation occurs mainly at the interface between the gas phase and the liquid phase, since a large amount of water is needed for the formation of hydrates.[243]

Another relevant aspect is the memory effect of hydrates, which indicates how the formation of hydrates on subsequent occasions occurs with increasingly shorter induction times.[259] This suggests that water maintains a certain structuring, favoring the formation of hydrates in the presence of gas. However, this memory effect tends to disappear when the aqueous solution is brought to temperatures above 30-35 °C, due to the destruction of the structures formed by the water induced by the temperature.[259]

The next step after nucleation is the growth of hydrate crystals, a process that is strongly influenced by the agitation of the system. Agitation promotes hydrate formation by clearing the interface of already formed hydrates and increasing the rate of diffusion of the gas into the water. However, the ability to absorb the latent heat associated with hydrate formation can become the limiting factor of the process, especially in plants of significant size.

Although some research groups have proposed models to interpolate experimental data related to the kinetics of hydrate formation, these remain strongly tied to the original data set and are not easily transferable to different systems, indicating that there are still unidentified experimental parameters that influence this kinetics.

4.3.3 Co-Formers

As mentioned above, clathrate hydrates form under specific conditions of pressure and temperature; the presence of certain substances (usually small organic molecules), called co-formers, can significantly influence these conditions, making clathrate formation easier or more stable at higher temperatures or lower pressures than would be required in their absence, and this is particularly useful for practical applications where environmental conditions are not ideal for their natural formation. Co-formers can be classified into two main categories: promoters and inhibitors. Promoters aid in clathrate formation by reducing the pressure and/or temperature required for their formation. Inhibitors, on the other hand, prevent clathrate formation under certain conditions, which can be

useful for preventing unwanted clathrate formation, for example in natural gas pipelines.

4.3.4 Promoters

In the field of gas hydrate formation, two types of promoters play a crucial role: thermodynamic and kinetic promoters.

Thermodynamic promoters, such as tetrahydrofuran (THF), cyclohexane, and propylene oxide, are substances that facilitate hydrate formation by lowering the equilibrium pressures and temperatures required for hydrate formation. This makes the process more favorable under milder conditions, which is advantageous for applications such as gas storage and transportation. However, these co-formers are not without their drawbacks: they must be used in significant quantities, often in high mole percent, which can lead to a decrease in the space available for the gases we are interested in capturing within the hydrate structure. This not only makes the process less efficient, but also raises environmental concerns due to the potential release of these co-formers into the environment.[260]

Kinetic promoters, on the other hand, work according to a different mechanism. These substances, which include surfactants such as sodium lauryl sulfate (SDS) and sodium dodecylbenzene sulfonate, are used to accelerate the rate of hydrate formation by increasing the number of gas-water interfaces, where their formation occurs. Although kinetic promoters can lead to faster gas uptake, they can also result in lower selectivity in the separation process, and this is a trade-off that must be considered.[260]

Thermodynamic promoters of hydrogen hydrates

As regards hydrogen hydrates, the various thermodynamic promoters can favor, based on their characteristics, the formation of one of the three main structures forming binary hydrates H_2 + promoter:

- the sI structure is favored by small molecules such as methane, carbon dioxide, ethane, ethylene oxide and cyclopropane;

- the sII structure is favored by larger molecules, such as tetrahydrofuran, cyclopentane, 1,3-dioxolane and certain gases such as nitrogen and argon, which will occupy the L cages;
- the sH structure is favored by molecules such as 1,1-dimethylcyclohexane, methylcyclohexane methyl-tert-butyl ether and 2,2,3-tetramethylbutane;
- The hydrated semiclathrates are favored by quaternary ammonium salts such as TBAB and TBACl.[261]

However, one aspect to consider is that the above-mentioned molecules occupy part of the cavities, reducing the space available for hydrogen and therefore the overall storage capacity. Further research is therefore needed to optimize the composition of the semi-clathrate hydrates and maximize the trapping efficiency.
Tetrahydrofuran and cyclopentane will be used in the experimental part of this thesis.

Tetrahydrofuran (THF)

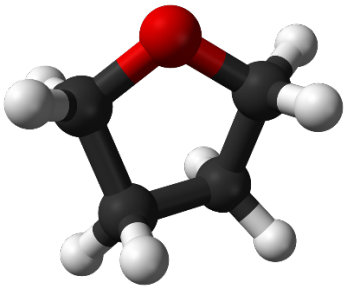


Figure 99. THF structure. Carbon atoms are indicated in black; hydrogen atoms are indicated in white, oxygen atom is indicated in red.

Tetrahydrofuran is a thermodynamic promoter that, as previously reported, together with hydrogen and water leads to the formation of binary hydrates H_2+THF of type sII. THF is a cyclic ether with chemical formula $(CH_2)_4O$ that presents chemical-physical characteristics such as low viscosity, absence of color and solubility in water. Due to its structure (Figure 99) that gives it a

certain polarity, THF mixes easily with polar liquids. Initially, it was thought that hydrogen was not able to form hydrate crystals due to its small molecular size that did not provide the desired crystalline stabilization; however, subsequent studies have shown that the addition of THF can significantly reduce the pressure required for the formation of hydrogen hydrate. Florusse et al. (2004) proposed the use of THF to decrease the pressure required for hydrogen hydrate formation by two orders of magnitude, to 5 MPa at 279.6 K, but this reduced the hydrogen storage capacity to 1 wt%, as THF occupies the larger crystal cages, leaving only the small cages available for hydrogen.[262]

THF is often referred to as a "tuning effect", whereby the hydrogen storage capacity in hydrate crystals can be increased by varying the THF concentration. However, there have been conflicting studies on this tuning effect, with some studies supporting it, reporting a hydrogen storage capacity of up to 4.03 wt% at a THF concentration of 0.15 mol%,[263] while others refute it, finding a maximum capacity of only 1 wt%, regardless of the THF concentration.[264]

Other researchers have examined the effect of porosity on hydrate formation times, and the use of preformed hydrate seeds and liquid nitrogen, as well as nano-emulsions stabilized by amphiphilic molecules to improve formation kinetics.

4.3.5 Inhibitors

Hydrate inhibitors are mostly used in industry to prevent blockages in deep-water oil and gas pipelines; they can be divided into thermodynamic inhibitors (THIs), kinetic inhibitors (KHIs) and anti-caking agents (AAs); THIs, like methanol and some ethylene glycols, alter thermodynamic conditions to make hydrate formation more difficult, but they can be expensive and potentially polluting as they must be used in large quantities; KHIs and AAs are used in lower doses and can be cheaper and less harmful to the environment. In this regard, new types of LDHIs (Low Dosage Hydrate Inhibitors) have been developed that require very low dosages, thus

reducing costs and environmental impact. These include water-based polymers such as poly-N-vinylcaprolactam (PVCap) and poly-N-vinylpyrrolidone (PVP). Research is moving towards green inhibitors such as amino acids, ionic liquids, anti-icing proteins and biodegradable polymers, which are more environmentally friendly, as well as recyclable inhibitors, such as those based on magnetic nanoparticles decorated with organometallic frameworks (MOFs), which can be recovered and reused, offering an environmentally friendly and low-cost approach.[265]

4.3.6 Self-preservation of hydrates

Self-preservation of gas hydrates is a phenomenon of great scientific and technological interest, particularly for its implications on natural gas transport. This phenomenon refers to the ability of gas hydrates to remain stable at atmospheric pressure for extended periods, if they are within a certain temperature range.[266] Studies have shown that there is a temperature zone, between 242 and 271 K, in which hydrates show half-lives on the order of days. Outside this range, particularly at temperatures above 273.15 K, the half-life of hydrates is drastically reduced to a few minutes.[266,267] The discovery of self-preservation has opened new perspectives for the transport of so-called "remote" gas, i.e., gas found in isolated reservoirs or associated with the production of oil fields located in areas far from consumer markets.

4.4 Aim of this work

In light of the energy emergency we are experiencing, the urgency of finding alternative and sustainable solutions to meet our energy needs is increasingly evident. Among all the sources that could represent a concrete response to this challenge, hydrogen emerges as one of the most promising elements. Thanks to its high energy content, hydrogen is establishing itself as one of the main protagonists of the ongoing energy change. It is no coincidence that we increasingly speak of a "hydrogen economy", that is, an

economy that revolves around the use of hydrogen as a primary source of energy.

However, although the potential of hydrogen is widely recognized, its large-scale diffusion is hindered by some technical criticalities, including one of the most relevant: storage. Hydrogen, being a low-density gas, is difficult to store safely and efficiently, representing one of the main brakes on the development of technologies based on it.

In this context, this work aims to address one of the most complex challenges related to the storage of molecular hydrogen, trying to analyze and improve the processes and chemical compositions for its more effective conservation. The use of clathrate hydrates, a technology that offers interesting prospects for storing hydrogen in solid form, in the form of crystalline cages that trap it, reduces the risk of dispersion and improves the overall efficiency of hydrogen storage.

4.5 References

225. Qureshi, F., Yusuf, M. & Abdullah, B. A Brief Review on Hydrogen production to Utilization Techniques. in *2021 Third International Sustainability and Resilience Conference: Climate Change* 66–71 (IEEE, 2021). doi:10.1109/IEEECONF53624.2021.9668127.

226. Hydrogen storage. https://www.energy.gov/eere/fuelcells/hydrogen-storage.

227. Shin, H. K. & Ha, S. K. Techno-economic analysis of type III and IV composite hydrogen storage tanks for fuel cell vehicles. *Advanced Composite Materials* 33, 527–559 (2024).

228. Qureshi, F. *et al.* A State-of-The-Art Review on the Latest trends in Hydrogen production, storage, and transportation techniques. *Fuel* 340, 127574 (2023).

229. Seelam, P. K., Rathnayake, B., Pitkäaho, S., Turpeinen, E. & Keiski, R. L. Overview on recent developments on hydrogen energy: Production, catalysis, and sustainability. in *Current Trends and*

Future Developments on (Bio-) Membranes 3–32 (Elsevier, 2020). doi:10.1016/B978-0-12-817110-3.00001-1.

230. Petitpas, G. & Aceves, S. M. Modeling of sudden hydrogen expansion from cryogenic pressure vessel failure. *Int J Hydrogen Energy* 38, 8190–8198 (2013).
231. Burgess, R. M., Post, M. B., Buttner, W. J. & Rivkin, C. H. *High Pressure Hydrogen Pressure Relief Devices: Accelerated Life Testing and Application Best Practices*. (2017) doi:10.2172/1408284.
232. Aceves, S. M. *et al.* High-density automotive hydrogen storage with cryogenic capable pressure vessels. *Int J Hydrogen Energy* 35, 1219–1226 (2010).
233. Moradi, R. & Groth, K. M. Hydrogen storage and delivery: Review of the state of the art technologies and risk and reliability analysis. *Int J Hydrogen Energy* 44, 12254–12269 (2019).
234. Preuster, P., Papp, C. & Wasserscheid, P. Liquid Organic Hydrogen Carriers (LOHCs): Toward a Hydrogen-free Hydrogen Economy. *Acc Chem Res* 50, 74–85 (2017).
235. Xia, Y., Yang, Z. & Zhu, Y. Porous carbon-based materials for hydrogen storage: advancement and challenges. *J Mater Chem A Mater* 1, 9365 (2013).
236. Anik, M., Karanfil, F. & Küçükdeveci, N. Development of the high performance magnesium based hydrogen storage alloy. *Int J Hydrogen Energy* 37, 299–308 (2012).
237. Zinatloo-Ajabshir, S., Morassaei, M. S., Amiri, O., Salavati-Niasari, M. & Foong, L. K. Nd2Sn2O7 nanostructures: Green synthesis and characterization using date palm extract, a potential electrochemical hydrogen storage material. *Ceram Int* 46, 17186–17196 (2020).
238. Zinatloo-Ajabshir, S., Salehi, Z., Amiri, O. & Salavati-Niasari, M. Simple fabrication of Pr2Ce2O7 nanostructures via a new and eco-

friendly route; a potential electrochemical hydrogen storage material. *J Alloys Compd* 791, 792–799 (2019).

239. Gencer, A., Surucu, G. & Al, S. MgTiO3Hx and CaTiO3Hx perovskite compounds for hydrogen storage applications. *Int J Hydrogen Energy* 44, 11930–11938 (2019).
240. Lahlou Nabil, M. A., Fenineche, N., Popa, I. & Sunyol, J. J. Morphological, Structural and Hydrogen Storage Properties of LaCrO3 Perovskite-Type Oxides. *Energies (Basel)* 15, 1463 (2022).
241. Zacharia, R. & Rather, S. ullah. Review of Solid State Hydrogen Storage Methods Adopting Different Kinds of Novel Materials. *J Nanomater* 2015, (2015).
242. Davoodabadi, A., Mahmoudi, A. & Ghasemi, H. The potential of hydrogen hydrate as a future hydrogen storage medium. *iScience* 24, 101907 (2021).
243. Sloan Jr., E. D., Koh, C. A. & Koh, C. A. *Clathrate Hydrates of Natural Gases*. (CRC Press, 2007). doi:10.1201/9781420008494.
244. Siažik, J., Malcho, M. & Lenhard, R. Proposal of experimental device for the continuous accumulation of primary energy in natural gas hydrates. *EPJ Web Conf* 143, 02106 (2017).
245. Fahed Qureshi, M. *et al.* Laboratory demonstration of the stability of CO2 hydrates in deep-oceanic sediments. *Chemical Engineering Journal* 432, 134290 (2022).
246. Filarsky, F., Schmuck, C. & Schultz, H. J. Development of a biogas production and purification process using promoted gas hydrate formation — A feasibility study. *Chemical Engineering Research and Design* 134, 257–267 (2018).
247. *Managing Impacts of Deep Sea Resource Exploitation Methane from Marine Gas Hydrates*. www.eu-midas.net.
248. Claßen, T. *et al.* Review on the food technological potentials of gas hydrate technology. *Curr Opin Food Sci* 29, 48–55 (2019).

249. T. Pearson. *Experiments and Observations on Different Kinds of Air and Other Branches of Natural Philosophy Connected with the Subject (in Three Volumes)*. (1790).
250. Hammerschmidt, E. G. Formation of Gas Hydrates in Natural Gas Transmission Lines. *Ind Eng Chem* 26, 851–855 (1934).
251. v. Stackelberg, M. Feste Gashydrate. V Die Bindungsenergien. *Zeitschrift für Elektrochemie, Berichte der Bunsengesellschaft für physikalische Chemie* 58, 104–109 (1954).
252. Ratcliffe, C. I. The Development of Clathrate Hydrate Science. *Energy & Fuels* 36, 10412–10429 (2022).
253. Cai, W., Huang, X. & Lu, H. Instrumental Methods for Cage Occupancy Estimation of Gas Hydrate. *Energies (Basel)* 15, 485 (2022).
254. Martín, Á. A Simplified van der Waals-Platteeuw Model of Clathrate Hydrates with Multiple Occupancy of Cavities. *J Phys Chem B* 114, 9602–9607 (2010).
255. Tzirakis, F., Karakatsani, E. & Kontogeorgis, G. M. Evaluation of the Cubic-Plus-Association Equation of State for Ternary, Quaternary, and Multicomponent Systems in the Presence of Monoethylene Glycol. *Ind Eng Chem Res* 55, 11371–11382 (2016).
256. Avlonitis, D. The determination of kihara potential parameters from gas hydrate data. *Chem Eng Sci* 49, 1161–1173 (1994).
257. Chen, X. & Li, H. New pragmatic strategies for optimizing Kihara potential parameters used in van der Waals-Platteeuw hydrate model. *Chem Eng Sci* 248, 117213 (2022).
258. Strobel, T. A., Koh, C. A. & Sloan, E. D. Thermodynamic predictions of various tetrahydrofuran and hydrogen clathrate hydrates. *Fluid Phase Equilib* 280, 61–67 (2009).
259. Kou, X., Feng, J.-C., Li, X.-S., Wang, Y. & Chen, Z.-Y. Memory effect of gas hydrate: Influencing factors of hydrate reformation and dissociation behaviors. *Appl Energy* 306, 118015 (2022).

260. Majid, A. A. A., Worley, J. & Koh, C. A. Thermodynamic and Kinetic Promoters for Gas Hydrate Technological Applications. *Energy & Fuels* 35, 19288–19301 (2021).
261. Saikia, T., Patil, S. & Sultan, A. Hydrogen Hydrate Promoters for Gas Storage—A Review. *Energies (Basel)* 16, 2667 (2023).
262. Florusse, L. J. *et al.* Stable Low-Pressure Hydrogen Clusters Stored in a Binary Clathrate Hydrate. *Science (1979)* 306, 469–471 (2004).
263. Zhang, Y., Bhattacharjee, G., Kumar, R. & Linga, P. Solidified Hydrogen Storage (Solid-HyStore) via Clathrate Hydrates. *Chemical Engineering Journal* 431, 133702 (2022).
264. Strobel, T. A., Koh, C. A. & Sloan, E. D. Hydrogen storage properties of clathrate hydrate materials. *Fluid Phase Equilib* 261, 382–389 (2007).
265. Zhao, J., Lang, C., Chu, J., Yang, L. & Zhang, L. Flow Assurance of Hydrate Risk in Natural Gas/Oil Transportation: State-of-the-Art and Future Challenges. *The Journal of Physical Chemistry C* 127, 13439–13450 (2023).
266. Majid, A. A. A. & Koh, C. A. Self-preservation phenomenon in gas hydrates and its application for energy storage. in *Intra- and Intermolecular Interactions Between Non-covalently Bonded Species* 267–285 (Elsevier, 2021). doi:10.1016/B978-0-12-817586-6.00008-6.
267. Dieing, T. , H. O. , & T. J. *Confocal Raman Microscopy*. vol. 66 (2018).

CHAPTER 5

Hydrogen storage: experimental section

5.1 Investigation of tuning effect of THF-H_2 binary clathrates

5.1.1 *Introduction*

The main objective of this work is to explore the potential of clathrate hydrates as a storage system for hydrogen, a key element for the development of future energy technologies. Hydrogen, in fact, is one of the most promising elements in the field of renewable energies, but the challenges related to its safe and efficient storage are still considerable. Clathrate hydrates, which are crystalline structures capable of trapping gas molecules within a network of water molecules, represent a potentially revolutionary solution to this problem.

The specific objectives of this experimentation are mainly two. First, a method for the preparation of reversed-phase micro-emulsions has been developed, which act as enhancers in the process of formation of binary hydrates, specifically between hydrogen and tetrahydrofuran (THF). This step is crucial because micro-emulsions can improve the efficiency of the hydrate formation process, increasing the exchange surface between the

water phase and the hydrate phase, and consequently the amount of hydrogen that can be trapped in the crystalline cages.

The second objective concerns the deepening of the tuning effect of the THF co-former. THF is a molecule that, in combination with water, facilitates the formation of hydrates. However, one of the main challenges is to control its concentration. By limiting the amount of THF, in fact, we can increase the amount of molecular hydrogen (H_2) that can be trapped inside the hydrate cages, without compromising the stability of the structure and maintaining, at the same time, favorable pressure and temperature conditions for the formation of the clathrate. In other words, the idea is to optimize the composition of the system to maximize the efficiency of hydrogen storage, without requiring extreme conditions that can complicate the industrial management of the process.

In conclusion, this work tries to address and solve some of the main issues related to hydrogen storage, combining chemical innovation and applied research.

5.1.2 *Materials and methods*

The anionic surfactant Sodium Dioctyl Sulfosuccinate or AOT, to obtain reverse micelles was purchased from Sigma-Aldrich. Anhydrous Isooctane 99.8% purchased from Sigma-Aldrich was used as the dispersing or external organic phase. Hydrogen H2 was supplied by Alphagaz 1, (Air Liquide); while ultra-pure water (0.05 lS) came from an Elix 3 ion exchanger model Millipore. Finally, THF ≥ 99.9% purchased from Sigma-Aldrich was used as the clathrate co-former.

Dynamic Light Scattering (DLS) was used during the preparation of the reversed-phase micro-emulsion, the presence of micelles in solution can be monitored and detected by spectroscopic analysis, starting from the principle that micelles represent a nanoscopic heterogeneous entity that interacts with radiation in different ways. In our case, Dynamic Light Scattering (DLS, Brookhaven, ZetaPlus) was used to detect the presence of micelles, this tool also provides information on their quantity and size

distribution. The measurements were carried out starting from 1.5 ml of organic solution inserted into quartz cuvettes with an optical path of 1 cm, to which water and then THF were added drop by drop, using a variable volume micropipette in the range 2-20 μL calibrated at 20 μL. Inside the DLS, the cuvette was housed in an aluminum cell holder, whose temperature was regulated by a Peltier element and set at 25 °C. The light source was a He-Ne ion laser operating at a wavelength of 635 nm. The light was scattered at 90° to the cuvette and collected by a coherence area and imaged on a photomultiplier tube. The autocorrelation function was used to calculate and display the scattering coefficient, D, and associated derived parameters from cumulant analysis that fit the intensity autocorrelation function.

Hydrate formation was performed in a fully controlled AISI 316L stainless steel reactor (HM3), designed and assembled by RDPower srl (Terni, Italy), having an internal volume of 500 ml, with operating pressures reaching 20 MPa. The reactor was equipped with a Peltier cooling/heating unit that allowed operating temperature ranges from 253 K to 353 K. A chiller with a cooling power of 1000 W was used as a heat sink for the Peltier unit. The contents were stirred with a magnetically coupled stirrer rod at 150 rpm. The experiment was carried out in pressure drop with operating pressures of approximately 100 bar. A micro-dosing valve of the CC series (Tescom, USA) was also present in the plant, with which the gas flow could be measured by means of a thermo-mass flow meter of the F131M series (Bronkhorst High-Tech B.V., The Netherlands) with a measuring range of 5–500 NmL/min and an operating pressure of 40 mPa, but its use was not necessary when working in pressure drop. Potentially, constant pressure operation could also be achieved by refueling the reactor with gas during hydrate formation using a combination of a Kammer electropneumatic actuator and a low-flow ball valve, both from Flowserve (USA), but in this case, for the same reason, its use was not necessary.

The reactor was also equipped with a 4–20 mA pressure transducer (Gems Sensors & Controls, UK) with a measuring range of 0–25 MPa. Two additional pressure transducers were mounted along the gas loading line to

measure the pressure during the loading process. PT100 class 1/3 DIN resistive temperature detectors (RTD) (OMEGA Engineering, INC., USA) were also installed. A process controller for pressure, temperature and gas flow was assembled using an Arduino microcontroller (arduino.cc). This controller reads the temperatures of each reactor and drives the Peltier power supply to apply cooling or heating power when required. The temperature set-point was maintained using a PID algorithm integrated into the Arduino controller. A schematic of the experimental setup is shown in Figure 100.

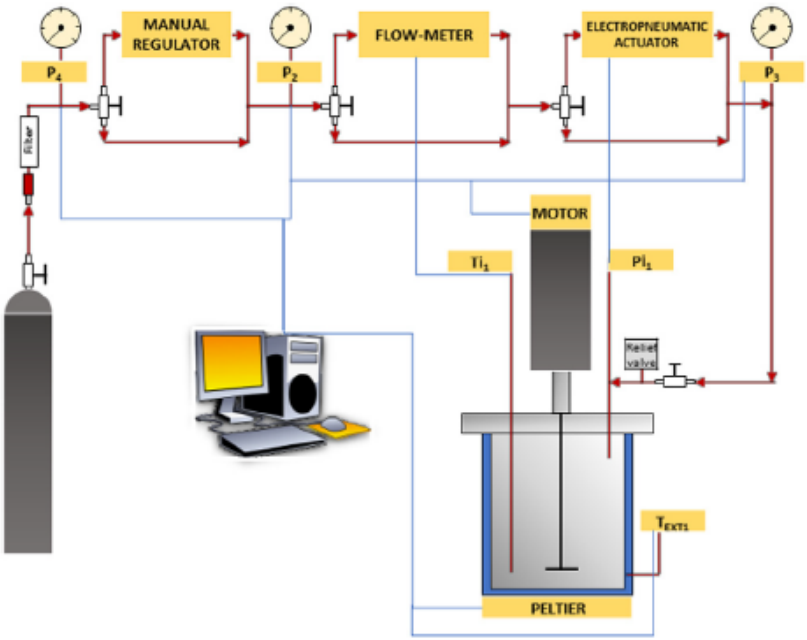


Figure 100. Schematic representation of the apparatus used.

5.1.3 *Discussion and characterization*

Micro-emulsions used for clathrate formation

A total of five different 100 ml preparations were created and introduced into the clathrate formation plant. The compositions of the emulsions are reported in Table 14. The only variable in these systems was the percentage of THF. The stoichiometric concentration of THF in relation to water reported in the literature, equal to 5.56 mol%,[268] was assumed as the solubilized in the other solutions were then calculated to obtain percentages of 80-60-40-20% compared to the reference one.

Table 14. Microemulsions compositions.

% THF referred to the stoichiometric concentration	THF volume	H_2O volume	Organic dispersing phase of 0.1 M AOT in isooctane
100%	5,586 mL	9.778 mL	84.635 mL
80%	4.469 mL	9.778 mL	85.753 mL
60%	3.351 mL	9.778 mL	86.871 mL
40%	2.234 mL	9.778 mL	87.998 mL
20%	1.117 mL	9.778 mL	89.105 mL

Starting from the molar stoichiometric concentration of the reference THF, the others were obtained through proportions, the volume of THF progressively reduced was compensated by adding an equal volume of organic dispersing phase.
To trace the volume of water to be inserted in the five preparations, a small sample of micro-emulsion monitored by DLS was prepared.

Micro-emulsion sample preparation method

To prepare the W/O micro-emulsion system, we started with a volume of 1.5 ml of dispersing organic phase of Isooctane and AOT 0.1 M inserted inside a quartz cuvette. Using a micropipette calibrated at 20 μL, ultra-pure water was added drop by drop, subjecting the preparation to stirring for a time of

about 3 minutes after each addition. As a reference on the maximum volume of water to be added, the stability region of the inverse micelles was considered, which can be evaluated by the Gibbs equation on the interfacial tension. The value of W_0, i.e., the molar ratio between water and surfactant, of a reversed-phase micellar system that is in the stability region is typically around $W_0 = 80$. By subjecting the micro-emulsion system to DLS analysis following each addition, it was observed that the system remained stable up to a $W_0 = 64$, i.e., until a volume of water equal to 173.25 μL was added. Once this volume was exceeded, the micro-emulsion became cloudy and tended to phase separation. Finally, the THF co-former was added, again using the dropwise method, until the maximum volume at which the dispersion was still stable was reached. Also, in this case, the evolution of the micro-emulsion was observed following each addition using DLS analysis. Each DLS analysis was performed in triplicate. In the following Table 15 and Table 16, the data obtained from the DLS analyses on the micellar populations obtained are reported; the average diameters of the micelles are described and information on the quantity and distribution of the micellar populations is provided.

Table 15. Characteristics of micellar populations of 0.1 M AOT in isooctane and water.*

H_2O volume	Averge diameter	Standard Error±dm	Polydispersity (pd)	Standard Error±pm	Average particle counting rate per second	W_0
132 µL	20,2 nm	±0,1 nm	0,115	±0,009	113,1 Kcps	48,7
140,25 µL	20,7 nm	±0,01 nm	0,111	±0,008	159,9 Kcps	51,7
148,5 µL	21,6 nm	±0,01 nm	0,129	±0,011	227,7 Kcps	54,7
156,75 µL	22,5 nm	±0,1 nm	0,098	±0,006	287,4 Kcps	57,8
165 µL	23,1 nm	±0,1 nm	0,116	±0,009	379,5 Kcps	60,0
173,25 µL	24,5 nm	±0,1 nm	0,098	±0,010	492,5 Kcps	63,9

*Selected parameters:

$d_{H_2O}^{25°C} =$ 0,997 g/mL

$V_{drop} =$ 8.25 µL

The volume chosen for the preparation of the micro-emulsion was:

$$V_{21\ \text{drops}} = (8.25\ \mu\text{L} \cdot 21) = 173.25\ \mu\text{L}$$

The proportion to be set to calculate the volume of water to be inserted in 100 mL is:

$$water\ in\ the\ cuvette : total\ solution\ in\ the\ cuvette = x : 100\ mL$$

$$0.1733\ \text{mL} : 1.772\ \text{mL} = x : 100\ \text{mL}$$

$$x = 9.778\ \text{mL}\ H_2O$$

Table 16. Characteristics of micellar populations of 0.1 M AOT in 0.173 mL water and THF.*

THF volume	Averge diameter	Standard Error±dm	Polydispersity (pd)	Standard Error±pm	Average particle counting rate per second
8,25 µl	25,5 nm	±0,1 nm	0,102	±0,006	389,6 Kcps
16,5 µl	27 nm	±0,1 nm	0,118	±0,005	519,8 Kcps
24,75 µl	30,1 nm	±0,2 nm	0,140	±0,008	254,4 Kcps
33 µl	34 nm	±0,2 nm	0,133	±0,010	295,7 Kcps
41,25 µl	39 nm	±0,5 nm	0,139	±0,005	388,4 Kcps
49,5 µl	44,9 nm	±0,7 nm	0,134	±0,007	458,3 Kcps
57,75 µl	53 nm	±1,5 nm	0,126	±0,009	519,1 Kcps
66 µl	67,4 nm	±1,8 nm	0,125	±0,005	321,1 Kcps
74,25 µl	81,9 nm	±2,8 nm	0,105	±0,026	397,0 Kcps
82,5 µl	109,7 nm	±3,4 nm	0,070	±0,008	467,5 Kcps
90,75 µl	146,8 nm	±4,9 nm	0,078	±0,018	653,4 Kcps
99 µl	210,1 nm	±9,4 nm	0,065	±0,013	695,1 Kcps

*Selected parameters:

$d_{H_2O}^{20°C} =$ 0,889 g/mL

$V_{drop} = 8.25$ µL

The volume chosen for the preparation of the micro-emulsion was:

$$V_{12\ drops} = (8.25\ \mu L \cdot 12) = 99\ \mu L$$

This volume allows us to obtain, in the dispersion, the stoichiometric concentration of THF reported in the literature.

$$THF\ in\ the\ cuvette : total\ solution\ in\ the\ cuvette = x : 100\ mL$$

$$0.099\ mL : 1.772\ mL = x : 100\ mL$$

$$x = 5.586\ mL\ THF$$

Finally, we can get back to the volume of Isooctane and AOT 0.1 M by proportion:

$$0.1\ \text{M AOT in isooctane (V)} : \text{H}_2\text{O and THF (V)} = x : 15.364\ mL$$

$$1.5\ \text{mL} : 0.2723\ \text{mL} = x : 15.364\ \text{mL}$$

$$x = 84.365\ \text{mL dispersing organic phase in 100 mL emulsion}$$

The volumes to be used in subsequent 100 ml preparations which progressively reduce the percentage of THF present are obtained through proportions starting from the preparation just described.

Induction and clathrate formation method

To induce clathrate formation, controlled pressures and temperatures are required, maintained within a certain range of values. With respect to temperature, we started from a temperature of 8 °C in order to be sure of being outside the clathrate formation curve. At this T, we proceeded with the saturation of the reactor by loading up to approx. 100 bars of hydrogen inside. The magnetically coupled stirring shaft was then activated at 150 rpm, which kept the micro-emulsion stirring inside. At this point, we proceeded by lowering the temperature by 1 °C every hour until reaching approximately −4 °C, the temperature at which clathrate formation was observed in almost all the tests carried out. Since hydrates are intrinsically stochastic systems with respect to induction times, i.e., governed by probabilistic and non-deterministic laws, the timing of the experiments was quite variable, ranging from a few hours to a few days. These experiments were performed in triplicate, the reported results are derived from their mean and have an average variance below 3%. The clathrate formation event is clearly visible since there is a sudden increase in temperature inside the reactor, justified by the fact that clathrate formation is an exothermic process, which is accompanied by a moderate gas absorption, justified by the fact that hydrogen is trapped inside the cages at the time of their formation.

Data analysis

The clathrates adsorption pressures were deducted from the pressure drop recorded by the pressure detector inside the reactor.
A systematic analysis of the data obtained for each of the five preparations subjected to clathrate formation is carried out. Five graphs with a double Y-axis were created in order to describe the pressure and temperature trends as a function of the clathrate formation time (X-axis).
Figures 101, 102, 103, 104, and 105 show the signals of formation of the hydrate structure from the emulsion containing respectively 100%, 80%, 60%, 40%, and 20% of stoichiometric concentration of THF.
A peak of temperature is associated with the pressure drop that occurs approximately at −4 °C. The two pressure and temperature peaks are perfectly synchronized to confirm the effective formation of the clathrate, an event characterized by an increase in temperature inside the reactor due to the exothermic process characteristic of the crystallization of the hydrate, with a reduction in the entropy of the system, since the reticular organization of the water molecules occurs to form the cages of the clathrate. The pressure reduction inside the reactor is particularly evident and caused by the trapping of hydrogen gas inside the clathrate formed. The gas equation of state (Equation 56) was used to calculate the moles of gas absorbed by the hydrate, the mass of H_2 in the hydrate, thus the gravimetric percentage yield.

$$PV = znRT \tag{56}$$

Where:
P: pression (Pa)
V: volume (m^3)
z: compressibility factor (1.001)
n: moles of gas (mol)
R: gas constant ($J\ K^{-1}mol^{-1}$)
T: temperature (K)

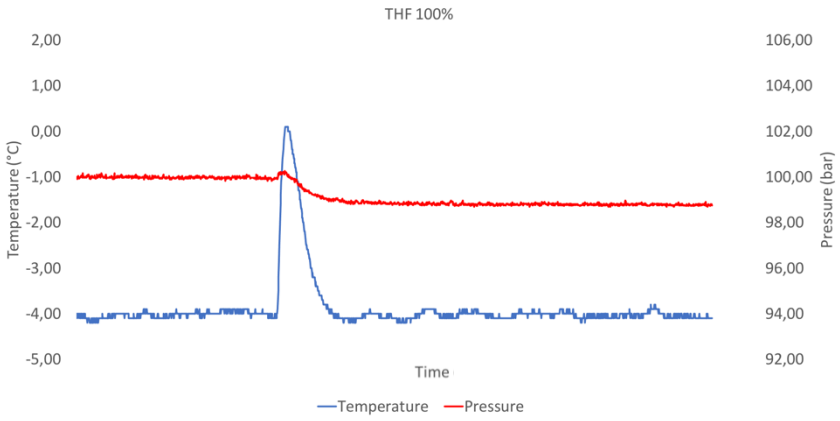


Figure 101. Formation conditions of 100 bar and −4 °C of the hydrate containing 100% THF stoichiometric concentration.

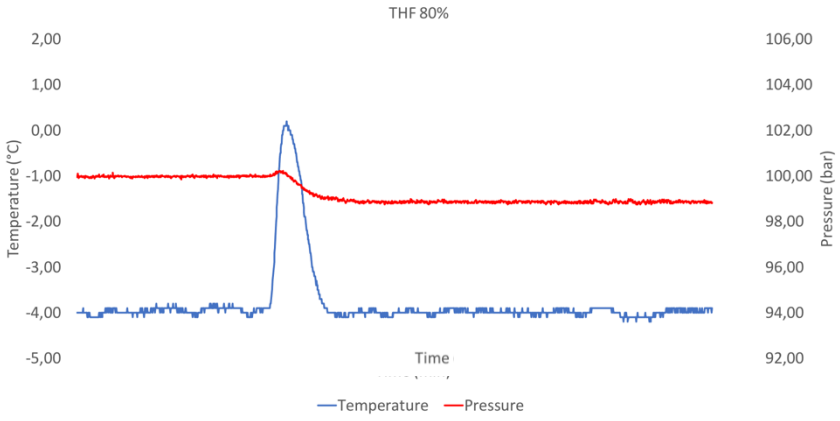


Figure 102. Formation conditions of 100 bar and −4 °C of the hydrate containing 80% THF stoichiometric concentration.

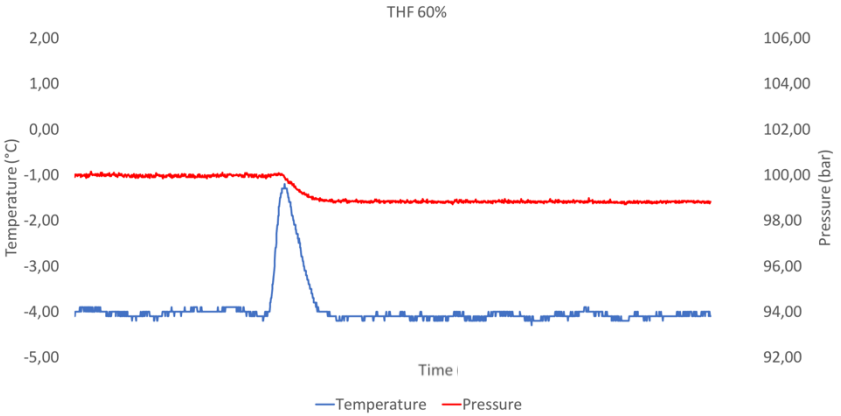


Figure 103. Formation conditions of 100 bar and −4 °C of the hydrate containing 60% THF stoichiometric concentration.

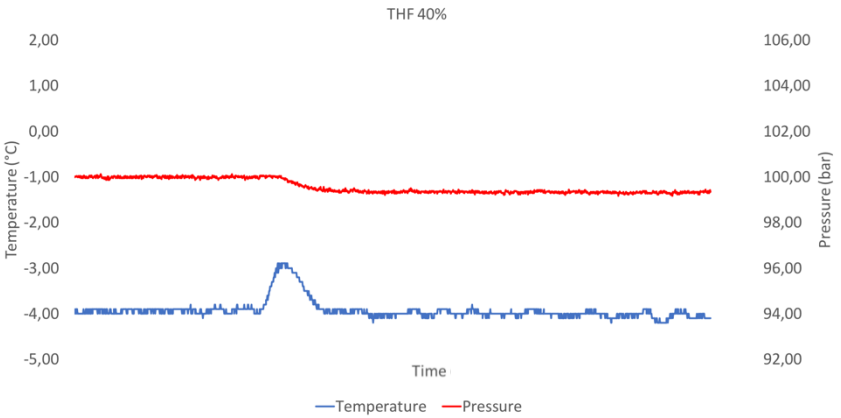


Figure 104. Formation conditions of 100 bar and −4 °C of the hydrate containing 40% THF stoichiometric concentration.

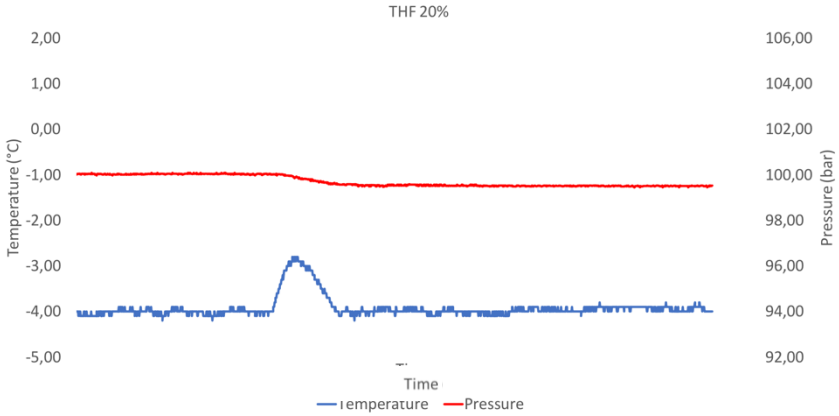


Figure 105. Formation conditions of 100 bar and −4 °C of the hydrate containing 20% THF stoichiometric concentration.

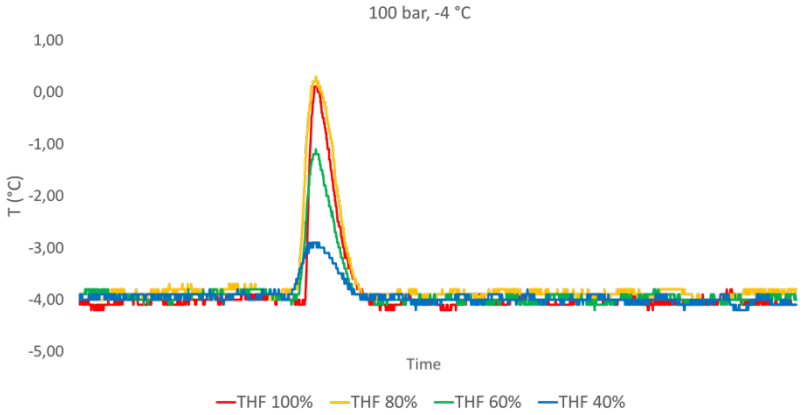


Figure 106. Temperature rise derived from the hydrates' formation containing 100-80-60-40 % of the stoichiometric concentration of THF at constant pressure (100 bar) and temperature (−4 °C).

Figure 106 shows the temperature increase curves following the formation of the hydrate structure from emulsions containing 100, 80, 60, and 40% of the stoichiometric concentration of THF.

From the graphs obtained, in line with the decrease in THF concentration contained in the emulsions, a progressive decrease in the thermal rise is observed during the formation of the hydrate. This is especially observable

in emulsions containing 40 and 20% of the stoichiometric concentration of THF, where the promoting effect of THF is reduced. Furthermore, the decrease in thermal rise is believed to be partly due to compensation by the reactor cooling system, confirming a slow and more controlled formation kinetics.

In the sample containing 20% of the stoichiometric concentration of THF, the instrument was not able to detect the exothermic peak because the formation of the clathrate occurred very slowly, there was no perceptible heat development because the cooling system completely compensated for the temperature increase. The process was not very exothermic and also in this case it is possible to attribute the cause to the reduced quantity of THF present as a co-former and therefore promoter of the formation of the clathrates. It was possible to trace the actual formation of the hydrate thanks to a slight peak of pressure drop. In Figure 107 the pressure drops of the hydrates containing 100-80-60-40 % of the stoichiometric concentration of THF are shown.

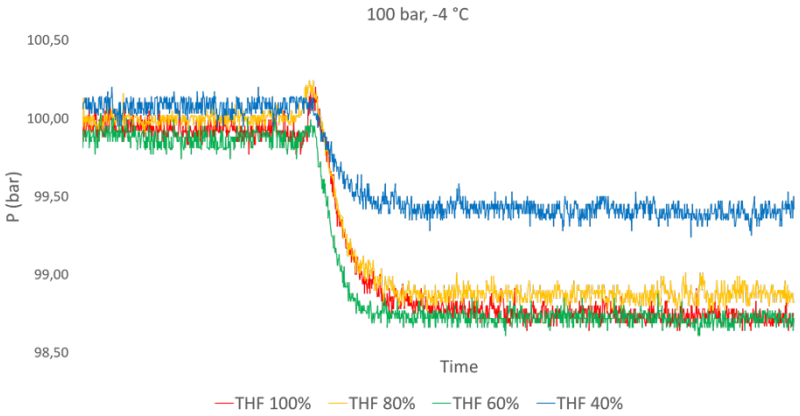


Figure 107. Pressure drop of the hydrate containing 100-80-60-40 % of the stoichiometric concentration of THF at constant pressure (100 bar) and temperature (−4 °C).

Tables 17 and 18 show, respectively, the pressure drop values and hydrogen adsorption results in clathrates obtained at different % of THF coformer.

Table 17. Hydrate adsorption pressures.

% THF	THF volume	Pressure drop
100%	5,586 mL	1.20 bar
80%	4.469 mL	1.12 bar
60%	3.351 mL	1.15 bar
40%	2.234 mL	0.70 bar
20%	1.117 mL	0.45 bar

Table 18. Hydrogen absorption results in clathrates obtained at different % of THF coformer.

% THF	n_{H_2}	m_{H_2}	yield
100%	0.0217 mol	0.043 g	0.44 wt%
80%	0.0202 mol	0.0405 g	0.41 wt%
60%	0.0207 mol	0.0416 g	0.42 wt%
40%	0.0126 mol	0.0253 g	0.26 wt%
20%	0.0081 mol	0.0162 g	0.17 wt%

5.1.4 *Conclusions*

From the study and the data obtained, it is possible to observe an interesting result regarding the percentage yield of absorbed gas in relation to the concentration of water present. In particular, we can note how the percentage yield of absorbed gas, expressed as wt%, is almost comparable in the preparations containing THF at concentrations of 100%, 80% and 60%. This result confirms our expectations regarding the tuning effect of the co-former: in fact, the presence of THF, both at its maximum stoichiometric concentration and in a moderate sub-stoichiometric concentration, is able to guarantee a similar absorption of hydrogen. This suggests that the co-former, although present at lower concentrations, does not significantly

compromise the effectiveness of the storage process. Even by slightly increasing the working pressures, an increase in the absorption yield could be appreciated at THF concentrations lower than the stoichiometric one, while maintaining pressure and temperature conditions still considered mild for a future scale-up. This would allow for more space to accommodate the hydrogen inside the crystalline cages, further optimizing the storage process.

The method used for the production of binary hydrogen hydrates showed a moderate, but interesting, efficiency in terms of gravimetric H_2 storage. In fact, this approach allowed a hydrogen storage of approximately 0.5 wt%, calculated by integrating high-precision gas flow data. According to the scientific literature, this value corresponds to a usable energy content that exceeds the one stored in a 20 MPa hydrogen tank of the same weight. This demonstrates that our method, despite being moderate in its performance, offers a very interesting energy storage capacity.

Another aspect that deserves attention is the kinetics of the process, which turned out to be very fast compared to other processes described in the literature. For example, our process clearly differs from that involving the pressurization of a previously formed solid co-former hydrate. This rapidity of the process is probably related to the enormous increase in the surface-to-volume ratio of the available water, which facilitates interactions with dissolved hydrogen in the bulk organic phase. In other words, a larger contact surface allows a faster reaction and a more efficient absorption.

Finally, it is important to highlight the crucial role of the coformer in the stabilization of the large cages inside the hydrogen hydrates. The co-formant not only facilitates the formation of the hydrates but is also essential to keep the crystalline structures stable, allowing to trap a greater amount of hydrogen without compromising the stability of the system.

In conclusion, the obtained results suggest that our approach offers promising prospects for the improvement of hydrogen storage technologies, with a fast formation kinetics and a good storage capacity, paving the way for future process optimizations.

5.2 References

268. Gupta, A. *et al.* Hydrogen Clathrates: Next Generation Hydrogen Storage Materials. *Energy Storage Mater* **41**, 69–107 (2021).

Posters and Orals

1. *"Clathrate Hydrates for the Separation of CO_2 and CH_4 from Biogas: Study of Potential Kinetic Promoters*", European Conference on Gas Hydrate 2022, Lyon (FR) – Poster

2. *"Improvement of hydrogen clathrate formation by reverse micelles and optimization of kinetic parameters by tuning the THF concentration"*, Journées du GDR 2022, Rueil-Malmaison (FR) – Oral presentation

3. *"Potential Kinetic Promoters for CO_2/CH_4 Separation: IR in-situ Raman determinations",* European Conference on Gas Hydrate 2024, Trieste, IT – Poster

4. *"Basic Solvents for High-pressure CO_2-containing Streams: Experimental Investigations and Energy Evaluations"*, SPE Europe Energy Conference & Exhibition, Turin, IT – Oral

5. *"Non-conventional, low energy strategies for carbon capture and storage and upgrading of strategic gases",* ASU School of Sustainable Engineering and the Built Environment, Arizona State University, Tempe, AZ – Oral

Publications

1. *"Preparation of Fe_3O_4-Reduced Graphene-Activated Carbon from Wastepaper in the Dispersive Solid-Phase Extraction and UHPLC-PDA Determination of Antibiotics in Human Plasma"*, Separation, 10(2), 115.

   Pantaleone Bruni, Pasquale Avino, Vincenzo Ferrone, Serena Pilato, Nadia Barbacane, Valentino Canale, Giuseppe Carlucci, Stefania Ferrari

2. *"Emerging green strategies for biogas upgrading through CO2 capture: From unconventional organic solvents to clathrate and semi-clathrate hydrates",* Journal of Molecular Liquids, Volume 391, part A.

   Pietro Di Profio, Michele Ciulla, Stefano Di Giacomo, Nadia Barbacane, Rafal Damian Wolicki, Antonella Fontana, Samanta Moffa, Serena Pilato, Gabriella Siani

3. *"Basic Sorbents for High-pressure CO_2-Containing Streams: Experimental Investigations and Energy Evaluations",* Paper presented at the SPE Europe Energy Conference and Exhibition, June 26-28, 2024, Turin, Italy.

   Nadia Barbacane, Michele Ciulla, Stefano Di Giacomo, Rafal Damian Wolicki, Beatrice Castellani, Gabriella Siani, Serena Pilato, Samanta Moffa, Pietro Di Profio

4. *"Possible Alternative to Established CCS Technologies: Technical and Economical Evaluation",* Paper presented at the Mediterranean Offshore Conference, October 20-22, 2024, Alexandria, Egypt.

   Rafal Damian Wolicki, Nadia Barbacane, Michele Ciulla, Simone Arca, Emilio D'Alessandro, Piergiorgio Parisi, Francesco Morodei, Pietro Di Profio

Acknowledgments

My deepest and heartfelt gratitude goes to Prof. Pietro Di Profio, my friend and thesis supervisor, for his constant encouragement, patience, and guidance throughout the entire duration of this work. He has consistently given me space to express my ideas and creativity, making me feel like a point of reference within our team since the very beginning of this journey. Under his guidance, I have had a genuinely formative experience on both a professional and personal level. He is always ready to offer encouragement during moments of uncertainty and I am immensely grateful to him for giving me the freedom to choose Arizona as a foreign destination, as this experience has been one of my greatest dreams I have ever realized.

I would also like to express my deepest gratitude to Prof. Dennis Lichtenberger, my tutor at the University of Arizona in Tucson, for hosting me during a significant portion of my doctoral research. The academic environment, resources, humanity and the warm welcome I received from faculty and staff greatly enriched my experience during a very hard time of my private life. My time at the University of Arizona was both productive and inspiring, and I am incredibly thankful for the opportunity to be part of such a vibrant academic community.

I am also sincerely grateful to DG Impianti Industriali SpA for their generous support and sponsorship throughout my PhD journey. Their commitment to research and innovation not only made this work possible but also provided me with invaluable opportunities for professional growth and practical insight. I am especially thankful to my colleagues and mentors at DG Impianti Industriali SpA for their encouragement, guidance, and collaborative spirit during every stage of this project.